Dynamics and Oligomerisation of ABCG2 Investigated Using Various Fluorescence Techniques

Kelvin Wong, MPharm.

Thesis submitted to the University of Nottingham
for the degree of Doctor of Philosophy

July 2015

Abstract

The human ABCG2 (second member of ABC transporter G-subfamily) is an important ATP-dependent exporter in the body with broad substrate specificity including xenobiotics (e.g. anticancer agents) and endogenous compounds (e.g. sterols and lipids). ABCG2 was first discovered in a multidrug resistant breast cancer cell line and it is suggested to cause resistance to chemotherapy in certain cancers such as acute myeloid leukaemia and small cell lung cancer. Physiologically, ABCG2 is found in the protective sanctuary sites of the body, for instance the gut and blood-brain-barrier, affecting pharmacokinetics and treatment efficacies of small molecule drugs. Structurally, the polypeptide chain of ABCG2 contains a single nucleotide binding domain and a single transmembrane domain, which is half the number of domains required for a fully functional ABC transporter. Although many have suggested that ABCG2 function as dimer or higher order oligomer, studies so far have been unable to convincingly address the oligomeric state of ABCG2.

We aim to bridge this knowledge gap by resolving the oligomerisation of ABCG2 using fluorescence techniques in mammalian cells. The expression and function of fluorescent proteins tagged ABCG2 were verified using confocal imaging and fluorescence accumulation assays, prior to the fluorescence studies. As the membrane dynamics of ABCG2 are unknown, we first measured the diffusion of ABCG2 in live HEK293T cells using fluorescence recovery after photobleaching (FRAP) microscopy, in comparison to membrane localised fluorescent proteins and a full length (i.e 4 domain) ABC transporter (ABCC4). We also demonstrated oligomerisation of ABCG2 by measuring a specific increase in fluorescence resonance energy transfer (FRET) efficiency between CFP- and YFP-tagged ABCG2 expressed in live

HEK293T cells in comparison to non-specific control interactions, including with the adenosine A3 receptor.

Subsequently, we employed high resolution and single particle fluorescence techniques to resolve the oligomeric organisation of ABCG2. First, fluorescence fluctuations of tagged ABCG2 within a confocal volume, positioned on the upper plasma membrane, were measured using fluorescence correlation spectroscopy (FCS) at “single molecule” resolution. Photon counting histogram (PCH) analysis of the FCS measurements was performed to determine the molecular brightness of the fluorescent species detected within the confocal volume. Using CD86 and CD28 as monomer and oligomer controls respectively, PCH analysis demonstrated higher order oligomer formation of ABCG2, with increased brightness (up to 4-fold) observed for both ABCG2 and CD28, compared to CD86. For validation of the oligomeric organisation of ABCG2, we acquired a series of single particle photobleaching images of cells expressing fluorescent protein tagged ABCG2 using total internal reflection fluorescence (TIRF) microscopy at the lower plasa membrane, and employed a step detection algorithm to identify the number of photobleaching steps within the distinguished fluorescent spots. Statistical modelling of the photobleaching step frequency histogram provided credible evidence of tetrameric organisation of ABCG2 in the plasma membrane. The findings and methodology presented in this study have provided further insights into the membrane dynamics and oligomerisation of ABCG2. This could lead to future studies to explore new pharmacological avenues that target the oligomerisation interfaces of ABCG2.

Acknowledgements

First of all, I woud like to express my most heartfelt gratitude to my supervisors, Dr Ian Kerr and Dr Nick Holliday. I am extremely grateful for their invaluable advice and guidance on my research in the past 3 and half years. The continuous encouragement I received from Ian and Nick has been central to the completion of my PhD, especially during challenging periods. I am also greatly indebted to their time and admirable efforts in correcting my thesis chapters in spite of busy schedules. I also enjoyed sharing their enthusiasm and humour during our weekly meetings and I wish to thank my supervisors for all the pleasant Monday afternoons during my PhD.

Second, I would like to acknowledge all those within the School of Life Sciences whose assistance has been influential in completing my research. I am very grateful to Deb Briggs for her patience in providing numerous training of experimental techniques that have been essential to my research. I also wish to express my sincere appreciation to Dr Laura Kilpatrick, Seema Rajani, Dr Steve Briddon, and Tim Self within the Cell Signalling Resarch Group for their valuable training and insightful advice on the use of various microscope systems and discussions regarding experimental data analysis. I am thankful to Chris Robinson and Marleen Groenen for their assistance in immunohistochemistry assay and the generation of several control cDNA vectors, respectively. My sincere thanks also goes to members of the Cell Signalling Research Group for inspiring discussions during lab meetings and Aaron Horsey, George Janes, and Natalie Jones in particular for proofreading some of the chapters of this thesis.

I would like to extend my gratitude to Prof. Simon Davies (University of Oxford) for kindly providing cDNA vectors as controls for my experiments and

Dr Rikaard Blunck (University of Montreal) for allowing access to the automated step detection algorithm required for data analysis.

My profound gratefulness is extended to the School of Life Sciences, University of Nottingham for this excellent opportunity and generous funding to further my studies, without which none of this would have been possible. Additionally, the unparalleled facilities provided by the University, particlarly within the Cell Signalling Research Group and the School of Life Sciences Imaging Facility, have been fundamental to all my research performed in the past 3 and half years.

Last but not least, I would also like to take this opportunity to express my deepest appreciation to my family, in particular my mother and my wife, who have been hugely supportive throughout my studies and especially during the completion of this thesis.

Declaration

I hereby declare that this thesis entitled “Dynamics and Oligomerisation of ABCG2 Investigated Using Various Fluorescence Techniques” is the result of my own work, which has been undertaken during my period of registration for this degree at The University of Nottingham, under the guidance of Drs Ian Kerr and Nick Holliday. This thesis is a presentation of my original research work, and to the best of my knowledge and belief, contains no material previously published or written by another person, except where due reference has been made in the text.

Kelvin Wong
Student ID: 4166380
February 2015

Abbreviations

ABC	ATP-binding cassette
ADP	Adenosine diphosphate
Akt	Protein kinase B
AML	Acute myeloid leukaemia
AMP-PNP	Adenosine 5’-(β,γ-imido)triphosphate
ATP	Adenosine triphosphate
BCRP	Breast cancer resistant protein
BiFC	Bimolecular fluorescence complementation
BSA	Bovine serum albumin
cAMP	Cyclic adenosine monophosphate
CF	Cystic fibrosis
CFP	Cerulean fluorescent protein
CFTR	Cystic fibrosis transmembrane conductance regulator
CMV	Cytomegalovirus
DAPI	4’,6-Diamidino-2-phenylindole
DMEM	Dulbecco’s Modified Eagle’s Medium
DMSO	Dimethyl sulphoxide
DNTP	Deoxynucleotide solution mix
DSS	Disuccinimidyl suberate
DTT	Dithiothreitol
EC_{50}	50% effective concentration
ECF	Energy-coupling-factor
EDTA	Ethylenediaminetetraacetic acid
EGFP	Enhanced green fluorescent protein
FBS	Foetal bovine serum
FCS	Fluorescence correlation spectroscopy
FITC	Fluorescein isothiocyanate

FRAP	Fluorescence recovery after photobleaching
FRET	Fluorescence resonance energy transfer
FTC	Fumitremorgin C
GAP	Growth associated protein 43
GFP	Green fluorescent protein
GPCR	G-protein-coupled receptor
GSH	Glutathione
H33342	Hoechst 33342
HDL	High-density lipoprotein
HEK293T	Human embryonic kidney 293 cells expressing SV40 large T antigen
HisP	Histidine permease
HIV	Human immunodeficiency virus
HRas	Harvey rat sarcoma oncogene encoding GTPase
HlyB	Haemolysin B
IAAP	iodoarylazidoprazosin
ICL	Intracellular loop
K_{ATP}	ATP-sensitive K^+ channel
Kir6.1/6.2	Inward rectifying K^+ channels
KRas	Kirsten rat sarcoma oncogene encoding GTPase
MalK	ABC subunit of maltose transporter
MDR	Multidrug resistance
MRP1	Multidrug resistance associated protein 1
MX	Mitoxantrone
NBD	Nucleotide binding domain
NPY	Neuropeptide-Y receptors
P-gp	P-glycoprotein
PAGE	Polyacrylamide gel electrophoresis
PBS	Phosphate buffered saline
PCH	Photon counting histogram

PCR	Polymerase chain reaction
PEI	Polyethylenimine
PFA	Paraformaldehyde
PFO	Perfluoro-octanoic acid
PhIP	2-Amino-1-methyl-6-phenylimidazo(4,5-b)pyridine
Pim-1L	44 kDa serine/threonine protein kinase
Rho6G	Rhodamine 6G
RibU	Riboflavin transporter
SBP	Solute binding protein
SDS	Sodium dodecyl sulphate
SfGFP	Superfolder green fluorescent protein
SUR	Sulphonylurea receptor
TAP	Transporter associated with antigen processing
TBE	Tris/Borate/EDTA buffer
ThiT	Thiamine transporter
TIRF	Total internal reflection fluorescence
TM	Transmembrane helices
TMD	Transmembrane domain
UV	Ultraviolet
YFP	Yellow fluorescent protein

Table of contents

CHAPTER 1 INTRODUCTION **1**

1.1 The ABC protein superfamily **1**

1.1.1 Composition of ABC transporter – the four core domains 2

1.1.2 Roles of NBD motifs in ATP hydrolysis 4

1.2 The human ABC transporters **9**

1.2.1 Cholesterol transport and regulation 9

1.2.2 Immune response 10

1.2.3 Ion channel activity and regulation 11

1.3 The multidrug efflux pumps **14**

1.3.1 ABCB1 – the P-glycoprotein 14

1.3.2 ABCC1 – the multidrug resistant associated protein 1 15

1.3.3 ABCG2 – a “half MDR transporter” 16

1.4 Structure and mode of action – ABC exporters **20**

1.4.1 Structures of ABC exporters 21

1.4.2 Homology modelling of ABCG2 25

1.4.3 The ATP-switch model for ABC exporters 25

1.5 Mutational effects on ABCG2 **30**

1.5.1 Function 30

1.5.2 Localisation 32

1.5.3 Post-translational modifications 33

1.6 Oligomerisation of ABCG2 **34**

1.6.1 Oligomeric state of ABCG2 34

1.6.2 Residues or domains responsible for ABCG2 oligomerisation 35

1.7 Fluorescence microscopy **37**

1.7.1 Principles of fluorescence 37

1.7.2 The green fluorescent protein 39
1.7.3 Confocal microscopy – how it works 45

1.8 Aims of study 47

CHAPTER 2 METHODS 49

2.1 Molecular biology 49
2.1.1 Materials and reagents 49
2.1.2 Cloning 50
2.1.3 Transformation and preparation of competent cells 52
2.1.4 Plasmid preparation and long-term storage 52
2.1.5 Primer design for mutagenesis and amplification 53
2.1.6 Polymerase chain reaction – mutagenesis and amplification 54
2.1.7 DNA sequencing 57

2.2 Tissue culture 58
2.2.1 Cell lines and reagents 58
2.2.2 Cell passage maintenance and storage 58
2.2.3 Seeding cell count and transfection 59
2.2.4 Poly-L-lysine coating of cover glass 60
2.2.5 Cell fixing and mounting 60
2.2.6 Stable cell line selection 60
2.2.7 Dilution cloning to obtain low expressing cell lines 61

2.3 Detection of proteins using SDS-PAGE and western blot analysis 61
2.3.1 Cell harvest and protein assay 61
2.3.2 SDS-PAGE 62
2.3.3 Western blot analysis 63

2.4 Functional studies of ABCG2 64
2.4.1 Accumulation assay – fluorescence intensities 64
2.4.2 Accumulation assay – multiwavelength cell scoring analysis 65

2.5 Detection of cytoskeletal disruption 66
2.5.1 Staining protocol 66
2.5.2 Fluorescence imaging 67

2.6 Standard confocal imaging 67
2.6.1 Confocal imaging to determine low expressing clones and localisation of cytoplasmic sfGFP constructs 68

2.7 FRAP acquisition and analysis 68

2.8 FRET acquisition and analysis 70
2.8.1 Lambda image acquisition 70
2.8.2 FRET data collection and % FRET efficiency determination 71

2.9 Fluorescence correlation spectroscopy and photon counting histogram brightness analysis 72
2.9.1 FCS data acquisition and autocorrelation analysis 72
2.9.2 Calibration of FCS experiments and diffusion coefficient calculations 74
2.9.3 PCH analysis 75

2.10 TIRF microscopy and stepwise bleaching analysis 76
2.10.1 TIRF imaging and data collection 77
2.10.2 Stepwise bleaching analysis using PIF algorithm 78
2.10.3 Statistical modelling of photobleaching step frequency histograms using binomial distributions 83

2.11 General statistical analysis methods 85

CHAPTER 3 PLASMID CONSTRUCTS REQUIRED FOR FLUORESCENCE STUDIES 86

3.1 Engineering and design of fluorescent protein tagged ABCG2 constructs 86

3.2 Generation of sfGFP-ABCG2 construct 88

3.2.1 Cloning of YFP-ABCG2 constructs into pcDNA3.1zeo vector 88

3.2.2 Introduction of A206K mutation into sfGFP starting vector 91

3.2.3 Cloning of pcDNA3.1zeo_sfGFP-ABCG2 92

3.3 Generation of CFP-ABCG2 and YFP- truncated ABCG2 constructs 94

3.3.1 Generation of CFP-ABCG2 constructs 94

3.3.2 Generation of YFP-fused truncated ABCG2 constructs 94

3.4 Generation of oligomerisation controls for single particle fluorescence studies 96

3.5 Generation of C603A and T362A ABCG2 mutants 98

3.6 Summary 100

CHAPTER 4 MEMBRANE DIFFUSION OF ABCG2 STUDIED USING FLUORESCENCE RECOVERY AFTER PHOTOBLEACHING (FRAP) 101

4.1 Theory of fluorescence recovery after photobleaching (FRAP) 101

4.2 Construct characterisation 104

4.2.1 Localisation and expression of sfGFP-ABCG2 constructs 105

4.2.2 Function of sfGFP-ABCG2 108

4.3 ABCG2 FRAP experimental design and data analysis 111

4.4 FRAP of ABCG2 compared to control membrane proteins 114

4.4.1 Effects of substrate on ABCG2 FRAP 117

4.4.2 Effects of cytoskeleton disruption in ABCG2 FRAP 118

4.5 Discussion 122

4.5.1 FRAP of ABCG2 – comparison with other membrane proteins 122

4.5.2 FRAP reveals differences in protein sizes 122

4.5.3 Prediction of ABCG2 cellular environment 123

4.5.4 Potential experimental limitations 125

4.5.5 Conclusion 126

CHAPTER 5 OLIGOMERISATION OF ABCG2 IN LIVE CELLS DEMONSTRATED BY FLUORESCENCE RESONANCE ENERGY TRANSFER (FRET) MICROSCOPY 128

5.1 Background and theory – fluorescence resonance energy transfer microscopy 128

5.2 FRET construct characterisation 133

5.2.1 Construct localisation and expression 134

5.2.2 Function of CFP- and YFP-ABCG2 138

5.3 FRET acquisition and data analysis 141

5.4 FRET method optimisation 144

5.4.1 Effects of using different lambda scan bandwidths 144

5.4.2 Effects of YFP excitation on FRET efficiency 145

5.5 Oligomerisation of ABCG2 in live cells demonstrated by FRET microscopy 147

5.5.1 Effects of expression levels on FRET efficiency 148

5.5.2 Effects of substrate and inhibitors on ABCG2 FRET 150

5.5.3 Investigating the potential roles of different domains in ABCG2 oligomerisation 151

5.6 Discussion 153

5.6.1 Establishing the oligomerisation of ABCG2 in live cells 153

5.6.2 Simultaneous YFP excitation does not affect measured FRET efficiency 154

5.6.3 Expression levels did not affect FRET of ABCG2 155

5.6.4 No effect on FRET of ABCG2 in the presence of substrate 156

5.6.5 Roles of different domains in the oligomerisation of ABCG2 156

5.6.6 Conclusion 157

CHAPTER 6 FLUORESCENCE FLUCTUATION MEASUREMENTS TO STUDY THE DIFFUSION AND OLIGOMERISATION OF ABCG2 159

6.1 Background and theory – FCS and PCH 159

6.1.1 Fluorescence correlation spectroscopy (FCS) 159

6.1.2 Photon counting histogram (PCH) analysis – theory and application 163

6.2 Construct characterisation and clonal selection for FCS and PCH studies 166

6.2.1 Characterisation of sfGFP and tandem-sfGFP constructs 167

6.2.2 Generation and characterisation of stable HEK293T clones expressing low levels of transfected protein 168

6.3 FCS data acquisition 173

6.4 Diffusion of ABCG2 measured by FCS at "single molecule level" 176

6.5 Estimation of molecular brightness of controls cytoplasmic sfGFP and tandem-sfGFP using PCH analysis 180

6.6 Oligomerisation of ABCG2 demonstrated by PCH analysis 181

6.6.1 PCH analysis – binning time and data fitting 181

6.6.2 1-component PCH analysis supports oligomerisation of ABCG2 184

6.6.3 High order oligomeric structure in ABCG2 indicated by 2-component PCH analysis 186

6.6.4 Ratio of C2: C1 supports tetrameric formation for ABCG2 and CD28 188

6.7 Discussion 189

6.7.1 Establishing diffusion coefficient of ABCG2 at "single molecule" level 189

6.7.2 Oligomerisation of ABCG2 demonstrated by FCS and PCH analysis 190

6.7.3 Experimental limitations 193
6.7.4 Concluding remarks 196

CHAPTER 7 TOTAL INTERNAL REFLECTION FLUORESCENCE MICROSCOPY AND STEPWISE PHOTOBLEACHING ANALYSIS TO RESOLVE THE OLIGOMERISATION OF ABCG2 198

7.1 Background and theory – TIRF microscopy and stepwise photobleaching analysis 198
7.1.1 Evanescent field theory 199
7.1.2 TIRF microscopy instrumentation 200
7.1.3 Single particle imaging in TIRF and stepwise photobleaching analysis 202
7.1.4 Aims of current study 207

7.2 TIRF imaging and photobleaching 207

7.3 Stepwise photobleaching analysis 208
7.3.1 Algorithm optimisation: pixel size of fluorescent spots 212
7.3.2 Algorithm determination: Determination of analysis parameters using spot fluorescence intensity and photobleaching step distribution histograms 214

7.4 Determination of ABCG2 oligomeric state in HEK293T cell membranes, compared to CD28 and ABCC4 216
7.4.1 SfGFP-ABCG2 photobleaching step frequency histogram is best fit by a tetrameric model 218
7.4.2 Single oligomeric model analysis suggests tetrameric organisation of sfGFP-ABCG2 218
7.4.3 Multiple component oligomeric model suggests that sfGFP-ABCG2 exists predominantly as tetramers 221
7.4.4 Photobleaching step distribution variation among experimental data sets 224

7.5 Discussion **226**

7.5.1 Single particle TIRF imaging and binomial distribution analysis demonstrate that ABCG2 exist as a tetramer in mammalian cell membrane 226

7.5.2 Critical appraisal of TIRF stepwise photobleaching method 229

7.5.3 Assumptions in the binomial fitting of histograms 230

7.5.4 Excluded traces to compensate for experimental limitations 233

7.5.5 Concluding remarks 234

CHAPTER 8 FINAL DISCUSSION AND FUTURE PERSPECTIVES **235**

8.1 Key findings **235**

8.2 General advantages and limitations of experimental methods **236**

8.3 Future perspectives **240**

8.3.1 Significance of ABCG2 tetrameric organisation 240

8.3.2 Establishing the pharmacology of ABCG2 242

8.3.3 Potential new imaging methods to study ABCG2 242

REFERENCES **244**

APPENDIX **271**

List of figures

Figure 1.1: The four core domains of ABC transporter.. 4
Figure 1.2: "Head-to-tail" dimer arrangement of NBD dimer. 8
Figure 1.3: Crystal structures of ABC transporters. 23
Figure 1.4: ATP switch model showing the transport cycle for an ABC exporter. 29
Figure 1.5: A schematic Jablonski diagram. 38
Figure 1.6: Schematic representation of excitation and emission spectra for a typical green fluorophore. 39
Figure 1.7: X-ray crystal structure of GFP and formation of its chromophore.42
Figure 1.8: Schematic representation of a confocal laser scanning microscopy set up. 47
Figure 3.1: Schematic illustration of a standard DNA vector in this study. 87
Figure 3.2: Cloning plan to generate pcDNA3.1zeo_YFP-ABCG2. 89
Figure 3.3: Digestion with *SpeI* restriction enzyme to confirm the size of pcDNA3.1zeo_YFP-ABCG2. 90
Figure 3.4: DNA chromatogram of pcDNA3.1zeo_nostop_sfGFP with the successful A206K mutation highlighted in red. 92
Figure 3.5: Cloning plan to generate pcDNA3.1zeo_sfGFP-ABCG2. 93
Figure 3.6: Sequencing data of pcDNA3.1zeo_sfGFP-ABCG2 using primers SeqGFP-rev and T7F. 94
Figure 3.7: An illustration of 2D membrane topology of ABCG2. 96
Figure 3.8: Cloning plan to generate pcDNA3.1zeo_CD86-sfGFP and CD28-sfGFP. 97
Figure 3.9: DNA chromatogram of pcDNA3.1zeo_YFP-ABCG2_C603A aligned against the ABCG2 wild type sequence. 99
Figure 3.10: DNA chromatogram of pcDNA3.1zeo_sfGFP-ABCG2_T362A aligned against the wild type ABCG2 sequence. 100
Figure 4.1: Schematic illustration of a standard FRAP experiment. 102

Figure 4.2: Schematic summary of the DNA constructs required for FRAP studies. 105
Figure 4.3: Confocal images of HEK293T cells stably expressing sfGFP-ABCG2 transporters (wild type, C603A, and T362A). 106
Figure 4.4: Confocal images of HEK293T cells stably expressing sfGFP-kRas and GAP-sfGFP, and HEK293T cells transiently expressing ABCC4-sfGFP. ... 107
Figure 4.5: Western blot analysis of the different fluorescent proteins investigated in FRAP studies. 108
Figure 4.6: Accumulation of mitoxantrone (MX) in the presence of various concentrations of Ko143. 109
Figure 4.7: Function of sfGFP-ABCG2 wild type and mutants when expressed in HEK293T cells. 110
Figure 4.8: Example of a FRAP experiment. 112
Figure 4.9: Bleach percentages achieved with the FRAP experimental photobleaching settings did not affect the kinetic parameters. 113
Figure 4.10: Reduced bleached size radius is associated with more consistent values of the diffusion coefficient. 114
Figure 4.11: Fluorescence recovery of ABC transporters and membrane localised sfGFP. 115
Figure 4.12: Diffusion coefficients of sfGFP-ABCG2 compared to the control membrane proteins. 116
Figure 4.13: Reduced mobile fractions of ABC transporters compared to the membrane localised sfGFP. 117
Figure 4.14: ABCG2 diffusion was not affected by substrate transport. 118
Figure 4.15: Effects of cytochalasin D treatment on sfGFP-ABCG2 expressing HEK293T cells demonstrated by immunofluorescence microscopy. 119
Figure 4.16: Effects of nocodazole treatment on sfGFP-ABCG2 expressing HEK293T cells demonstrated by immunofluorescence microscopy. 120
Figure 4.17: Effects of cytoskeleton disruption on the FRAP of sfGFP-ABCG2 and sfGFP-kRas. 121
Figure 5.1: Schematic representation of emission and excitation spectra of cerulean and yellow fluorescent proteins (CFP and YFP). 130

Figure 5.2: Schematic representation of acceptor photobleaching (AcPb) FRET employed to measure FRET efficiency in this study. 132
Figure 5.3: Schematic representation of DNA constructs generated for the investigation of oligomerisation of ABCG2 using FRET microscopy. 133
Figure 5.4: Confocal images and the corresponding phase contrast images for the various fluorescent proteins expressed in single or co-transfected HEK293T cells. 135
Figure 5.5: Confocal images and the corresponding phase contrast images for various fluorescent proteins transiently co-expressed in HEK293T cells. 136
Figure 5.6: Western blot analysis of the DNA constructs employed in this FRET study. 137
Figure 5.7: Fluorescence images acquired during the accumulation assay in HEK293T cells transiently expressing CFP-ABCG2. 139
Figure 5.8: CFP-ABCG2 and YFP-ABCG2 are functional mitoxantrone (MX) exporters when expressed transiently in HEK293T cells. 140
Figure 5.9: Limitations of FRET due to signal bleed-throughs caused by the overlapping of CFP and YFP excitation and emission spectra. 141
Figure 5.10: FRET spectral unmixing data analysis. 143
Figure 5.11: Differences between collecting the emission spectra at every 10 or 20 nm. 144
Figure 5.12: Comparing the differences in FRET efficiency % when the lambda emission spectra were collected at every 10 nm or every 20 nm. 145
Figure 5.13: Effects of YFP excitation during data acquisition on the FRET efficiencies. 146
Figure 5.14: Increased FRET efficiency demonstrates oligomerisation of ABCG2. 147
Figure 5.15: Effects of expression levels on FRET of ABCG2. 149
Figure 5.16: Effects of substrate and inhibitors on FRET of ABCG2. 150
Figure 5.17: Transmembrane domain, rather than C603 disulphide bonds or the NBD, contributes to the oligomerisation of ABCG2. 152

Figure 5.18: Non-reducing western blot analysis demonstrates the expression and capacity for oligomerisation of the YFP-fused ABCG2 proteins. 153
Figure 6.1: Schematic representation of basic FCS instrumentation and autocorrelation analysis. 162
Figure 6.2: Schematic representation of PCH theory and application. 165
Figure 6.3: Schematic summary of the constructs generated for FCS and PCH experiments. 167
Figure 6.4: Localisation and expression of sfGFP and tandem-sfGFP. 168
Figure 6.5: Selection of a low expressing CD86-sfGFP stably transfected HEK293T clone. 170
Figure 6.6: Selection of a low expressing CD28-sfGFP stably transfected HEK293T clone. 171
Figure 6.7: Selection of a low expressing sfGFP-ABCG2 stably transfected HEK293T clone.. 172
Figure 6.8: Western blot analysis indicating the observed molecular weights of sfGFP-ABCG2, CD28-sfGFP and CD86-sfGFP. 173
Figure 6.9: Positioning of the confocal volume in FCS experiments. 174
Figure 6.10: FCS traces and autocorrelation curves obtained with various acquisition/photobleaching conditions..... 178
Figure 6.11: Examples of FCS traces and autocorrelation curves. 179
Figure 6.12: Diffusion coefficients (*D*) and concentrations (*C*) of sfGFP-ABCG2 compared to the membrane protein controls. 180
Figure 6.13: Validation of PCH analysis methods. 181
Figure 6.14: Effects of binning time on PCH distributions. 183
Figure 6.15: Example of PCH analysis from sfGFP-ABCG2 data set..... 184
Figure 6.16: Increased molecular brightness (ε) of sfGFP-ABCG2 indicating possible oligomeric formation. 185
Figure 6.17: Presence of multiple species and higher oligomeric states in sfGFP-ABCG2 and CD28-sfGFP revealed by 2-component PCH analysis. 187
Figure 6.18: Molecular brightness ratios indicate possible tetrameric formation in ABCG2 and CD28. 188

Figure 7.1: Schematic illustration of the generation of an evanescent field through the total internal reflection phenomenon. 200
Figure 7.2: Schematic representations to compare TIRF and epifluorescence illumination methods. 201
Figure 7.3: Illustrative representation of single particle TIRF imaging in combination with stepwise photobleaching analysis to determine the oligomeric state of fluorescent membrane proteins. 204
Figure 7.4: Epifluorescence and TIRF imaging of a fixed HEK293T cell expressing sfGFP-ABCG2. 208
Figure 7.5: Automated PIF algorithm used for stepwise photobleaching analysis of the TIRF videos. 210
Figure 7.6: Magnified pixel-by-pixel of raw TIRF images for the determination of fluorescent spots size. 213
Figure 7.7: Determination of various parameters for stepwise photobleaching analysis using PIF algorithm. 215
Figure 7.8: Examples of photobleaching step detection analysis in sfGFP-ABCG2 expressing cell. 217
Figure 7.9: Effects of non-fluorescent GFP molecules. 217
Figure 7.10: Fitting of the photobleaching step frequency histogram of sfGFP-ABCG2 data set with different oligomeric models. 220
Figure 7.11: Determination of oligomerisation of ABCG2 using photobleaching step frequency histograms and oligomeric modelling. 221
Figure 7.12: Multiple-component oligomeric models to determine mixture of oligomeric species in sfGFP-ABCG2 and CD28-sfGFP. 223
Figure 7.13: Normalised average frequency histograms to examine the variability between experiments. 225

List of tables

Table 1.1: Summary of different members within the ABC transporter families and their general function and clinical significance. 13
Table 1.2: Summary of the main ABC exporters structures reported to date. 22
Table 1.3: Summary of mutational effects on ABCG2. 31
Table 1.4: Summary of the different mutations and properties associated with the fluorescent proteins. 44
Table 2.1: List of the starting vectors employed in this study. 50
Table 2.2: Composition of restriction digest reaction in this study. 51
Table 2.3: Composition of ligation mixtures and vector only control. 52
Table 2.4: List of primers designed in this study for DNA construct generation. 55
Table 2.5: Standard composition of PCR experiments. 55
Table 2.6: PCR cycling protocol for site-directed mutagenesis reaction. 56
Table 2.7: PCR cycling protocol for amplification reaction. 57
Table 2.8: ABCG2 sequencing primers. 57
Table 2.9: Seeding cell count and transfection set ups for the different plates or dishes used in this study. 59
Table 2.10: Filter sets employed to detect the fluorescence intensities of the nucleus stain, CFP or YFP, and mitoxantrone. 66
Table 2.11: Key parameters defined for stepwise photobleaching analysis of the TIRF videos using the PIF algorithm. 79
Table 2.12: Double binomial distributions to determine the photobleaching step frequency distributions for a tetrameric oligomer state. 84
Table 3.1: Summary of the various pcDNA3.1zeo constructs generated through two different methods in this study. 88
Table 3.2: Sequencing results to confirm YFP-ABCG2 sequences within new pcDNA3.1zeo vector. 91

Table 7.1: Subunit and complex organisation of the proteins investigated using single particle TIRF imaging and stepwise bleaching analysis. 206
Table 7.2: Key parameters defined for stepwise photobleaching analysis of the TIRF videos using PIF algorithm..... 211
Table 7.3: Summary of the expression systems, fluorescent proteins employed and probability of fluorescent GFP reported in various TIRF stepwise photobleaching studies. 232
Table 8.1: Comparison of the fluorescence techniques employed in this study. 239

Chapter 1 Introduction

1.1 The ABC protein superfamily

ABC (ATP-binding cassette) proteins were first discovered in the 1980s when a group of ATP binding proteins in bacteria were found to possess related functions in membrane transport (Higgins et al., 1986). The ABC proteins are now established as one of the largest protein superfamilies distributed across the prokaryotic and eukaryotic genomes. There are three main functional categories of ABC systems – exporters (class 1), soluble ATPases (class 2) and importers (class 3) (Dassa, 2011). The ABC proteins that are established to function as exporters (in both prokaryotes and eukaryotes) and importers (potentially exclusively in prokaryotes) are also known as the ABC transporters (Hyde et al., 1990). The number of ABC proteins varies across different species. In *Escherichia coli*, almost 5 % of its entire genome was reported to encode for proteins of ABC systems, most of which act as transporters in the uptake of nutrients and elimination of waste products (Linton and Higgins, 1998). In man, 48 ABC proteins have been identified and they are further classified into seven different families (A-G). Depending on their distribution in the human body, the ABC proteins are known to perform a wide range of important physiological roles, e.g. transport of endogenous compounds (urate and cholesterol), expelling toxic molecules (antibiotics and anticancer agents), and translational roles (see section 1.2 later; (Dean et al., 2001)).

1.1.1 Composition of ABC transporter – the four core domains

The organisation of four core domains is established as the minimal prerequisite for functional eukaryotic (and some prokaryotic) ABC transporters (Hyde et al., 1990). Typically two nucleotide binding domains (NBD_1 and NBD_2) and two transmembrane domains (TMD_1 and TMD_2) are required for substrate transport by an ABC transporter (Figure 1.1). The NBD contains sequences that bind and hydrolyse ATP and it is located in the cytoplasm. Each membrane-spanning TMD of an ABC protein normally consists of four to eight α-helices, joined together by intracellular and extracellular loops. The sequence and number of TMDs vary across the ABC families or even members within the same family (see discussion on ABCC proteins later) (Dassa, 2011). This divergence suggests that the TMDs are likely to be important for substrate or function specificity. The four (or more) core domains of an ABC transporter may be formed from a single polypeptide chain such as the human ABCB1 and ABCC1, or multiple polypeptide chains, for instance the bacterial ribose transporter (Davidson et al., 2008) and the human transporter associated with antigen processing (TAP1 and TAP2; (Gadola et al., 2000)). Certain ABC transporters are known to require additional domains for effective function. For example, the extracytoplasmic solute binding proteins (SBPs) are important for the function of bacterial ABC importer systems by recognising substrates (mostly nutrients) with high affinity, for example the bacterial maltose and vitamin B_{12} importer systems (Davidson et al., 2008). While most bacterial ABC importer systems require SBPs for function, the energy-coupling-factor (ECF) transporters are a group of ABC importers that does not employ SBPs for substrate recognition. Instead, ECF transporters are comprised of a conserved module – a transmembrane protein (EcfT) and two homologous NBDs (EcfA and EcfA') for core transport activity, while utilising different S-components for substrates recognition (Rodionov et al., 2009). The S-components are thought to be typically 20-25 kDa in size with 4-6 hydrophobic membrane spanning segments such as the biotin transporter BioMNY (Hebbeln et al., 2007),

riboflavin transporter RibU (P. Zhang et al., 2010) and thiamine transporter ThiT (Erkens et al., 2011). In man, several members of the ABCC transporter family (class 1 exporters, e.g. ABCC1) contain an additional transmembrane domain (the TMD_0) at the N-terminus of the transporter preceding TMD_1. These members of the ABCC family therefore consist of five domains (TMD_0-TMD_1-NBD_1-TMD_2-NBD_2) in a single polypeptide chain. Also, the cystic fibrosis transmembrane conductance regulator (CFTR, or ABCC7) contains the four core domains (TMD_1-NBD_1-TMD_2-NBD_2) with an additional regulatory domain inbetween the NBD_1 and TMD_2 identified as a region required for its function as an ion channel regulator (Riordan et al., 1989; Winter and Welsh, 1997).

Sequence alignments have identified at least seven conserved motifs present in the NBD of ABC transporters (Hyde et al., 1990; Lawson et al., 2008; Linton, 2007), shown in Figure 1.1. Unsurprisingly, two well known ATP binding sequences were identified – the Walker-A and Walker-B motifs (Walker et al., 1982). The Walker-A motif is a glycine-rich sequence (GXXXXGK{S/T}, X = any residue) that is important for nucleotide binding through formation of hydrogen bond interactions between the glycine residues and the phosphate moieties of ATP. The serine or threonine residue coordinates the binding of Mg^{2+} ion whilst the basic residue, lysine, is thought to have a catalytic role through neutralisation of the negatively charged oxygen atom between the β- and γ- phosphate groups (Matte and Delbaere, 2010). The Walker-B motif (hhhhDE, h = any hydrophobic residue) contains an aspartate residue for the coordination of Mg^{2+} binding or to act as a base to abstract hydrogen atoms from the water molecules during ATP hydrolysis (Hanson and Whiteheart, 2005; Walker et al., 1982). The glutamate residue within the Walker-B motif was also found be important for ATP hydrolysis in ABC proteins, see next section. Other conserved motifs identified are the aromatic residue, ABC signature motif (also known as the linker peptide or Walker-C motif), and the Q-, D-, and H-loops (containing glutamine, aspartate, and histidine residues respectively). The roles of these residues in ATP hydrolysis will be discussed in

the next section. These NBD motifs are unique to the ABC transporter family and they are frequently used for identification or delineation purposes (Higgins, 1992; Higgins et al., 1986). The seven ABC families (A-G) in human (and other eukaryotes) are further classified based on their domain organisation (see section 1.2) and amino acid homology, as suggested in an initial phylogenetic analysis performed on yeast *Saccharomyces cerevisiae* ABC proteins (Decottignies and Goffeau, 1997).

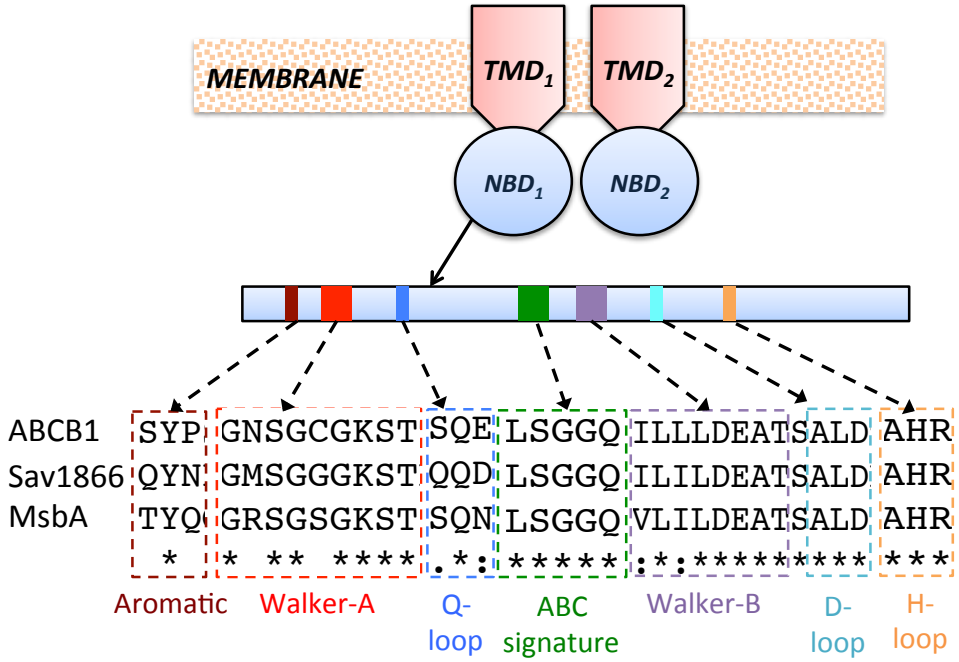

Figure 1.1: The four core domains of ABC transporter. Top panel: Schematic representation of a typical ABC transporter consisting of two transmembrane domains (TMDs) and two nucleotide binding domains (NBDs). Bottom panel: Alignment results of human ABCB1, *Staphylococcus aureus* Sav1866, and *Vibrio cholera* MsbA sequences highlighting the seven conserved motifs within the NBD of ABC proteins. Sequence alignment was generated using the Clustal Omega alignment tool (Sievers et al., 2011). The sequence of ABCG2 (protein of interest in this study) was not shown in the alignment due to poorly conserved sequence in the NBD of ABCG2.

1.1.2 Roles of NBD motifs in ATP hydrolysis

The NBD motifs identified in Figure 1.1 are all implicated by structural or mutagenesis studies as crucial for NBD function and coupling to the TMDs in ABC systems (Lawson et al., 2008). Mutations within the Walker-A and Walker-B sequences have been studied extensively. Various studies have demonstrated that the lysine residue (G**K**ST, Figure 1.1) within the Walker-A

motif is critical for ATPase activity, however the importance of this residue in the binding affinity of ATP is not yet conclusive (Azzaria et al., 1989; Henriksen et al., 2005a; Lerner-Marmarosh et al., 1999; Müller et al., 1996; Urbatsch et al., 2003). For example, in CFTR, mutations of the lysine residues within the Walker-A motif of either NBD_1 or NBD_2 in CFTR reduced the ATPase activity of the ion channel (Ramjeesingh et al., 1999; Smit et al., 1993). The glutamate residue (D**E**AT, Figure 1.1) within the Walker-B motif was also shown to be important for NBD function. Substitution of this glutamate residue with its neutral form, glutamine, has resulted in generation of non-functional mutants of ABC proteins with tightly bound nucleotide within the NBDs (Hou et al., 2009; Janas, 2003; Procko et al., 2006; Smith et al., 2002; Tombline et al., 2005). It was suggested that the highly conserved glutamate residue acts as a "catalytic carboxylate" that is responsible for cleaving of the phosphate bond during ATP hydrolysis. Mutation of this residue to glutamine resulted in trapping of the NBD in an "occluded state" in which the ATP is tightly bound but not hydrolysed (Tombline et al., 2005).

The ABC signature motif (LSGGQ, Figure 1.1, (Hyde et al., 1990)) has also been regularly shown to be important for transporter function and ATPase activity. Mutations in the leucine and second glycine residues of the **L**SG**G**Q motif were shown to reduce ATPase activity compared to the wild type protein, in isolated membrane preparations of ABCB1 from insect cells (Bakos et al., 1997). In addition to the leucine and glycine residues, the serine residue has also been demonstrated as important for the function of ABC proteins. Mutation of serine residues (in both NBDs) of ABCB1 resulted in further reduction of ATPase activity (compared to single mutation), suggesting possible synergistic action between the two NBDs (Tombline et al., 2004). Elsewhere, the activity of the ion channel CFTR was inhibited when the serine residue within the ABC signature motif was replaced with a cysteine (Cotten and Welsh, 1998). Another functional study demonstrated that replacing the second glycine residue within the signature motif in the NBDs with aspartate

affected the function of ABCC1 whilst the substitution of the leucine residue with arginine did not (Szentpétery et al., 2004). Mutating the ABC signature motifs of TAP1 (LSGGQ) and TAP2 (LAAGQ) to L**A**G**A**Q and LAA**A**Q respectively has also shown to abolish peptide translocation activity completely (Hewitt and Lehner, 2003). Furthermore, structural studies of NBD-NBD dimers (see Figure 1.2) also indicated that the ABC signature motif forms the ATP binding interface with the Walker-A motif of the opposing NBD (Procko et al., 2006; Smith et al., 2002).

Amongst the other conserved motifs highlighted in Figure 1.1, the aromatic residue was also believed to contribute to the binding of ATP potentially through π-π stacking interaction with the adenine of ATP, as shown in several structural studies (Dawson and Locher, 2006; Hung et al., 1998; Smith et al., 2002). Mutational studies have also demonstrated that the aromatic residue is required for ATPase activity and transporter function, as only a tyrosine or phenylalanine residue (20-30 amino acids N-terminal to Walker-A motif) in ABCB1 showed maximal ATPase activity (Ambudkar et al., 2006; Carrier et al., 2007; Kim et al., 2006). The D-loop (AL**D**, Figure 1.1) is also present near the binding interface of the "head-to-tail" NBD dimer (see Figure 1.2) and it was proposed to mediate communication between active sites in the two NBDs (Hopfner et al., 2000; Jones and George, 1999; Procko et al., 2006). A recent molecular dynamics simulation study also suggested that the D-loop may be involved in coordinating the water attack during ATP hydrolysis and modulate the formation of the "occluded state" of NBDs (Jones and George, 2012). The Q-loop was proposed to act as a flexible role for NBD and TMD communication. Mutations of the glutamine residues (S**Q**E, Figure 1.1) in the NBDs of ABCB1 to alanine or glutamate were shown to reduce drug-stimulated transport activity, but did not affect ATP binding (Urbatsch et al., 2000). Structural and molecular dynamics studies also suggested a highly flexible structure of the Q-loop, and it was shown to be closely located to the intracellular loop-2 in a homologue structure of ABCB1, indicating a potential

role of the Q-loop in NBD and TMD communication (Jones and George, 2002; Lawson et al., 2008; Smith et al., 2002). Elsewhere, mutations in the H-loop have caused reduced ATPase activity in multiple bacterial ABC systems, e.g. the histidine permease (HisP subunit; (Shyamala et al., 1991)), maltose transporter (MalK subunit; (Davidson and Sharma, 1997)) or haemolysin B transporter (HlyB subunit; (Zaitseva et al., 2004)). Further structural studies of the H662A mutant of HlyB in *E. coli* revealed that the H-loop could act as an important 'linchpin' that holds the γ-phosphate group of ATP while acting as a catalyst during ATP hydrolysis (Zaitseva et al., 2005). Although the exact roles of the Q-, D-, and H- loops are yet to be identified universally, evidence presented thus far suggests that they are likely to act as important switch regions and mediate the signalling process between the NBD catalytic sites and the TMD active sites (Jones and George, 2004).

NBD "head-to-tail" dimer conformation

While it was predicted that the two NBDs interact with each other in a "head-to-tail" conformation (Jones and George, 1999), early structural studies presented conflicting data as only the monomeric structure of NBD was generated (Hung et al., 1998). UV-induced photocleavage of vanadate trapped NBD subunits of the maltose transporter (MalK) produced highly specific cleavage fragments that indicated formation of ATP binding site by the Walker-A and ABC signature motifs of the opposing MalK subunits (Fetsch and Davidson, 2002), suggesting that the NBDs of ABC transporter could share a common dimer conformation as reported in the structural data of DNA repair ABC protein Rad50 (Hopfner et al., 2000). Neutralisation of the Walker-B glutamate residue (as discussed above) has successfully generated ATP-bound NBD dimeric X-ray crystal structures (Procko et al., 2006; Smith et al., 2002), as shown in Figure 1.2A. This arrangement is consistent with the formation of ATP binding and hydrolytic sites at an interface that is comprised of the Walker-A motif of one NBD and the ABC signature motif of the opposing NBD (Figure 1.2B), as suggested in the earlier studies. The aromatic residue was shown to be located closely to the ATP molecule in Figure 1.2B.

As discussed earlier, the Q-, D- and H- loops are also shown to form part of the NBD dimer interface in Figure 1.2B (Smith et al., 2002). The relevance of this "occluded" NBD dimer state (Figure 1.2A) in the function of ABC protein systems was demonstrated in a study where additional mutations to the Q-loops and Walker-A motifs (serine and lysine residues) of ABCB1 affected the ATP binding of the tightly "occluded" Walker-B ABCB1 mutant (E552A/E1197A) (Tombline et al., 2005).

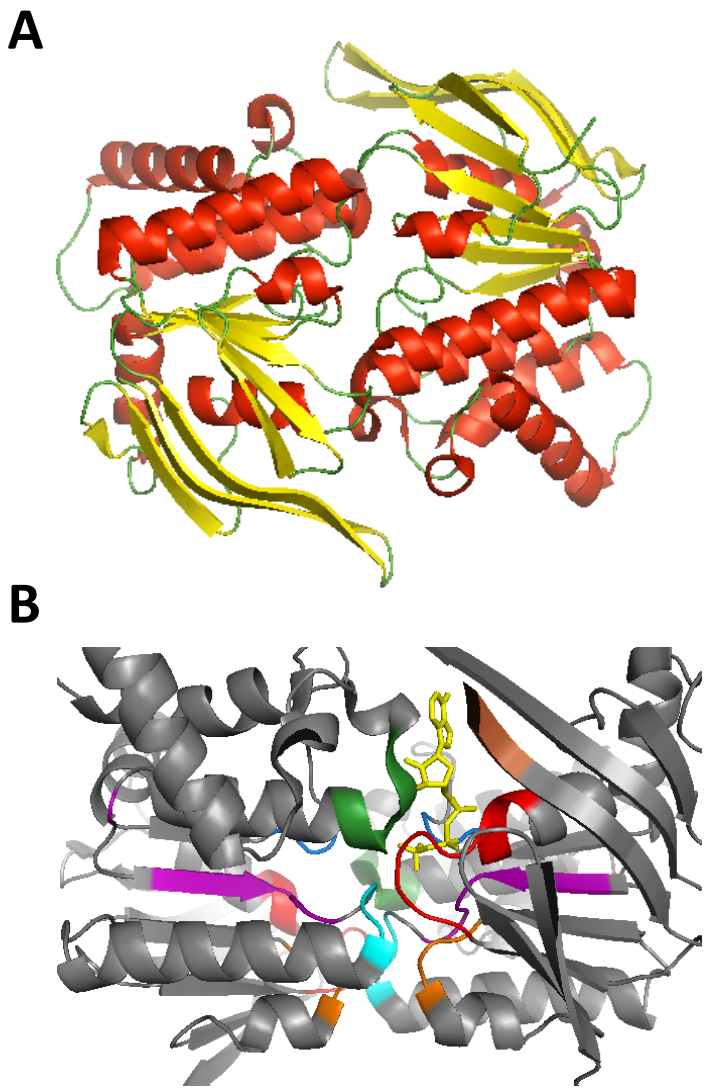

Figure 1.2: "Head-to-tail" dimer arrangement of NBD dimer. A – X-ray crystal structure (ribbon representation) of the MJ0796 in *E. coli* (E171Q mutant) shows that the NBD subunits organised as a sandwich dimer in the "head-to-tail" manner. **B –** Enlarged image of ATP binding site in A showing the ATP molecule (yellow) and the different NBD motifs highlighted as follows: aromatic (brown), Walker-A (red), Q-loop (blue), ABC signature (green), Walker-B (purple), D-loop (cyan), and H-loop (orange) (Smith et al., 2002). PDB: 1L2T. Figure was generated using PyMOL.

1.2 The human ABC transporters

The majority of the 48 known human ABC proteins are localised at the membrane, with the exception of ABCE and ABCF protein families, which are involved in translational control, and do not contain any transmembrane domains (Dean et al., 2001). The general roles of several ABC transporters/proteins found in man are summarised in this section and in Table 1.1 below. Further attention will be given to the three key multidrug efflux pumps (ABCB1, ABCC1 and in particular ABCG2) in the next section.

1.2.1 Cholesterol transport and regulation

The ABCA transporters are established as "key players" in the homeostasis of cellular phospholipid and cholesterol. ABCA1 especially is known as one of the main regulators in the metabolism of cellular high-density lipoprotein (HDL) (Langmann et al., 1999). The polypeptide of ABCA1 contains all four domains required for a functional ABC transporter (TMD_1-NBD_1-TMD_2-NBD_2). It has a highly conserved hydrophobic region at the N-terminus and two large extracellular loops (approximate total of 800 amino acid residues, 550 and 250 respectively) in between transmembrane helices 1 and 2 of the two TMDs (Schmitz and Langmann, 2001). The absence of functional ABCA1 in patients with Tangier disease causes impaired cholesterol efflux and reduced ABCA1 binding of apolipoprotein A1 (component of high density lipoprotein, HDL) in the liver and intestine, leading to undesired accumulation of cholesterol in the peripheral tissues (Brunham et al., 2006; Timmins et al., 2005). Additionally, there is growing evidence that suggests ABCA1 is found in the brain and is involved in the indirect regulation of amyloid-β production (Hirsch-Reinshagen et al., 2008; Kim et al., 2011).

Two members within the ABCG family, ABCG5 and ABCG8, are also implicated in cholesterol transport. The polypeptide chain of ABCG subfamily proteins only consists of a single NBD and single TMD (NBD_1-TMD_1), therefore they are

also known as “half transporters” (Kerr et al., 2011). In contrast to the ABCA subfamily, ABCG proteins do not contain the large extracellular loops or the conserved hydrophobic regions. Reduced expression of these transporters causes sitosterolaemia, where impaired efflux of plant derived sterols into the bile in the liver results in cholesterol or sitosterol accumulation in the body (Berge et al., 2000; Lee et al., 2001). Further studies suggest that these proteins may form heterodimers for the efflux of wide range of dietary sterols (Graf et al., 2003).

1.2.2 Immune response

The TAP1 and TAP2 (transporter associated with antigen processing) are two members of the ABCB family, each containing a single TMD and single NBD (TMD_1-NBD_1). They are known to form heterodimers within the membrane of endoplasmic reticulum (ER) and are involved in cellular immune responses. The TAP1 and TAP2 heterodimers recognise and transport peptides that act as major histocompatibility complex (MHC) class I antigens from the cytoplasm into the lumen of the ER, for binding with MHC class I molecules. This process facilitates subsequent antigen presentation in the cells for the recognition by T-lymphocytes for further immune responses (Momburg et al., 1994; Neefjes et al., 1993). Improved functionality of TAP1 and TAP2 transporters in defective mice has also been shown to reduce tumour malignancies through increased self-defence immune response by the T-lymphocytes (Agrawal et al., 2004). The diffusion of functional TAP complex (investigated using fluorescence recovery after photobleaching, FRAP, see section 4.1) was found to decrease in the presence of peptide substrates during translocation (Reits et al., 2000). Truncated TAP1 (transmembrane helices 2-6, TM2-6) and TAP2 (TM1-4) did not reduce the mobility of TAP complex when co-transfected with full length TAP1 (TM1-6) or TAP2 (TM1-5), providing evidence for alignment of TAP1 and TAP2 in a head-to-head and tail-to-tail orientation (Vos et al., 2000).

1.2.3 Ion channel activity and regulation

Within the ABCC family, several members were found to perform a unique role as ion channels or channel regulators. The CFTR (or ABCC7) is a cAMP-activated chloride ion channel (Sheppard and Welsh, 1999). It contains the four core domains (TMD_1-NBD_1-TMD_2-NBD_2) linked together by an additional regulatory (R) domain inbetween the NBD_1 and TMD_2 (Riordan et al., 1989). The TMDs are proposed to form a chloride anion selective pore whilst the ATP hydrolysis by the NBDs are suggested to regulate channel gating. Increased levels of cAMP causes activation of protein kinase A, which in turn phosphorylates several serine residues within the R domain, thereby activating the ion channel for efflux of chloride ions (Sheppard and Welsh, 1999). Genetic defects in CFTR, most commonly the deletion of Phe-508 amino acid residue (△F508), are the primary pathology in cystic fibrosis (CF) (Cutting, 2005). Dysfunctional CFTR causes a reduction in chloride anion and water conductance at the epithelial surfaces, resulting in the thickening of mucous (Frizzell, 1999). Therefore, patients with CF are often found to have viscous mucous at the epithelial surfaces of lungs and pancreas. Accumulation of fluids in the lungs and inadequate secretion of pancreatic enzymes (due to organ dysfunction or pancreatic duct blockage) often result in bacterial chest infections and lack of nutrition in CF patients (Dean et al., 1990; Riordan et al., 1989). Studies have demonstrated that the △F508 mutant of CFTR showed reduced expression at the plasma membrane (Kälin et al., 1999; Lukacs et al., 1993; Ostedgaard et al., 2007) and small molecule compounds (such as VRT-325) have been identified as chemical chaperones that improve △F508 CFTR expression at the plasma membrane for the treatment of cystic fibrosis (Brown et al., 1996; Molinski et al., 2012; Pedemonte et al., 2005).

On the other hand, the sulphonylurea receptors (SUR1 in β-cells of pancreas, and SUR2A in cardiac and skeletal muscles) within the ABCC family (ABCC8 and ABCC9 respectively) are known to associate with the inward-rectifying K^+ channel subunits (Kir6.1 or Kir6.2) to form the ATP-sensitive K^+ (K_{ATP})

channels. Similar to ABCC1 as discussed earlier, the SUR1 and SUR2A also have five core domains including the additional transmembrane domain (TMD_0). Inactivating polymorphisms in the SUR1 and Kir6.2 genes are associated with persistent hyperinsulinaemic hypoglycaemic of infancy, in which the K_{ATP} channels are closed leading to membrane depolarisation and uncontrolled insulin secretion (Dunne et al., 1997; Kane et al., 1996). In contrast, spontaneous mutations in SUR1 or Kir6.2 genes that cause increased opening of K_{ATP} channels (reduced calcium ion influx and insulin secretion) are linked with permanent neonatal diabetes (Polak and Cavé, 2007; Støy et al., 2007). The sulphonylurea drugs used in type II diabetes mellitus are known to inhibit the activity of K_{ATP} channels in the β-cells of pancreas through the binding to SUR1, resulting in increased insulin secretion in diabetic patients (Aguilar-Bryan et al., 1998). It has been suggested that SUR1 and Kir6.2 form a hetero-octamer with 1: 1 molar ratio in functional and structural studies (Clement et al., 1997; Inagaki et al., 1997; Mikhailov et al., 2005; Shyng and Nichols, 1997). A domain organisation study using the changes in fluorescence resonance energy transfer (FRET; see section 5.1) signal suggested that the C-terminus of Kir6.2 was centrally located within the K_{ATP} channel and the NBD_1 of SUR1 is located closer to the C-terminus of Kir6.2 than the N-terminus (Wang et al., 2013). The activity of the K_{ATP} channels is controlled through relative levels of intracellular ATP and ADP, where an increase in the ATP/ADP ratio is thought to result in the closure of K_{ATP} channels (Miki et al., 1999). Although it has been suggested that the SUR1 and SUR2A may regulate the K_{ATP} channels by detecting changes of ATP levels within the cells (Aguilar-Bryan et al., 1995; Inagaki et al., 1996), the exact relationship between ATP hydrolysis and channel-gating is yet to be established (Miki et al., 1999).

Table 1.1: Summary of different members within the ABC transporter families and their general function and clinical significance.

ABC family	Example members identified	Expression sites	Function and clinical significance	References
ABCA	ABCA1	Ubiquitous	Cholesterol transport, atherosclerosis Amyloid formation, Azheimer's disease	(Kaminski et al., 2006; Kim et al., 2011; Yvan-Charvet et al., 2010)
	ABCA4	Rod cells	Transport of retinyldene-phosphatidylethanolamine Stargardt disease	(Quazi and Molday, 2014; Shroyer et al., 2001)
ABCB	ABCB1 (P-gp)	Brain, intestine, liver, kidney	Exporter of multiple substrates Organ defence and multidrug resistance	(Alfred H, 1999; Cascorbi, 2011; Leslie et al., 2005; Steinbach and Legrand, 2007)
	ABCB2/ ABCB3 (TAP1/2)	All organs	Transport of major histocompatibility class I peptides Immune response	(Momburg et al., 1994)
	ABCB4/ ABCB11	Liver	Secretion of phosphatidylcholine and bile salts Intrahepatic cholestasis	(Dixon et al., 2000; van Helvoort et al., 1996)
ABCC	ABCC1 (MRP1)	All organs	Exporter of multiple substrates Organ defence and multidrug resistance	(Cole, 2014; Leslie et al., 2005)
	ABCC7 (CFTR)	Most cells	Chloride ion conductance Cystic fibrosis, pancreatitis	(Andersson et al., 2002; Riordan et al., 1989)
	ABCC8/ ABCC9 (SUR1/2)	Pancreas, heart, muscle	Sulphonylurea receptors Hyperinsulinaemia in infant, type II diabetes	(Goksel et al., 1998; Thomas et al., 1995)
ABCD	ABCD1	Most cells (peroxis-omes)	Transport of long chain fatty acids X-linked adrenoleukodystrophy	(Wanders et al., 2006)
ABCG	ABCG2 (BCRP)	Brain, intestine, kidney, placenta	Exporter of multiple substrates Organ defence and multidrug resistance, development of gout	(Dehghan et al., 2008; Eisenblätter et al., 2003; Gedeon et al., 2006; Gutmann et al., 2005)
	ABCG5/ ABCG8	Liver, intestine	Elimination of plant sterols Sitosterolaemia and atherosclerosis	(Berge et al., 2000; Wilund et al., 2004)

1.3 The multidrug efflux pumps

In cancer treatment, one of the biggest challenges is the development of multidrug resistance (MDR) to chemotherapy in cancer cells. Solid tumours localised at the original site can be treated with surgery or radiotherapy. However, in systemic cancers (e.g. leukaemia and lymphoma) and metastatic cancers spread from solid tumours, chemotherapy remains the treatment of choice. The development of chemoresistance is known to reduce the long-term survival rate in leukaemia or metastatic cancers (Gottesman and Pastan, 1993; Leith et al., 1997). Overall, several major mechanisms of drug resistance in cancer have been established (Krishna and Mayer, 2000), for example, 1) reduced vascularisation in the growth pattern of non-dividing solid tumours induces resistance to drugs that target cell proliferation, 2) reduced cellular damage through glutathione (GSH) S-transferase mediated cellular detoxification and repair, 3) alterations to drug targets (e.g. topoisomerase (Drake et al., 1987) and apoptosis regulation (e.g. reduced p53 transcriptional activity and bcl-2 expression (Reed, 1995)). Another common mechanism by which chemoresistance develops in cancer cells is the increased ATP-dependent efflux of hydrophobic cytotoxic drugs, a process mediated by the ABC transporters. The ABCB1, ABCC1, and ABCG2 are three main multidrug efflux pumps of ABC transporters known to perform such function and are implicated in the MDR of cancer cells (Szakács et al., 2006).

1.3.1 ABCB1 – the P-glycoprotein

The ABCB1, or P-glycoprotein (P-gp), was the first human ABC transporter identified, comprising of two TMDs (12 transmembrane helices) and two NBDs within its polypeptide chain (TMD_1-NBD_1-TMD_2-NBD_2) (Juliano and Ling, 1976). It is known to confer resistance in cancer cells through the ATP-dependent export of various cytotoxic agents, such as doxorubicin and vinblastine (Sharom, 2011; Ueda et al., 1987). ABCB1 was first associated with poor treatment outcomes in acute leukaemia by causing chemoresistance in

cancer cells (Marie et al., 1991). Increased expression of ABCB1 was also associated with poorer clinical outcomes in breast cancer (Trock et al., 1997) and soft tissue sarcomas (Abolhoda et al., 1999). Physiologically, ABCB1 is highly expressed in various sanctuary sites of the human body, such as the blood-brain-barrier, intestine, liver bile ducts, placenta and kidney proximal tubules; acting as a protective efflux mechanism in these tissues by removing xenobiotics into the blood (Cascorbi, 2011; Cordon-Cardo et al., 1989; Leslie et al., 2005; Schinkel, 1999). In addition to cytotoxic agents, other compounds have also been identified as ligands of ABCB1, these include calcium channel blockers, anti-arrhythmics, antibiotics, (Gottesman and Pastan, 1993) and also fluorescent dyes (e.g. Hoechst bisbenzamide 33342 (H33342) (Shapiro et al., 1997)). ABCB1 was also implicated in the transport of synthetic and natural opioid compounds (Callaghan and Riordan, 1993). Loperamide is an opioid compound that was identified as a much better substrate of ABCB1 compared to other opioid compounds such as morphine and fentanyl, and it only exhibits peripheral opioid effects (anti-diarrhoeal) due to the increased efflux of loperamide by ABCB1 at the blood-brain-barrier (Wandel et al., 2002).

1.3.2 ABCC1 – the multidrug resistant associated protein 1

The ABCC1, also known as the multidrug resistant associated protein 1 (MRP1), was first identified in a MDR lung cancer cell line (Cole et al., 1992). In contrast to ABCB1, it has a distinct 5-domain organisation including the additional TMD_0 as discussed earlier, consisting of 17 transmembrane helices. Although the role of the extra domain TMD_0 is still unclear, it has been suggested to be important in ABCC1 dimerisation (Yang et al., 2007). ABCC1 is suggested to be clinically relevant in chemoresistance of cancer cells (e.g. non-small-cell lung cancer, prostate cancer, and breast cancer) through the efflux of cytotoxic agents (e.g. etoposide, doxorubicin, and vincristine) (Deeley et al., 2006; Slot et al., 2011). In neuroblastoma (a common extracranial solid tumour in children), poor clinical outcomes were associated with high expression levels or single nucleotide polymorphisms of ABCC1

(Haber et al., 2006; Pajic et al., 2011). In the human body, ABCC1 is important in the efflux of numerous endogenous or xenobiotic GSH conjugates in phase II metabolism (Cole and Deeley, 2006). Leukotriene C4-GSH conjugate is the most well known endogenous metabolite transported by ABCC1, as demonstrated in *in vitro* and *in vivo* studies (Leier et al., 1994; Schultz et al., 2001; Wijnholds et al., 1997). Similar to ABCB1, ABCC1 is also found in most normal tissues in the body (with increased distribution in lungs and testes) and contributes to tissue defence from toxic xenobiotics (Cole, 2014).

1.3.3 ABCG2 – a "half MDR transporter"

The ABC transporter of interest in this study, ABCG2, is another known multidrug efflux pump implicated in chemoresistance. It is a 655-amino acid polypeptide chain, also known as the breast cancer resistant protein (BCRP) first discovered in a MDR breast cancer cell line (MCF-7), which did not express ABCB1 or ABCC1 (Doyle et al., 1998). As a "half-transporter", the polypeptide chain of ABCG2 only consists of half the number of domains (single NBD and single TMD) compared to the expected number of domains for a full-length ABC transporter (e.g. ABCB1). Clinically, ABCG2 is known to be important in cancer chemoresistance, drug pharmacokinetics, and the development of gout.

Substrates of ABCG2

Thus far, hydrophobic cytotoxic agents, such as mitoxantrone, methotrexate, and tyrosine kinase inhibitors (e.g. erlotinib), are all identified as substrates of ABCG2 (Clark et al., 2006; Dohse et al., 2010). Using radiolabelled daunomycin as the trace ligand and insect cell membranes expressing ABCG2 (R482G mutant, see section 1.5), Clark et al. established the binding affinities of several substrates of ABCG2 in competition binding experiments. Mitoxantrone (substrate for both wild type and R482G ABCG2) was shown to be more potent than unlabelled daunomycin in displacing radiolabelled daunomycin. However, the displacement of the total binding was incomplete

(approximately 60 %). Together with the incomplete displacement result when H33342 was employed (less potent than mitoxantrone), Clark et al. suggested multiple daunomycin binding sites in ABCG, i.e. mitoxantrone and H33342 could displace the radioligand from one binding site, but not the other. The slow and incomplete dissociation of radiolabelled daunomycin in the presence of mitoxantrone and H33342 is also indicative of 'stabilisation' of one of the daunomycin binding sites, leading to suggestions of potential allosteric communication between the two drug binding sites (Clark et al., 2006). Apart from anticancer agents, other classes of drugs such as the calcium channel blockers (e.g. nifedipine), antibiotics (e.g. ciprofloxacin) and the HIV protease inhibitors (e.g. abacavir) have also been shown to be transported by ABCG2 (Merino et al., 2006; Shukla et al., 2006; Weiss et al., 2006).

ABCG2 in cancer multidrug resistance

Perhaps the most interesting aspect of ABCG2 in the clinic is its ability to confer resistance to chemotherapy as a multidrug efflux pump. Extensive investigations have been performed in leukaemia patients, and mixed evidence has been presented thus far. For example, high levels of ABCG2 and ABCB1 in samples from patients with acute myeloid leukaemia (AML) were shown to be associated with poorer prognosis (Benderra et al., 2004, 2005). Similarly, Uggla et al. showed that AML patients with the highest expression of ABCG2 had significantly shorter overall survival compared to those with lowest expression (Uggla et al., 2005). In contrast, flow cytometry detection of ABCG2 expression and determination of ABCG2 gene expression did not show clear up-regulation of ABCG2 in relapse cases of AML (Galimberti et al., 2004; van der Kolk et al., 2002). The importance of ABCG2 and ABCB1 expression in the multidrug resistance of AML was however reinforced in a recent review, and the authors concluded that accurate determination of the multidrug efflux pump expression in AML patients is important for finding the optimal cancer treatment (Xia and Smith, 2012). A recent study further demonstrated that resistance to anticancer agents (e.g. daunorubicin,

imatinib, and nilotinib) strongly depends on the expression levels of ABCG2 and ABCB1 in human leukaemia cells (Kosztyu et al., 2014). In addition to AML, presence of ABCG2 was also reported in other cancers (Diestra et al., 2002). High expression of ABCG2 in biopsy specimens of patients with small cell lung cancer was shown to be associated with poorer clinical response and progression free-survival, but not for the other multidrug efflux pumps (e.g. ABCB1 and ABCC1) (Kim et al., 2009). However, the importance of ABCG2 in other solid tumours is inconclusive and for example, studies have shown that chemoresistance caused by ABCB1 could be more clinically relevant in breast cancer compared to ABCG2 (Burger et al., 2003; Kanzaki et al., 2001).

The pharmacological targetting of ABCG2 or indeed ABCB1 remains unachievable thus far in the clinic. Although inhibitors such as tariquidar (Fox and Bates, 2007) were shown to be effective in *in vitro* and *in vivo* studies, increased toxicity and lack of multidrug efflux pump expression have often halted their progress in clinical trials (Nobili et al., 2006; Tamaki et al., 2011). A promising specific ABCG2 inhibitor, Ko143, structurally related to the first ABCG2 inhibitor (FTC, fumitremorgin C), was developed and reported to be less neurotoxic compared to FTC (Allen et al., 2002) but its effectiveness in the clinic is not yet demonstrated. Recently, the phosphodiesterase-5 inhibitor sildenafil was shown to increase intracellular accumulation of mitoxantrone and fluorescently labelled prazosin in ABCG2 overexpressing cells, suggesting that it may be useful as an adjuvant in chemotherapy (Shi et al., 2011). Thus far, limited success in the search for pharmacological agents targetting ABCG2 in cancer suggests that further understanding of the multidrug efflux pumps (expression, structure, functional mechanism) is required to improve the current drug design or chemotherapy treatment strategies.

ABCG2 in drug pharmacokinetics

Similar to ABCB1 and ABCC1, ABCG2 is also found in many organs, including the blood-brain-barrier, adrenal glands, lungs, mammary glands, intestines, testes and kidneys (Gutmann et al., 2005; Maliepaard et al., 2001; Mao and Unadkat, 2005; Zhang et al., 2003). Owing to its wide substrate specificity and distribution, physiologically, ABCG2 is suggested to be important for tissue defence through the export of xenobiotics. Brain perfusion studies in Abcb1-knockout mice indicated increased radiolabelled prazosin and mitoxantrone uptake into brain in the presence of ABCB1/ABCG2 inhibitor, GF120918. Further quantitative reverse transcription-PCR investigations demonstrated the expression of ABCG2 in the brain microvessels, thereby confirming a role for ABCG2 in tissue defence at the blood-brain-brarrier (Cisternino et al., 2004). In addition to organ defence, clinically, ABCG2 plays an important role in the pharmacokinetics of medicinally active compounds, affecting their bioavailability. For example, a single nucleotide polymorphism at nucleotide position 421 (cytosine to adenine) in the ABCG2 coding region, which results in Q141K mutation in the amino acid sequence, has been shown to increase the bioavailability and clinical efficacy of topotecan (Sparreboom et al., 2005). The same polymorphism was also reported to significantly affect the pharmacokinetics of atorvastatin and potentially influence the efficacy and toxicity of rosuvastatin (Keskitalo et al., 2009). In recognition of this, the Food and Drug Administration recommended that new drug molecules should be tested for their interaction with ABCG2 during the drug development process (Giacomini et al., 2010). Recently, a comprehensive genomic study reported that the same single nucleotide polymorphism is important in the development of gout. In this study the Q141K ABCG2 variant was shown to cause 53 % reduction of urate transport in the kidney, resulting in the increase risk of gout. Clinical data suggested that at least 10 % of gout cases in whites can be attributed to this polymorphism (Woodward et al., 2009). The effects of this polymorphism will be discussed in detail in section 1.5.

ABCG2 is shown to have “contrasting” physiological roles in pregnancy and breastfeeding. High expression of ABCG2 was reported at the apical membrane of the placenta. Jonker et al. first demonstrated that foetal penetration of topotecan was 2x higher in the vehicle treated, *Abcb1*-knockout pregnant mice, compared to the ABCG2/ABCB1 inhibitor GF120918-treated mice (Jonker et al., 2000). An *ex vivo* perfusion study using a human placenta model also revealed that inhibition of ABCG2 using nicardipine (a calcium channel blocker) resulted in significant increase in glibenclamide (antidiabetic) concentration in the foetal circulation (Gedeon et al., 2006). These studies suggested that ABCG2 may protect the foetus by exporting harmful compounds back into the maternal circulation (Gedeon et al., 2006; Jonker et al., 2000; Pollex et al., 2008). At the mammary glands however, ABCG2 was shown to export harmful substances including dietary carcinogens and other xenobiotics out of the maternal body and into the breast milk and may be harmful to the infant (Herwaarden et al., 2006; Jonker et al., 2005; Merino et al., 2005; Olsen et al., 2007). Alfred Schinkel’s lab identified that several compounds such as dietary carcinogens, PhIP (heterocyclic amine) and aflatoxin B1, along with the anticancer agent topotecan, were concentrated in the milk of wild type mice but not *Abcg2*-knockout mice (Herwaarden et al., 2006; Merino et al., 2005).

1.4 Structure and mode of action – ABC exporters

The MJ0796 NBD structure shown in Figure 1.2 above does not represent the full details of a native ABC transporter, as it only shows the dimeric NBD subunits of an ABC system. The significance of ABC exporters in human, particularly in cancer as discussed above, has prompted various efforts to obtain full length ABC exporter structures.

1.4.1 Structures of ABC exporters

To date, several crystal structures of ABC exporters have been identified, as summarised in Table 1.2. Overall the structural investigations showed that ABC transporters can either adopt an inward facing (ABCB1) or outward facing (Sav1866) conformation, as shown in Figure 1.3A. This fits well to the widely recognised mechanism of action for ABC exporters, the ATP switch model (see next section) and the "head-to-tail" NBD dimer formation as shown in Figure 1.1 above (Higgins and Linton, 2004). The structure of homodimeric Sav1866 was the first accurate ABC transporter structure reported and is still the highest resolution multidrug resistance-type ABC exporter structure resolved to date (Figure 1.3A) (Dawson and Locher, 2006). This structure first revealed the topology of the six transmembrane helices (TM), in which the bundle of the dimeric helices forms two discrete "wings" that point towards opposite extracellular directions (Figures 1.3B), and each wing consists of TM1-2 of one NBD subunit and TM3-6 of another (Figures 1.3B and 1.3C). The transmembrane helices are joined together by long intracellular loops (ICL) and short extracellular loops. The intracellular loops were suggested to extend the transmembrane helices beyond the membrane, approximately 25 Å into the cytoplasm (Figure 1.3A). Both ICLs in Sav1866 were proposed as "coupling helices" and primary contact to the NBD of opposing subunit was demonstrated in the structure, suggesting possible involvement in conformational changes during substrate transport and ATP hydrolysis (Dawson and Locher, 2006), consistent with data from mutational studies of the predicted ICLs of ABC exporters elsewhere (Cotten et al., 1996; Currier et al., 1992). The first Sav1866 structure was resolved in the presence of ADP (Dawson and Locher, 2006), and the authors concluded that it was likely to be affected by the crystallisation conditions, rather than the presence of ADP. A subsequent outward facing structure bound to a non-hydrolysable ATP analogue was resolved, suggesting this could be one of the conformations adopted by ABC exporters in ATP-bound state (Dawson and Locher, 2007). Although the structure of mouse ABCB1a represents an

important breakthrough due to its high sequence similarity to human ABCB1 (96 %) and the presence of substrate in the reported X-ray crystal structure, it has been reviewed recently and substantial changes to the structure were proposed, following comparison with the *C. elegans* ABCB1 structure (Li et al., 2014; Ward et al., 2013).

Table 1.2: Summary of the main ABC exporters structures reported to date.

ABC transporter	Species	Resolution (Å)	References	PDB code
Sav1866	*S. aureus*	3.0	(Dawson and Locher, 2006, 2007)	2HYD, 2ONJ
MsbA	*E. coli*	3.7	(Ward et al., 2007)	3B60
ABCB1a	Mouse	3.8 to 4.2	(Ward et al., 2013)	4KSB, 4KSC, 4KSD
	Mouse	3.8	(Li et al., 2014)	4M1M, 4M2S, 4M2T
ABCB1	*C. elegans*	3.4	(Jin et al., 2012)	4F4C
ABCB10	Human (mitochondria)	2.9	(Shintre et al., 2013)	4AYT, 4AYX, 4AYW, 3ZDQ
McjD	*E. coli*	2.7	(Choudhury et al., 2014)	4PL0
TM287/288	*Thermotoga maritima*	2.9	(Hohl et al., 2012)	3QF4

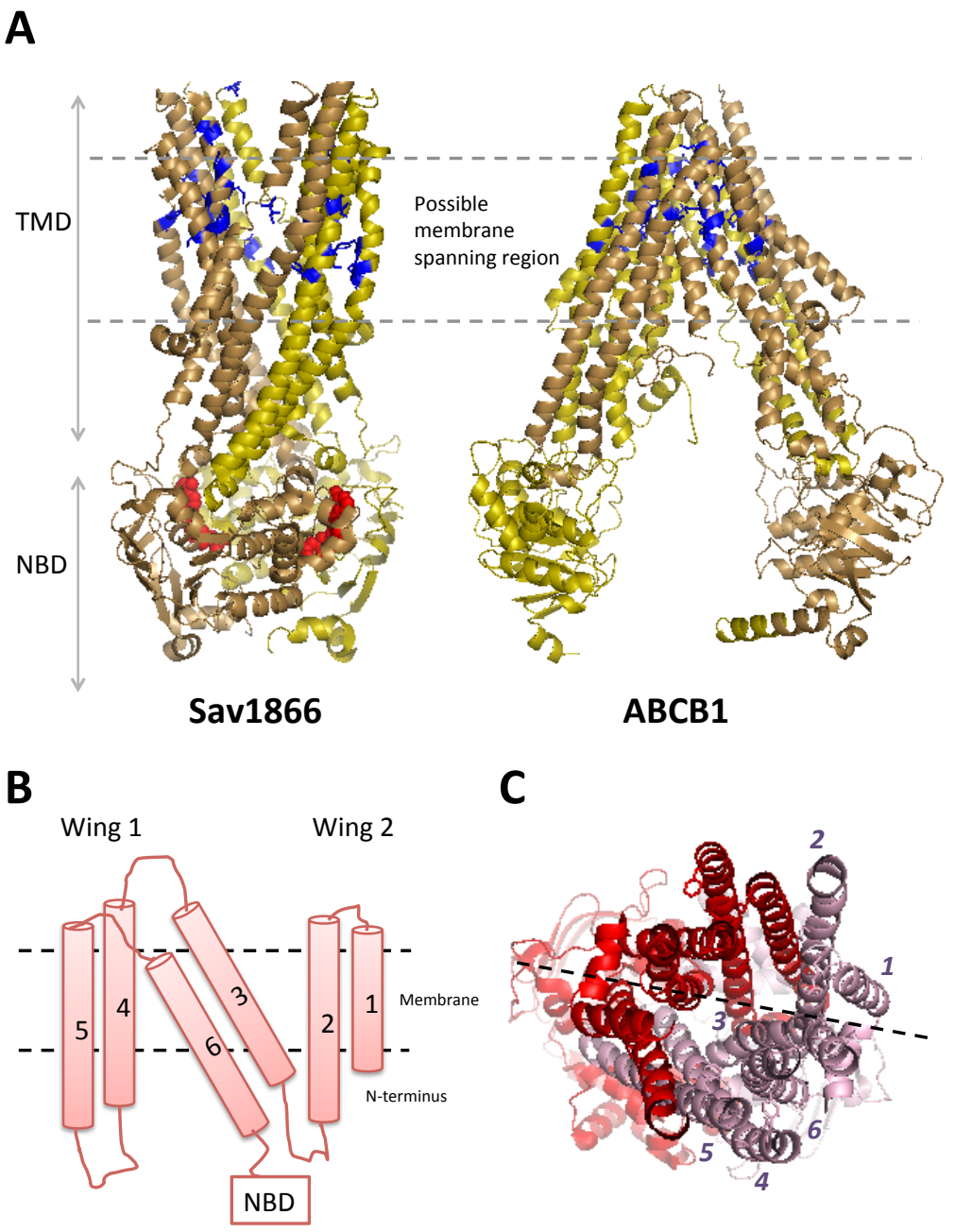

Figure 1.3: Crystal structures of ABC transporters. The outward facing dimeric *S. aureus* Sav1866 (PDB: 2YHD) and inward facing *C. elegans* ABCB1 (PDB: 4F4C) structures are shown in ribbon representation. Non-hydrolysable ATP analogue (AMP-PNP) in Sav1866 is shown as red balls. The different protomers in Sav1866 and two halves of ABCB1 are differentiated using yellow and gold colour (**A**). The topology of 'wing' conformation of the transmembrane helices is schematically represented in (**B**). Top-down view of the Sav1866 dimeric structure showing the two "wings" separated by a black dotted line (**C**) (Dawson and Locher, 2006). In (**A**), the substrate binding residues (blue) identified in mutational studies of human ABCB1 (primarily in (Loo et al., 2004, 2006)) were mapped onto the two structures as reviewed in (Wong et al., 2014). Sequence alignment (Figure S1.1) was performed using Clustal Omega (Sievers et al., 2011) and figures were generated using PyMOL.

Investigation of these crystal structures shows that conformational changes in the ABC transporters (from inward facing to outward facing) could potentially alter the hydrophobicity of the binding pockets in the TMDs. In Figure 1.3A, the sequences of Sav1866 and *C. elegans* ABCB1 were aligned against the human ABCB1 sequence (Figure S1.1 in Appendix) and the residues corresponding to the substrate binding sites identified biochemically (mutational studies) in human ABCB1 was highlighted in blue. Studies of sequential cysteine introductions in a cysteine-less human ABCB1 (Loo and Clarke, 1995) using thiol-reactive compounds such as methanethiosulphonate analogues and dibromobimane have identified various potential substrate binding sites in human ABCB1 (Loo and Clarke, 2000; Loo et al., 2004, 2006), as reviewed in (Wong et al., 2014). The binding sites were seen as clustered in the inward facing conformation and dispersed in the outward facing conformation (Figure 1.3A). Surface-accessibility calculations performed also reported a reduction in the overall hydrophobicity of the drug binding pocket in the outward facing conformation (Wong et al., 2014). As the binding sites were also seen high up in the TMD regions of both structures in Figure 1.3A, it supports the "hydrophobic vacuum cleaner" or "flippase" models suggested previously, in which substrates could gain entry into the binding sites of ABC transporters through the membrane lipid bilayer (Higgins and Gottesman, 1992).

In summary, crystallisation of membrane ABC transporters has proven to be extremely challenging in recent years due to the complexity of purifying membrane proteins and obtaining suitable crystals, as suggested in the relatively few successful structures reported so far. A high-resolution crystal structure of human ABC exporter remains highly desirable for in-depth study of ABC exporters but it is yet to be discovered. Also for ABCG2, although 3D structural data were generated using electron microscopy analysis of single particles of ABCG2 protein samples purified from insect cells, the final resolution was too low and only the overall shape and the estimated

oligomeric organisation of ABCG2 were deduced from the final data (McDevitt et al., 2006). Nevertheless, the current structures have provided a general knowledge of the different conformational states and possible substrate binding pockets for the ABC exporters (e.g. ABCB1 modelled in Figure 1.3A).

1.4.2 Homology modelling of ABCG2

The high sequence similarities of human ABCB1 with Sav1866 (Kerr et al., 2010) and *C. elegans* ABCB1 (46% identical overall) allowed the mapping of drug binding sites on the structures as shown in Figure 1.3A and reliable determination of various homology models that can be validated by biochemical data (Becker et al., 2009; McDevitt et al., 2008a; O'Mara and Tieleman, 2007; Stockner et al., 2009), see Figure S1.1 in Appendix for sequence alignment. However, in ABCG2, sequence similarity is low, e.g. 23 % and 6 % identical with the NBD and TMD of Sav1866 respectively, implying that the homology models reported thus far (Hazai and Bikádi, 2008; Rosenberg et al., 2010) are unlikely to be reliable, as suggested in (Kerr et al., 2010).

1.4.3 The ATP-switch model for ABC exporters

The exact functional mechanism for ABC exporters is not yet established universally and the mechanism of action may vary among different ABC transporters (e.g. importers versus exporters). However, biochemical and structural evidence from both ABC importers (Chen et al., 2003; Locher et al., 2002) and exporters presented thus far support a widely accepted ATP-switch model that can be used to describe the ABC exporter functional mechanism (Figure 1.4), and some features in this model may well be similar to those of the ABC importer mechanism. It is also not inconceivable that some of the human ABC systems, for example the ion channels/regulators (e.g. ABCC7, SUR1/2) and half transporters (e.g. ABCG2) may adopt a slightly different

mechanism in their mode of transport. The ATP-switch model is proposed based on a fundamental theory where the NBDs form a close dimer (outward facing conformation) upon binding of ATP molecule, and dissociate to an open dimer (inward facing conformation) after ATP hydrolysis and the release of ADP and P_i (inorganic phosphate) (Higgins and Linton, 2004).

Step 1: Transport cycle initiation. Thus far, evidence suggests that substrate binding to the high affinity binding pocket in the TMDs is the first step to initiate the transport cycle, in which the transporter is likely to adopt an initial inward facing conformation (*C. elegans* ABCB1 structure in Figure 1.3A). This was demonstrated when the ligand-independent mutants of bacterial histidine and maltose transporters were shown to possess increased ATP hydrolytic activity, compared to wild type transporters in the absence of substrate, indicating that substrate binding is required to initiate the transport cycle of ABC transporter (Davidson et al., 1992; Petronilli and Ames, 1991). Tryptophan quenching experiments in purified ABCB1 (reconstituted in liposomes) also indicated possible small conformational change in the NBDs after ATP hydrolysis, and ABCB1 may adopt different conformations upon binding of transport substrate in the presence and absence of ATP (Sonveaux et al., 1999). Pharmacological assays with radiolabelled ligands also demonstrated increased binding affinity of vinblastine to ABCB1 (purified in membrane vesicles) in the absence of ATP analogues (Martin et al., 2001).

Step 2: Closure of NBD dimers. Substrate binding is currently proposed to enhance the binding of ATP to NBDs and reduce the energy required for a closed dimer formation. ATP binding then acts as the “switch” that induces the formation of a closed dimer, as shown in the NBD structural studies (Procko et al., 2006; Smith et al., 2002), (see section 1.1.2). This conformational change converts the high affinity substrate binding pocket to a low affinity state, and the transporter now adopts the outward facing conformation (e.g. Sav1866 structure in Figure 1.3A), resulting in the release

of substrate. Martin et al. showed that presence of the non-hydrolysable ATP analogue (AMP-PNP) resulted in a 9-fold reduction in the binding affinity of radiolabelled vinblastine to ABCB1 (Martin et al., 2001). Comparable findings were also reported in ABCG2 and ABCC1 where binding of ATP or AMP-PNP resulted in reduced binding of radiolabelled substrate daunomycin and oestrone sulphate (in the presence of glutathione), respectively (McDevitt et al., 2008b; Rothnie et al., 2006). Furthermore, structural data for ABCB1 also suggested that binding of AMP-PNP causes considerable conformational change in the TMDs that requires repacking of the transmembrane α-helices (Rosenberg et al., 2003). At present, the exact number of ATP molecules hydrolysed during each transport cycle is still not fully known. It is generally assumed that the binding of two ATP molecules is required for the stabilisation of the closed NBD dimer system, as seen in the NBD crystal structures of MJ0796 and MalK subunits (Chen et al., 2003; Smith et al., 2002). However, in terms of ATP hydrolysis, it is unclear if both ATP binding pockets in the NBDs hydrolyse the bound ATP molecules at the same time or the hydrolysis of ATP molecules occurs in an alternating fashion, as reviewed in (Higgins and Linton, 2004). Also, a single functional NBD subunit has been shown to be sufficient for ATP hydrolysis and function in bacteria histidine permease (Nikaido and Ames, 1999).

Step 3: ATP hydrolysis. Upon release of the substrate, the transporter is likely to undergo another conformational change that triggers the hydrolysis of ATP. It was initially thought that hydrolysis of ATP would trigger the change of transporter back to the outward facing basal conformation in Step 1. However, studies have consistently shown that the NBDs remain in the closed state after hydrolysis of ATP. Using vanadate to trap ABCB1 transporters in their catalytic transition state (a complex consisting of MgADP and vanadate) that mimics the MgADP and P_i after the hydrolysis of ATP, studies have demonstrated that ABCB1 remained in its low affinity state (Martin et al., 2001; Ramachandra et al., 1998). Elsewhere, low substrate binding affinities

were also reported for ABCG2 (radiolabelled daunomycin) and ABCC1 (radiolabelled oestrone sulphate in the presence of glutathione) when the transporters were trapped in the post-hydrolytic state by vanadate (McDevitt et al., 2008b; Rothnie et al., 2006). The crystal structure of the maltose transporter with a closed NBD conformation, consisting of the SBP, one maltose molecule, and two bound ATPs, suggests that the ABC importers and exporters may share a "common" ATP hydrolysis coupling mechanism, in which ATP hydrolysis triggers the substrate release from SBP to the importer and from the exporter to the extracellular medium (Oldham et al., 2007).

Step 4: Restoration. The release of P_i and ADP finally triggers the restoration of the transporter to its basal, inward facing conformation with high substrate affinity, as the closed NBD dimer conformation is disrupted. This proposal was based on the initial vanadate-trapping experiment where the MgADP remained in the system to form the MgADP-vanadate complex in ABCB1 as P_i was replaced by vanadate, leading to suggestion that P_i was released before the ADP (Senior et al., 1995). Martin et al. showed that the ABCB1 complex covalently crosslinked with 8-azidoADP (not containing vanadate) restored its high affinity state for radiolabelled vinblastine, suggesting that the release of ADP may not be the main trigger for this restoration step and binding of vinblastine may occur before the release of ADP. As binding of non-hydrolysable ATP analogue to ABCB1 causes a reduction in substrate binding affinity, this is also indicative of a possible passive role of ATP in the opposing NBD; hence, Martin et al. proposed that an alternating catalytic cycle could be responsible for the transport of vinblastine in ABCB1 (Martin et al., 2001). This final step and the several other mechanisms within the catalytic cycle of ABC exporters, is therefore yet to be fully characterised.

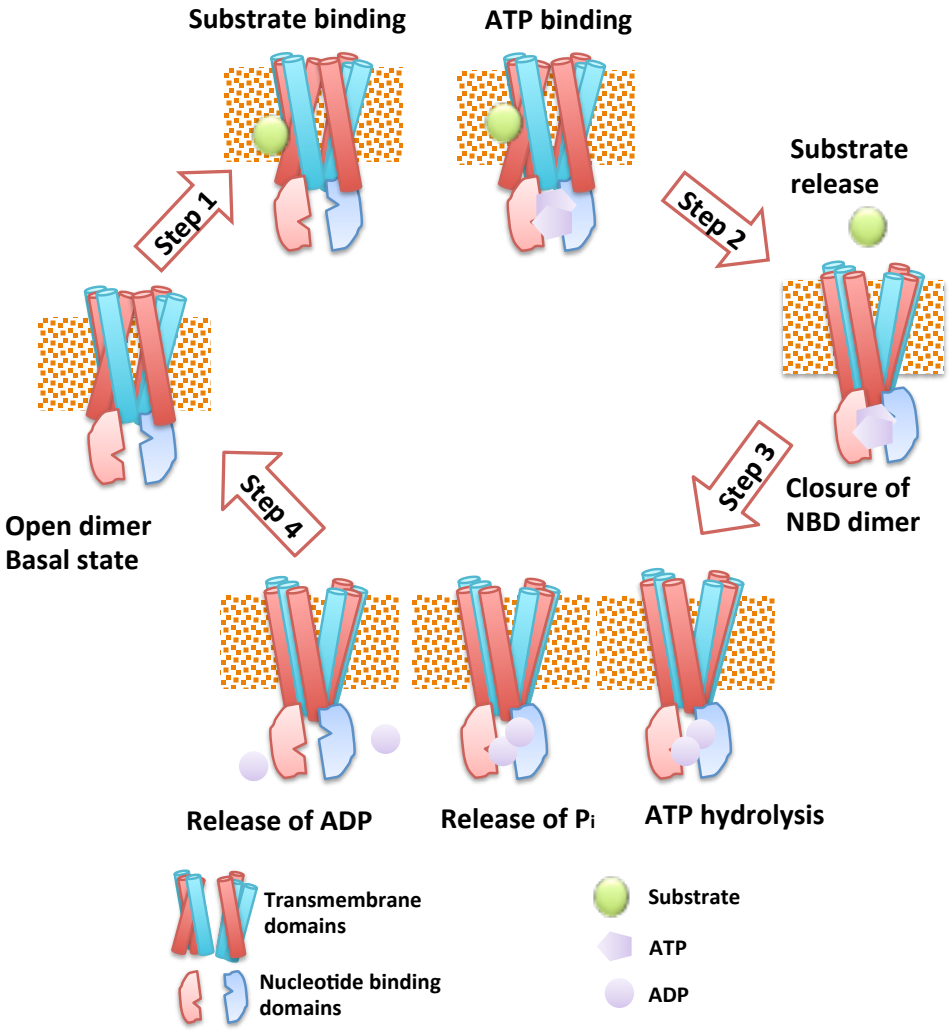

Figure 1.4: ATP switch model showing the transport cycle for an ABC exporter. Substrate binding initiates a conformational change in the ABC transporter and results in the increase of NBD affinity to ATP (**Step 1**). ATP binding then induces a conformational change from inward facing to outward facing conformation with reduced affinity to substrate. Substrate is released at this stage (**Step 2**). ATP hydrolysis within the NBD close dimer occurs (**Step 3**). Release of inorganic phosphate (P_i) and ADP triggers another conformational change and ABC transporter is restored back to its basal inward facing conformation with high substrate affinity, ready for the next cycle (**Step 4**). Figure adapted from (Higgins and Linton, 2004).

1.5 Mutational effects on ABCG2

Thus far, various mutations in ABCG2 that affect its function, localisation and post-translational modifications have been reported and these are summarised in Table 1.3 below and will be discussed in this section. Further discussion on possible mutations in ABCG2 that may affect its oligomerisation will be discussed in the following section.

1.5.1 Function

Unsurprisingly, mutation of the lysine residue at the Walker-A motif of ABCG2 (see section 1.1), K86A (GPTGGG**K**SS) resulted in impaired ABCG2 function, as first demonstrated in (Ozvegy et al., 2002). Immunohistochemistry analysis demonstrated reduced expression levels and impaired membrane trafficking of this ABCG2 variant, compared to wild type (Henriksen et al., 2005a). The E211Q mutation in ABCG2 (SILFLD**E**PT; glutamate to glutamine mutation in the Walker-B motif as described in section 1.1), was also reported to abolish ATPase activity of purified ABCG2 mutant reconstituted in membrane vesicles (Hou et al., 2009). Additionally, mutation at the neighbouring aspartate residue to asparagine (D210N) was shown to result in non-functional ABCG2 mutant (Bhatia et al., 2005). Surface expression of both E211Q and D210N ABCG2 mutants was not affected compared to wild type.

The arginine residue at position 482 (R482) was identified as important for substrate specificity in ABCG2. Honjo et al. first reported efflux of doxorubicin and rhodamine in R482T and R482G variants of ABCG2 but not the wild type, and all three variants (R482T, R482G and wild type) demonstrated transport activity for mitoxantrone (Honjo et al., 2001). Cytotoxicity assays showed that cells expressing the ABCG2 mutants (R482T and R482G) produced higher resistance to cytotoxic agents such as doxorubicin, daunorubicin, and epirubicin compared to wild type, whereas novorubicin was found to be a more effective ABCG2 inhibitor in cells expressing the wild type variant

compared to the mutants (Robey et al., 2003). An extensive study of six different R482 mutations (R482G, R482H, R482K, R482P, R482T, and R482Y) reported different ATPase activities in the presence of [^{125}I]iodoarylazidoprazosin (IAAP). The authors reported that all the R482 mutants (including those that showed impaired transport and ATPase function) were able to bind [^{25}I]IAAP. This implies that the R482 residue may function in other roles such as signalling in the transmembrane domain or conformational changes during substrate transport (Ejendal et al., 2006).

Table 1.3: Summary of mutational effects on ABCG2.

Mutation	Location	Effects on ABCG2	References
Function:			
K86M	Walker-A motif	Reduced surface expression and ATPase activity	(Henriksen et al., 2005a; Ozvegy et al., 2002)
D210N	Walker-B motif	Abolished transport activity	(Bhatia et al., 2005)
E211Q	Walker-B motif	Abolished transport activity	(Hou et al., 2009)
R482X	Transmembrane segment 3	Altered substrate specificity	(Ejendal et al., 2006; Honjo et al., 2001; Robey et al., 2003)
Expression and localisation:			
G406L/G410L (T402L)	Transmembrane segment 1, GXXXG motif	Reduced surface expression and transport activity	(Polgar et al., 2004, 2010)
Q141K	NBD	Reduced surface expression and transport activity	(Morisaki et al., 2005)
F142△	NBD	Reduced expression and loss of ATPase activity	(Sarankó et al., 2013; Woodward et al., 2013)
Phosphorylation by Pim1-kinase:			
T362A	NBD	Reduced expression and function	(Xie et al., 2007)
Glycosylation:			
N596A	Extracellular loop-3	Reduced glycosylation	(Diop and Hrycyna, 2005)

1.5.2 Localisation

The LIXXGVXXGVXXT motif was first identified in the dimerisation interface of transmembrane helices in glycophorin A (Lemmon et al., 1994). Further statistical analysis (TMD sequences in Protein Data Bank) reported common occurrences of the GXXXG motif in transmembrane helices while another *in vitro* selection study (using a vector that generates hybrid proteins with random substitutions in a transmembrane helice backbone) suggested possible global role of GXXXG motif in transmembrane helix interactions (Russ and Engelman, 2000; Senes et al., 2000). Polgar et al. analysed the role of GXXXG motif in the transmembrane segment 1 of the predicted topology of ABCG2 and found that mutations of the glycine residues to leucine (G406L/G410L) resulted in impaired function and reduced surface expression; however no effect was observed in the G406A/G410A mutant. Both mutants were reported to have no effect on ABCG2 oligomerisation using non-reducing SDS-PAGE and western blot analysis (see next section) (Polgar et al., 2004). Further mutations of the Thr-402 residue next to the GXXXG motif did not have any significant impact on the expression or function of ABCG2 wild type or double mutant G406L/G410L (Polgar et al., 2010).

Early *in vitro* studies of the gout-causing single nucleotide polymorphism (Woodward et al., 2009) revealed that the Q141K mutation resulted in reduced function (ATP activity and drug efflux) and impaired surface expression of ABCG2, as demonstrated using transport and ATPase assays and immunohistochemistry fluorescence (Kondo et al., 2004; Mizuarai et al., 2004; Morisaki et al., 2005). Recently two other studies suggested that the processing defect caused by Q141K mutation could be rescued using the histone deacetylase inhibitor 4-phenylbutyrate, which is known to protect misfolded proteins from endoplasmic reticulum degradation (Sarankó et al., 2013; Woodward et al., 2013). Treatment of HEK293T cells expressing the Q141K variant of ABCG2 with VRT-325 (effective corrector molecule of the CFTR △F508 mutant) indicated improved ABCG2 expression and reduced uric

acid accumulation (Woodward et al., 2013). The deletion of Q141 neighbouring residue Phe-142, homologous to F508 in ABCC7, was also shown to significantly reduce the expression level of ABCG2, suggesting that this deletion causes major folding defects and loss of ATPase function in ABCG2 (Sarankó et al., 2013; Woodward et al., 2013).

1.5.3 Post-translational modifications

Three asparagine residues with the consensus sequence of Asn-X-Thr/Ser were established as acceptor sites for N-glycosylation in ABCB1. Mutations of these three asparagine residues to glutamine resulted in the migration of ABCB1 protein sample at a lower molecular weight compared to wild type before N-glycanase treatment in SDS-PAGE and western blot analysis (Schinkel et al., 1993). In ABCG2, three potential asparagine residues with the consensus sequence were identified in the extracelluar loops 1 and 3. The N596 residue in extracellular loop-3 was identified as an acceptor site for the N-linked glycosylation of wild type. The N596Q ABCG2 mutant migrated at lower molecular weight compared to wild type without N-glycosidase F treatment and at identical molecular weight as wild type after treatment. However, the cell surface expression and function of the N596Q mutant were indistinguishable from wild type ABCG2 (Diop and Hrycyna, 2005), consistent with results reported in ABCB1 and ABCC1 (Bakos et al., 1997; Schinkel et al., 1993), implying that the N-linked glycosylation may not be important for cell surface expression and function of ABC transporters.

The phosphorylation of ABCG2 has also been subjected to investigation. Takada et al. first showed that treatment with phosphatidylinositol 3-kinase (PI3K) inhibitors resulted in the internalisation of ABCG2 when expressed in LLC-PK1 cells, detected using immunohistochemical staining. Further analysis also suggested a potential role of protein kinase B (Akt) in the modulation of ABCG2 cell surface expression (Takada et al., 2005). Activation of Akt was

previously demonstrated as one of the components that induces transcription of *pim-1* promoter (Krishnan et al., 2003). The *pim-1* proto-oncogene encodes for two isoforms of a serine/threonine kinase – the 33 kDa and 44 kDa Pim-1 kinases (Saris et al., 1991), and they are thought to be important in the regulation of cancer development and progress. For example, reduced expression of Pim-1 kinase is related to significantly poorer patient outcome in prostate cancer (Dhanasekaran et al., 2001) and the use of a Pim kinase inhibitor (SGI-1776) has been shown to improve the effectiveness of taxane-based chemotherapies on resistant prostate cancer cells (Mumenthaler et al., 2009). A study on the mechanism of 44 kDa Pim-1 kinase (Pim-1L) showed increased expression levels of Pim-1L and ABCG2 in mitoxantrone and docetaxel resistant prostate cancer cell lines. An immunoprecipitation assay using anti-phosphothreonine-362 of ABCG2 indicated that the T362A mutation could affect the phosphorylation of ABCG2 by Pim-1L. Cells expressing Pim-1L and T362A variant of ABCG2 also showed increased viability upon treatment with docetaxel (compared to wild type), suggesting that the Pim-1L-induced chemoresistance in prostate cancer cells may be mediated through the phosphorylation of ABCG2 (Xie et al., 2007).

1.6 Oligomerisation of ABCG2

As discussed above, ABCG2 is a “half transporter”, and it is recognised that it has to function as a dimer or higher order oligomer. The dimerisation of ABCG2 was first detected in non-reducing SDS-PAGE and western blot analysis (in the absence of reducing agent DTT (dithiothreitol)), in which ABCG2 migrated at molecular weights of approximately 160 kDa compared to 80 kDa (monomer) in reducing conditions (Litman et al., 2002; Xu et al., 2004).

1.6.1 Oligomeric state of ABCG2

Xu et al. further characterised the oligomeric state of ABCG2 using varying concentrations of denaturing (SDS) and non-denaturing agents (perfluoro-

octanoic acid, PFO and Triton-X) in combination with PAGE, gel fitration and gradient sedimentation methods, and ABCG2 samples extracted from membrane preparations from a multidrug resistant cell line (MCF7/AdrVp3000). The techniques employing non-denaturing detergents revealed higher order oligomer formation of ABCG2, such as tetramers and dodecamers. Furthermore, SDS-PAGE (reducing conditions) analysis of ABCG2 treated with crosslinking agent DSS (disuccinimidyl suberate) in live cells prior to sample preparation also showed possible existence of monomeric, dimeric, trimeric and tetrameric species of ABCG2. The authors suggested that ABCG2 is likely to exist as a minimal stable complex of homotetramer and proposed a possible dodecameric formation between the tetrameric subunits (Xu et al., 2004). Elsewhere, 3D structural data of purified ABCG2 expressed in insect cells revealed a possible octameric complex of ABCG2 formed by four dimers, using single particle electron microscopy analysis and modelling methods (McDevitt et al., 2006). However, the study was inconclusive due to insufficient resolution and samples were purified from insect cells expressing high levels of ABCG2 following infection with high recombinant baculovirus. In another study of purified ABCG2 protein samples from both insect and mammalian cells (Flp-In-293), the final blue native gel electrophoresis (which showed a single band between 140 kDa and 440 kDa) and electron microscopy analysis of ABCG2 samples (extracted from Flp-In-293 cells) suggested that tetrameric organisation of ABCG2 is likely (Dezi et al., 2010).

1.6.2 Residues or domains responsible for ABCG2 oligomerisation

Other studies have focussed on establishing the residues or domains that could be responsible for oligomerisation of ABCG2. In particular the roles of three cysteine residues identified in the extracellular loop-3 of ABCG2 predicted topology – Cys-592, Cys-603, and Cys-608, have been extensively studied. Mutations at the Cys-603 residue to seven different amino acids (D, H, R, S, Y, A, and W) resulted in the increased migration of ABCG2 as monomers (instead of dimers) in SDS-PAGE analysis under non-reducing

conditions (Henriksen et al., 2005b; Kage et al., 2005). These results suggest that the Cys-603 residue is required for the formation of an intermolecular disulphide bridge. However, both studies reported that all the Cys-603 mutants remained functional, indicating that the intermolecular disulphide bridge is not essential for ABCG2 expression and function. Two independent fluorescence studies using bimolecular fluorescence complementation (BiFC) and fluorescence resonance energy transfer (FRET) techniques also demonstrated that the C603A mutation did not affect oligomerisation of ABCG2 in mammalian cells (Haider et al., 2011; Ni et al., 2010), see chapter 5 for further discussion on ABCG2 oligomerisation investigated using the fluorescence techniques employed in these two studies.

The roles of Cys-592 and Cys-608 are less well understood as contradictory evidence has been presented. Henriksen et al. reported that the function of the ABCG2 double mutants (C592A/C603A and C603A/C608A) were impaired whilst the expression of triple mutant C592A/C603A/C608A was non-detectable (Henriksen et al., 2005b). In contrast, studies elsewhere have shown that the triple alanine (or serine) mutations, C592A/C603A/C608A, was non-detrimental to the function of ABCG2 (Bhatia et al., 2005; Shigeta et al., 2010), although reduced surface expression of the triple serine mutant was observed (Shigeta et al., 2010). The roles of Cys-592 and Cys-608 therefore remain inconclusive and it is possible that they are involved in the folding and localisation of ABCG2 but only to a certain extent – and may not have significant effect on its oligomerisation or function. Another study generated various truncated ABCG2 mutants (e.g. NBD only, TMD only, and transmembrane helices 5-6) and studied the potential roles of different domains in the oligomerisation of ABCG2 using co-immunoprecipitation pull down assay. Although the membrane localisation of truncated ABCG2 mutants was not convincingly demonstrated, the authors proposed that the transmembrane helices 5-6 (TM5-6) contain residues implicated in the formation of ABCG2 oligomers (Xu et al., 2007). Further analysis of the TM5-6

construct using identical non-denaturing protein analysis methods (described earlier in (Xu et al., 2004)) demonstrated consistent dodecamer formation of the transmembrane helices 5-6, supporting the suggestion by the authors that ABCG2 could exist as homododecamers (Xu et al., 2007).

The precise determination of ABCG2 oligomeric state is important, as it will provide further understanding of the function of the ABCG transporter family and could lead to new drug development strategies that target the oligomerisation of these transporters. However, the studies discussed in this section show that the oligomerisation of ABCG2 is not well understood. Results from most studies were inconclusive (in particular the oligomeric state) and limited by either the use of biochemically purified ABCG2 protein samples (affected by choice and concentration of detergents) or the use of techniques that could not reliably determine the protein oligomeric state (e.g. low resolution electron microscopy analysis).

1.7 Fluorescence microscopy

Fluorescence techniques are heavily employed to investigate the dynamics and oligomerisation of ABCG2 in this study. The background and theory of each of these fluorescence techniques will be described in the beginning of the respective results chapter. In this section, the basics of fluorescence microscopy and fluorescent proteins will be described.

1.7.1 Principles of fluorescence

The process of light emission as a result of the electronic transition of excited state to ground state in any substance is termed as luminescence, which is divided into phosphorescence and fluorescence. In phosphorescence, this transition is slow and light emission typically lasts for milliseconds to seconds, as seen in glow-in-the-dark toys.

In fluorescence, the transition of the excited valence electron (of a fluorophore) back to its ground state is much faster, usually in nanoseconds or less. Amongst the first autofluorescent molecules (fluorophores) identified were quinine (blue), fluorescein (green) and rhodamine (red). These small molecules typically contain 1 or more aromatic groups. Following the initial observation of fluorescence in quinine, the process of light absorption and emission in fluorescence is now commonly described using the Jablonski diagram, schematically represented in Figure 1.5. As high energy light (shorter wavelength) from an incandescent lamp or laser source excites a fluorophore, a valence electron within the fluorophore moves up to its higher energy states. Light of lower energy (longer wavelength) is subsequently emitted as the electron returns to its ground state; a process that usually lasts for nanoseconds in fluorescence. The energy emitted from this process is lower than the excitation or absorption energy, because energy is lost as the valence electron moves in the high energy states, e.g. from A to B in Figure 1.5. This difference between the absorption (or excitation) and emission energy is known as the Stokes shift.

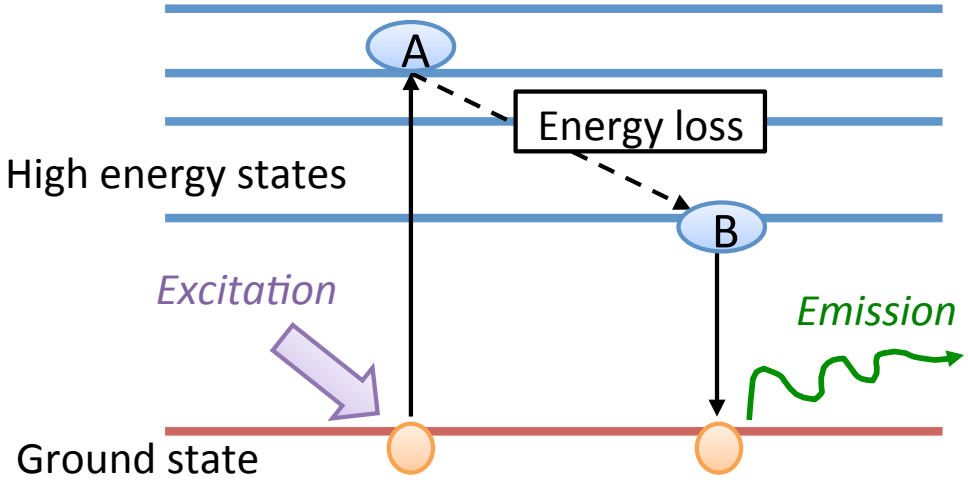

Figure 1.5: A schematic Jablonski diagram. When a fluorophore is excited by high energy light (purple), a valence electron (orange) moves to its higher energy states. Upon returning to its original state, lower energy light is emitted (green).

The range of wavelengths of light over which a particular fluorophore can be excited by is known as the excitation spectrum whilst the subsequent

wavelengths range of light emitted by the fluorophore is known as the emission spectrum (Figure 1.6). The excitation spectrum ensures that the wavelengths of light can be chosen to excite selectively the fluorophore of interest using appropriate filter sets (incandescent lamp) or the right laser wavelength. Conversely, the use of appropriate range of filters according to the emission spectrum of the fluorophores ensures that fluorescence signal can be selectively detected and separated from the excitation illumination and potential background fluorescence. The fluorophores will continue to fluoresce in a cyclical manner upon continuous excitation until photobleaching occurs. Photobleaching is a quenching phenomenon whereby continuous high intensity or long duration of excitation light source results in irreversible chemical conversion within the fluorophore and loss of fluorescence.

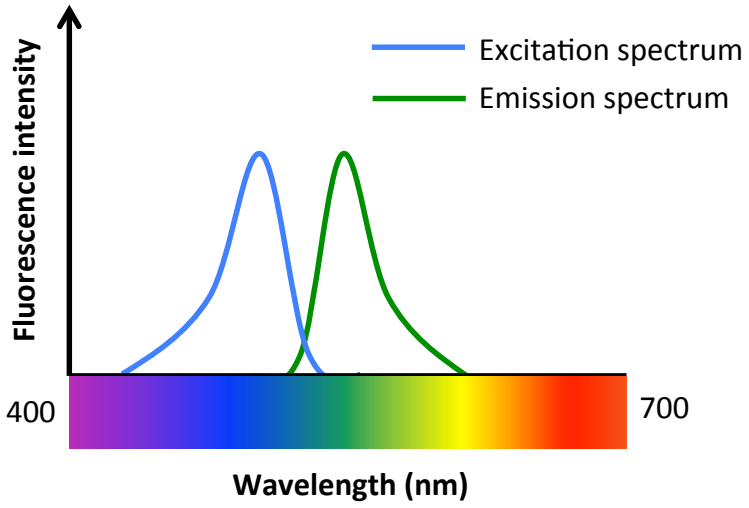

Figure 1.6: Schematic representation of excitation and emission spectra for a typical green fluorophore.

1.7.2 The green fluorescent protein

Fluorescent proteins are now routinely employed in various biological applications, particularly as a genetic fusion partner to the protein of interest, making visualisation of the protein of interest possible. The resulting fusion protein that retains the protein's normal function and localisation then can be

studied using a wide range of fluorescence techniques, several of which were employed in this study and will be presented in the coming chapters.

The green fluorescent protein (GFP) was first discovered as a 23 kDa protein by Shimomura during the purification of aequorin from the *Aequorea victoria* jellyfish (Shimomura et al., 1962). It is now known that aequorin itself generates blue light and activates the GFP in a resonance energy transfer process, giving rise to the greenish colour of the jellyfish, a process known as bioluminescence (Morin and Hastings, 1971). The GFP chromophore, the molecule responsible for its fluorescence, was later resolved as the 4-(p-hydroxybenzylidiene)-imidazolin-5-one molecule (Cody et al., 1993; Shimomura, 1979), see Figure 1.7. The major breakthrough of GFP came in the 1990s when the cDNA of GFP was cloned (Prasher et al., 1992) and expressed in *C. elegans* (Chalfie et al., 1994) – leading to the possibility of GFP being employed as a marker for the studies of proteins in living cells. Further understanding of GFP was gained when the X-ray crystal structure of GFP was solved by two independent research groups (Ormö et al., 1996; Yang et al., 1996). GFP is a 238-amino acid protein, with a structure that has four α-helices in either end of the protein and eleven β-pleated sheets that forms a cylindrical β-barrel. The chromophore of GFP is found in the only α-helix that runs through the centre of the β-barrel, shown in Figure 1.7A (Ormö et al., 1996). The current accepted mechanism of the formation of chromophore in GFP by three specific amino acid residues, is illustrated in Figure 1.7B, based on various evidence as reviewed in (Tsien, 1998). First, a folding process is required to achieve the conformation as shown in the initial chemical structure in Figure 1.7B. Successful folding will then facilitate the nucleophilic attack of the amide group of Gly-67[1] on the carbonyl group of Ser-65, followed by a dehydration process to form the imidazolinone ring, indicated

[1] The position of the GFP amino acid residues described in this section refers to the original GFP sequence, which does not contain an extra valine residue that is present at the start of the GFP sequences employed today for enhanced expression.

as the cyclisation process in Figure 1.7B. Finally, a subsequent oxidisation process generates the C=C bond (highlighted in Figure 1.7B) inbetween the aromatic and the imidazolinone rings, resulting in the formation of a conjugated system between the two chemical groups. The chromophore is only fluorescent when this final molecule is formed. As fluorescent GFP has been successfully expressed in various organisms, the formation of mature GFP chromophore is thought to be spontaneous or dependent on ubiquitous enzymes or other naturally occurring molecules. Heim et al. showed that the oxidisation process is not dependent on any enzymes but requires the presence of oxygen molecule (Heim et al., 1994). The kinetics of GFP chromophore formation was also extensively characterised in (Reid and Flynn, 1997) where the final oxidation step was proposed as the rate-limiting step of the chromophore formation, with a half time of approximately 76 minutes at room temperature.

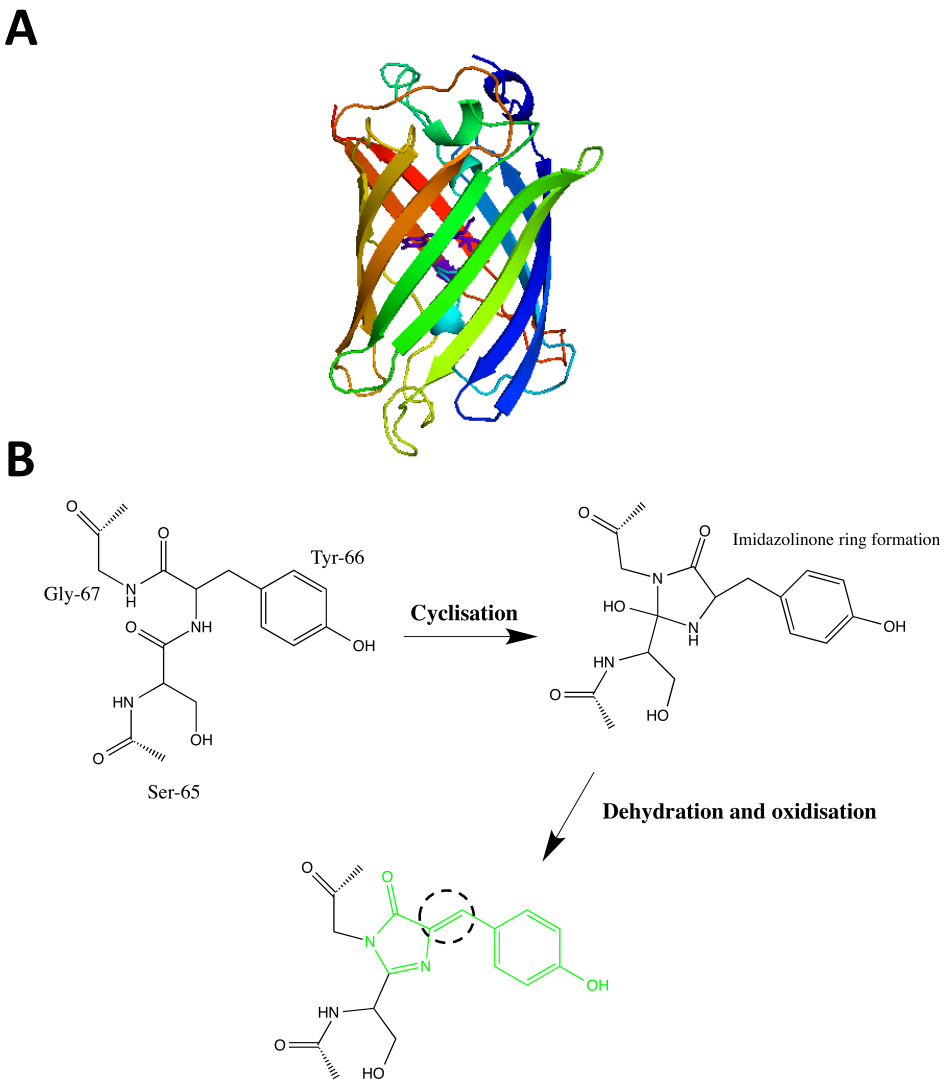

Figure 1.7: X-ray crystal structure of GFP and formation of its chromophore. Crystal structure (ribbon representation) of GFP with the chromophore molecule shown as blue in the centre of the β-barrel, PDB: 1EMA (Ormö et al., 1996). Figure generated using PyMOL (**A**). A mature GFP chromophore molecule (green) is formed through the cyclisation and oxidation (highlighted C=C) processes of three amino acid residues (Ser-65, Tyr-66 and Gly-67) (**B**).

In the past two decades, extensive research has been performed on GFP to establish suitable fluorescent proteins that can be employed in various conditions and have different excitation and emission properties. The different types of GFP are classified according to the structural mutations of residues within/close to the chromophore that generated fluorescent proteins of unique properties, as summarised in Table 1.4 (Tsien, 1998). As the wild type GFP of *Aequorea victoria* has slow maturation rate and low fluorescence signal at higher temperatures (37 °C) (Kaether and Gerdes,

1995), the F64L/S65T (Ser-65 in Figure 1.7B) GFP variant was developed with 30-fold enhanced fluorescence signal detected at 30 °C, indicating improved folding efficiency of the GFP chromophore (Cormack et al., 1996; Heim et al., 1995). Currently, most studies employ a modified version of fluorescent protein, in which its cDNA is specially designed for high expression of GFP in mammalian cells. This was achieved with base substitutions in the wild type GFP cDNA to produce codons more commonly seen in the mammalian genome and facilitate the protein translation process (Zolotukhin et al., 1996). To date, this modified GFP variant F64L/S65T (known as the enhanced GFP, EGFP) is one of the most widely used fluorescent proteins in biological studies.

The Thr-203, structurally adjacent to the phenolate anion of Tyr-66 in the chromophore, was verified as a key residue to generate yellow fluorescent proteins. Mutation of Thr-203 to polar aromatic residues such as tyrosine and tryptophan produced non-covalent aromatic interactions ($\pi - \pi$ stacking) with the Tyr-66 residue in the chromophore and resulted in shifting of the emission peak to > 520 nm (Ormö et al., 1996). The enhanced version of yellow fluorescent protein (abbreviated as YFP in this study) is subsequently established as the GFP variant containing three key mutations, S65G/S72A/T203Y (Miyawaki et al., 1997; Nagai et al., 2002). Mutation of the Tyr-66 residue to tryptophan (Y66W) generated a new group of fluorescent proteins with blue emission, known as the cyan fluorescent proteins (Heim et al., 1994). The enhanced cyan fluorescent protein with improved fluorescent properties was established with 7 mutations, F64L/S65T/Y66W/N146I/M153T /V163A/N164H (Heim and Tsien, 1996; Miyawaki et al., 1997). Further improvement of the enhanced cyan fluorescent protein with three additional mutations (S72A/Y145A/H148D) generated the cerulean fluorescent protein (abbreviated as CFP in this study), which has 2.5-fold improved brightness compared to the cyan fluorescent proteins and was shown to produce substantially improved signal-to-noise ratio in fluorescence resonance energy

transfer (FRET) experiments (Rizzo et al., 2004). The enhanced yellow and the cerulean fluorescent proteins (YFP and CFP) described here are employed as the acceptor and donor fluorescent proteins in the FRET experiments of this study (Chapter 5).

Table 1.4: Summary of the different mutations and properties associated with the fluorescent proteins. λ_{ex}: Excitation wavelength. λ_{em}: Emission wavelength.

Mutation	λ_{ex} (nm)	λ_{em} (nm)	Folding and maturation properties	Reference
Green fluorescent proteins:				
Wild type	395, 475 (3-fold lower)	503	Low fluorescence detected at high temperatures, e.g. 37 °C	(Kaether and Gerdes, 1995)
F64L/S65T	488	507	Increased fluorescence signal detected at 30 °C	(Cormack et al., 1996; Heim et al., 1995)
Yellow fluorescent proteins:				
T203Y	514	528	-	(Miyawaki et al., 1997; Nagai et al., 2002; Wachter et al., 1998)
Cyan fluorescent proteins:				
Y66W	405, 458	480	-	(Heim and Tsien, 1996; Miyawaki et al., 1997)
S72A/Y145A/H148D (**Cerulean**)	405, 458	480	2.5-fold improved brightness	(Rizzo et al., 2004)

The main fluorescent protein employed in this study is a modified superfolder variant of GFP (abbreviated as sfGFP in this study), as described in section 2.1.1. The initial superfolder GFP variant was first described in Pedelacq et al. where mutations to the initial EGFP template (F64L/S65T) significantly improved the folding robustness of GFP (formation of the β-barrel) and increased resistance of GFP to urea denaturation at 37 °C in *E. coli* (Pedelacq et al., 2006). The sfGFP variant employed in this study contains the additional S30R/Y39N/M153T/V163A mutations from the EGFP template. Amongst the

superfolder mutations described in (Pedelacq et al., 2006), the S30R mutation contributes most to improving GFP folding and resistance to urea denaturation, by mediating an ionic network formation that offers stabilisation effect to the β-barrel. The Y39N mutation provides an additional hydrogen bond with the side chain of D36, stabilising the α-helical chain found between the second and third β-pleated sheets (Pedelacq et al., 2006). The M153T and V163A mutations were shown to improve the fluorescence signal of GFP in two earlier independent studies (Crameri et al., 1996; Heim and Tsien, 1996). Using a DNA shuffling method in *E. coli* for three cycles of initial screening, Crameri et al. generated a version of GFP mutant (containing the M153T and V163A mutations) that produced up to 40-fold increase in fluorescence signal detected in mammalian cells using fluorescence spectroscopy (Crameri et al., 1996). Simultaneously, Heim and Tsien also identified that the M153T and V163A improved the brightness (quantum yield) of Y66W cyan fluorescent proteins (Heim and Tsien, 1996). Another mutation, A206K was also introduced to the sfGFP template employed throughout this study. GFP has high tendency of forming dimers, as seen in the dimeric GFP X-ray crystal structure (Yang et al., 1996). Zacharias et al. suggested that replacing the hydrophobic residues (Ala-206, Leu-221, Phe-223) found at the dimer interface to positively charged residues such as lysine could reduce the dimerisation of GFP. The GFP containing A206K mutation was suggested as “extremely monomeric”, and the determination of the dissociation constant of a hypothetical dimer was not feasible (reported as 78 mM) compared to the wild type GFP with a reported dissociation constant of 0.11 mM (Zacharias et al., 2002).

1.7.3 Confocal microscopy – how it works

Confocal microscopy produces sharp fluorescence images by excluding light emitted from the sample that is not from the focal plane. Confocal laser scanning microscopes are routinely employed today for high quality imaging in fluorescence studies. In addition to imaging, various biophysical

applications can also be employed to study the fluorescent proteins of interest using confocal microscopes, some of which will be described in this study.

The principle of confocal was first invented by Marvin Minsky and it was patented in 1957 (Minsky, 1988). Minsky invented a microscope that has a pinhole in front of the light source and generated point-by-point images, by focusing the point of light sequentially on the sample whilst moving the sample, removing any out-of-focus light in the process. As Minsky's set up could not produce high quality images and the biological samples had to be moved during data acquisition, its application was not favourable at that time. Since then, the improvement in the technology of light detection and image generation using computers has greatly improved the confocal microscope set up, although the concept of confocal invented by Minsky is still applied to date.

The modern confocal microscope combined with fluorescence microscopy is schematically represented in Figure 1.8. In today's confocal microscope, a laser beam is typically employed as the source of excitation of the fluorophore. The laser beam is first reflected to the sample through the objective by a dichroic mirror. The scanning mirror within the microscope system allows laser to be scanned across the sample (without moving it). Light emitted from the excited sample then passes through the dichroic mirror. The dichroic mirror only allows the emission light, which is of longer wavelength, to pass through and blocks the passage of the excitation light. As the emitted light propagates towards the detector, filters are also present to ensure that only the desired wavelengths of emitted light are being detected. The confocal pinhole allows only light emitted from the focal point of the system (the focal plane) to reach the detector whilst removing all the out-of-focus light emitted from the sample. The detector consists of a photodetection device (e.g. photomultiplier tube), which converts the light

source (photons) into an electronic signal. Finally, a computer attached to the detector records this electronic signal and generates the high resolution image one pixel at a time.

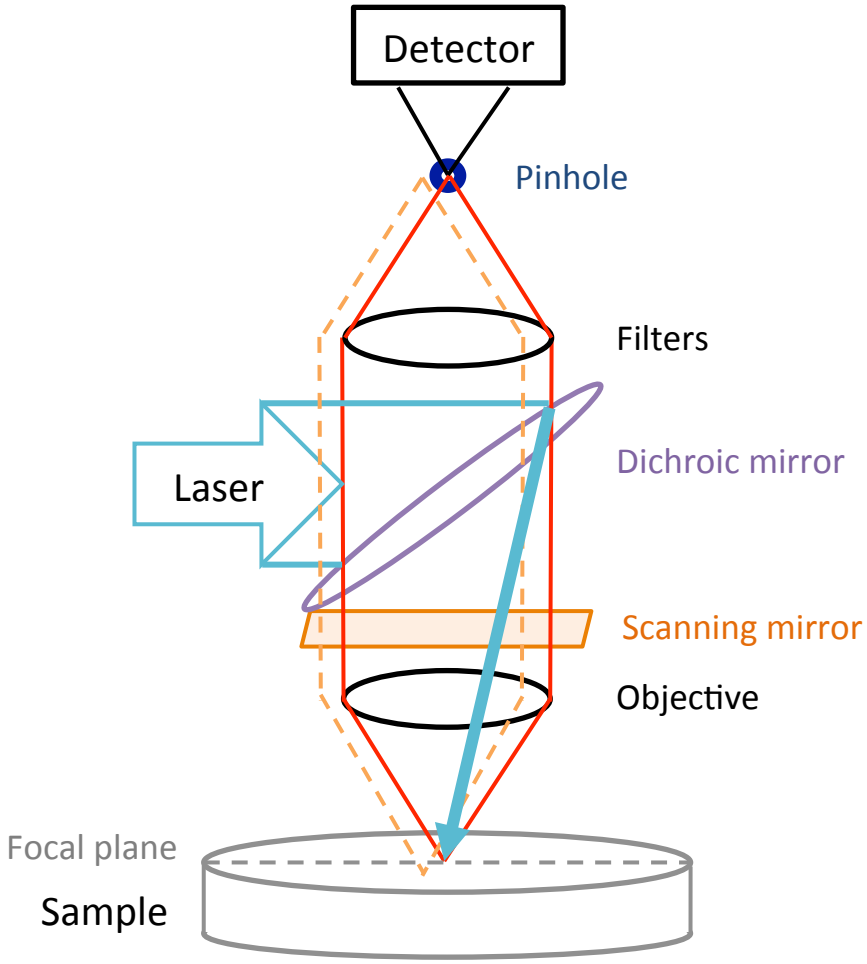

Figure 1.8: Schematic representation of a confocal laser scanning microscopy set up. Blue arrow: excitation laser beam. Solid red line: in-focus light emitted from sample. Orange dotted line: out-of-focus light emitted from sample.

1.8 Aims of study

To date, our understanding of the oligomerisation of ABCG2 and the dynamics of the transporter, either self assembly or interaction with other components in the membrane or cell cytoskeleton is far from complete. The main purpose of this research is to first characterise the dynamics and oligomerisation of ABCG2 in the plasma membrane of mammalian cells – determining if there are any changes upon presence of substrates and mutations. Second, we aim

to establish the oligomeric organisation of ABCG2 to resolve the current proposals as discussed in section 1.6, primarily using fluorescence techniques. A better understanding of ABCG2 dynamics and oligomerisation may offer a new therapeutic strategy that targets ABCG2-ABCG2 interactions using protein-protein interactions inhibitors (Mullard, 2012), providing potential new avenues in the on-going research of multidrug resistance in cancer chemotherapy.

To do so, we aim to first genetically tag ABCG2 with fluorescent proteins and characterise the ABCG2 fusion fluorescent proteins when expressed in mammalian cells. Subsequently, our goal is to characterise and demonstrate the dynamics and oligomerisation of ABCG2 in live cells using three different fluorescence techniques that complement each other, including the fluorescence recovery after photobleaching (FRAP), fluorescence resonance energy transfer (FRET), and fluorescence correlation spectroscopy (FCS). Finally, we propose to establish the oligomeric organisation of ABCG2 using photon counting histogram (PCH) analysis and total internal reflection fluorescence (TIRF) microscopy combined with stepwise photobleaching analysis. In these fluorescence studies, we also aim to employ suitable membrane proteins tagged with identical fluorescent proteins (compared to ABCG2) as reliable controls.

In the next chapter, the experimental methods employed in this work will be described, followed by a description of the generation of the fluorescent protein fusion constructs. The results of ABCG2 investigations using the different fluorescence techniques will then be presented in the subsequent chapters along with the background and theory of the respective fluorescence techniques. A final discussion will also be provided at the end of this thesis.

Chapter 2 Methods

2.1 Molecular biology

2.1.1 Materials and reagents

The starting DNA vectors were obtained from sources as listed in Table 2.1 below. The main backbone employed in this study was the pcDNA3.1 vector containing eukaryotic neomycin (neo) or zeocin^{TM} (zeo) resistance genes. All the vectors contain the prokaryotic ampicillin resistance gene for selection purposes. The fluorescent proteins encoded in the respective vectors that were employed in this study are the enhanced yellow fluorescent protein (YFP), the super-folder green fluorescent proteins (sfGFP; enhanced GFP containing mutations M153T, V163A, S30R, and Y39N, from the template described in (Pedelacq et al., 2006)), and the cerulean fluorescent protein (CFP). GAP (growth associated protein-43) or kRas (Kirsten rat sarcoma oncogene encoded GTPase transductor protein) represent the membrane targetting sequences obtained from these proteins, which facilitates localisation of the attached sfGFP to the raft (GAP) or non-raft (kRas) regions of the plasma membrane (see section 4.2 for more details). The tandem-sfGFP vector contains two sfGFP molecules joined together with a two amino acid linker (Leu-Glu). Construct generation in this study is illustrated in chapter 3 and characterisation of the fusion proteins employed can be found in the relevant results sections (chapters 4, 5, and 6).

All molecular biology reagents were purchased from New England Biolabs (NEB, Hitchen, UK) and other reagents were obtained from Sigma-Aldrich (Poole, UK), unless stated otherwise.

Table 2.1: List of the starting vectors employed in this study. The "vYNL" within the ABCG2_C603A vector represents the N-terminal half of venus YFP (2-173) as described previously (Haider et al., 2011). C603A represents the mutation of ABCG2 at position Cys-603 to alanine (section 1.6.2). The "nostart" within the pcDNA3.1zeo_nostart-sfGFP indicates the absence of the start ATG in the vector. CD28 and CD86 were provided in the mammalian pHR sin vector containing the prokaryotic ampicillin resistance gene. The "Halotag" and "SNAP" represent sequences present in the vector for specific labelling using small molecule fluorescent compounds. These were not employed in this study.

DNA vectors	Source
pcDNA3.1neo_YFP-ABCG2 pcDNA3.1zeo_SNAP-ABCG2 pcDNA3.1zeo_vYNL-ABCG2_C603A pcDNA3.1zeo_ABCC4-sfGFP	Dr Ian D. Kerr, University of Nottingham
pcDNA3.1zeo_nostart-sfGFP pcDNA3.1zeo_GAP-sfGFP pcDNA3.1zeo_sfGFP-kRas pcDNA3.1zeo_CFP	Dr Nicholas D. Holliday, University of Nottingham
pcDNA3.1zeo_sfGFP pcDNA3.1zeo_sfGFP-sfGFP (tandem-sfGFP)	Marleen Groenen, University of Nottingham
pcDNA3.1_adenosine A3-YFP	Dr Steve J. Briddon, Univsersity of Nottingham
pHR_CD28-Halotag (CD28 truncated at R185) pHR_CD86-Halotag (CD86 truncated at R277)	Professor Simon J. Davis, University of Oxford

2.1.2 Cloning

Restriction digest

Restriction digest reactions of DNA vectors were set up as Table 2.2 below. For double digest reactions, the optimal buffer conditions for both enzymes were selected. Where this was not feasible, sequential digest was employed. The restriction digest reactions were usually performed at 37 °C for 1 h (2 h for a sequential digest). 6x DNA loading dye (0.25 % (w/v) bromophenol blue, 40 % (w/v) sucrose) was then added to the reaction and the final mixtures were loaded on 1 % (w/v) agarose gels containing 0.1 mg/mL ethidium bromide (from Thermo Fisher Scientific, Loughborough, UK). Electrophoresis was performed in TBE buffer (90 mM Tris, 90 mM boric acid and 2 mM EDTA

pH 8.0). Digested DNA bands on the agarose gels were visualised using a 312 nm ultraviolet transilluminator and compared against 1 kb molecular weight marker loaded alongside the DNA samples.

Table 2.2: Composition of restriction digest reaction.

Materials	Quantity
Water	Made up to 15 µL
DNA vector	200-500 ng
Enzyme 1	5-10 units
Enzyme 2 (if necessary)	5-10 units
10x enzyme buffer	1.5 µL
10x BSA (bovine serum albumin)	1.5 µL

Ligation

The desired bands on the agarose gels were excised with clean scalpels. The DNA (vector or insert) was recovered from the agarose bands by purification (melting of agarose) using the QIAquick Gel Extraction kit from QIAGEN (Manchester, UK) or the NucleoSpin Gel and PCR Clean-up kit from MACHEREY-NAGEL (Düren, Germany) according to the manufacturers' instructions. Aliquots of purified DNA were analysed with agarose gel electrophoresis (as described above) to confirm the presence of the correct band size DNA and to estimate the vector: insert ratios. Purified vectors (plasmid backbones) were routinely incubated with 2.5 units of shrimp alkaline phosphatase (Promega, Southampton, UK) at 37 °C for 30 min and the phosphatase was deactivated by a following incubation at 65 °C for 20 min. This step was performed to prevent self-ligation of the vectors, by removing the 5' end phosphates. Ligation reactions were set up as Table 2.3 below using an estimated 1: 3 vector: insert molar ratio. Ligation reactions were performed overnight at 16 °C or 2 h at room temperature.

Table 2.3: Composition of ligation mixtures and vector only control. Amount of vector and insert used was estimated at a vector: insert molar ratio of 1: 3 for optimal ligation conditions.

Materials	Ligation mixture	Vector only control
Water	Made up to 20 µL	Made up to 20 µL
Dephosphorylated vector	X µL	X µL
Insert	Y µL	0
T4 DNA ligase	400 cohesive end units	400 cohesive end units
10x T4 ligase buffer	2 µL	2 µL

2.1.3 Transformation and preparation of competent cells

For transformation, 100 µL competent DH5α *E. coli* was first thawed on ice. DNA was then added to the competent cells (5 µL of ligation reaction or 100-500 ng of circular DNA). The competent cells were left on ice for 30 min, treated at 42 °C for 90 s (heat shock), and left on ice for a further 2 min. 900 µL of Luria-Bertoni (LB) medium (1 % (w/v) NaCl, 1 % (w/v) tryptone, 0.5 % yeast extract) was added to the competent cells and left in a shaker incubator for 60 min at 37 °C. The transformed competent cells were then plated on pre-warmed LB supplemented agar plates (1.5 % (w/v) agar; containing 100 µg/mL ampicillin). For ligated products transformation, $^{1}/_{10}$ and $^{9}/_{10}$ of the transformation reaction volumes were plated. For circular plasmid transformation, $^{1}/_{100}$ of the transformation reaction volume was plated. Transformed competent cells were grown on the agar plates overnight at 37 °C.

2.1.4 Plasmid preparation and long-term storage

For DNA extraction, single DH5α *E. coli* colonies were picked from the transformed agar plates and inoculated into 5 mL of LB medium containing 100 µg/mL of ampicillin. Bacterial cultures were grown overnight at 37 °C, with orbital shaking at 180-220 rpm. For long-term storage, glycerol stocks were made up with 500 µL of grown cultures and 500 µL 30 % (v/v) glycerol and these were stored at -80 °C. For plasmid preparation, cultures were

centrifuged (2000-4000 g, 10 min) and DNA was extracted from the bacterial pellets according to the manufacturers' protocols in QIAprep Miniprep kit (QIAGEN) or NucleoSpin Plasmid kit (MACHEREY-NAGEL). Briefly, bacteria pellets were lysed under alkaline conditions before the bacterial chromosomal DNA was co-precipitated with insoluble complexes (salt, detergent, and protein) as the lysate solution was neutralised and adjusted to high-salt conditions. Lysates were then cleared by centrifugation and double-stranded DNA products were adsorbed to the silica columns. DNA products were then washed with ethanol-containing solution and finally eluted in low-salt buffer. The concentration and purity of DNA products were determined by measuring the sample absorbance using Nanodrop 2000 (Thermo Fisher Scientific). This was determined using the knowledge that 50 µg/mL double stranded DNA has an absorbance of 1.0 at 260 nm (A_{260}). The purity of the DNA was assessed using the A_{260}/A_{280} ratio, where the A_{280} measures the protein concentration within the samples (due to absorbance by phenylalanine and tyrosine aromatic rings). Only DNA samples with A_{260}/A_{280} ratios of 1.7-1.9 were used for transfection in the HEK293T cells. For further DNA preparation, glycerol stocks were streaked on agar plates (containing selection antibiotics), inoculated in LB medium and extracted as described in this section.

2.1.5 Primer design for mutagenesis and amplification

Various oligonucleotide primer pairs (forward and reverse; Table 2.4) were designed for the generation of DNA constructs described in chapter 3. These primers were designed to insert the desired mutation or cloning sites into the amplified sequences from the template DNA. Primers sequences were analysed using Netprimer (Premier Biosoft) for the prediction of primer properties. The percentage of GC (guanine cytosine content) in the oligonucleotides was kept to 40-60 % and the sequences were modified to minimise chances of dimer and hairpin formation. The BLAST local alignment

tool (Altschul et al., 1990) was also employed to ensure binding of the primers to unique positions on the template DNA.

2.1.6 Polymerase chain reaction – mutagenesis and amplification

Polymerase chain reaction (PCR) was employed for the mutation of nucleotides in template DNA (mutagenesis) and for amplification of constructs of interest for further cloning purposes. Table 2.5 below shows a general reaction set up for PCR experiments performed in this study. Phusion-HF DNA Polymerase (Thermo Fisher Scientific) was used in the majority of the PCR experiments, unless stated otherwise. The high-fidelity (HF) version of the polymerase was employed to ensure accurate insertion of nucleotide with the presence of a 3' → 5' proof reading exonuclease domain, which removes any incorrectly incorporated nucleotide during the polymerisation process. PCR cycles (Table 2.5) were performed in a Thermocycler (SensoQuest, Göttingen, Germany) using thin-wall polypropylene PCR tubes to ensure optimal heat transfer to the samples.

Table 2.4: List of primers designed in this study for DNA construct generation. The restriction/mutation sites involved in cloning/mutagenesis are indicated as lower case in the primer sequences. The number of base pairs (bps), melting temperature (Tm), % GC (guanine cytosine content) component and the restriction sites involved for the primers are also indicated in the table. The Tm shown here does not correspond to the annealing temperatures used in PCRs, as the optimum annealing temperatures for the reactions are generally lower than the Tm of primers.

Primers	Sequence (5'➔3')	Length bps	Tm °C	% GC	Cloning site
A206K_F	GCACCCAGTCCaaaCTGAGCAAAGAC	26	69	54	-
A206K_R	GTCTTTGCTCAGtttGGACTGGGTGC	26	69	54	-
Kozak-sfGFP_F	CCAGCACAGTGGgctagcatgGAGGTGAGCAAG	33	81	61	*NheI*/ATG start
Kozak-sfGFP_R	GGGCCCTCTtccggaCTTGTACAGCTC	27	72	60	*BspEI*
T362A_F	GAAGAAGATCgcaGTCTTCAAGG (Xie et al., 2007)	23	60	48	-
T362A_R	CCTTGAAGACtgcGATCTTCTTC (Xie et al., 2007)	23	60	48	-
CFP-nostop_F	GAGgctagcATGGTGAGCAAGGGC	24	70	62	*NheI*
CFP-nostop_R	GGGCCCTCTtccggaCTTGTACAGCTC	27	72	60	*BspEI*
NBD_F	GACTCAGATctcgagCTCAAGCTT	24	50	62	*XhoI*
NBD_R	CGGGTctctagaTTACTGGGGATTACCCAGCAA	33	75	50	*XbaI*
TMD_S_F	TCCTTCctcgagAGCAACTCAGATGGGTTTCT	32	77	53	*XhoI*
TMD_S_R	ATTAGGAAAGGACAGTGGGA	20	54	45	-
TMD_L_F	TCTTTCctcgagAGGGTTATCACTGTGAGGCC	32	75	53	*XhoI*
TM1-2_R	CGCCGCtctagaTTAAGATAACAGTTTTCC	30	68	43	*XbaI*
TM1-4_R	CGCCGCtctagaTTAAGAAACCACACTCTG	30	71	50	*XbaI*
CD28_F	TTCACCgaattcACCATGCTCAGGCTGCTC	30	78	53	*EcoRI*
CD28_R	GTAAATctcgagCCTGCTCCTCTTACTCCT	30	69	50	*XhoI*
CD86_F	TTAATCggatccACCATGGAGCCCCAGTGCACT	33	80	55	*BamHI*
CD86_R	TCATGActcgagCCGAGGCCGCTTCTTCTT	30	79	57	*XhoI*

Table 2.5: Standard composition of PCR experiments.

Materials	Quantity
Water	Made up to 50 µL
DNA template	100 ng
DNA polymerase	2 units
5x enzyme buffer	10 µL
Forward primer	50 pmoles
Reverse primer	50 pmoles
10 mM dNTP mix	1 µL

Site-directed mutagenesis

For mutagenesis reactions, PCR cycling protocols were modified in accordance with guidance in the Stratagene QuikChange Site-Directed Mutagenesis manual (Table 2.6). A lower number of PCR cycles (16-20) was employed in the mutagenesis PCR to prevent undesired additional second site mutation. PCR products generated for mutagenesis were incubated with *DpnI* enzyme at 37 °C for 1 h for the digestion of parental (methylated) DNA, leaving behind only non-methylated PCR products as circular DNA is required for efficient transformation. 5 µL of digested PCR products were then transformed into competent DH5α *E. coli* as described above.

Table 2.6: PCR cycling protocol for site-directed mutagenesis reaction. Denaturation temperature (step 1) was set at 95 °C and extension temperature (step 4) was lowered to 70 °C where KOD Hot-Start Polymerase (Thermo Fisher Scientific) was employed.

Step	Cycles	Temperature (°C)	Time
1	1	98	30 s
2	18	98	10 s
3		52-60	20 s
4		72	≈ 1 min/kb
5	1	72	5 min
6	1	4	Hold

Amplification

Typical PCR conditions for amplification of cDNAs are indicated in Table 2.7 below. The PCR products were purified using QIAquick PCR Purification kit (QIAGEN) or the NucleoSpin Gel and PCR Clean-up kit (MACHEREY-NAGEL) according to the manufacturers' instructions. The resultant amplified constructs were digested and ligated into the desired vectors using the cloning methods as described above (section 2.1.2).

Table 2.7: PCR cycling protocol for amplification reaction. The extension time (Step 4) was determined as 30 s per kb, depending on the size of the predicted products.

Step	Cycles	Temperature (°C)	Time
1	1	98	30 s
2		98	10 s
3	30	52-60	20 s
4		72	30-90 s
5	1	72	1 min
6	1	4	Hold

2.1.7 DNA sequencing

Once the sizes of the DNA products were confirmed using restriction digests, the constructs were sent to Source BioScience Life Sciences (Nottingham, UK) for DNA sequencing. Gene-specific sequencing primers employed in this study are listed in Table 2.8 below. The majority of the constructs generated were sequenced using the T7F promoter primer to confirm the start of the constructs. SeqF0, SeqF2, and Seq482 were forward primers designed to fully sequence the ABCG2 construct. SeqR1 is a reverse primer designed to sequence any early ABCG2 sequence that could not be read by T7F or SeqF0. SeqGFP-rev is another reverse primer design to read the reverse sequences from the middle of fluorescent proteins. DNA chromatograms from the sequencing data were analysed using Chromas Lite 2.1.1 or 4Peaks and sequence data were aligned with the predicted sequences using the BLAST local alignment tool (Altschul et al., 1990).

Table 2.8: ABCG2 sequencing primers. The ABCG2 nucleotide positions to which the primers bind to in the ABCG2 sequence are indicated.

Primers	Sequences
SeqR1	339 – TCGTGGTGCTCCATTTAT – 322
SeqF0	147 – GAGTGGCTTTCTACCTTGTC – 166
SeqF2	699 – GCAGGGACGAACATTC – 714
Seq482	1337 – AACTCTTTGTGGTAGA – 1352
SeqGFP-rev	GCTGTTGTAGTTGTATCCAG

2.2 Tissue culture

2.2.1 Cell lines and reagents

HEK293T cells (ATCC code CRC-1573) were used as the tool for expression of recombinant proteins. They were chosen primarily due to their human origin, high transfection efficiency, and preferable growth pattern (flat and single-layered, which facilitate fluorescence imaging). All reagents were obtained from Sigma-Aldrich unless stated otherwise. Transfection agent polyethyleneimine (PEI) was obtained from Polysciences Inc. (Warrington, USA). Stable cell line selection agent zeocin^{TM} powder was obtained from Melford Laboratories (Ipswich, UK). Foetal bovine serum (FBS) was obtained from Life Technologies (Paisley, UK).

2.2.2 Cell passage maintenance and storage

HEK293T cells (and stable transfectants) were grown in DMEM (Dulbecco's Modified Eagle Medium, containing 4.5 g/L D-glucose, 0.11 g/L sodium pyruvate and 0.58 g/L L-glutamine) supplemented with 10 % (v/v) FBS and 100 units/mL penicillin and 100 μg/mL streptomycin, in either T25 or T75 flasks at 37 °C and 5 % CO_2. When cells were 80-100 % confluent, medium was removed and cells were washed once with PBS (phosphate buffered saline, containing 137 mM NaCl, 10 mM Na_2HPO_4, 2.7 mM KCl, and 2 mM KH_2PO_4, adjusted to pH 7.4) and incubated with 0.5-1 mL of 1x trypsin/EDTA made up in PBS at 37 °C for at least 1 min. Detached cells were then removed from the flasks in 5 mL of medium and cells were centrifuged at 2000-4000 g for 5 min. Pellets were resuspended in medium and passaged depending on circumstances (normally $^1/_{10}$ or $^1/_{20}$) into new flasks.

For storage, cells pellets were first suspended in ice cold freezing medium (10 % DMSO in FBS). Cell aliquots (typically 1 x 10^6 cells/1 mL in cryotubes) were then frozen in -80 °C using a freezing container filled with isopropyl

alcohol to ensure approximate cooling rate of 1 °C/minute. When frozen, cell aliquots were transferred into liquid nitrogen for cryopreservation of the HEK293T cell lines.

2.2.3 Seeding cell count and transfection

Cells were seeded in various plates or dishes for different purposes (assays or fluorescence experiments). Table 2.9 below shows the approximate number of cells (determined using a haemocytometer) seeded on the plates or dishes and the amount of DNA and PEI used in transfection. Transfection was performed 24 h after seeding and cells were incubated with 5 % (v/v) FBS supplemented medium for 2 h prior to transfection. During transfection, PEI was added to DNA (approximate 15: 1 nitrogen: phosphate ratio (Boussif et al., 1995)) and the transfection mixtures were left to stand for 6-8 min for the formation of PEI/DNA complexes. Transfection mixtures were then added drop-wise to the cells. Cells were further incubated for 24 h before they were harvested for protein assays or used for other experiments.

Table 2.9: Seeding cell count and transfection set ups for the different plates or dishes used in this study. Uncoated 35 mm glass-bottom-dishes were obtained from MatTek Corporation (Ashland, USA) with product code P35G-1.5-14-C. Nunc™ Lab-Tek™ 8-well chambered cover glasses were obtained from Thermo Fisher Scientific.

Plates / dishes	Growth area (cm^2)	Cells/well	DNA (µg)	PEI 10 mM (µL)
6-well plate	9.5	250,000-350,000	2-4	9-18
12-well plate	3.8	100,000-150,000	1-2	4.5-9
96-well plate	0.32	10,000-20,000	0.1-0.2	0.5-0.9
Glass-bottom-dish (MatTek)	9.5	250,000-350,000	2-4	9-18
8 well chamber (Nunc™ Lab-Tek™)	0.8	10,000-20,000	0.3-0.5	1.5-2.3

2.2.4 Poly-L-lysine coating of cover glass

Poly-L-lysine was employed to ensure HEK293T cells attachment to any untreated growing surfaces, e.g. glass-bottom-dishes, 8-well chambered cover glasses, and round coverslips (13 mm diameter, 0.08-0.12 mm thickness, from Thermo Fisher Scientific). Poly-L-lysine powder (hydrobromide, MW ≥ 300,000) was prepared as a 5 mg/mL aqueous solution and stored at -20 °C. The final working solution (0.1 mg/mL), obtained by dilution with sterile distilled water was further filter sterilised, prior to coating of the growth surface by immersion for at least 30 min. Excess poly-L-lysine solution was removed by washing twice with PBS before cells were seeded. Poly-L-lysine coating was also employed in experiments that involved extensive washing (e.g. functional assays) to enhance cell attachment.

2.2.5 Cell fixing and mounting

For cell fixing, 4 % (w/v) paraformaldehyde (PFA) in PBS was used. Live cells in medium were first washed once with PBS, treated with 4 % PFA for 10 min then washed twice with PBS. For imaging, cells grown on round coverslips were also mounted onto microscope slides using FluoroGeL mounting medium (GeneTex, Hsinchu City 300, Taiwan).

2.2.6 Stable cell line selection

For generation of stable HEK293T cell lines expressing various constructs, zeocin™ was employed as the selection agent. Successfully transfected HEK293T cells in 6-well plates were transferred into two T25 flasks by detachment with trypsin. Cells were left to settle overnight before medium was replaced with selection medium containing 200 μg/mL of zeocin™. When confluent, cells were transferred into T75 flasks and maintained in selection medium for the successive 10-15 days, with the medium replaced every 2-3 days. Once healthy colonies were observed after the selection period, cells were maintained and passaged as described in section 2.2.2 above with

DMEM containing zeocin™ at 20-40 μg/mL. Stable cell lines were frozen at -80 °C and stored in liquid nitrogen as described above.

2.2.7 Dilution cloning to obtain low expressing cell lines

For the selection of low expressing clones from the stable cell lines, a dilution cloning method was first used to isolate single cell derived colonies. A stock of 10,000 cells/mL was diluted into 20 mL of 10 cells/mL, which was further diluted into 20 mL of 1 cell/mL. The two different diluted cell suspensions were plated into 96 well plates (200 μL/well). Wells containing single cell colonies were identified and colonies were allowed to grow. When confluent, the clones identified were gradually scaled up to 48-, 24-well plates, T25s and finally T75s before they were frozen at -80 °C as described above. For the identification of low expressing clones, fluorescence intensities of the different clones (fixed or live) were compared under identical acquisition conditions.

2.3 Detection of proteins using SDS-PAGE and western blot analysis

2.3.1 Cell harvest and protein assay

Cells were harvested in ice-cold lysis buffer (PBS containing 10 % (v/v) glycerol) by trypsinisation or scraping from 6-well plates or T25 flasks. Cell suspensions were centrifuged (2000-4000 g, 5-10 min) to remove any residual media, resuspended in fresh lysis buffer, and centrifuged again. Cell pellets were stored at -20 °C if not used immediately. For cell lysis, cell pellets were first suspended in 250-500 μL ice-cold lysis buffer supplemented with protease inhibitor cocktail set III at 1: 100 dilution (containing 4-(2-aminoethyl)-benzenesulfonyl fluoride hydrochloride, aprotinin, bestatin, E-64 protease inhibitor, leupeptin hemisulphate, and pepstatin A; Merck Milipore, Watford, UK). Cells were lysed by sonication with 3 x 10 s bursts, using a Vibra-Cell sonicator (Sonics & Materials UK, Suffolk, UK).

Protein concentrations were subsequently determined with a modified Lowry assay method (Lowry et al., 1951), using reagents from the Bio-Rad DC (Hercules, USA) protein assay kit and according to the microplate assay protocol provided by the manufacturer. Protein concentrations were calculated by comparison against a standard curve generated using 0.2 mg/mL to 2 mg/mL of BSA (bovine serum albumin; from Sigma-Aldrich).

2.3.2 SDS-PAGE

One-dimensional SDS-PAGE (sodium dodecyl sulphate polyacrylamide gel electrophoresis) analysis was adapted from the Laemmli method (Laemmli, 1970). First, protein samples were made up in protein loading buffer (62.5 mM Tris base, 2 % (w/v) SDS, 10 % (v/v) glycerol, and 0.01 % (w/v) bromophenol blue, 0.5 % (w/v) dithiothreitrol (DTT)). Samples were heated at 37 °C for 30 min or 75 °C for 10 min. For non-reducing conditions, the DTT was omitted from the protein loading buffer.

Discontinuous acrylamide gels were prepared using 8-12 % (w/v) acrylamide resolving gels in separating buffer (375 mM Tris base, pH 8.8, 0.1 % (w/v) SDS) and 4 % acrylamide stacking gels in 125 mM Tris base, pH 6.8, 0.1 % (w/v) SDS. Heated samples were loaded (usually 20 µg of proteins) along with molecular weight markers (ColorPlus™ Prestained Protein Ladder, from NEB or SeeBlue® Plus2 Pre-stained Protein Standard, from Life Technologies.) using gel loading tips and separated by electrophoresis at constant current (30-60 mA) in protein electrophoresis buffer (25 mM Tris base, pH 8.3, 190 mM glycine, 0.1 % (w/v) SDS) until the dye front was eluted from the gel bottom.

2.3.3 Western blot analysis

Transfers of proteins from the polyacrylamide gels onto nitrocellulose membranes (Pall Corporation, Port Washington, USA) were carried out in a western transfer tank filled with western transfer buffer (25 mM Tris, 192 mM glycine, 20 % (v/v) methanol), at constant current 200 mA for 2 h at room temperature. Ponceau S stain made up with 0.1 % (w/v) Ponceau S (Thermo Fisher Scientific) and 1 % (v/v) acetic acid was used to stain the resultant nitrocellulose membranes to compare protein loading and to judge if the transfers were complete. The stain was subsequently removed by rinsing the blots with distilled water. Molecular weight marker bands were marked with a pencil before the stain was completely removed to facilitate later identification.

For non-specific blocking, blots were incubated in blocking solution (5 % (w/v) of non-fat milk in PBST, PBS containing 0.1 % (v/v) Tween 20, Thermo Fisher Scientific) for 1 h at room temperature. Subsequently, blots were incubated with primary antibody (monoclonal anti-GFP mouse IgGκ antibody; Roche, Burgess Hill, UK) in blocking solution (1: 2000 dilution) for 1 h at room temperature or overnight at 4 °C. Blots were then washed four times for 5 min with PBS to remove unbound primary antibody before they were incubated with secondary antibody, polyclonal rabbit anti-mouse IgG antibody conjugated with horse radish peroxidase (HRP), obtained from Dako (Glostrup, Denmark), in blocking solution (1: 2000 dilution) for 1 h at room temperature. The washing steps were repeated again to remove any unbound secondary antibody.

For the detection of secondary antibody on the nitrocellulose membranes, SuperSignal West Pico Chemiluminescent Substrate (Thermo Fisher Scientific) was used as the enhanced chemiluminescent (ECL) HRP substrate. Blots were incubated in Working Solution (mixing equal amounts of Stable Peroxide

Solution and Luminol/Enhancer Solution) for 1 min before they were drained, wrapped in cling film and placed face up inside an X-ray developing cassette. Final western blots were exposed onto X-ray films for various intervals (30 s to 15 min) before they were developed in the dark room.

2.4 Functional studies of ABCG2

Two different accumulation assays were employed in this study. To establish the function of fluorescently tagged ABCG2 expressed in stable HEK293T cell lines, well-based fluorescence intensities of mitoxantrone (MX; Sigma-Aldrich) were measured, normalised, and compared directly. For confirming the function of transiently expressed ABCG2 constructs, multiwavelength cell scoring analysis was employed following cell imaging to ensure that only cells expressing fluorescently tagged ABCG2 constructs were taken into account in the measurements of MX fluorescence intensities.

2.4.1 Accumulation assay – fluorescence intensities

Stable HEK293T cell lines expressing the respective sfGFP-ABCG2 variants were seeded on poly-L-lysine coated 96-well plates (black, clear bottom, Greiner Bio-One, Stonehouse, UK). When confluent, cells were incubated with MX and various concentrations of Ko143 (Sigma-Aldrich), MX alone, or DMSO alone as a solvent control (maximum DMSO concentration employed was 0.1 % (v/v)), in normal growth medium for 2 h. Cells were then washed twice in ice-cold PBS and fixed with PFA as described above. Intensities of MX (accumulation in cells) were measured using a benchtop microplate reader, (Flexstation; Molecular Devices, Wokingham, UK), with 608 nm and 684 nm as the excitation and emission wavelengths respectively.

The non-linear regression dose response equation (log (agonist) vs. response (3 parameters) equation in GraphPad Prism 6.0) was employed to fit the data

sets upon normalisation of the fluorescence intensities in each data set and the pEC_{50} for Ko143 was determined, see below for equation:

$$R = R_{min} + \frac{R_{max} - R_{min}}{1 + 10^{(\log EC_{50} - X)}}$$

Where the response (R), is related to the minimum response (R_{min}), maximum response (R_{max}), log of drug concentration (X) and EC_{50} (drug concentration required to achieve 50 % response). For determination of the percentage of Ko143 inhibitable MX accumulation in the different stable cell lines, the fluorescence intensities obtained from the cells incubated with 4 µM MX alone and 4 µM combined with 1 µM Ko143 were first corrected by subtracting the average baseline fluorescence intensities obtained from cells incubated with 0.1 % (v/v) DMSO only (maximum solvent DMSO concentrations in the wells). Percentages of Ko143 inhibitable accumulation (A_{Ko143}) were finally obtained according to the equation below:

$$A_{Ko143} = \frac{I_{MX+Ko143}}{I_{MX}} * 100\%$$

Where $I_{MX+Ko143}$ is the corrected fluorescence intensity obtained from cells treated with combination of MX and Ko143 and I_{MX} is the corrected fluorescence intensity obtained from cells incubated with MX alone.

2.4.2 Accumulation assay – multiwavelength cell scoring analysis

HEK293T cells were seeded on 96-well plates overnight and transiently transfected with CFP-ABCG2 and YFP-ABCG2. Twenty-four hours post-transfection, cells were incubated with medium containing either 4 µM MX only or 4 µM MX in the presence of 1 µM Ko143, for 0-60 min. Cells were then fixed with PFA as discussed above. Cell nuclei were counterstained with Hoechst 33342 (H33342, Life Technologies) at 2 µg/mL for 15 min. Images of the cells were acquired using an ImageXpress Micro (IX Micro) High Content Screening System (Molecular Devices), equipped with suitable fluorescence filter sets and a Nikon 20x long working distance air objective. Table 2.10 below shows the excitation (λ_{ex}) and emission (λ_{em}) bandpass filter sets

employed in this system for the detection of the nucleus stain, CFP or YFP, and MX fluorescence intensities respectively.

Table 2.10: Filter sets employed to detect the fluorescence intensities of the nucleus stain, CFP or YFP, and mitoxantrone. The wavelengths for the excitation and emission bandpass filter sets are also indicated.

Filters	Excitation (λ_{ex} nm)	Emission (λ_{em} nm)	Detection
DAPI	377/50	447/60	Nucleus stain (Hoechst 33342)
FITC	482/35	536/40	CFP or YFP
Cy5	628/40	692/40	Mitoxantrone

To obtain the average MX fluorescence intensities, images acquired from 4 different sites in each well were first subjected to the Multiwavelength Cell Scoring analysis in MetaXpress 5.3 software (Molecular Devices) to identify the cells within the images according to the nucleus staining. This allows calculation of the average MX fluorescence intensities (from the Cy5 channel) and the detection of CFP-ABCG2 or YFP-ABCG2 expression (from the FITC channel) within each cell. Approximately 85 % of the cells were found to be expressing CFP-ABCG2 and 42 % of the cells were expressing YFP-ABCG2, estimated using the % of positive cells detected (FITC channel) in each well. A further Cell Measurement analysis was performed on the same data sets using AcuityXpress 2.0 software (Molecular Devices) to include only MX fluorescence intensities in cells expressing CFP-ABCG2 or YFP-ABCG2 for the final average calculations, i.e. only the average Cy5 fluorescence intensities in cells ranked positive for FITC fluorescence were taken into account.

2.5 Detection of cytoskeletal disruption

2.5.1 Staining protocol

Stable HEK293T cells expressing sfGFP-ABCG2 were seeded on round poly-L-lysine coated coverslips in 12-well plates. 24 h later, cells were treated with either 1 µM cytochalasin D or 1 µM nocodazole (unless specified otherwise) for 15 and 45 min before they were fixed with 4 % PFA as described above.

Cells were then incubated with 50 mM NH_4Cl in PBS for 15 min to quench free aldehyde leftover from PFA fixation. For blocking and permeabilisation, cells were incubated in blocking buffer (0.05 % (w/v) saponin and 0.5 % (w/v) BSA in PBS) for another 15 min. For the detection of actin and microtubules, cells were then incubated with Texas Red-X-phalloidin conjugate (Life Technologies) or primary mouse anti-α-tubulin antibody (Merck Milipore) respectively. Round coverslips with cells face down were incubated in small volumes of antibody solutions diluted at 1: 1000 in blocking buffer for 30 min. Coverslips were returned into the 12-well plates and washed four times with blocking buffer. Secondary incubation with Alexa-Fluor568 goat anti-mouse antibody (Life Technologies) diluted at 1: 2000 in blocking buffer (30 min) detected the bound anti-α-tubulin. Finally, cells were washed again with blocking buffer and mounted onto microscope slides as described earlier.

2.5.2 Fluorescence imaging

Fixed and mounted cells were imaged using a Leica DMRB inverted fluorescence microscope equipped with a monochrome digital camera (Hamamatsu C4742-95) and 63x Plan-Apochromat NA 1.3 oil objective. Cells were imaged with the phase contrast channel, FITC channel (bandpass filter sets; λ_{ex} = 480/40 nm and λ_{em} = 525/20 nm), and TRITC channel (bandpass filter sets; λ_{ex} = 545/20 nm, λ_{em} = 610/30 nm) to observe the cell morphology, sfGFP-ABCG2 localisation and actin or microtubules distribution before and after treatments.

2.6 Standard confocal imaging

Standard confocal imaging was performed on a LSM710 confocal laser scanning microscope from Carl Zeiss Microscopy (Jena, Germany) equipped with a 63x Plan-Apochromat NA 1.4 M27 oil objective and argon laser. For the detection of sfGFP-fusion proteins, 2 % 488 nm argon laser power (according to the acousto-optic tunable filters (AOTF) controller) was used as the

excitation source and the emission of GFP was collected at 500-598 nm (freely tuneable emission bandwidths and dichroic beam splitter MBS 488). To confirm the expression and localisation of the sfGFP-fusion constructs, high resolution fluorescence channel images (1024 x 1024 pixels, image depth 8 bits) were acquired together with the corresponding phase contrast images.

2.6.1 Confocal imaging to determine low expressing clones and localisation of cytoplasmic sfGFP constructs

For determination of the low expressing stable clones of CD86-sfGFP and CD28-sfGFP (derived from single cell colonies from dilution cloning methods described earlier), cells were imaged live on 48-well plates using a modified LSM inverted confocal microscope (Carl Zeiss Microscopy) equipped with a 20x EC Plan-Neofluar NA 0.5 M27 objective and 488 nm argon laser. Emission was collected at 500-598 nm (freely tuneable emission bandwidths and dichroic beam splitter MBS 488). For tandem-sfGFP and sfGFP, HEK293T cells transiently expressing the constructs seeded on 6-well plates were imaged using the same LSM710 confocal laser scanning microscope set up as per section 2.6 using an 10x EC Plan-Neofluar NA 0.3 M27 objective (instead of the 63x oil objective).

2.7 FRAP acquisition and analysis

For the investigation of ABCG2 membrane diffusion, fluorescence recovery after photobleaching (FRAP) was performed using a confocal laser microscope on stably transfected HEK293T cells expressing sfGFP-fusion constructs. This technique measures the diffusion of neighbouring (non-photobleached) fluorescent molecules into the photobleached region and provides information on the kinetics of the fluorescent molecules; see section 4.1 for detailed explanation.

FRAP was performed at 37 °C on the LSM 710 confocal laser scanning microscope as described in section 2.6 earlier. Cells were seeded on MatTek glass-bottom-dishes 24 h (for stable cell lines) or 48 h (for transient expressing cells) prior to the FRAP experiments. Immediately before the experiments, cells were washed with phenol red free Hanks' Balanced Salt Solution (HBSS; from Sigma-Aldrich) pre-warmed to 37 °C. For FRAP experiments, the pinhole was set to 1 Airy unit, and the focal plane was set to lower plasma membrane. Ten scans (512 x 512 pixels, 8 bits) were acquired as baseline measurements using 2 % 488 nm laser power. A circular region of interest (ROI) with radius (r) of 2 µm was photobleached with 30 iterations of 100 % laser power at the 11^{th} scan. FRAP recovery was monitored for a further 50 scans, using the baseline excitation and emission settings. For data correction and obtaining the half time ($t_{1/2}$) of fluorescence recovery, Zen 2010 software (Carl Zeiss Microscopy) was employed. Fluorescence recovery intensities obtained from FRAP experimental ROI were first corrected for bleaching during acquisition at each time point, using the fluorescent intensity differences between a background (non-fluorescent area outside the cell) and a reference (neighbouring cell) areas. The corrected recovery curve was fitted using the single component exponential equation:

$$I(t) = I0 - I1 * e^{-t/T1}$$

Where I0 = end value of recovered intensity (arbitrary units), I1 = amplitude of recovered fraction (arbitrary units), T1 = exponential decay time (s), and t = time (s). The $t_{1/2}$ (s) and mobile fraction (F1) were obtained from the software using the equations below:

$$t_{1/2} = - T1 * \ln 0.5$$

$$F1 = 100 * I1 / (I_{initial} - I_{postbleach})$$

Where $I_{initial}$ = initial fluorescence intensity (arbitrary units) and $I_{postbleach}$ = fluorescence intensity (arbitrary units) immediately after photobleaching, see chapter 4. The diffusion coefficient (D; $\mu m^2 s^{-1}$) was finally calculated using the equation below, based on the radius (r; µm) of the circular ROI area:

$$D = r^2 / 4t_{1/2}$$

Final results (diffusion coefficients and mobile fractions) were presented as the mean ± SEM with the total number of cells and experiments indicated as appropriate. The recovery curves for the different data sets were normalised using pre-bleach fluorescence intensities as 100 % in GraphPad Prism 6.0.

2.8 FRET acquisition and analysis

To investigate the oligomerisation of ABCG2 in live cells, fluorescence resonance energy transfer (FRET) microscopy was employed to study cells transiently expressing CFP- and YFP-fusion proteins. The acceptor photobleaching (AcPb) FRET method was employed to establish the close interactions between two ABCG2 molecules. In AcPb FRET, the increase in CFP (donor) emission immediately after photobleaching of YFP (acceptor) is measured as the FRET efficiency between two fluorophores and provides evidence of close interaction between the proteins they are fused to. Detailed principles of this technique are outlined in section 5.1.

2.8.1 Lambda image acquisition

FRET was performed at 37 °C on a LSM710 cofocal laser scanning microscope (Carl Zeiss Microscopy) equipped with a 63x Plan-Apochromat NA 1.4 M27 oil objective, a 405 nm diode laser, and a 514 nm argon laser. For the acquisition of CFP and YFP, the confocal pinhole was set at 2 Airy units whilst the excitation wavelength was set at AOTF 4 % 405 nm (for CFP) and 2 % 514 nm (for YFP). Dichroic beam splitters 458/513 nm (for YFP) and MBS-405 (for CFP) were used to direct the excitation laser beams to the sample. To collect CFP and YFP emission concurrently, spectral imaging was employed, where lambda (wavelength) scans with images from 417-730 nm at every 10 nm were acquired. To confirm the expression and localisation of the CFP- and YFP- tagged constructs, high resolution confocal lambda images (1024 x 1024

pixels, 8 bits) were acquired together with the corresponding phase contrast images.

2.8.2 FRET data collection and % FRET efficiency determination

Acceptor photobleaching FRET was used to measure the FRET efficiency between CFP and YFP. Cells were first seeded on MatTek glass-bottom-dishes before being transfected with CFP- or YFP-fusion constructs. Before acquisition, transiently transfected cells were washed with HBSS and left to equilibrate for 15 min at 37 °C on the heated stage. For FRET data acquisition, the lower plasma membrane of the cell was chosen as the focal plane and image size was set at 512 x 512 pixels, 12 bit depth. Five scans were first collected before the specified round ROI with radius of 4 µm was photobleached with 30 iterations of 100 % 514nm laser. Ten more scans were collected after photobleaching at normal acquisition laser power. Master gain and digital offset were adjusted before data acquisition to ensure the final images did not contain any oversaturated pixels.

For data analysis, each FRET data set was subjected to linear unmixing algorithm analysis (Zimmermann et al., 2002) using reference spectra (obtained from single transfected CFP- or YFP-fusion constructs) to separate the CFP and YFP intensities in Zen 2010 software (Carl Zeiss Microscopy), see chapter 5 for further explanation. The % FRET efficiency (F_E) was finally calculated from the intensity values using the equation:

$$F_E = (I_A - I_B) * 100 / I_B$$

Where I_A is the intensity of CFP immediately after YFP photobleaching and I_B is the intensity of CFP before YFP photobleaching. Final results were presented as mean ± SEM of % FRET efficiencies comparing across different constructs with the number of cells and experiments indicated where appropriate.

2.9 Fluorescence correlation spectroscopy and photon counting histogram brightness analysis

For the study of membrane kinetics and oligomerisation of ABCG2 at "single molecule" resolution, sfGFP fusion proteins were investigated with fluorescence correlation spectroscopy (FCS) and photon counting histogram (PCH) analysis. FCS measures the fluorescence fluctuations derived from fluorescent molecules within the confocal volume over time and the resultant analysis yields kinetic information about these fluorescently tagged proteins. The molecular brightness of the fluorescent proteins can be extracted by performing PCH analysis on the same FCS measurements, and this provides evidence of oligomerisation for the fluorescent proteins. See section 6.1 for a detailed description of the principles of these two techniques.

2.9.1 FCS data acquisition and autocorrelation analysis

FCS measurements in this study were performed on a Confocor 2 fluorescence correlation spectrometer (Carl Zeiss Microscopy) equipped with a 40x c-Apochromat NA 1.2 M27 water immersion objective and 488 nm argon laser. Following calibration of the instrument with Rhodamine 6G solution (see section 2.9.2), cells were excited with 488 nm laser with a power density of 0.25 kW/cm^2 (0.3 % according to the AOTF controller) in this study, unless specified otherwise. GFP emission was collected with a 505-550 nm bandpass filter. For FCS, cells were seeded and grown on Nunc^{TM} Lab-Tek^{TM} 8-well chambered cover glasses 24 h (or 48 h to allow transfection of sfGFP and tandem-sfGFP) prior to experiments. Cells were washed 3 times with HBSS before equilibration at room temperature (22-25 °C) for 15 min. For cell selection, GFP fluorescence was detected using an external camera (QImaging, Surrey, Canada) with an epi-fluorescence lamp and standard GFP filter sets. The display range of the camera was altered to achieve oversaturation of normal expressing cells and allow selection of low expressing cells (typically < 100 kHz). The confocal volume was placed at the

upper plasma membrane of the cells by performing a *z*-scan (example shown in section 6.3) at low laser power, 0.05 kW/cm^2. Fluorescence fluctuation measurements (3 x 15 s traces) were recorded at laser power density of 0.25 kW/cm^2 after a 10-second pre-bleach with 0.60 kW/cm^2 laser power density. Autocorrelation analysis was performed using Zeiss Aim 4.2 software (Carl Zeiss Microscopy) and the autocorrelation curves were fitted using two different diffusion models. Autocorrelation curves were discarded if they did not reach a clear asymptote as $G(\tau)$ approached 1. This could be caused by sudden increase in concentrations of fluorescent proteins during data collection due to clustering of fluorescent molecules within the plasma membrane, presence of large slow moving particles, random movement of plasma membrane or photobleaching during acquisition of the FCS traces.

For the cytoplasmic proteins (sfGFP and tandem-sfGFP), a single-component model that assumes free 3D diffusion, with added pre-exponential factor (to account for fluorophore triplet state), was used to fit the autocorrelation curves:

$$G(\tau)=1 + \mathrm{A}\ \frac{1}{N}\left(1+\ \frac{\tau}{\tau_D}\right)^{-1}\left(1+\ \frac{\tau}{\mathrm{S}^2\tau_D}\right)^{-0.5}$$

Where the pre-exponential term, A is given by the equation:

$$\mathrm{A} = 1 + \left(T_\tau\ .\ e^{-\frac{\tau}{\tau_\tau}}\right).(1 -\ T_\tau)^{-1}$$

And N = particle number, τ_D = dwell time (µs), T_τ = triplet fraction, and τ_τ = triplet relaxation time (µs). The structural parameter (S), which relates to the dimensions of confocal volume, is given by the ratio w_z/w_{xy}, where w_z = axial parameter (µm) of the confocal volume and w_{xy} = radial parameter (beam waist radius; µm) of the confocal volume.

For the membrane proteins (CD86-sfGFP, CD28-sfGFP, and sfGFP-ABCG2), a two-component 2D diffusion model was used, where as S → ∞, the equation can be simplified as:

$$G(\tau)= 1 + A\ \frac{1}{N}\left(F_1\ \left(1+\frac{\tau}{\tau_{D1}}\right)^{-1} +\ F_2\ \left(1+\frac{\tau}{\tau_{D2}}\right)^{-1}\right)$$

In these experiments, F_1 was interpreted as the fraction of the fast diffusing component caused by GFP photophysics (corresponding dwell time obtained as τ_{D1} (µs), see section 6.7.3 for further discussion. F_2 represents the fraction of the curve that describes the diffusion of the membrane protein of interest, and the corresponding dwell time was obtained as τ_{D2} (µs). The particle number of the membrane proteins (N_2) was obtained using the total number of particles detected (N in the equation) and the known contributing fraction (F_2). Overall, the majority of the traces were found to have triplet fractions of less than 20 %, and the typical triplet relaxation time was < 10 µs. A small amount (less than 5 %) of the traces with > 20 % triplet fractions were discard from the final analysis to avoid underestimation of particle number in the autocorrelation analysis.

2.9.2 Calibration of FCS experiments and diffusion coefficient calculations

Prior to each FCS experiment, the acquisition system (with 488 nm as excitation) was calibrated using Rhodamine 6G solutions (Rho6G; from Life Technologies). First, the confocal system and laser were switched on and the system was allowed to equilibrate at room temperature (22-25 °C) for 1 h. 1 µM and 20 nM of Rho6G solutions were made up for the calibration experiments. 250 µL of the solutions were added to separate wells in 8-well chambered cover glasses. The confocal volume was positioned in the solution by placing the *z*-position 200 µm above the upper coverslip surface. The confocal pinhole was set to 1 Airy unit and the pinhole position (*x*, *y*) was adjusted to obtain maximum count rate using the 1 µM Rho6G solution. A count rate of 200-250 kHz at laser power density of 0.25 kW/cm^2 was usually obtained. Fluorescence fluctuation traces (3 x 15 s) were then collected from the 20 nM Rho6G solution at various laser powers (AOTF 1-5 %) after a 3-second pre-bleach with laser power density of 0.13 kW/cm^2. The τ_D and S from Rho6G autocorrelation curves were obtained (from the 2 % laser power

data set) using the same single-component 3D free diffusion autocorrelation model as described above. The τ_D of Rho6G was typically determined as 20-22 µs and the S values were normally obtained as 4-5, as expected for excitation with 488 nm (Briddon et al., 2011). Using the known diffusion coefficient of Rho6G (2.8 x 10^{-10} m^2s^{-1}) and the assumption of a Gaussian confocal volume, the waist radius of the confocal illumination, w_{xy} was calculated using the equation:

$$w_{xy} = (4.D^{R6G}.\tau_D^{R6G})^{0.5}$$

The waist radius of the confocal volume, typically determined as 0.14-0.16 µm, allows the subsequent calculation of diffusion coefficients (*D*; μm^2s^{-1}), from the dwell times of the proteins of interest using the equation:

$$D = w_{xy}^2/4\tau_D$$

The τ_{D2} values obtained from the two-component analysis were used (instead of τ_D) for the membrane proteins. The concentrations (*C*; number of particles per μm^2) of the proteins of interest were obtained from the equation:

$$C = N / (\pi .w_{xy}^2)$$

The N_2 values obtained from the two-component analysis were used (instead of *N*) for the membrane proteins. The pooled diffusion coefficient and particle concentration data were presented as mean ± SEM with the number of cells and experiments indicated where appropriate.

2.9.3 PCH analysis

For PCH, the raw fluorescence fluctuation traces accepted for autocorrelation analysis were analysed using 1-component or 2-component 3D PCH models (Huang et al., 2004) in Zen 2010. By fitting the models against the frequency distribution of the fluorescence fluctuation amplitudes obtained when the fluorescence record is sampled using a certain binning time, the average molecular brightness (ε; counts per molecules per second (cpms)) and number of molecules within the detection volume can be estimated. A

binning time of 1 ms was chosen to exclude the fast autocorrelation component due to GFP photophysics, unless stated otherwise. As the original PCH models were derived from two-photon system, a correction parameter (first order correction factor) was pre-determined to account for the variation from a Gaussian detection volume when single photon excitation system is employed (Huang et al., 2004). The first order correction factors in this study were determined from Rho6G calibration experiments by collecting single FCS trace for 60 s and fitting the data to a 1-component 3D PCH model using the Zeiss 4.2 Aim software. The first order correction factor obtained from each experiment (typically 0.15-0.17) was then applied to the PCH analysis of the FCS data sets. For PCH analysis (1- and 2-component), the molecular brightness and number of particles were allowed to vary freely whilst the first order correction factor was fixed as determined from the calibration experiments. Reduced chi^2 values obtained from the PCH analysis were used to assess the goodness of fit of the data with the different models. Where reduced chi^2 values were > 2, the data set was excluded from the final molecular brightness or component fraction results presented.

In some treatments of the data, the molecular brightness of CD28-sfGFP and sfGFP-ABCG2 were normalised against those of the CD86-sfGFP (monomer control) for each of the experiment to account for any day-to-day molecular brightness variations. The molecular brightness values of component 2 (C2) were also normalised against the respective brightness of component 1 (C1) to obtain the ratios of C2:C1. The final pooled data were presented as mean ± SEM with the number of cells and experiments indicated where appropriate.

2.10 TIRF microscopy and stepwise bleaching analysis

Single particle imaging using total internal reflection fluorescence (TIRF) microscopy in combination with stepwise photobleaching analysis was employed to establish the oligomeric organisation of ABCG2 in fixed HEK293T

cells. The detailed background and theory of the techniques are outlined in section 7.1.

2.10.1 TIRF imaging and data collection

Prior to TIRF imaging, cells were seeded and fixed on poly-L-lysine coated MatTek glass-bottom-dishes (section 2.2). Stable HEK293T cells expressing low levels of CD28-sfGFP or sfGFP-ABCG2 and HEK293T cells transiently expressing ABCC4-sfGFP were examined. TIRF imaging was performed using an Axio Observer Z1 (Carl Zeiss Microscopy) microscope equipped with a 100x Plan Apochromat NA 1.46 M27 oil immersion objective. The lower plasma membrane of the cells was illuminated under TIRF configuration using a 20 mW 488 nm TIRF laser producing an excitation field of less than 100 nm. Subsequent GFP emission was collected using an emission bandpass filter 510-542 nm. TIRF photobleaching videos were recorded using an EMCCD camera (QuantEM 512SC; Photometrics, Tucson, USA) at a rate of 10 Hz (100 ms per frame) for 80 s using the Zen 2012 software. The thickness and refractive index of the glass coverslips are 0.16-0.19 mm and 1.523 respectively as reported by the manufacturer, while immersion oil with refractive index of 1.518 was used. Minimal differences between the glass coverslip and oil immersion refraction indices ensured that the excitation laser beam arrived at the glass and aqueous medium interface at the appropriate TIRF angle, typically 62-65° as indicated by the TIRF slider on the software. For cell selection, AOTF 4 % excitation laser power was used whilst the display range of the camera was oversaturated to ensure minimal photobleaching of the sample and allow selection of low expressing cells. Photobleaching of the cells was performed using AOTF 80 % laser power throughout the acquisition period (80 s) under TIRF configuration. TIRF videos acquired in Zen 2012 as *CZI* files were not suitable for subsequent stepwise photobleaching analysis using the PIF algorithm in MATLAB. The videos were therefore converted and compiled as 8-bit *TIF* video files using LSM 5 Image Browser (Carl Zeiss Microscopy) and ImageJ (Schneider et al., 2012).

2.10.2 Stepwise bleaching analysis using PIF algorithm

The converted 8-bit *TIF* video files were analysed using the PIF algorithm provided in a standalone MATLAB Runtime Compiler (MathWorks) by Dr Rikard Blunck, University of Montreal (McGuire et al., 2012). First, a region of interest (ROI) was drawn manually in the software. Typically, a whole cell of interest was used as the ROI. Prior to the analysis, the parameters of the algorithm were determined. Most of these parameters were left as default or adjusted as recommended by the authors whilst several other parameters were adapted due to experimental variation (McGuire et al., 2012). The following sub-sections provide detailed descriptions of the PIF algorithm and the parameters required for stepwise photobleaching analysis in this study. The parameters involved in the software were quoted as 'parameter name' and a table summarising the key parameters is shown in Table 2.11 below. The parameters that were different from default values are indicated in this section and they are also discussed further in chapter 7.

Table 2.11: Key parameters defined for stepwise photobleaching analysis of the TIRF videos using the PIF algorithm.

General parameters	Spot detection	Filter	Step detection	Accepted/ Rejected
Time per frame 100ms Starting frame no. 1 No. of average frames for image display 20 No. of average frames for baseline estimation 20	Max no. of neighbours 2 Minimum amplitude 150 δF/F 10%	**Background removal** ☑ Fix filter size ☑ Fixed sigma 1.6 ☑ Symmetric filter Intensity calculation ☑ Theo. LoG intensity **Trace filter** ☐ Chung-Kennedy ☐ if SNR < 1.8	**1st approx. step detection** First SNR 0.75 Progress fraction 10 Progress fraction 1000 Min step length 3 Amp. Tolerance 0.6 Min. step amplitude 75	Proximity sigma 1.25 Counter fit/fit 1 Reduced chi^2 max. 1.5 Max. step amplitude 900 Step/Noise ratio (SNR) > 1.6

Fluorescent spot selection and fluorescence intensity calculation

The fluorescence intensities of the individual fluorescent spots were determined using a contributing region of 5 x 5 pixels, by setting the 'maximum number of neighbours' to 2 in the parameters section (see section 7.3). In the first step of the analysis, the fluorescent spots were determined by setting the following threshold parameters. First, the 'minimum amplitude' of the fluorescent spots was defined to ensure that fluorescent spots were separated from the background (see section 7.3 for example analysis). The fluorescence signal (δF) of the fluorescent spots were calculated (from a region of 5 x 5 pixels) by fitting the initial total fluorescence intensity (F) of

each spot to a two-dimensional Gaussian profile and subtracting the base line (estimated from the last 20 frames of recording) from the total intensities. The 'δF/F' parameter determines the minimum signal required for the fluorescent spots to be selected, using the average intensities from the first 20 frames. The default value of 10 % was employed in this study, which minimised incorrectly selected spots due to presence of background noise. Additionally, use of a proximity threshold rejected fluorescence spots that were too close to each other. A virtual parameter 'sigma' was used to define the surrounding of the Gaussian profiles of each fluorescent spot in this analysis. The 'proximity sigma' parameter was set at 1.25 (as default) to ensure that the fluorescent spots were free of neighbouring spots when the Gaussian profile had reached 20 % of its maximum. The intensity traces were rejected from the analysis if the fluorescent spots were deemed too close to each other.

Background removal by trace filtration

To clearly show the photobleaching steps within the fluorescence intensity traces, a deconvolution method was used to remove the background intensity within the fluorescence traces. This was achieved using a LoG (Laplacian of Gaussian) kernel-type filter. This method is identical to an algorithm commonly employed to improve resolution and remove blurring within the image (Wallace et al., 2001). The size of the kernel was determined according to the 'maximum number of neighbours' parameter (5 x 5 pixels). The parameter 'sigma' defines the shape of the Gaussian pattern (or the point spread function, PSF) of the fluorescent spot and this was determined before the LoG trace filtering was performed. In this study, the 'sigma' value was typically determined as 1.6-1.8, estimated using the maximum frequency obtained from PSF frequency histograms (see section 7.3 for example). A symmetrical LoG filter was applied to the fluorescent spots. The absolute intensity of the final traces was obtained using the 'theo LoG intensity' (theoretical estimation of the absolute intensity after LoG filtering) as the reference intensity.

Photobleaching step detection and quality control

The most important function of the PIF algorithm was to perform an automated photobleaching step detection analysis on the fluorescence intensity traces. To identify segments of constant intensity and establish photobleaching steps, the algorithm performed an iterative process of averaging the intensities in short time segments, in which the averaged data were repeatedly exposed to the same process. This gradual iterative process ensured that photobleaching steps were separated from noise and any blinking event (due to the photophysics of GFP) in the traces. Additionally, the variation of the fluorescence fluctuations among the adjacent frames were analysed to estimate the noise within the traces (N_{FF}). Using this value, the occurrence of a photobleaching step was determined when the reduction in fluorescence intensity signal was higher than that of N_{FF}. Finally, the initial traces were subjected to more successive iterations using higher threshold values to further eliminate noise and fluctuations, ensuring that only true photobleaching steps remained in the final idealised traces. A full detailed description of the step detection algorithm can be found in the supplementary materials published by the authors of PIF algorithm (McGuire et al., 2012).

Although most step detection parameters were set to default, several parameters had to be adapted to the TIRF data acquired in this study. For the PIF algorithm to work, a small starting step to noise ratio (SNR), the 'first SNR' in '1st approx. step detection', was set at 0.75, as recommended by the authors (0.25-1). SNR values were calculated (by the PIF algorithm) using the signal of photobleaching steps and N_{FF} obtained as described earlier. The 'progress fraction' parameter defines the number of progressive step performed on each trace in the averaging and iteration process. The 'progress fraction' values used in this study were identical to those recommended by the authors. For '1st approx. step detection', this value was set at 10. For the final idealisation, this value was set to 1000. The minimum step length ('min

step length') defines the minimum number of frames allowed inbetween each photobleaching step. This value was set as 3, as previously employed by the authors. The maximum step amplitude variation ('amp tolerance') allowed was set to 0.6 (as default) to reduce effects of background fluorescence fluctuation on the detection of photobleaching steps. The minimum step amplitude ('min step amplitude') was set as the lowest frequent step intensity observed in the step intensity frequency histograms obtained in an initial analysis (when 'min step amplitude' was set as 0), see section 7.3 for example. The maximum step amplitude allowed within a trace ('max step amplitude') was set to a constant value of 900 for all the analysis. This value was intentionally set to a constant value larger than majority of the photobleaching step intensities observed in this study to minimise variation in the analysis of the data sets, whilst avoiding under-detection of photobleaching steps.

Finally, several quality control parameters were incorporated in the PIF algorithm to ensure accurate step detection and that only appropriate traces were accepted. First, the minimum required 'counter fit/fit' ratio was set to 1, as per default. This parameter was calculated as the ratio of the goodness of fit of the counter idealisation (counter fit, performed by setting new positions in the middle of each steps) and the idealisation fits. Second, a reduced chi^2 value was calculated when the quality of the fit was assessed using the data and idealised traces. Poorer fitting of the idealised traces will lead to increase deviations of chi^2 values from 1. This parameter, known as the 'reduced chi^2 max', was set to 1.5 (as default), in which any traces with higher values were rejected. Finally, the minimal mean SNR allowed in each trace after the filtering process ('SNR') was set as 1.6, in which traces with low step to noise ratios (≤ 1.6) were rejected. This value was different compared to the value employed by McGuire et al. and the reasons for choosing this SNR value will be discussed further in sections 7.3 and 7.5.

2.10.3 Statistical modelling of photobleaching step frequency histograms using binomial distributions

The TIRF photobleaching videos of cells acquired as described in section 2.10.1 were analysed using the PIF algorithm to detect the number of photobleaching steps within each fluorescent spot. Only cells with > 20 % traces accepted were taken into account for final analysis with the acceptance criteria as described above. The main data sets were presented as frequency histograms of the total number of fluorescent spots observed for the various number of photobleaching steps. To assess for variability between experiments, some of the data sets were also normalised and presented as mean ± SEM of the percentage of fluorescent spots against the number of photobleaching steps.

For the interpretation of the frequency histograms, double binomial oligomeric models were generated to account for the proportion (%) of fluorescent GFP (p-value in the binomial distributions) and overlapping of fluorescent spots (10 % fluorescent spots to follow a second higher order binomial distributions). The binomial distribution equation employed is given as below:

$$b(\mathrm{x};\mathrm{n},\mathrm{p}) = \frac{\mathrm{n}!}{\mathrm{x}!\,(\mathrm{n}-\mathrm{x})!} * \mathrm{p}^{\mathrm{x}} * (1-\mathrm{p})^{\mathrm{n}-\mathrm{x}}$$

Where the probability (frequency) of observing x, the number of photobleaching steps, was dependent on p, the probability that the GFP-tagged protein is fluorescent and detected, and n, the total number of photobleaching steps predicted (corresponding to the total number of oligomeric state expected). To account for the overlapping fluorescent spots, 10 % of the expected number of fluorescent spots was modelled with a second binomial distribution model, using 2x the single oligomeric state expected. For example, for a tetrameric model, 10 % of the total number of fluorescent spots obtained were modelled with a binomial distribution of n = 8, whilst the remaining 90 % of the fluorescent spots were modelled with a

binomial distribution of n = 4, as shown in Table 2.12 below. The final expected frequency for the number of photobleaching steps (x) was calculated by summing up the resulting expected frequencies obtained for the two binomial distributions (Table 2.12). For multiple-component oligomeric models, the dimer and tetramer models were combined in appropriate proportions to calculate the expected number of photobleaching steps for comparison with the actual frequency histograms. The calculation to combine the two binomial oligomeric models was similar to the example shown in Table 2.12, in which the two binomial models were weighted according to expected percentages (%) of dimers and tetramers, and the final expected frequencies were obtained by summing both predicted models together.

Table 2.12: Double binomial distributions to determine the photobleaching step frequency distributions for a tetrameric oligomer state. Table shows an example double binomial calculation for a tetrameric model using 1000 spots, accounting for 10 % of overlapping spots when p = 0.55.

No. of photobleaching steps (n)	Expected no. of spots - tetramer (total 900 spots)	Expected no. of spots - "overlapping" (total 100 spots)	Final expected no. of spots (total 1000 spots)
1	188	2	190
2	347	7	354
3	281	17	298
4	84	26	110
5	-	26	26
6	-	16	16
7	-	5	5
8	-	1	1

To determine the most appropriate oligomeric models for describing the respective frequency histograms, the goodness of fit of the binomial models calculated using p-values of 0.50, 0.55, and 0.60 (proportion of fluorescent GFP) were assessed using the reduced chi^2 (R) values, which were calculated by comparing the expected frequencies obtained from various oligomeric models against the observed data, using the following equation:

$$R = \frac{\left[\sum_n \frac{(O-E)^2}{E}\right]}{(n-1)}$$

Where O represents the observed experimental frequencies, E represents the expected frequencies calculated from the binomial distributions (example shown in Table 2.12), and the degrees of freedom (n-1) was obtained using the total number of photobleaching steps expected from the combined binomial distributions (n). The oligomeric models that yielded the lowest R-values were determined as the best fit models for the respective photobleaching step frequency histograms to establish the oligomeric state of the membrane fluorescent proteins.

2.11 General statistical analysis methods

For statistical analysis, differences between the multiple (at least three independent) data sets were assessed for significance by either one-way or two-way ANOVA analyses followed by Bonferroni multiple comparisons post test. Non-parametric Kruskal-Wallis analysis followed by Dunnett's multiple comparisons post test was employed for data acquired from the diffusion and molecular brightness studies, as some data sets did not pass the D'Agostino & Pearson omnibus normality test ($p < 0.05$) and multiple species could exist within the data sets. One sample t-test was also employed to assess for significance of deviation from a theoretical mean. All statistical tests were performed in GraphPad Prism 6.0. The differences were deemed to be significant if $p < 0.05$.

Chapter 3 Plasmid constructs required for fluorescence studies

3.1 Engineering and design of fluorescent protein tagged ABCG2 constructs

For the study of ABCG2 membrane dynamics and oligomerisation using fluorescence techniques in HEK293T cells, the pcDNA3.1(+)zeo mammalian vector was chosen as the backbone for all DNA construct engineering. Figure 3.1 shows a schematic representation of a standard ABCG2 vector employed. Typically it contains a fluorescent protein (FP) fused N-terminally to ABCG2. C-terminal tagging of ABCG2 was previously reported to be detrimental to ABCG2 localisation (Haider et al., 2011). This mammalian vector also contains a strong cytomegalovirus (CMV) promoter regulatory region for increased protein expression in mammalian cells and zeocin^{TM} resistance gene for selection of stable cell lines. Additionally, it also has a bacterial ampicillin resistance gene and multiple restriction sites for genetic engineering. The common cloning and diagnostic restriction sites employed here are also indicated in Figure 3.1.

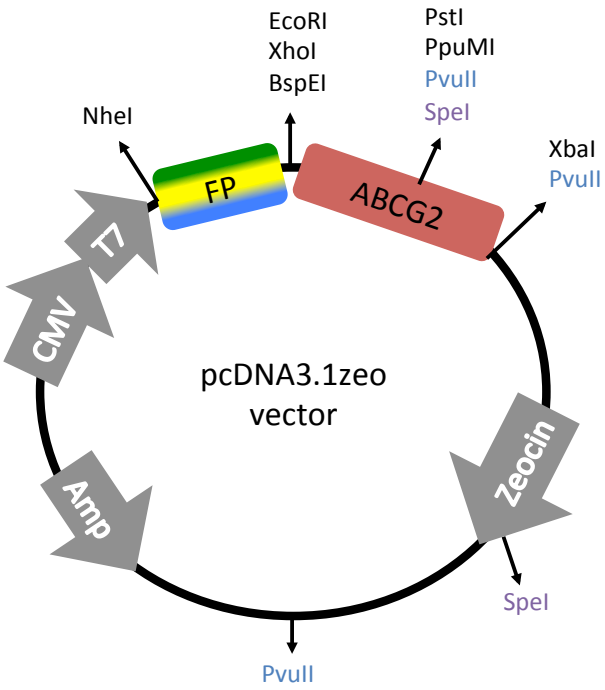

Figure 3.1: Schematic illustration of a standard DNA vector in this study. The vector normally contains a FP (fluorescent protein) fused with ABCG2 as the main construct of interest. For expression and sequencing purposes, the vector also contains a standard CMV promoter, the T7 promoter priming site, along with the ampicillin (amp) and zeocin™ resistance genes. The restriction sites employed in this study are also indicated with the restriction sites commonly employed to confirm the final size of plasmid highlighted in blue and purple, *PvuII and SpeI*.

A variety of fluorescent fusion protein constructs were generated in this study, which are summarised in Table 3.1 along with the techniques (cloning or PCR mutagenesis) utilised for their generation, and primers used for amplification/mutagenesis. The primer sequences can be found in chapter 2, Table 2.3. The methodology of the generation of these constructs will be presented in this chapter.

Table 3.1: Summary of the various pcDNA3.1zeo constructs generated through two different methods in this study. The primers employed and fluorescence experiments involved in are also indicated. TMD_S: short version of transmembrane domain (residues 376 to 655 of ABCG2 sequence). TMD_L: extended version of transmembrane domain (residues 281 to 655 of ABCG2 sequence).

Constructs	Primers	Fluorescence experiments
Restriction enzyme based cloning		
YFP-ABCG2	-	FRET
YFP-ABCG2_C603A	-	FRET
YFP-ABCG2_C603A	-	FRET
sfGFP-ABCG2	Kozak-sfGFP_F, Kozak-sfGFP_R	FRAP, FCS/PCH, TIRF
sfGFP-ABCG2_C603A	-	FRAP
CFP-ABCG2	CFP-nostop_F, CFP-nostop_R	FRET
CFP-ABCG2_C603A	-	FRET
YFP-NBD	NBD_F, NBD_R	FRET
YFP-TMD_S	TMD_S_F, TMD_S_R	FRET
YFP-TMD_L	TMD_L_F, TMD_S_R	FRET
YFP-TM1-2	NBD_F, TM1-2_R	FRET
YFP-TM1-4	NBD_F, TM1-4_R	FRET
CD28-sfGFP	CD28_F, CD28_R	FCS/PCH, TIRF
CD86-sfGFP	CD86_F, CD86_R	FCS/PCH
Mutagenesis		
nostart_sfGFPA206K	A206K_F, A206K_R	-
sfGFP-ABCG2_T362A	T362A_F, T362A_R	FRAP

3.2 Generation of sfGFP-ABCG2 construct

3.2.1 Cloning of YFP-ABCG2 constructs into pcDNA3.1zeo vector

Expression of fluorescent-tagged ABCG2 in pcDNA3.1zeo vector was desired for the selection of stable cell lines using zeocin™. Using the starting vectors pcDNA3.1neo_YFP-ABCG2 and pcDNA3.1zeo_SNAP-ABCG2 provided by Dr Ian Kerr (University of Nottingham), YFP-ABCG2 was sub-cloned by *NheI* and *XbaI* into the pcDNA3.1zeo vector (replacing the SNAP-ABCG2) to produce pcDNA3.1zeo_YFP-ABCG2, as illustrated in Figure 3.2 below.

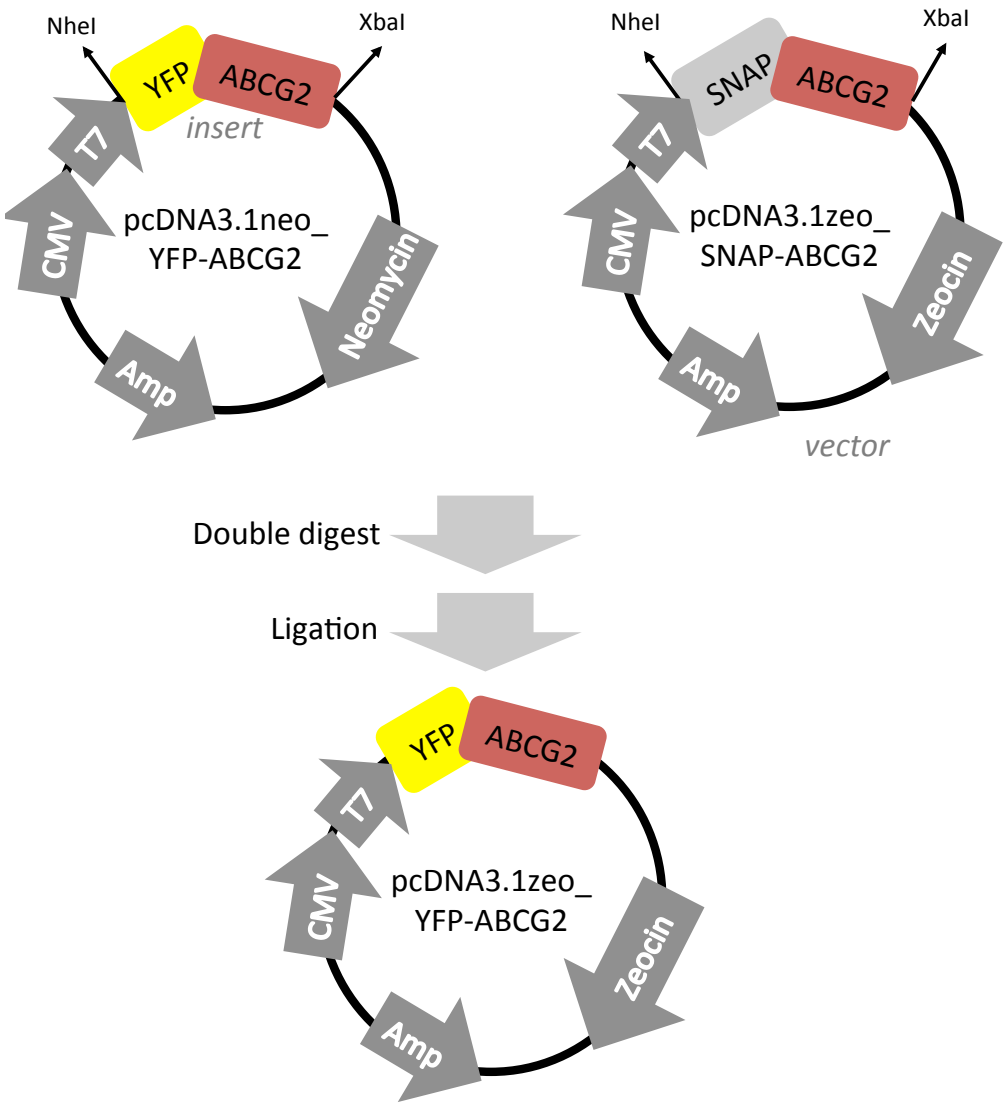

Figure 3.2: Cloning plan to generate pcDNA3.1zeo_YFP-ABCG2. Two starting templates (see Table 2.1) were digested with *NheI* and *XbaI* and the desired bands were purified and ligated to produce YFP-ABCG2 in a pcDNA3.1zeo vector.

The resulting DNA extracted from transformed competent cells was digested with restriction enzyme *SpeI* to confirm correct band sizes. Figure 3.3 shows the gel electrophoresis from the resultant restriction digest, confirming that the pcDNA3.1zeo_YFP-ABCG2 bands generated were of the right size of approximately 6000 and 2000 base pairs (bps).

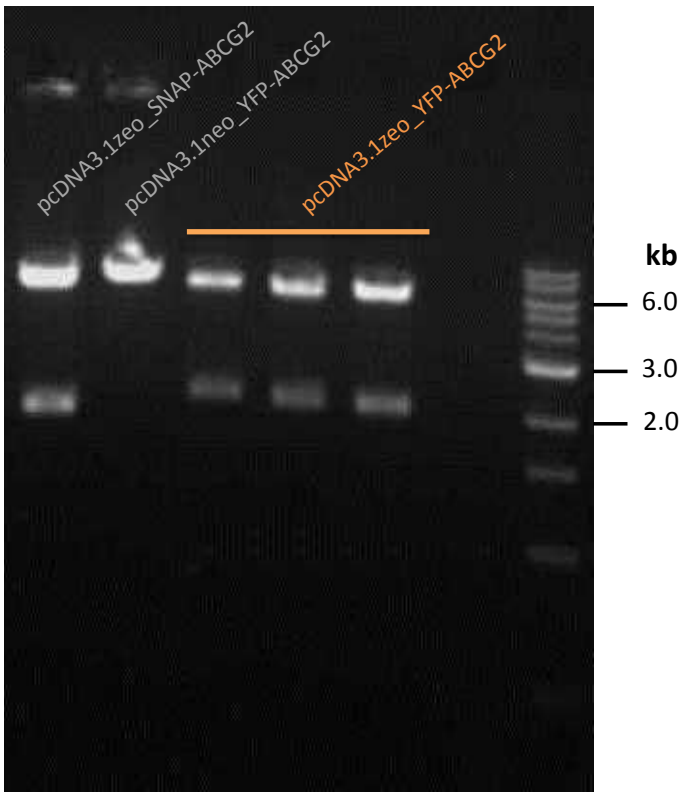

Figure 3.3: Digestion with *SpeI* restriction enzyme to confirm the size of pcDNA3.1zeo_YFP-ABCG2. 500 ng of the miniprep samples of pcDNA3.1zeo_YFP-ABCG2 (orange) was digested with 5 units of *SpeI* restriction enzyme and digested sample was loaded onto a 1 % (w/v) agarose gel. 1kb (kilo bases) DNA Ladder and two other reference samples were loaded alongside the samples.

One of the three samples (of pcDNA3.1zeo_YFP-ABCG2) shown in Figure 3.3 was sent for DNA sequencing to ensure the construct of interest contains the expected sequences. DNA chromatograms obtained were first used to confirm the reading frame and signal quality of the data. Using the BLAST local alignment tool (Altschul et al., 1990), sequence data were also aligned according to the predicted sequence. The alignment results are summarised as Table 3.2 below. Although the first 15 bases could not be confirmed due to incomplete data in the early sequencing results from T7F and SeqR1 primers, manual alignment of the sequences in DNA chromatograms revealed the complete sequence of YFP-ABCG2 construct (see Figures S3.1, S3.2, and S3.3 in Appendix for examples of DNA chromatograms and BLAST alignment data).

Table 3.2: Sequencing results to confirm YFP-ABCG2 sequences within the new pcDNA3.1zeo vector. Sequencing data were aligned against the predicted sequence and the positions matched within the vector are shown. Base positions 917-1670 of the vector corresponds to YFP and the linker sequence region, whilst the base positions 1671-3640 of the vector corresponds to the ABCG2 sequence region.

Primers	Positions matched 100%
T7F	930-1700 (YFP-ABCG2)
SeqR1	1130-1940 (YFP-ABCG2)
SeqF0	1870-2850 (ABCG2)
SeqF2	2430-3250 (ABCG2)
Seq482	3090-4100 (ABCG2)

3.2.2 Introduction of an A206K mutation into sfGFP starting vector

As discussed in chapter 1, the A206K mutation in GFP has previously been shown to reduce the potential for GFP dimerisation. Prior to tagging of ABCG2 cDNAs with sfGFP, the A206K mutation was first introduced into the starting template pcDNA3.1zeo_no-start-sfGFP (see section 2.1). The A206K mutation was introduced by performing the QuikChange PCR mutagenesis using primer pair A206K_F and A206K_R. DNA extracted from transformed competent cells was confirmed by restriction digest with *PvuII* enzyme and DNA sequencing. The DNA chromatogram in Figure 3.4 indicates the successful mutation of alanine-206 to a lysine residue.

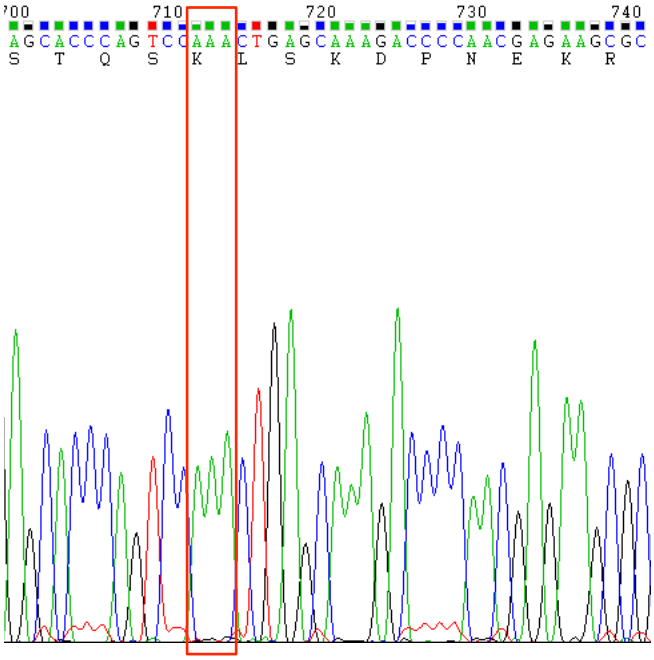

Figure 3.4: DNA chromatogram of pcDNA3.1zeo_nostop_sfGFP with the successful A206K mutation highlighted in red. DNA sequencing was performed using T7F primer to confirm the presence of A206K mutation, obtained from PCR mutagenesis of the pcDNA3.1zeo_nostop_sfGFP vector. Sequencing data was analysed using Chromas Lite 2.1.1.

3.2.3 Cloning of pcDNA3.1zeo_sfGFP-ABCG2

The cloning plan to generate pcDNA3.1zeo_sfGFP-ABCG2 is summarised in Figure 3.5. The starting template, pcDNA3.1zeo_nostart-sfGFP_A206K was only suitable for using sfGFP as a C-terminal extension. The plasmid has no ATG start sequence upstream of the sfGFP sequence, and contains a stop codon at the 3' end. For ABCG2 constructs, N-terminal tagging was required. Hence, PCR amplification was performed to generate a Kozak-sfGFP_nostop construct using the primer pair Kozak-sfGFP_F and Kozak-sfGFP_R, Figure 3.5, top right panel. In this construct, a "modified" consensus Kozak sequence (ATG start codon) and *NheI* cloning site were inserted at the N-terminus of sfGFP, and the stop codon was replaced with a *BspEI* cloning site. The cloning process was then repeated as above using the cloning sites *NheI* and *BspEI* to replace the YFP within the pcDNA3.1zeo_YFP-ABCG2 vector using the amplified sfGFP construct, thereby generating pcDNA3.1zeo_sfGFP-ABCG2.

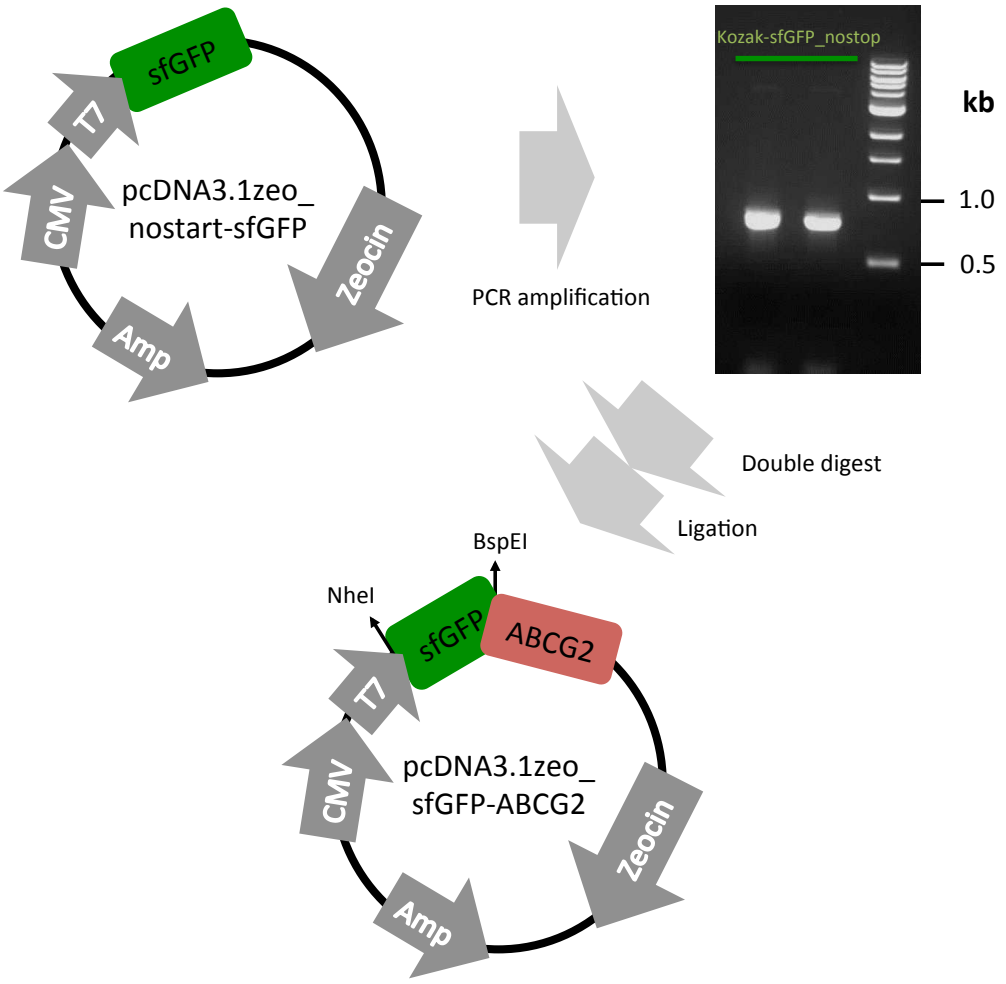

Figure 3.5: Cloning plan to generate pcDNA3.1zeo_sfGFP-ABCG2. Kozak-sfGFP_nostop construct was amplified from the pcDNA3.1zeo_nostart_sfGFP template with added start codon and restriction sites (*NheI* and *BspEI)* and the stop codon was removed. The gel electrophoresis result shows the purified Kozak-sfGFP_nostop construct with sizes of approximately 750 base pairs. 1kb DNA ladder was loaded alongside the samples. The sfGFP construct was then cloned into the pcDNA3.1zeo_YFP-ABCG2 vector by replacing the incumbent YFP.

Upon confirmation of the size of the DNA vector using *PvuII* restriction enzyme, a sample was sent for DNA sequencing. Figure 3.6 shows the sequencing results of pcDNA3.1zeo_sfGFP-ABCG2 using two different primers. The presence of the "modified" consensus ATG start codon and the restriction sites (*NheI* and *BspEI*) was confirmed. Figure 3.6 also indicates that sfGFP was correctly linked to the start of ABCG2 through a 10 amino acid linker. The full sequencing data were analysed by aligning against the predicted sequences as demonstrated above, and the successful generation of a vector containing sfGFP-ABCG2 was confirmed.

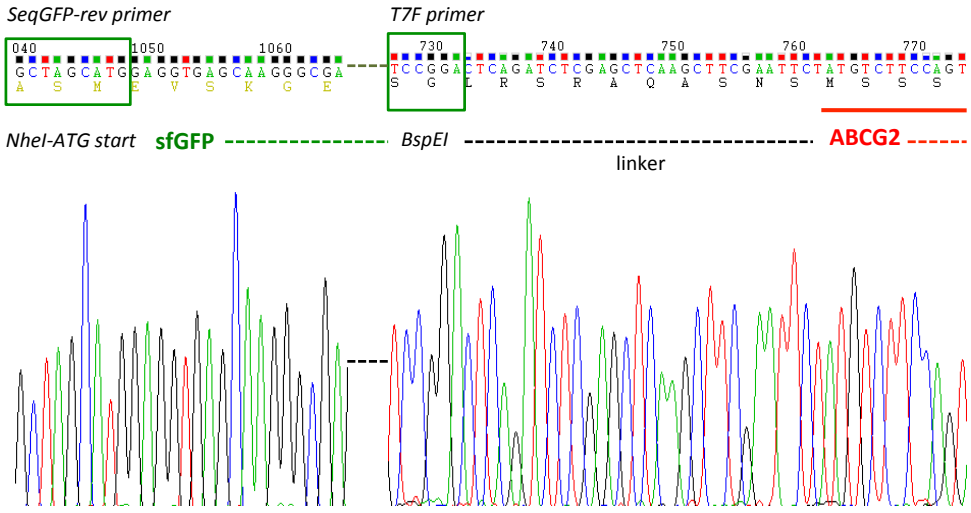

Figure 3.6: Sequencing data of pcDNA3.1zeo_sfGFP-ABCG2 using primers SeqGFP-rev and T7F. Figure shows that the "modified" Kozak ATG start codon of sfGFP was present and the stop codon was replaced by *BspEI* restriction site. The start of ABCG2 (red) following the linker region was also shown in the figure. The break in the sequencing data was manually inserted to show the coverage by two different primers. Sequencing data was analysed using Chromas Lite 2.1.1.

3.3 Generation of CFP-ABCG2 and YFP- truncated ABCG2 constructs

3.3.1 Generation of CFP-ABCG2 constructs

For the study of ABCG2 oligomerisation in live HEK293T cells using FRET microscopy, CFP-ABCG2 (cerulean fluorescent protein fused to ABCG2) was generated (as the FRET donor). An identical PCR amplification and cloning process as section 3.2.3 was repeated using pcDNA3.1zeo_CFP as the PCR template (instead of pcDNA3.1zeo_nostart-sfGFP) and CFP-nostop_F and CFP-nostop_R as the primer pair to generate the pcDNA3.1zeo_CFP-ABCG2.

3.3.2 Generation of YFP-fused truncated ABCG2 constructs

The pcDNA3.1zeo_YFP-ABCG2 generated in section 3.2.1 was used as the starting template for the generation of various YFP-fused truncated ABCG2 mutants for the investigation of the roles of different ABCG2 domains in its oligomerisation. Five different truncated ABCG2 constructs were generated

using the same strategy. Figure 3.7 shows an illustration of the membrane topology of ABCG2 predicted using TOPCONS (Bernsel et al., 2009). The beginning or the ends of the different YFP-fused truncated constructs are highlighted in the figure. PCR amplification of the truncated cDNA, using primers to add *XhoI* and *XbaI* restriction sites at the 5' and 3' ends respectively was first performed, followed by restriction enzyme based cloning and ligation into the pcDNA3.1zeo_YFP-ABCG2 vector. This replaced the full length ABCG2 sequence in the process. Table 3.1 gives a list of these constructs and the primers employed for their generation. A stop codon was introduced to the YFP-NBD and the YFP-TM1-2 and TM1-4 constructs.

The YFP-NBD construct contains the NBD (start of ABCG2) up to the amino acid residue 393Q, where 393 here is with respect to the ABCG2 primary sequence rather than that of the fusion protein. The YFP-TMD_S construct contains TMD starting from amino acid residue 376Q until the end of the ABCG2 primary sequence (residue 655). A longer version YFP-TMD_L was also generated (not shown in Figure 3.7) containing amino acid sequences from residue 281 to 655. The YFP-TM1-2 and YFP-TM1-4 constructs contain the NBD and part of the TMD up to amino acid residues 476S (TM1-2) and 535S (TM1-4), as shown in Figure 3.7. All the constructs were confirmed by restriction digest with *PvuII* and DNA sequencing.

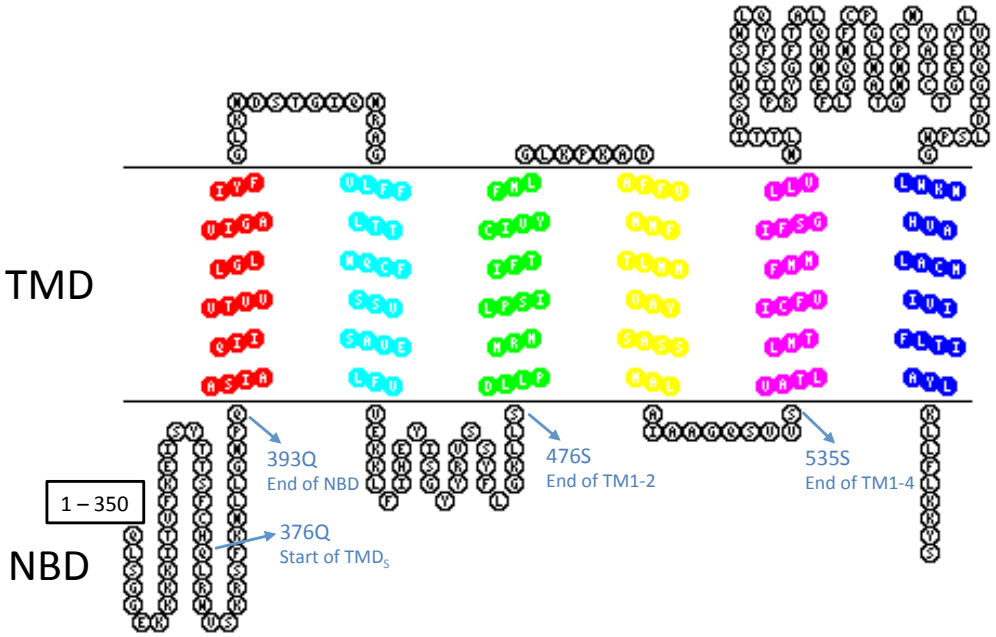

Figure 3.7: An illustration of 2D membrane topology of ABCG2. The transmembrane residues (coloured) and extracellular loops were predicted with TOPCONS (Bernsel et al., 2009) and the diagram was generated using TOPO2 transmembrane protein display software (http://www.sacs.ucsf.edu/TOPO2, accessed 06/05/2013). The start of ABCG2 is not shown (residues 1-350). The beginning of the TMD within the YFP-TMD_S construct and the ends of YFP-NBD, YFP-TM1-2 and YFP-TM1-4 are indicated in the figure. Although not shown in the figure, the TMD_L construct starts at position 281.

3.4 Generation of oligomerisation controls for single particle fluorescence studies

To facilitate the study of oligomerisation of ABCG2 using FCS/PCH analysis and TIRF microscopy, CD86-sfGFP and CD28-sfGFP were generated as controls. Figure 3.8 below summarises the generation of these two constructs in the pcDNA3.1zeo vector. First, the CD86 (truncated at R277) and CD28 (truncated at R185) constructs were amplified from the starting templates provided by Professor Simon J. Davis, University of Oxford. The cytoplasmic regions of CD86 (N278 to F329) and CD28 (L186 to S220) were removed in these truncated constructs to avoid potential cytoplasmic interactions that could affect the oligomeric behaviour of the controls as suggested in (James et al., 2007). C-terminal tagging was chosen to ensure that sfGFP is located at the intracellular end of the construct, comparable to ABCG2. Cloning sites

EcoRI or *BamHI* and *XhoI* were introduced during the amplification process (Figure 3.8, top left panel). Subsequently, the amplified constructs were cloned into the pcDNA3.1zeo_nostart-sfGFP_A206K vector, to produce pcDNA3.1zeo_CD28-sfGFP and pcDNA3.1zeo_CD86-sfGFP vectors (Figure 3.8). Upon verification of the size of the extracted DNA using *PvuII* enzyme, the constructs were sent for DNA sequencing using T7F primer to confirm the presence of CD28 or CD86 construct and that both constructs were correctly linked in frame to sfGFP.

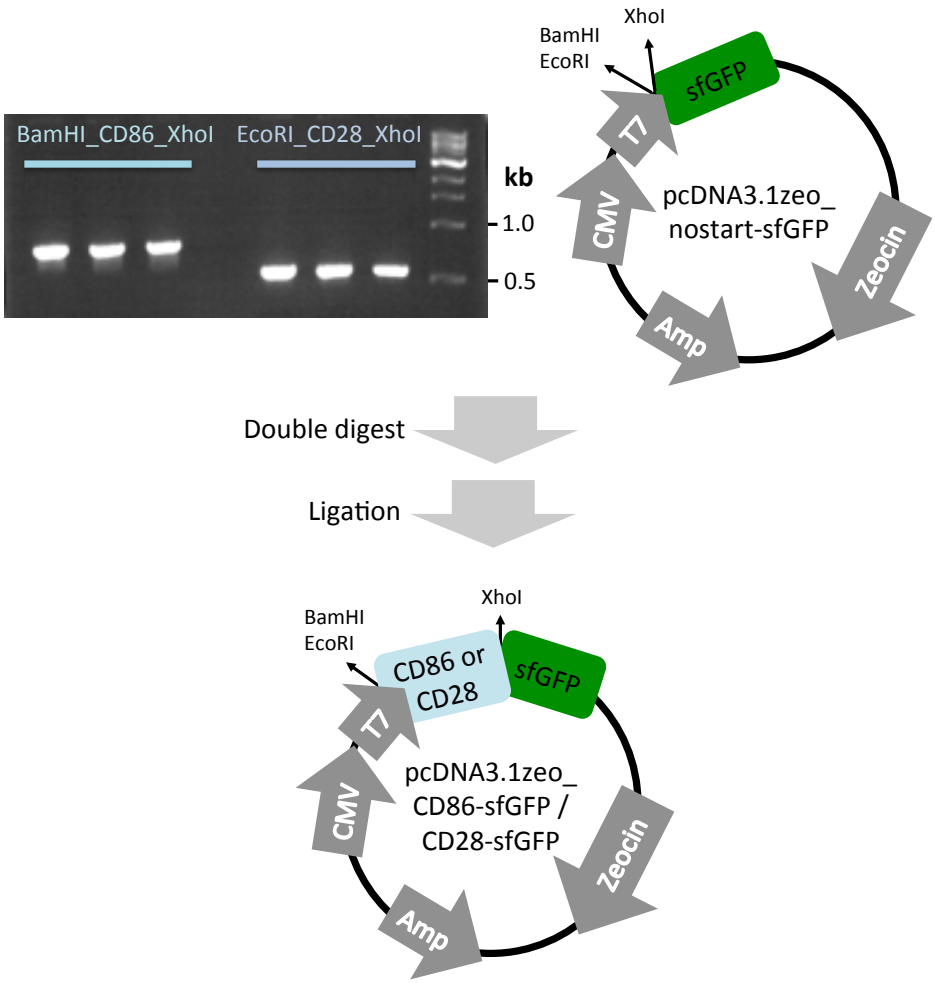

Figure 3.8: Cloning plan to generate pcDNA3.1zeo_CD86-sfGFP and CD28-sfGFP. CD86 and CD28 were first amplified from the starting vectors with the cloning sites introduced at the same time. Gel electrophoresis results shows that the amplified PCR products for CD86 and CD28 were of the correct size, approximately 800 and 550 base pairs respectively. 1kb DNA ladder was loaded alongside the samples. The amplified constructs were then cloned into the pcDNA3.1zeo_nostart-sfGFP_A206K vector to produce C-terminal sfGFP-tagged CD86 and CD28 in the pcDNA3.1zeo vector.

3.5 Generation of C603A and T362A ABCG2 mutants

The C603A ABCG2 single mutant is thought to be responsible for the formation of disulphide bonds between two ABCG2 molecules as demonstrated in various biochemical studies (section 1.6.2). This study also aims to investigate the effects of this mutation on ABCG2 dynamics using fluorescence microscopy. Hence, pcDNA3.1zeo_YFP-ABCG2_C603A was first generated as the starting template for further cloning. As the C603A mutant construct was readily available in another vector (pcDNA3.1zeo_vYNL-ABCG2_C603A; (Haider et al., 2011)), the mutation was simply transferred to the pcDNA3.1zeo_YFP-ABCG2 vector using a *PpuMI* and *XbaI* restriction digest to replace 1.6 kb of the ABCG2 sequence. Figure 3.9 reveals the presence of the C603A mutation in the DNA chromatogram (highlighted in red), when aligned against the DNA chromatogram of wild type ABCG2.

The same cloning process described in section 3.2.3 was performed in parallel using the pcDNA3.1zeo_YFP-ABCG2_C603A as starting vector to generate pcDNA3.1zeo_sfGFP-ABCG2_C603A. The C603A version of CFP-ABCG2 was generated by replacing the ABCG2 wild type in the CFP-ABCG2 vector as described in section 3.3.1 with ABCG2_C603A (from pcDNA3.1zeo_sfGFP-ABCG2_C603A) by cloning using restriction sites *XhoI* and *XbaI*.

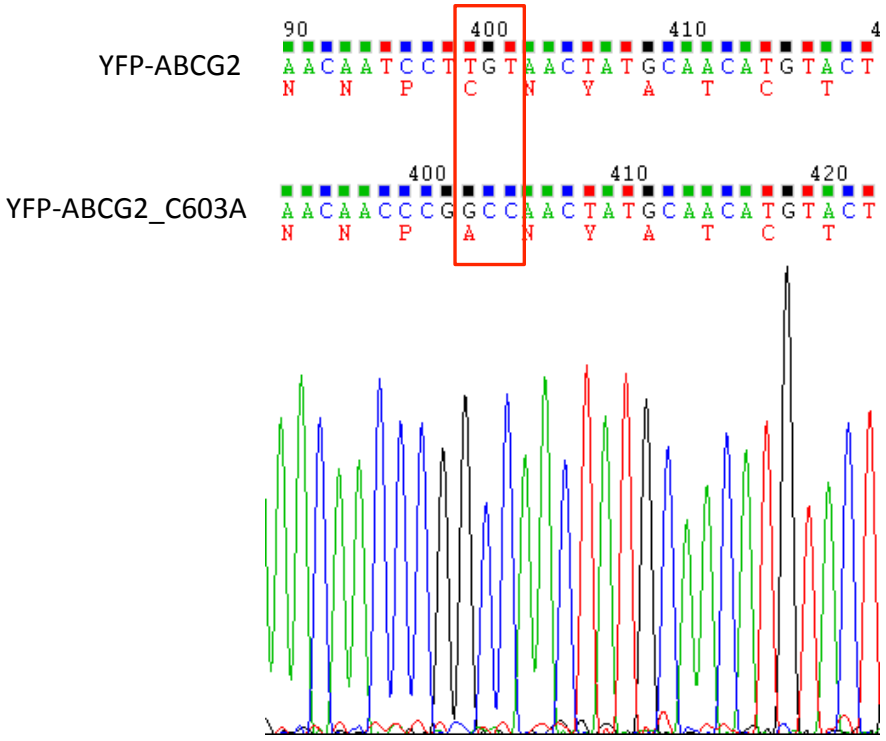

Figure 3.9: DNA chromatogram of pcDNA3.1zeo_YFP-ABCG2_C603A aligned against the ABCG2 wild type sequence. DNA sequencing was performed using Seq482 primer to confirm the presence of C603A mutation, generated from cloning of the pcDNA3.1zeo_YFP-ABCG2 and pcDNA3.1zeo_vYNL-ABCG2_C603A vectors. Sequencing data was analysed using Chromas Lite 2.1.1. The DNA sequence of the C603A mutant was aligned manually against the wild type sequence and the C603A mutation was highlighted in red.

The T362A mutation in ABCG2 is known to affect the phosphorylation of ABCG2 and this may have an impact on its oligomerisation (Xie et al., 2007), section 1.5. Using the primer pair T362A_F and T362A_R (Xie et al., 2007), the mutation was generated by PCR QuikChange mutagenesis. For the confirmation of this mutation, SeqF2 was employed to sequence the resulting plasmids across the mutated region (Figure 3.10), and one plasmid bearing this mutation was then fully sequenced across the sfGFP-ABCG2 cDNA to ensure the fidelity of mutagenesis.

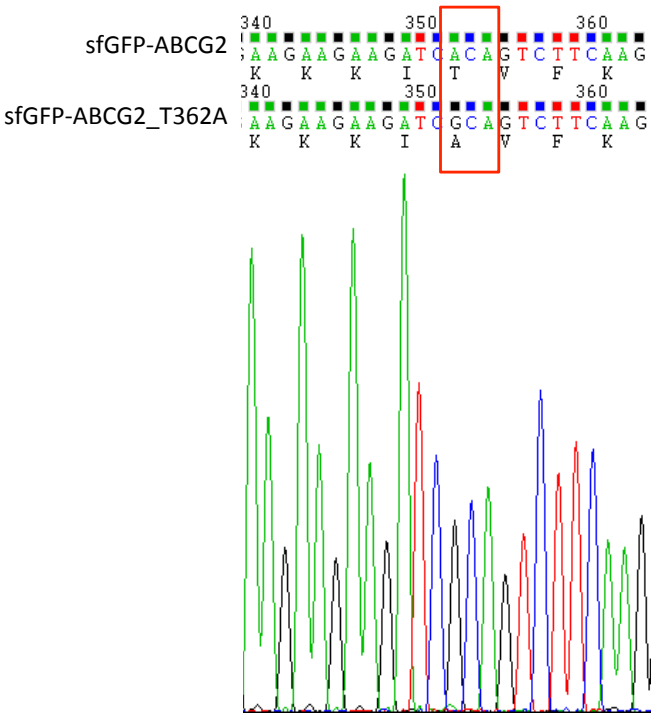

Figure 3.10: DNA chromatogram of pcDNA3.1zeo_sfGFP-ABCG2_T362A aligned against the wild type ABCG2 sequence. DNA sequencing was performed using primer SeqF2 to confirm the presence of T362A mutation, generated from PCR mutagenesis of the pcDNA3.1zeo_sfGFP-ABCG2 vector. Sequencing data was analysed using Chromas Lite 2.1.1. The DNA sequence of the T362A mutant was aligned manually against the wild type sequence and the T362A mutation was highlighted in red.

3.6 Summary

In this chapter, the cloning plan and engineering of the different fluorescent fusion protein DNA constructs were explained. In short, most of the constructs were generated by PCR amplification in combination with cloning (double digest and ligation) into the desired pcDNA3.1zeo vector. All constructs were verified using *PvuII* or *SpeI* restriction digest (to confirm correct band sizes) and DNA sequencing (to confirm correct sequences). In the subsequent results chapters, the characterisation (expression, localisation and function) of these DNA constructs when expressed in HEK293T cells will be presented in relation to the fluorescence techniques they were employed in.

Chapter 4 Membrane diffusion of ABCG2 studied using fluorescence recovery after photobleaching (FRAP)

4.1 Theory of fluorescence recovery after photobleaching (FRAP)

FRAP is a quantitative fluorescence microscopy technique commonly employed to study protein kinetics, by measuring the diffusion of unbleached fluorescent molecules into a photobleached region. It was first described by Koppel and Axelrod in the 1970s and together, they suggested that FRAP can be used to describe the mobility (diffusion) of fluorescent proteins (Axelrod et al., 1976; Koppel et al., 1981). In the 1990s, through the invention of confocal microscopy, the cloning of GFP and rapid development in fluorescent protein technology (see chapter 1), the use of FRAP microscopy to characterise the kinetics and diffusion of proteins was greatly expanded. Cole et al. first employed FRAP in confocal microscopy to determine the mobility of GFP fusion proteins in the Golgi membrane of living cells (Cole et al., 1996). This was quickly followed by many other kinetic studies of GFP fusion proteins in different compartments of the living cell (Reits and Neefjes, 2001; White and Stelzer, 1999), and specific examples will also be discussed in the later sections of this chapter.

Figure 4.1 provides an illustration of a typical FRAP experiment with an idealised bleach curve. Low laser power is used for image acquisition throughout the experimental period whilst high laser power is used to cause photobleaching in the selected bleached area as shown in Figure 4.1. The photobleached area shows a marked reduction in fluorescence intensity. Over time, the neighbouring unbleached fluorescent molecules diffuse into the

photobleached area, exchanging positions with the photobleached molecules and increasing the fluorescence intensity of the bleached area.

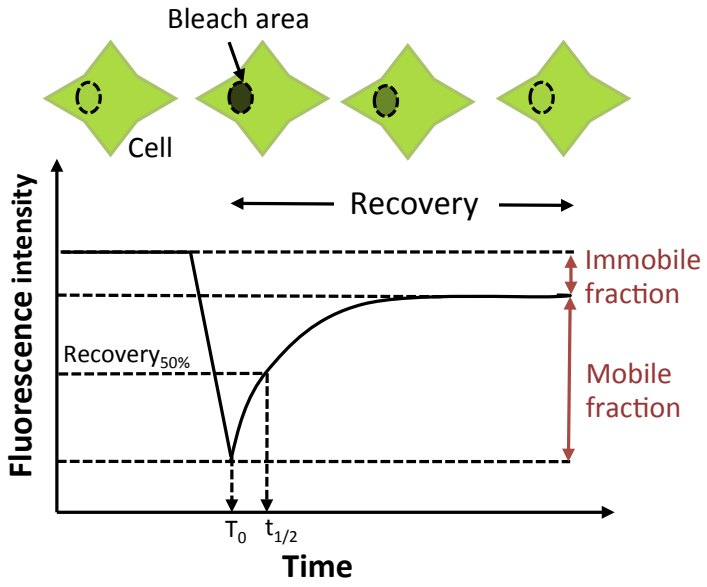

Figure 4.1: Schematic illustration of a standard FRAP experiment. The recovery of fluorescent molecules into the bleached area after photobleaching was schematically represented in the figure. An idealised bleach curve is also shown together with the various parameters that can be obtained from a FRAP recovery curve. The diffusion of the fluorescent molecules can be characterised as the fluorescence recovery half time ($t_{1/2}$), time when 50 % of maximal recovery is achieved. The fraction of fluorescent molecules that contributes to the fluorescence recovery can be quantified as the mobile fraction of the fluorescent molecules (relative to the pre-bleach fluorescence intensity) whilst the immobile fraction represents the rest of the fluorescent molecules that did not contribute to the fluorescence recovery.

Figure 4.1 also illustrates how two important kinetic parameters can be obtained from a standard FRAP experiment – the half time ($t_{1/2}$) and mobile fraction. The half time is the time taken to achieve 50 % fluorescence recovery, measured from time at photobleaching, T_0. This value can be obtained by fitting the curve with an exponential equation. The $t_{1/2}$ can then be used to calculate the diffusion coefficient (D) of the target protein using the following equation: (Axelrod et al., 1976)

$$D = r^2 / (4 * t_{1/2})$$

Where r = radius of bleached area, and D describes the diffusion rate of fluorescent molecules in an area per second, usually in the units of cm^2s^{-1} or μm^2s^{-1}. This equation assumes unrestricted two-dimensional diffusion of the

protein in a circular bleached area. It has been widely applied in many FRAP studies and is applicable to the determination of diffusion within membranes (Reits and Neefjes, 2001). Lippincott-Schawrtz et al. provided a comprehensive summary of the information about target protein that can be extracted from D obtained from FRAP (Lippincott-Schwartz et al., 2001). The Stokes-Einstein formula describes the diffusion constant for a particle as $D_{constant} = kT/6\pi\eta R$, where k is the Boltzmann constant, *T* is the absolute temperature, η is the viscosity of the solution, and R is the hydrodynamic radius of the particle. As the diffusion of a particle is inversely related to its size (R), a reduction in D could therefore indicate a change in the protein size, e.g. formation of large aggregates or oligomeric complexes (Sprague and McNally, 2005). Additionally, cellular environment may also affect protein diffusion and a change in D of a protein could suggest possible changes in the surrounding viscosity or interactions with other proteins and cell cytoskeleton.

The mobile and immobile fractions (Figure 4.1) also carry important kinetic information. The mobile fraction, which represents fluorescent molecules that contributed to the fluorescence recovery, can be obtained by calculating the ratio of full recovery fluorescence intensity to the initial pre-bleach fluorescence intensity (Cole et al., 1996; Feder et al., 1996). The immobile fraction accounts for the rest of the non-contributing fluorescent molecules. The presence of immobile fluorescent molecules could indicate that proteins might be bound to other fixed molecules in the cells or they could form large, immobile aggregates that are trapped in between the compartments within the plasma membrane (Lippincott-Schwartz et al., 2001; Feder et al., 1996; Edidin et al., 1994; Saxton, 1999). In summary, owing to its ability to produce quantitative (diffusion) and qualitative (prediction of cellular environment) information for proteins, FRAP in combination with confocal laser scanning microscopy is now established as a valuable technique for the study of mobility and diffusion of proteins in living cells.

To date, the knowledge of membrane diffusion in ABC transporters (particularly the multidrug efflux pumps) is still lacking. In this study, the diffusion of ABCG2 in live HEK293T cells was first investigated to lay down a foundation in this area for any future work. In this chapter, the characterisation of the DNA constructs encoding fluorescent protein tagged ABCG2 will be discussed. This is followed by the quantitative determination of ABCG2 membrane diffusion using FRAP microscopy in comparison to other membrane proteins. Finally, the effects of substrates and cytoskeleton disruption on the FRAP of ABCG2 will also be presented.

4.2 Construct characterisation

To enable the study of ABCG2 using FRAP, DNA constructs encoding fluorescent protein tagged ABCG2 (as summarised in Figure 4.2) were first generated. Wild type ABCG2 and two single mutants, C603A and T362A, were fused (N-terminally) to the super-folder GFP (sfGFP) template as described chapters 2 and 3. An additional A206K mutation was introduced to the sfGFP template employed to reduce GFP dimerisation (Zacharias et al., 2002). For controls, membrane localised sfGFP constructs were kindly provided by Marleen Groenen, University of Nottingham. These sfGFP constructs were targetted to the membrane using either the C-terminal prenylation motif of kRas protein, sfGFP-kRas (Hancock et al., 1990), or the N-terminal palmitoylation motif of GAP-43 protein, GAP-sfGFP (Denny, 2006). The kRas and GAP-43 motif sequences were expected to confine sfGFP to the non-raft (kRas) and raft regions (GAP-43) of the plasma membrane through non-saturated (kRas) and saturated (GAP-43) fatty acid attachments. Stable HEK293T cell lines expressing these constructs were generated through zeocin^{TM} selection. Another DNA construct encoding a full length ABC transporter, ABCC4 (Figure 4.2), fused C-terminally to sfGFP was kindly provided by Dr Ian Kerr, University of Nottingham. This was transiently transfected into HEK293T cells as control for a full length ABC transporter in

the FRAP experiments. In this section, the verification of the localisation, expression, and function of the ABCG2 constructs will be presented.

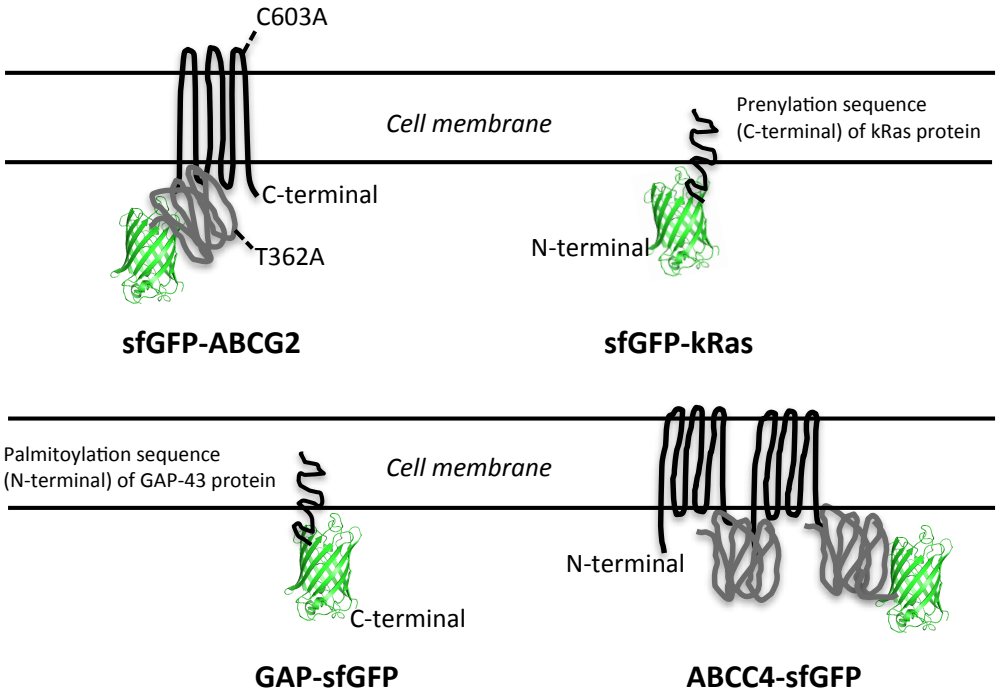

Figure 4.2: Schematic summary of the DNA constructs required for FRAP studies. From top left to bottom right: sfGFP-ABCG2 wild type and two single ABCG2 mutants (C603A, T362A), membrane localised sfGFPs (sfGFP-kRas, GAP-sfGFP), and a full length ABC transporter, ABCC4-sfGFP (with two transmembrane and two nucleotide binding domains). Full details of the construct generation can be found in chapters 2 and 3.

4.2.1 Localisation and expression of sfGFP-ABCG2 constructs

Figure 4.3 shows the confocal images of the stable HEK293T cells expressing sfGFP-ABCG2 wild type, mutants C603A and T362A. These constructs were expressed and localised to the plasma membrane and there was no visible difference in localisation between the stable cell lines. A minor fraction of the transporters were distributed in intracellular compartments, which may represent endocytosis or biosynthesis pathway.

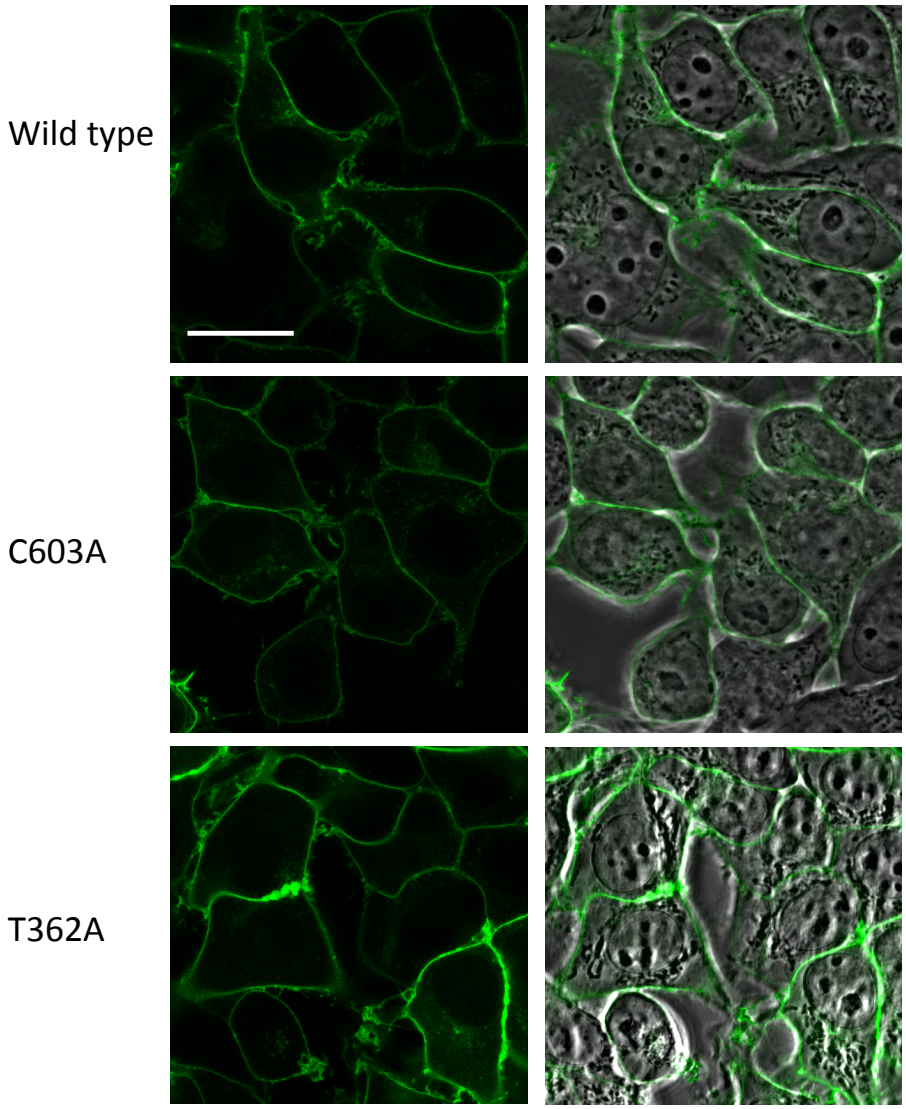

Figure 4.3: Confocal images of HEK293T cells stably expressing sfGFP-ABCG2 transporters (wild type, C603A, and T362A). GFP channel (left), merged phase and GFP channel (right). Scale bar = 20 µm. Representative images of at least 4 independent experiments were shown.

Confocal images in Figure 4.4 show that both the sfGFP-kRas and GAP-sfGFP controls were expressed and targetted to the plasma membrane in the respective stable cell lines. In addition, Figure 4.4 also confirms that ABCC4-sfGFP transiently expressed in HEK293T cells was localised to the plasma membrane.

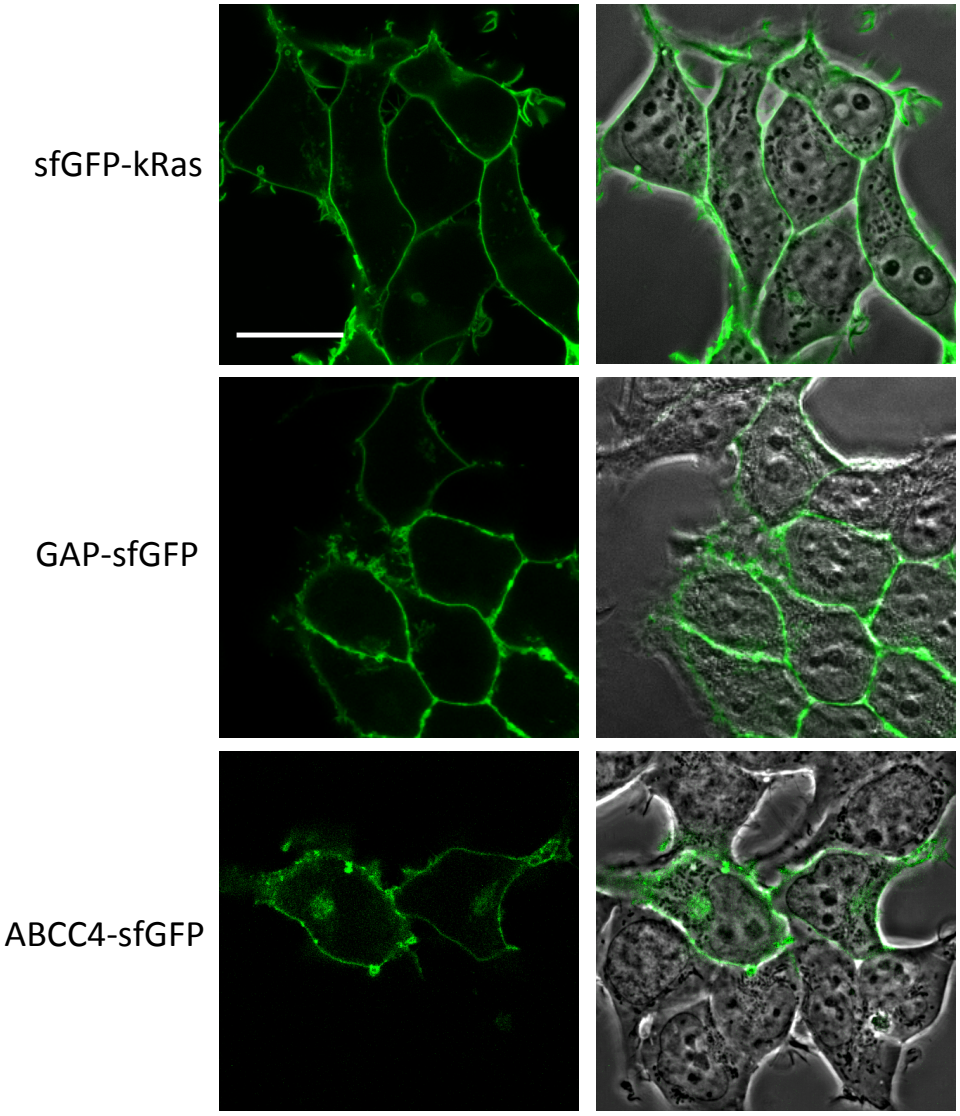

Figure 4.4: Confocal images of HEK293T cells stably expressing sfGFP-kRas and GAP-sfGFP, and HEK293T cells transiently expressing ABCC4-sfGFP. GFP channel (left), merged phase and GFP channel (right). Scale bar = 20 µm. Representative images of at least 4 independent experiments were shown.

SDS-PAGE and western blotting analysis of these fluorescent proteins were subsequently performed on cell lysates harvested from the respective stable cell lines. Figure 4.5 shows the resultant western blot where all the protein samples were found to correspond to their predicted sizes. The sfGFP-ABCG2 wild type, C603A and T362A mutants migrated at approximately 90 kDa (predicted to be 100 kDa using the Compute pI/MW tool (Wilkins et al., 1999)). All three migrated as multiple bands, indicating possible ABCG2 glycosylation, which was also reported elsewhere (Haider et al., 2011). As a

full length ABC transporter, the molecular weight of ABCC4-sfGFP was predicted to be 178 kDa using the same predictor tool (Wilkins et al., 1999) and Figure 4.5 confirms that ABCC4-sfGFP migrated at approximately 180 kDa. Finally, Figure 4.5 also shows that both sfGFP-kRas and GAP-sfGFP were highly expressed ($^1/_5$ of sample amount loaded on the SDS-PAGE gel), and migrated at approximately 30 kDa (predicted to be 27 kDa (Wilkins et al., 1999)). The lower molecular weight bands associated with sfGFP-kRas and GAP-sfGFP (Figure 4.5) could be associated with the membrane localisation modifications of the sfGFP proteins, as it was not observed in cytoplasmic sfGFP constructs (see Figure 6.4 later).

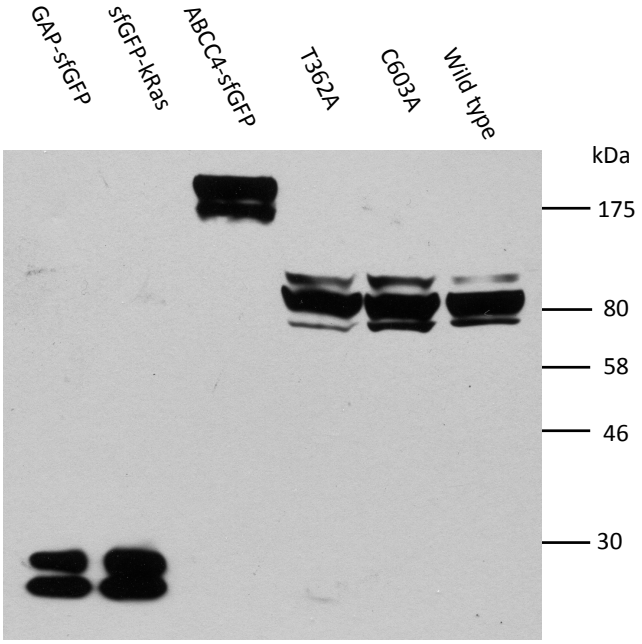

Figure 4.5: Western blot analysis of the different fluorescent proteins investigated in FRAP studies. Approximately 20 µg of cell lysates were used in the 8 % SDS-PAGE gel analysis (with the exception of sfGFP-kRas and GAP-sfGFP, 4-5 µg). The nitrocellulose membrane was probed using primary monoclonal anti-GFP mouse IgGκ antibody and secondary polyclonal rabbit anti-mouse IgG antibody conjugated with horseradish peroxidase, prior to chemiluminescent detection. Representative western blot of 3 independent experiments was shown.

4.2.2 Function of sfGFP-ABCG2

The function of sfGFP-ABCG2 wild type and mutants was subsequently verified by measuring the accumulation of a known fluorescent substrate of ABCG2, mitoxantrone (MX) (Clark et al., 2006) within the cells, in the

presence of a specific ABCG2 inhibitor, Ko143 (Allen et al., 2002). The pEC_{50} of Ko143 in HEK293T cells stably expressing sfGFP-ABCG2 was first determined before MX accumulation measurements in the absence or presence of Ko143 were compared in sfGFP-ABCG2 wild type, C603A and T362A expressing cells against the control sfGFP-kRas expressing cells.

The accumulation curve generated in Figure 4.6 shows the normalised % of MX accumulation in the presence of varying concentrations of Ko143 combined from three experiments. The fluorescence intensities were normalised using the maximum and minimum values in each data set so that they could be pooled together. The pEC_{50} of Ko143 determined from the curve fitting in Figure 4.6 was 7.8, with a 95 % confidence interval of 7.9 to 7.6. This indicates that 16 nM of Ko143 was sufficient to cause 50 % inhibition of sfGFP-ABCG2 expressed in the HEK293T cells (by causing 50 % increase in accumulation). This experiment also demonstrated functional wild type sfGFP-ABCG2 in HEK293T cells.

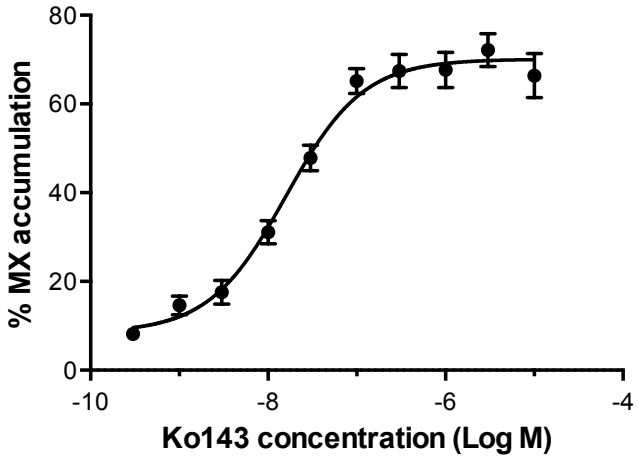

Figure 4.6: Accumulation of mitoxantrone (MX) in the presence of various concentrations of Ko143. HEK293T cells stably expressing sfGFP-ABCG2 wild type were incubated with 4 µM mitoxantrone and various concentrations of inhibitor Ko143 for 2 h. The intensity values of mitoxantrone were measured using a Flexstation. Data from three experiments (each with 8 internal replicates) were normalised using the respective minimum and maximum values and are presented as the combined % data (mean ± SEM) with the fitted accumulation curve (using the log (agonist) vs. response (3 parameters) equation in GraphPad Prism 6.0).

Another accumulation assay was employed to confirm the function of the C603A and T362A mutants, using sfGFP-ABCG2 wild type as positive control and sfGFP-kRas as negative control. Instead of multiple Ko143 concentrations, this assay was performed in the absence or presence of a single concentration of Ko143, 1 µM to ensure complete inhibition. The final data were presented in Figure 4.7, expressed as % accumulation of MX due to Ko143 inhibition (calculated as described in section 2.4.1). Cells expressing sfGFP-ABCG2 wild type, C603A and T362A mutants demonstrated significant increases in MX accumulation due to Ko143 inhibition, compared to the negative control sfGFP-kRas ($p < 0.05$). The accumulation of MX was dependent on specific Ko143 inhibition on ABCG2 and there was little inhibition in the sfGFP-kRas expressing cells, demonstrating that sfGFP-ABCG2 wild type, C603A, and T362A were functional when expressed in the respective stable cell lines. N-terminal tagging of ABCG2 with fluorescent proteins has been demonstrated previously to be non-detrimental to the protein localisation and function and the results in this section and section 4.2.1 are consistent with these observations (Haider et al., 2011).

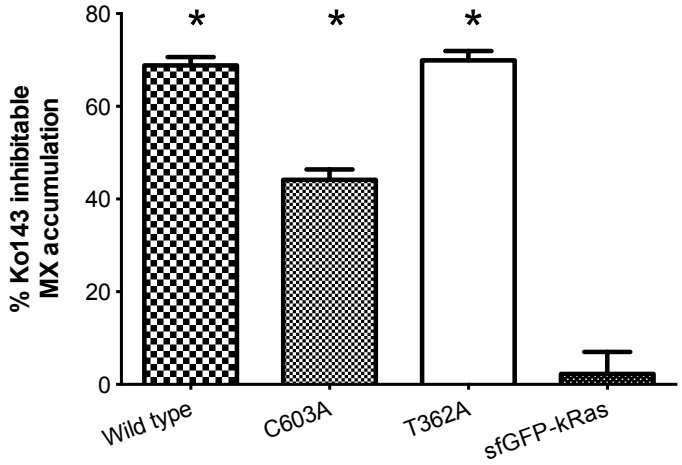

Figure 4.7: Function of sfGFP-ABCG2 wild type and mutants when expressed in HEK293T cells. MX (4 µM incubation) fluorescence intensity values were first corrected against basal intensity for solvent (DMSO) and the subsequent differences between presence and absence of Ko143 (1 µM incubation) were determined as the % Ko143 inhibitable MX accumulation. Data are plotted as the mean ± SEM from 3 independent experiments (each with 8 internal replicates). Statistical significance (*, $p < 0.05$) was assessed using one-way ANOVA analysis followed by Bonferroni multiple comparisons test.

4.3 ABCG2 FRAP experimental design and data analysis

Before the diffusion studies were carried out, optimisation of several parameters were required for the FRAP experiments. The optimal methodology of FRAP was described in section 2.7. In this section, the data acquisition and parameter optimisation is discussed.

Figure 4.8 shows a raw data set acquired from a FRAP experiment using sfGFP-ABCG2 expressing cells. The confocal images acquired at the lower plasma membrane of the cells show the initial state, photobleaching, and the fluorescence recovery of sfGFP-ABCG2 in the bleached region of interest (ROI, red). The fluorescence recovery curve obtained from the ROI curve (red) was corrected against the reference (pink) and background (green) fluorescence intensities in Zen 2010. The curve was then fitted to a single exponential equation in Zen 2010 from which the half time ($t_{1/2}$) and D were obtained. Mobile fractions can also be determined using the corrected intensities in Zen 2010 as discussed in sections 2.7 and 4.1.

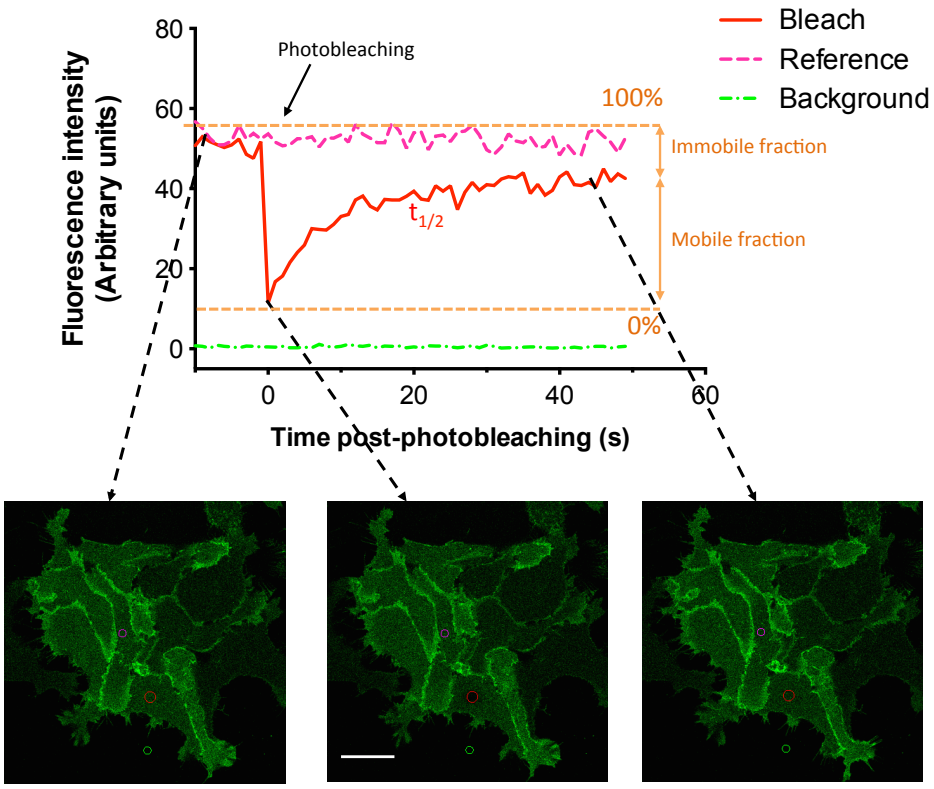

Figure 4.8: Example of a FRAP experiment. Fluorescence intensities of the different regions (red: region of interest, ROI; pink: reference region; and green: background region) at various time points are shown in the intensity plot. The confocal images at the corresponding time points (before, immediately after, and 50 s after photobleaching) are highlighted. The confocal image at time point immediately after photobleaching (middle) shows a dark circle in the bleached ROI (red circle) where sfGFP-ABCG2 molecules were photobleached. The confocal image at 50 s after photobleaching (right) shows unbleached neighbouring sfGFP-ABCG2 molecules diffused into the bleached ROI. The intensities of the reference and background regions were used for correction of the ROI intensities in Zen 2010. The kinetic parameters – half time ($t_{1/2}$), mobile and immobile fractions (%) were subsequently obtained as describe in section 2.7. Scale bar = 20 µm.

For optimisation, the shape and size of ROI, focal plane of the cell, and photobleaching conditions were determined prior to the FRAP experiments. First, a circular ROI was chosen for straightforward calculation of D using the two dimensional diffusion equation as described in section 4.1 (Axelrod et al., 1976). The basal membrane of the cell was chosen as the focal plane for the FRAP experiments because it is flat and does not easily drift out of focus during acquisition. Thirty iterations and 100 % 488 nm laser excitation were chosen as the photobleaching conditions in the FRAP experiments. Figure 4.9A shows that 65-85 % bleaching was consistently achieved in both sets of

cell lines (sfGFP-ABCG2 wild type and C603A) using these settings. This ensured that there was sufficient photobleaching for the monitoring of fluorescence recovery. Figure 4.9B shows that the kinetic parameters (D and mobile fraction) obtained from the sfGFP-ABCG2 wild type FRAP data were not affected by the photobleaching efficiency.

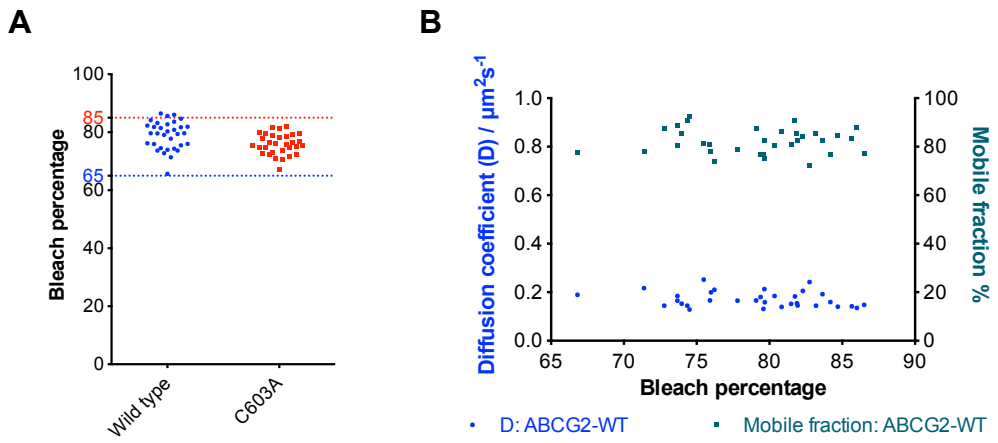

Figure 4.9: Bleach percentages achieved with the FRAP experimental photobleaching settings did not affect the kinetic parameters. A – Bleach percentages were calculated using the differences in fluorescence intensity values before and after photobleaching, as a proportion of the maximum reduction in intensity possible (set to 100 %). **B –** Effects of bleach percentages on the diffusion coefficients and mobile fractions (obtained from the ABCG2 wild type data set in A). **A and B –** Data were collected from 20 cells and two independent experiments and each data point represents the bleaching percentage collected from individual cells.

Further optimisation was performed to compare the diffusion coefficients obtained using different bleach radii, 2 µm or 3 µm. Figure 4.10 shows that for both wild type and C603A, the variability of the data was lower when 2 µm radius was used as the size of ROI. Therefore, this was adopted for the remaining experiments. The discrepancy between the diffusion coefficients in the different bleach sizes will be discussed again at the end of this chapter.

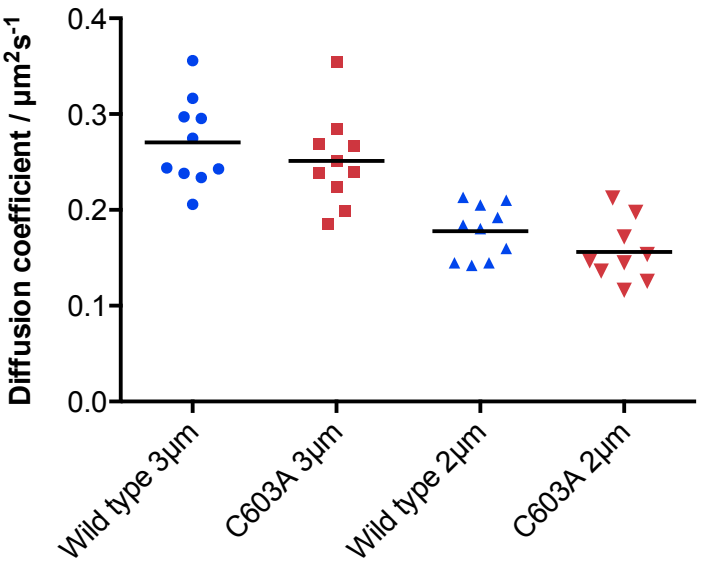

Figure 4.10: Reduced bleached size radius is associated with more consistent values of the diffusion coefficient. Figure shows a preliminary experiment to determine the effects of different sizes (2 µm and 3 µm) in the ROI employed, on the diffusion coefficients obtained. Data were collected from 10 cells for each data set in one experiment.

4.4 FRAP of ABCG2 compared to control membrane proteins

Using the optimised parameters, the FRAP of sfGFP-ABCG2 wild type and mutants (C603A and T362A) were compared with the membrane localised sfGFPs (GAP-sfGFP and sfGFP-kRas) and the full length ABC transporter, ABCC4-sfGFP.

Figure 4.11 shows the normalised fluorescence recovery curves of the various fluorescent proteins. Figure 4.11A shows that the smaller membrane localised sfGFPs (GAP-sfGFP and sfGFP-kRas) had much faster fluorescence recovery compared to sfGFP-ABCG2 wild type, achieving maximum plateau much earlier in the fluorescence recovery curves. The full length ABC transporter, ABCC4-sfGFP, was shown to have slightly slower diffusion compared to sfGFP-ABCG2. Figure 4.11B shows that the two ABCG2 mutants, C603A and T362A had similar fluorescence recovery to the wild type variant.

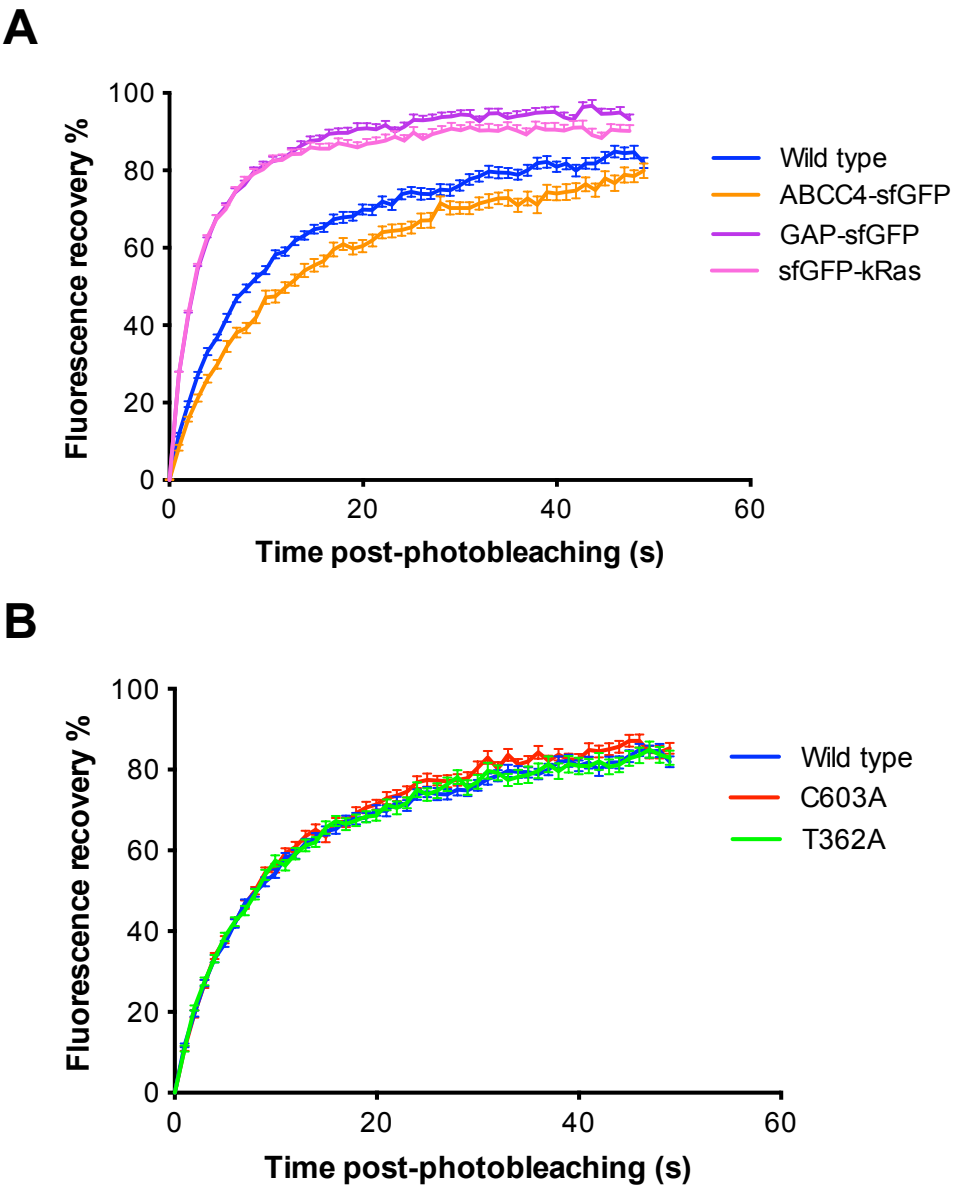

Figure 4.11: Fluorescence recovery of ABC transporters and membrane localised sfGFP. A – sfGFP-ABCG2 wild type, ABCC4-sfGFP, GAP-sfGFP, and sfGFP-kRa**s. B –** sfGFP-ABCG2 wild type, C603A, and T362A. **A and B –** Corrected recovery curves (mean ± SEM) were normalised against the pre-bleach fluorescence intensity values in the respective data sets. Data shown here were combined from at least 40 cells in 3 independent experiments.

The $t_{1/2}$ values were subsequently obtained by fitting the corrected recovery curves using a single component exponential equation (described in section 2.7). The diffusion coefficients were calculated and presented in Figure 4.12. The diffusion coefficients of the ABCG2 variants were determined as 0.18 ± 0.00 $\mu m^2 s^{-1}$ for wild type, 0.17 ± 0.01 $\mu m^2 s^{-1}$ for the C603A mutant, and 0.18 ± 0.01 $\mu m^2 s^{-1}$ for the T362A mutant. Kruskal-Wallis statistical analysis (with Dunnett's post test) revealed that there was no significant difference ($p >$

0.05) between the Ds of the three ABCG2 variants, suggesting that the two point mutations did not introduce any pronounced alteration in the mobility of the transporter. The D of full length ABCC4 transporter was determined as 0.13 ± 0.00 $\mu m^2 s^{-1}$, which is significantly lower than the D of ABCG2, $p < 0.05$. Finally, the Ds of the membrane localised sfGFPs were found to be significantly higher at 0.38 ± 0.01 $\mu m^2 s^{-1}$ for GAP-sfGFP, and 0.41 ± 0.01 $\mu m^2 s^{-1}$ for sfGFP-kRas, when compared to the ABCG2 variants, $p < 0.05$.

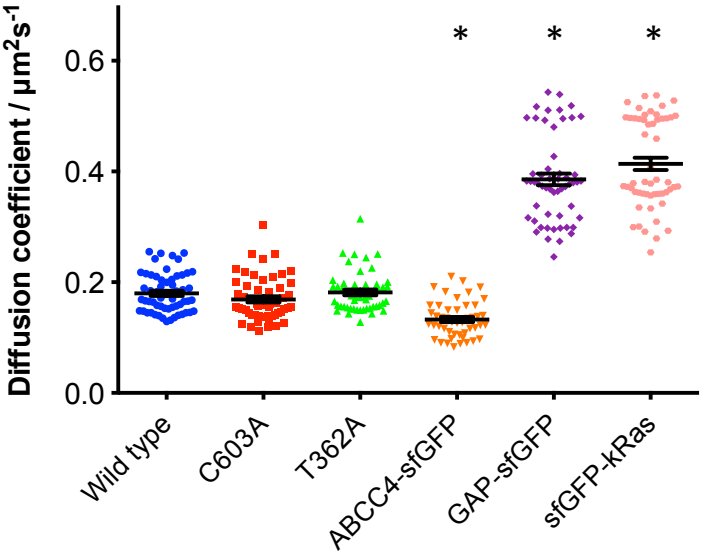

Figure 4.12: Diffusion coefficients of sfGFP-ABCG2 compared to the control membrane proteins. The diffusion coefficients of the sfGFP-ABCG2 variants (wild type, C603A, and T362A), full length ABCC4-sfGFP transporter, and the membrane localised sfGFP controls (GAP-sfGFP and sfGFP-kRas) were presented as a scatter dot plot with the mean ± SEM indicated. Data shown here were collected from at least 40 cells in 3 independent experiments. Statistical significance ($p < 0.05$, * when compared to sfGFP-ABCG2 wild type) was assessed using non-parametric Kruskal-Wallis analysis followed by Dunnett's multiple comparisons test.

As discussed earlier, FRAP experiments also provide information about the mobile fraction of the fluorescent proteins, which represents the proportion of the fluorescent molecules that contributed to the fluorescence recovery. This is a useful tool as the remaining immobile fractions could provide indication about increased binding of ABCG2 molecules to fixed immobile molecules or formation of large aggregates, resulting in restricted mobility. Figure 4.13 presents the mobile fractions extracted from the same data sets

in Figure 4.12. All the fluorescent proteins were shown to be highly mobile and the lowest mean mobile fraction was 77 % for ABCC4-sfGFP. This is not significantly different when compared to the sfGFP-ABCG2 variants, 82% for wild type, 82 % for C603A, and 81 % for T362A ($p > 0.05$). The mobile fractions of the membrane localised sfGFP constructs (GAP-sfGFP, sfGFP-kRas) were significantly higher at 89 % and 92 % ($p < 0.05$), when compared to the ABCG2 variants, Figure 4.13.

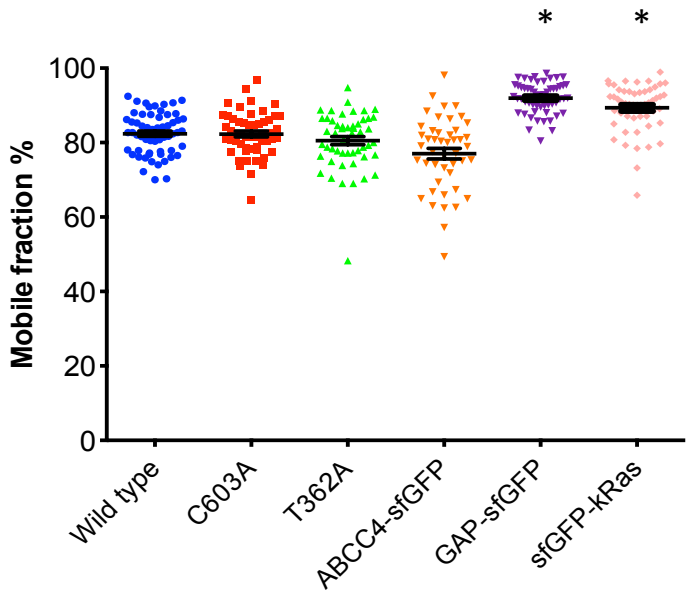

Figure 4.13: Reduced mobile fractions of ABC transporters compared to the membrane localised sfGFP. Mobile fractions (mean ± SEM) of the sfGFP-ABCG2 wild type, C603A, and T362A, full-length ABCC4-sfGFP, and the membrane localised GAP-sfGFP and sfGFP-kRas were calculated as described in section 2.7. Data shown here were collected from at least 40 cells in 3 independent experiments. Statistical significance ($p < 0.05$, * when compared to sfGFP-ABCG2 wild type) was assessed using non-parametric Kruskal-Wallis analysis followed by Dunnett's multiple comparisons test.

4.4.1 Effects of substrate on ABCG2 FRAP

As discussed in section 1.5, evidence of allosteric drug binding in ABCG2 has been described previously (Clark et al., 2006). It is plausible that substrate/drug binding could affect the protein-protein interactions between ABCG2 molecules and thereby affecting the diffusion coefficients of ABCG2. Therefore, the effects of ABCG2 substrate addition on the FRAP of sfGFP-ABCG2 was investigated. Figure 4.14 below shows that addition of MX (4 µM) did not have any significant effect on the Ds of sfGFP-ABCG2 or sfGFP-kRas

($p > 0.05$), suggesting that substrate interaction with ABCG2 does not affect its membrane mobility.

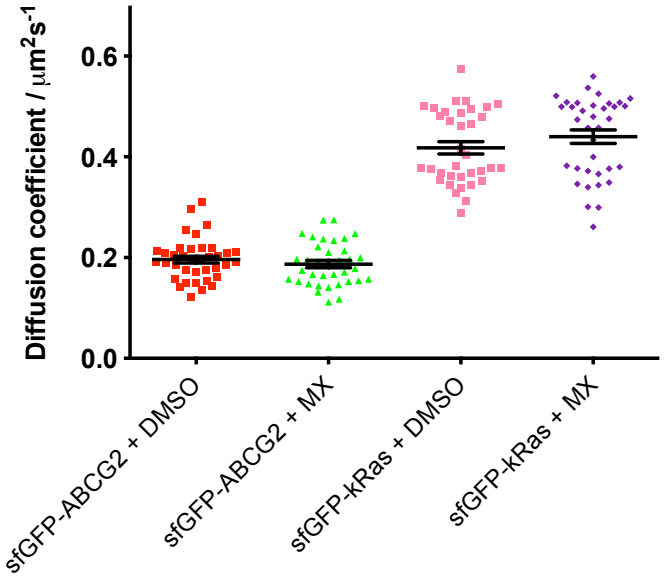

Figure 4.14: ABCG2 diffusion was not affected by substrate transport. Mean ± SEM of diffusion coefficients of sfGFP-ABCG2 and control sfGFP-kRas in the presence of solvent (DMSO) or mitoxantrone (MX) are presented. Cells were incubated with HBSS containing 4 µM MX or the equivalent amount of DMSO (0.02 % (v/v)) for at least 30 min prior to data collection. Data were collected from at least 30 cells in 3 independent experiments. Control and MX-treated groups did not differ significantly, as assessed using non-parametric Kruskal-Wallis analysis followed by Dunnett's multiple comparisons test.

4.4.2 Effects of cytoskeleton disruption in ABCG2 FRAP

The cell cytoskeleton, specifically actin and microtubules (polymers of tubulin), are known to affect the diffusion of membrane proteins (Edidin et al., 1994). In this section, the effects of cell cytoskeleton disruption on the FRAP of ABCG2 will be presented. Cytochalasin D and nocodazole were employed to disrupt the cell actin (Casella et al., 1981) and microtubules (Xu et al., 2002) respectively.

First, the effects of the two drugs at 1 µM and the time required for cytoskeleton disruption were confirmed by immunofluorescence microscopy to visualise the changes in actin and microtubules within the cells. Figure 4.15 shows the effects of 15 and 45 min 1 µM cytochalasin D treatment on cell actin (detected with phalloidin stain) when compared to the untreated cells.

The cell actin structure (Figure 4.15, TRITC channel) was notably disrupted upon 15 min of treatment. In addition, substantial alteration in cell morphology (Figure 4.15, phase channel) was also observed after 15 min of treatment. The effects of 15 and 45 min incubation were found to be similar. Images of the FITC channel in Figure 4.15 show that sfGFP-ABCG2 remained at the plasma membrane despite the disruption of cell actin. To ensure complete actin disruption in the subsequent FRAP experiments, cells were incubated with HBSS containing 1 µM cytochalasin D for a minimum of 20 min before the FRAP data were collected.

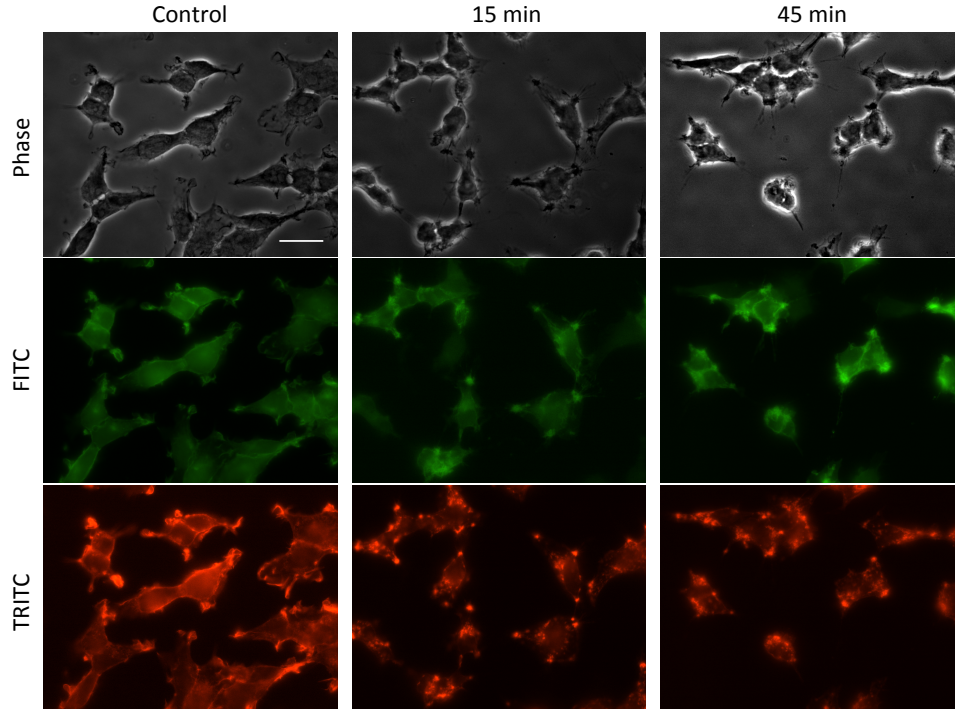

Figure 4.15: Effects of cytochalasin D treatment on sfGFP-ABCG2 expressing HEK293T cells demonstrated by immunofluorescence microscopy. Fluorescence images of fixed cells treated with 1 µM cytochalasin D for different periods (as indicated in the figure) compared to the untreated control cells. Cells were first incubated with cytochalasin D, fixed with 4 % paraformaldehyde, and actin was finally stained with Texas Red-X-phalloidin conjugate. Phase contrast channel (top), FITC channel (middle), TRITC channel (bottom). Scale bar = 20 µm. Representative images of 3 independent experiments were shown.

Figure 4.16 shows the effects of 1 µM nocodazole treatment (15 and 45 min) on the microtubular structure (detected with primary anti-α-tubulin and secondary Alexa-Fluor568 staining) when compared to the untreated cells. Microtubule structure were moderately disrupted after 15 min and more

significantly so after 45 min treatment with nocodazole. The disruption was indicated by the increased dispersion of the red counterstained anti-tubulin (Figure 4.16, TRITC channel). Similar to actin disruption above, alteration of cell morphology was also observed (Figure 4.16, phase channel), with slight alteration after 15 min and more considerable changes after 45 min treatment with nocodazole. FITC channel images in Figure 4.16 also show that sfGFP-ABCG2 remained at the plasma membrane upon disruption of microtubules in the cells. Finally, to ensure sufficient microtubule disruption and maintain cell viability in the subsequent FRAP experiments, cells were incubated with HBSS containing 1 µM nocodazole for a minimum of 30 min before any data were collected.

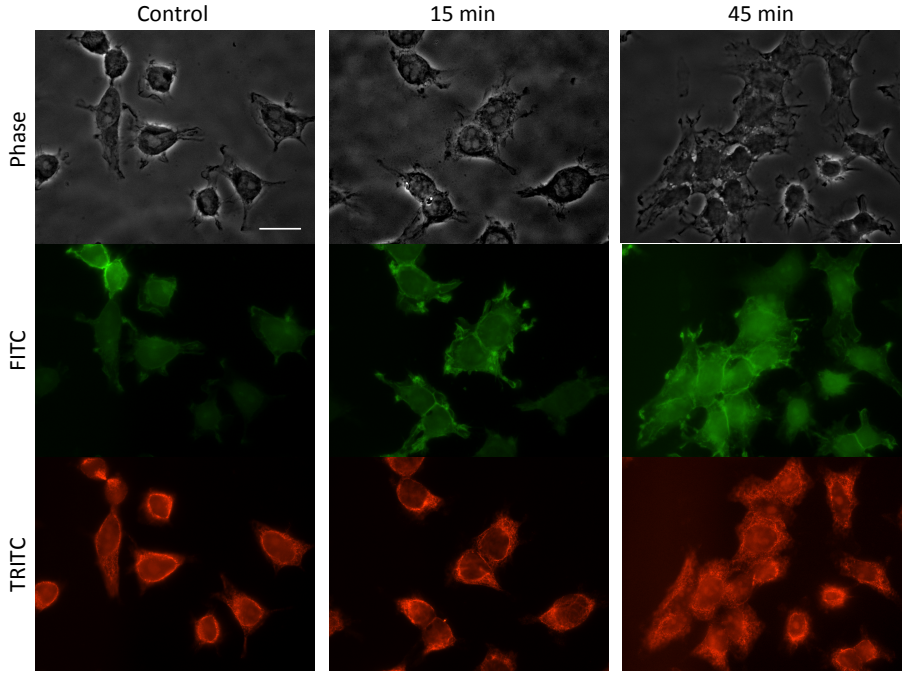

Figure 4.16: Effects of nocodazole treatment on sfGFP-ABCG2 expressing HEK293T cells demonstrated by immunofluorescence microscopy. Fluorescence images of fixed cells treated with 1 µM nocodazole for different periods (as indicated in the Figure) compared to the untreated control cells. Increased dispersion of microtubules (TRITC) was detected upon treatment with nocodazole. Cells were first incubated with nocodazole, fixed with 4 % paraformaldehyde, and microtubules were detected with primary anti-α-tubulin antibody and secondary Alexa-Fluor568 antibody staining. Phase contrast channel (top), FITC channel (middle), TRITC channel (bottom). Scale bar = 20 µm. Representative images of 3 independent experiments were shown.

Figure 4.17 presents the FRAP of ABCG2 (diffusion coefficients in 4.17A, and mobile fractions in 4.17B) in the presence of cytochalasin D and nocodazole.

The disruption of actin and microtubules by cytochalasin D and nocodazole respectively did not have any significant effect on the diffusion coefficients or the mobile fractions of sfGFP-ABCG2 and sfGFP-kRas, when compared to treatment with an equivalent amount of solvent DMSO ($p > 0.05$).

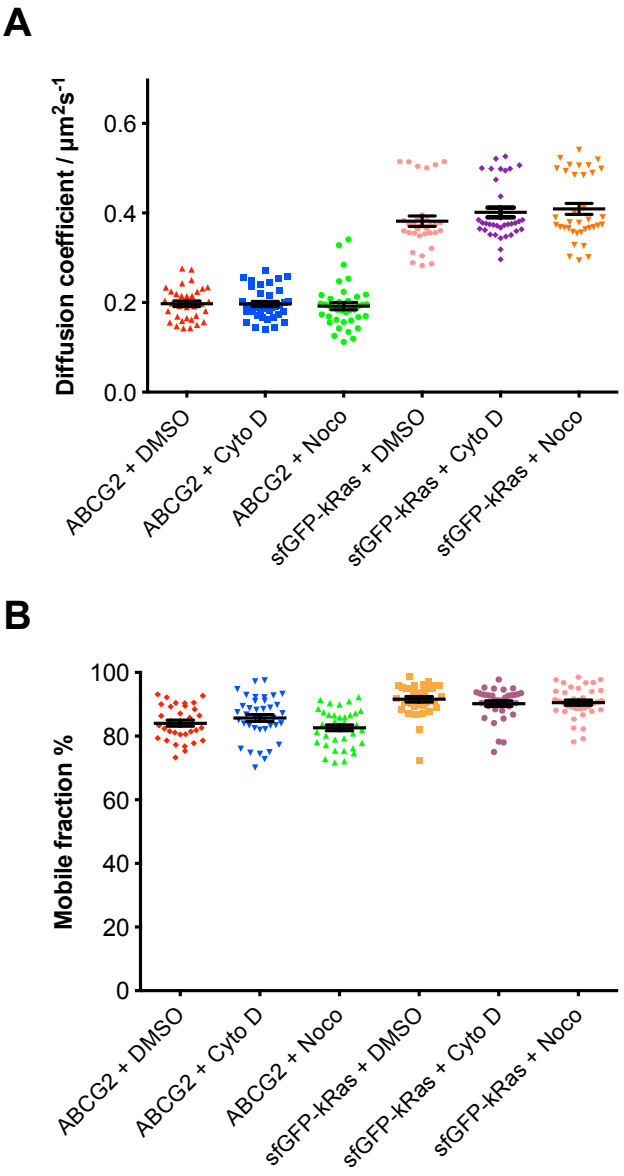

Figure 4.17: Effects of cytoskeleton disruption on the FRAP of sfGFP-ABCG2 and sfGFP-kRas. Mean ± SEM of diffusion coefficients (**A**) and mobile fractions (**B**) of sfGFP-ABCG2 and sfGFP-kRas expressing cells upon incubation of 1 µM cytochalasin D (20 min) and 1 µM nocodazole (30 min), compared to the equivalent amount of solvent DMSO (30 min), prior to data collection. Data were collected from at least 30 cells in 3 experiments. No significant difference was obtained between the control and treated groups ($p > 0.05$), assessed using non-parametric Kruskal-Wallis analysis followed by Dunnett's multiple comparisons test.

4.5 Discussion

4.5.1 FRAP of ABCG2 – comparison with other membrane proteins

The FRAP results in this study yielded D and mobile fraction values of ABCG2 (and control membrane proteins) which are similar to the values reported in the literature for other membrane proteins (section 4.4). Frick et al. performed FRAP on small GFP chimeric proteins (such as the Lyn protein and the TMD domain of the LDL receptor) using similar measurement techniques (Frick et al., 2007), and reported diffusion coefficients of 0.25 to 0.5 $\mu m^2 s^{-1}$ for the membrane proteins. Another study on the FRAP of proteins in different microdomains of the plasma membrane reported Ds ranging from 0.1 to 1.25 $\mu m^2 s^{-1}$ for various membrane-anchored GFP fusion proteins – including the linker-for-activated T cells (LAT) protein, vesicular stomatitis virus G (VSV-G) protein, HRas and kRas proteins (Kenworthy et al., 2004) whilst the D of β2-adrenoceptor was reported at 0.13 $\mu m^2 s^{-1}$ (Kaya et al., 2011). Using an almost identical sfGFP template as the fluorescent tag and comparable FRAP methods to this study, Kilpatrick et al. reported that the Ds of neuropeptide-Y (NPY) receptors were ten-fold lower at 0.01-0.02 $\mu m^2 s^{-1}$, potentially due to aggregation of NPY receptors and may suggest a limited long-range diffusion of the NPY receptors (Kilpatrick et al., 2012), see also section 6.7.1. These studies together reported mobile fractions of 80-90 % for all the GFP fusion membrane proteins of interest. Despite the differences in FRAP methodologies (focal planes, shape and size of bleach areas; see later for experimental factors affecting FRAP) being employed, FRAP of the membrane proteins shown in this study – diffusion coefficients of 0.1-0.4 $\mu m^2 s^{-1}$ (Figure 4.12) and mobile fractions of 75-90 % (Figure 4.13), generally correlate well with the reported FRAP data thus far.

4.5.2 FRAP reveals differences in protein sizes

The diffusion coefficient of a particle in free volume is inversely related to the hydrodynamic radius of the particle, as described by the Stokes-Einstein

equation. For a soluble spherical protein, an eight-fold increase in size will result in two-fold reduction in the D (Lippincott-Schwartz et al., 2001). In this study, the differences in size between the membrane localised sfGFP (GAP-sfGFP and sfGFP-kRas) compared to sfGFP-ABCG2 were shown by the apparent differences in Ds obtained from FRAP (Figure 4.12). Also, FRAP results were consistent with ABCC4-sfGFP moving as a larger fluorescent species with a slightly lower D, compared to the ABCG2 variants. The FRAP results, which provided diffusion information of the native GFP-fusion proteins in live HEK293T cells, corresponded well with the differences in size of the denatured fusion proteins as revealed by SDS-PAGE and western blot analysis (Figure 4.5). Several inferences could be drawn from the FRAP results with regards to the native size of the protein complexes. Assuming the sfGFPs are monomers in their native form, then the two-fold reduction in the diffusion coefficients of ABCG2 could potentially suggest that ABCG2 exists as a dimer or larger complexes, with a molecular weight of at least 180 kDa. The slight reduction in the D of ABCC4 (180 kDa) compared to ABCG2, could also suggest formation of larger complexes by ABCC4. This hypothesis fits well to some of the current suggestions that ABCG2 functions as a dimer from biochemical (Bhatia et al., 2005) and fluorescence (Haider et al., 2011) studies, and that full length ABC transporters are capable of forming higher order oligomers (Boscoboinik et al., 1990; Poruchynsky and Ling, 1994). However, there are other environmental factors (see next section) that can affect the diffusion/FRAP of membrane proteins. Therefore, definitive conclusions on the oligomeric status of ABCG2 cannot be drawn.

4.5.3 Prediction of ABCG2 cellular environment

As mentioned briefly in section 4.1 earlier, it is possible to extract further information on the protein cellular environment using the changes in FRAP parameters (D and mobile fraction). This is made possible as FRAP/diffusion of membrane proteins is affected by other factors (in addition to size), e.g. the viscosity of the membrane, the presence of protein in a restricted

compartment, and interactions with other components within the cells. The common notable factors are thought to be the interactions of target protein with other components in the membrane (e.g. lipid rafts, functional complexes) and the cytoskeletal structures in the cytoplasm (Edidin et al., 1994; Lippincott-Schwartz et al., 2001; Sprague and McNally, 2005). In a study of raft-associated proteins, Kenworthy concluded that the diffusion of membrane proteins is strongly related to membrane anchoring instead of their partitioning in the raft or non-raft regions (Kenworthy et al., 2004). The lack of differences between the FRAP of the two membrane localised sfGFPs, sfGFP-kRas (non-raft) and GAP-sfGFP (raft), were therefore not surprising. Kenworthy also proposed that the transmembrane proteins (VSV-G) had much lower D compared to the acylated or prenylated proteins (Fyn, kRas), which are known to partition in the inner leaflet of the membrane (Kenworthy et al., 2004). Saxton and Jacobsen also summarised that, for multi-helical proteins with transmembrane and extracellular domains, hydrodynamic interactions and percolation effects (due to the transmembrane segments) along with the extracellular obstructions (due to glycosylation) are the key factors likely to affect the protein diffusion in the plasma membrane (Saxton and Jacobson, 1997). Hence, the lower D observed in the sfGFP-ABCG2 variants (transmembrane proteins) compared to the membrane localised sfGFPs (inner membrane partitioning) could also be due to the differences in membrane anchoring of the transmembrane domains and the slightly glycosylated nature of ABCG2, in addition to the size differences as discussed above.

It was also suggested that membrane proteins could have reduced mobility due to cytoplasmic interactions below the membrane lipid bilayer (Edidin et al., 1994). To date, the disruption of cell cytoskeleton has been shown to affect the mobility and function of various membrane proteins. Charrier et al. observed an increase in glycine receptor diffusion after cytoskeleton (actin or microtubules) disruption and this was associated with changes in the synaptic

and extrasynaptic compartment (Charrier et al., 2006). More recently two different studies from the same research group reported that actin disruption affected the function of ABCB1 (Hummel et al., 2011) whilst the function of ABCC1 was retained (Meszaros et al., 2013). However, the mobility of the ABC transporters was not investigated. The disruption of cell actin and microtubules with small molecules was demonstrated to have no effect on the FRAP (diffusion and mobile fraction) of ABCG2 in this study, suggesting that similar to ABCB1, ABCG2 does not make significant interactions with the cell cytoskeleton. As discussed in section 4.5.2, mobile fractions for most membrane proteins with unrestricted diffusion were reported to have 80-90 % mobile fractions, whereas proteins with known impeded diffusion such as the E-cadherins (Adams et al., 1998) (during cell-to-cell contact), the immobilised membrane proteins using antibodies in the studies of class-I MHC molecules (Edidin et al., 1994) and the CD28 and CD86 fusion proteins (Dorsch et al., 2009), have reported mobile fractions of less than 50-60 %. The FRAP results in Figures 4.13 and 4.17 consistently reported that the ABCG2 variants have mobile fractions of 80-90 %, suggesting that the mobility of ABCG2 is unlikely to be restricted and the diffusion of ABCG2 can be more accurately described as “complete but restricted due to anomalous diffusion” (see next section) as suggested in (Feder et al., 1996).

4.5.4 Potential experimental limitations

Anomalous diffusion has been established since the 1990s. This phenomenon is used to describe the diffusion of molecules that does not follow typical Brownian motion due to variation in the structures of complex systems (Metzler and Klafter, 2000). This type of disordered diffusion is increasingly being recognised in affecting the diffusion of membrane proteins, first reported in a single-particle study of LDL receptors (Ghosh and Webb, 1994). It is therefore suggested that anomalous diffusion can affect the parameters obtained from FRAP. The constrained diffusion model suggested by Feder et al. explains that the changes observed in FRAP diffusion coefficients as the

bleach radii changes could be attributed to anomalous diffusion, in which the measurements obtained for various bleach radii could indicate the diffusion of proteins in different compartments of the plasma membrane (Feder et al., 1996). Figure 4.10 shows that the diffusion coefficients of ABCG2 wild type and C603A reduced as a smaller bleached ROI was employed (2 µm instead of 3 µm). This noticeable change could potentially indicate anomalous diffusion behaviour of ABCG2 in the plasma membrane, which could also explain the lower diffusion coefficients reported when a smaller ROI was employed in (Kilpatrick et al., 2012). Sprague and McNally also suggested that changes in D when the bleach size changes could be attributed to the diffusion-coupled FRAP recovery, where diffusion and binding (to the various membrane components) occur throughout the recovery phase (Sprague and McNally, 2005). For a more accurate description of ABCG2 anomalous diffusion/binding behaviour, multiple modelling of the fluorescence recovery curves using diffusion-coupled (binding) and anomalous diffusion equations are required to compare against the simple diffusion model (Feder et al., 1996; Saxton, 1999; Sprague et al., 2004). These analyses were not performed, as they were not the key aims in this study. For an uncomplicated account of ABCG2 diffusion in this study, the single-component exponential equation in Zen 2010, which describes simple diffusion, was used to fit the FRAP recovery curves.

4.5.5 Conclusion

Thus far, for the first time, FRAP experiments in this study provided both quantitative and qualitative insights into the diffusion of ABCG2 in the plasma membrane of living cell. The diffusion coefficient of sfGFP-ABCG2 was determined at approximately 0.2 $\mu m^2 s^{-1}$. The larger protein complexes, sfGFP-ABCG2 and sfGFP-ABCC4, had slower diffusion compared to the much smaller membrane localised sfGFPs. These differences are likely to be resulted by the differences in sizes and membrane anchoring of the proteins. Two point mutations (C603A and T362A), which were suggested to affect the

oligomerisation of ABCG2 in different manners – disulphide bridge formation in ABCG2 dimers (C603A) and phosphorylation of ABCG2 by kinases (T362A), were found to be inconsequential to the diffusion of ABCG2. Disruption of the cell cytoskeleton (actin and microtubules), by the addition of cytochalasin D and nocodazole, also did not affect the diffusion and the mobility of ABCG2. The high mobile fractions (> 80 %) obtained throughout the FRAP experiments indicated that the diffusion of ABCG2 can be most accurately described as unimpeded and complete, but restricted by the presence of anomalous diffusion. Whilst no definite suggestion of the oligomer state of ABCG2 can be drawn from the diffusion coefficients, results have provided a good understanding of membrane diffusion of ABCG2 and a platform for further experiments using fluorescent protein tagged ABCG2.

Chapter 5 Oligomerisation of ABCG2 in live cells demonstrated by fluorescence resonance energy transfer (FRET) microscopy

In the previous chapter, the membrane diffusion of ABCG2 was determined using FRAP microscopy, but it provides only indirect indication of ABCG2 oligomerisation through the limited influence of protein complex size differences on membrane mobility. In contrast, fluorescence resonance energy transfer (FRET) microscopy detects and measures intermolecular protein interactions and offers a more direct opportunity to study protein oligomerisation. Therefore, it was employed to investigate the oligomerisation of ABCG2. In this chapter, an introduction to FRET principles will first be presented. This is followed by the characterisation of constructs generated for the FRET experiments. The optimisation of FRET experiments and spectral imaging analysis method employed will also be explained. Finally, a full account of the results from FRET experiments conducted will be discussed in detail.

5.1 Background and theory – fluorescence resonance energy transfer microscopy

FRET is a phenomenon of energy transfer from one fluorophore (the donor) to another (the acceptor) under certain circumstances. In combination with fluorescence microscopy, this technique is now commonly employed to study protein-protein interaction. This opportunity was first described in the 1970s, and it remains one of the key milestones achieved in fluorescence microscopy (Fernandez and Berlin, 1976). Stryer provided a comprehensive description on this fluorescence energy transfer phenomenon based on the Förster theory (Förster, 2012; Stryer, 1978). It was summarised by Stryer that this energy transfer depends primarily on the distance and orientation between the

acceptor and donor. Using this technique, the close proximity (< 100 Å or 10 nm) between two biological macromolecules could be revealed. The most challenging factor during the early years was the search for suitable donors and acceptors (Stryer, 1978). Through recent advances in confocal microscopy and fluorescent protein engineering (as discussed in section 1.7), FRET microscopy has now become a powerful technique for the investigation of inter- or intra- molecular protein interactions in live cells (Piston and Kremers, 2007). This is primarily due to the finding of the first effective FRET donor and acceptor pair, in which the cyan fluorescent protein (donor) and yellow fluorescent protein (acceptor) were successfully employed to determine the increased interaction between calmodulin and calmodulin binding peptide M13 during calcium binding (Miyawaki et al., 1997). To date, FRET microscopy has been employed in various applications for investigating protein-protein interaction in live cells, e.g. oligomer formation in GPCRs (Busnelli et al., 2013; Patowary et al., 2013), dimerisation of receptor protein-tyrosine phosphatases (Tertoolen et al., 2001), and heteromeric interactions between different ABC transporters (ABCD1 and ABCD3) (Hillebrand et al., 2007) and growth factor receptors (FGF-receptor 1 and PDGF-receptor-α) (Faraone et al., 2006)

As briefly mentioned above, FRET is a distance dependent energy transfer process from an excited fluorophore (the donor) to another fluorophore (the acceptor). Three basic factors have been identified for FRET to occur (Clegg, 1995; Stryer, 1978):

1. Overlap between the donor emission and acceptor excitation spectra (Figure 5.1)
2. Close proximity (< 100 Å) between the donor and acceptor
3. Favourable orientation of the transition dipole moment (direction of electrical charges) between the initial and final states of donor and acceptor (not perpendicular to each other)

Combination of these three factors will result in the excitation of the acceptor by the donor emission, which indicates close range interactions between the two fluorophores, or the proteins they are attached to.

In this study, CFP (cerulean fluorescent protein) and YFP (enhanced yellow fluorescent protein) were employed as the donor and acceptor fluorophores. Figure 5.1 shows the schematic representation of excitation and emission spectra of CFP and YFP and highlights the overlapping area between the emission spectrum of CFP and excitation spectrum of YFP (spectral overlap), a prerequisite for FRET to occur.

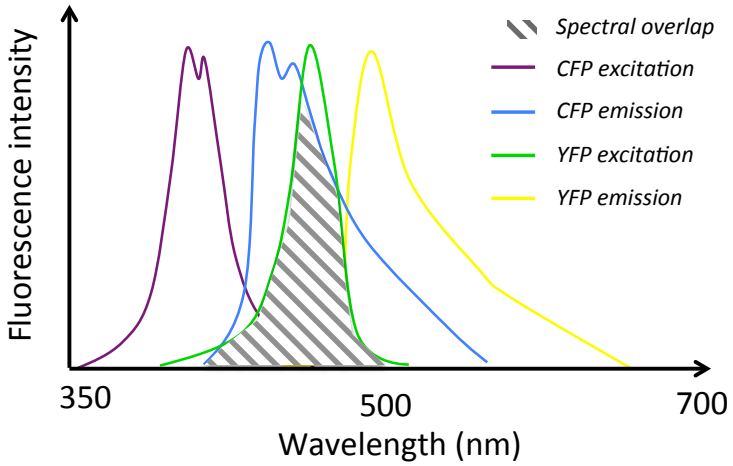

Figure 5.1: Schematic representation of emission and excitation spectra of cerulean and yellow fluorescent proteins (CFP and YFP). "Spectral overlap" highlights the overlapping area of CFP emission and YFP excitation spectra, one of the key requirements for FRET to occur.

For the detection of protein signalling complexes and changes in protein interactions in living cells, various methods have been developed to measure FRET efficiencies (Jares-Erijman and Jovin, 2003). Typically, these techniques exploit measurement of the consequences of FRET, in which the donor (CFP) has quenched emission and the acceptor (YFP) has increased emission, as schematically represented in Figure 5.2A. Experimentally, the key challenge is often to define the extent of this FRET signal using comparison with appropriate baseline controls. Two common techniques that have been

routinely proposed for measuring FRET signals are the sensitised emission method and the acceptor photobleaching (AcPb) method. In sensitised emission, the donor is excited by a specific wavelength of light and the resulting acceptor emission is determined as the FRET efficiency. This method requires extensive correction and careful controls as it is restricted by bleed-through limitations (i.e. undesired detection of donor emission due to overlapping between emission spectra of donor and acceptor, see section 5.3; (van Rheenen et al., 2004)). Piston and Kremers have even suggested that this technique is inappropriate if the FRET signal is small and may only be advantageous in biosensor experiments in which a large change in FRET signal is expected (Piston and Kremers, 2007).

Acceptor photobleaching (AcPb) FRET was first employed in a cofocal laser scanning microscope system in the early 2000s (Karpova et al., 2003). As illustrated in Figure 5.2B, AcPb FRET measures the increased emission of the donor (CFP) immediately after the photobleaching of the acceptor (YFP). In this study AcPb FRET was the method of choice for measuring the FRET signal. The FRET efficiency can be obtained by calculating the differences in CFP intensities before and after YFP photobleaching. This is advantageous because under most circumstances, fluorescence intensities should reduce upon photobleaching, therefore the increase in CFP emission is most likely to have resulted from FRET. Additionally, this technique also minimises the bleed-through limitations as discussed above as YFP intensity is ablated (see section 5.3). However, as photobleaching is irreversible, repeated AcPb FRET measurements on the same sample are not possible.

As a half transporter, ABCG2 was suggested to exist and function as oligomers and this was demonstrated in various biochemical and fluorescence studies (see section 1.6). However, the biochemical studies thus far were restricted to investigating the ABCG2 protein outside its cellular environment and the only live cell approach to study the dimerisation of ABCG2 was limited by the

irreversible formation of the bimolecular fluorescence complementation (BiFC) complexes (Haider et al., 2011). Additionally, ABCG2 oligomerisation could not be clearly predicted based on the FRAP diffusion results in chapter 4. In contrast, this chapter presents successful demonstration of ABCG2 oligomerisation in live cells using AcPb FRET microscopy.

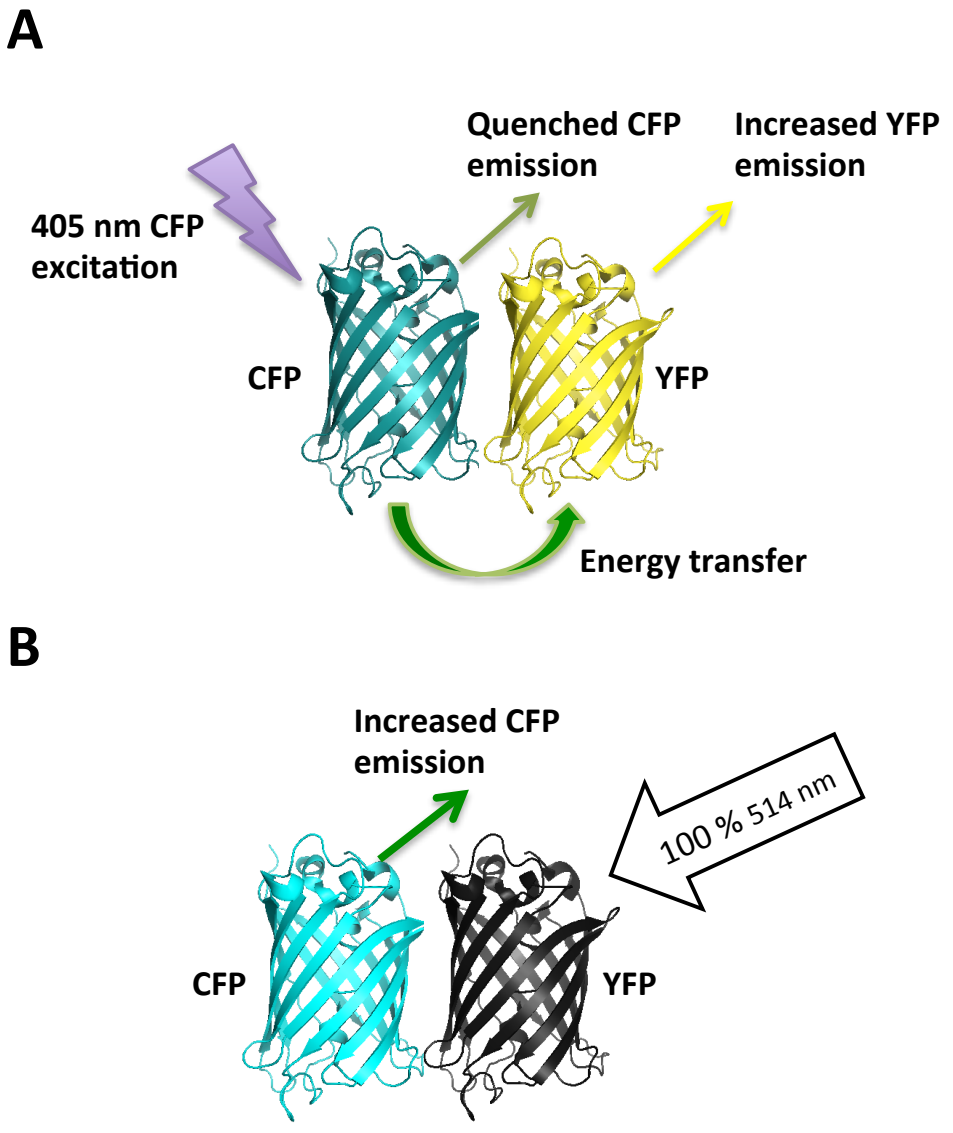

Figure 5.2: Schematic representation of acceptor photobleaching (AcPb) FRET employed to measure FRET efficiency in this study. A – When the donor (CFP) is excited, energy is transferred to the acceptor (YFP), resulting in quenched emission of the donor and excitation of the acceptor. **B –** In AcPb FRET, YFP is photobleached with high power (100%) 514 nm laser excitation and the subsequent increase in CFP emission allows FRET efficiency to be determined.

5.2 FRET construct characterisation

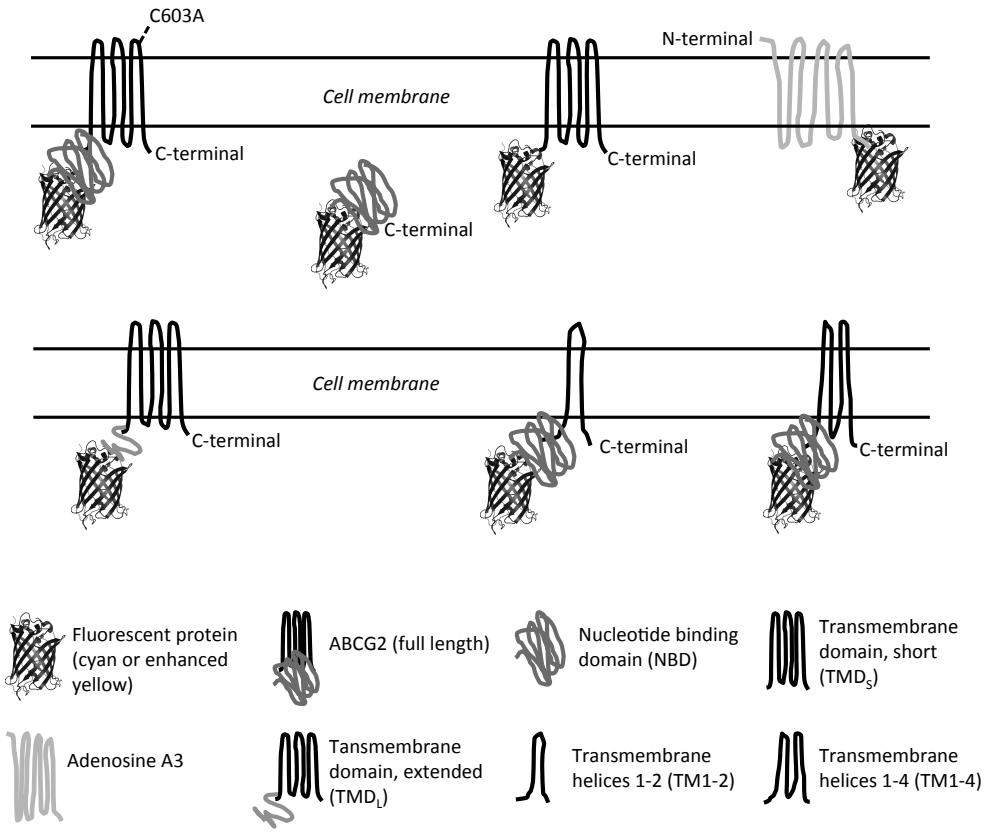

Figure 5.3: Schematic representation of DNA constructs generated for the investigation of oligomerisation of ABCG2 using FRET microscopy. Upper panel (left to right): Full length ABCG2 tagged with fluorescent proteins (including CFP-ABCG2, YFP-ABCG2, CFP-ABCG2_C603A, and YFP-ABCG2_C603A), YFP-NBD (nucleotide binding domain), YFP-TMD_S (shorter version of transmembrane domain), and adenosine A3-YFP. Lower panel (left to right): YFP-TMD_L (extended version of transmembrane domain), YFP-TM1-2 (NBD and transmembrane helices 1-2), and YFP-TM1-4 (NBD and transmembrane helices 1-4).

For the study of oligomerisation of ABCG2 using AcPb FRET microscopy, various CFP- and YFP-tagged constructs were generated (as schematically represented in Figure 5.3). Briefly, CFP or YFP were fused to ABCG2 wild type, or the ABCG2 mutant C603A, residue responsible for disulphide bond formation between ABCG2 molecules (Henriksen et al., 2005b). A vector containing the adenosine A3 receptor fused C-terminally with YFP was kindly provided by Dr Steve J. Briddon, University of Nottingham. This construct was used as a control to measure non-specific FRET between ABCG2 and a different membrane protein. Additionally, Figure 5.3 shows various truncated

ABCG2 constructs fused to YFP (N-terminally) generated to identify the roles of different ABCG2 domains in oligomerisation. These include YFP-NBD (nucleotide-binding domain only), YFP-TMD_S (short version of transmembrane domain), YFP-TMD_L (extended version of transmembrane domain), YFP-TM1-2 (truncated ABCG2 containing the NBD and transmembrane helices 1-2), and YFP-TM1-4 (truncated ABCG2 containing the NBD and transmembrane helices 1-4).

5.2.1 Construct localisation and expression

The localisation and expression of the constructs shown in Figure 5.3 were first confirmed using confocal imaging and SDS-PAGE western blot analysis of transiently transfected HEK293T cells. Figure 5.4 shows that CFP-ABCG2 and YFP-ABCG2 were each localised to the plasma membrane, as well as intracellular compartments, and no notable differences were observed in the co-transfected cells (CFP-ABCG2 + YFP-ABCG2). Cytoplasmic CFP was expressed and localised intracellularly when co-transfected with YFP-ABCG2 (cytoplasmic CFP + YFP-ABCG2, Figure 5.4). Adenosine A3-YFP was also localised to the plasma membrane as expected. When co-transfected with CFP-ABCG2, both constructs were localised at the plasma membrane (CFP-ABCG2 + Adenosine A3-YFP, Figure 5.4).

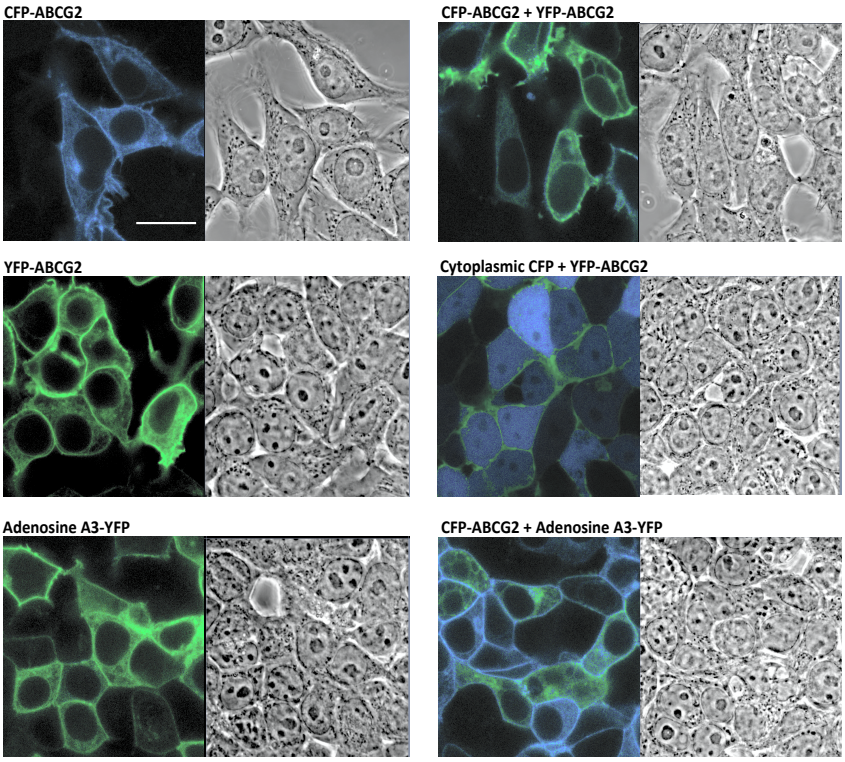

Figure 5.4: Confocal images and the corresponding phase contrast images for the various fluorescent proteins expressed in single or co-transfected HEK293T cells. Cells seeded on MatTek dishes were first transfected with 2 µg of the respective constructs as indicated in the figure. High resolution images (1024 x 1024 pixels, 8 averages) were acquired 18-24 hours post-transfection. Emission lambda scans (417-730 nm) were collected using 405 nm (2 %) and 514 nm (4 %) for CFP and YFP excitation respectively. Blue represents the CFP emission channels and green represents YFP emission channels. Scale bar = 20 µm. Representative images of at least 3 independent experiments were shown.

Figure 5.5 shows confocal images of HEK293T cells transiently co-expressing the two C603A mutants of ABCG2 (YFP- and CFP-tagged), and the various YFP-tagged truncated versions of ABCG2, with CFP-ABCG2. As expected, CFP-ABCG2_C603A and YFP-ABCG2_C603A were localised predominantly at the plasma membrane and YFP-NBD was localised intracellularly. However, both the extended (YFP-TMD_L) and shorter (YFP-TMD_S) versions of TMD were not able to reach the plasma membrane when co-expressed with CFP-ABCG2. Figure 5.5 shows that the constructs containing NBD with transmembrane helices 1-2 (YFP-TM1-2) and transmembrane helices 1-4 (YFP-TM1-4) were also retained intracellularly. The intracellular localisation pattern of YFP-TMD_S, YFP-TMD_L and YFP-TM1-4 was consistent with retention in the

endoplasmic reticulum whilst YFP-TM1-2 showed more diffusive localisation within the cytoplasm, similar to those of YFP-NBD. Similar localisation patterns were observed for the YFP-truncated ABCG2 constructs in the absence of CFP-ABCG2 co-transfection (Figure S5.1 in Appendix).

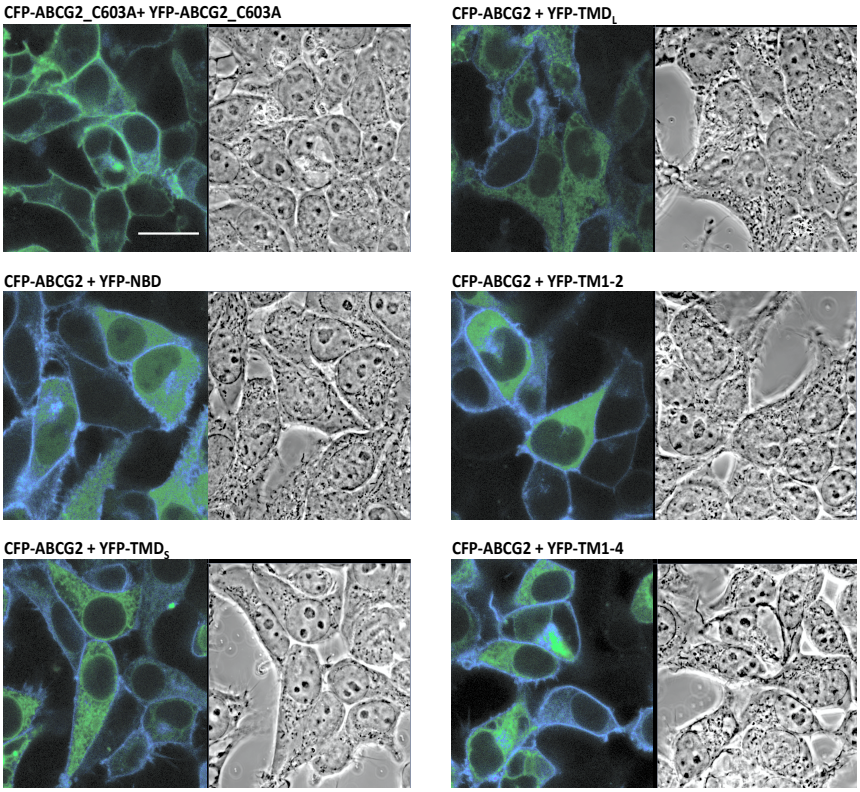

Figure 5.5: Confocal images and the corresponding phase contrast images for various fluorescent proteins transiently co-expressed in HEK293T cells. Cells seeded on MatTek dishes were first transfected with 2 µg of the respective constructs as indicated in the figure. High resolution images (1024 x 1024 pixels, 8 averages) were acquired 18-24 hours post-transfection. Emission lambda scans (417-730 nm) were collected using 405 nm (2 %) and 514 nm (4 %) for CFP and YFP excitation respectively. Blue represents the CFP emission channels and green represents YFP emission channels. Scale bar = 20 µm. Representative images of at least 3 independent experiments were shown.

The expression of these constructs was confirmed using SDS-PAGE and western blot analysis under reducing conditions. Figure 5.6 (left panel) shows that CFP-ABCG2, YFP-ABCG2, CFP-ABCG2_C603A, and YFP-ABCG2_C603A migrated at approximately 90 kDa as expected, similar to the molecular weights of sfGFP-ABCG2 and the C603A mutant reported in chapter 4. Multiple bands were also observed for these samples, again supporting varying degrees of glycosylation. The adenosine A3-YFP was not as effectively

solubilised using the loading conditions and migrated as large aggregates. However, its expression was still detected in Figure 5.6 and was also confirmed by the confocal images in Figure 5.4.

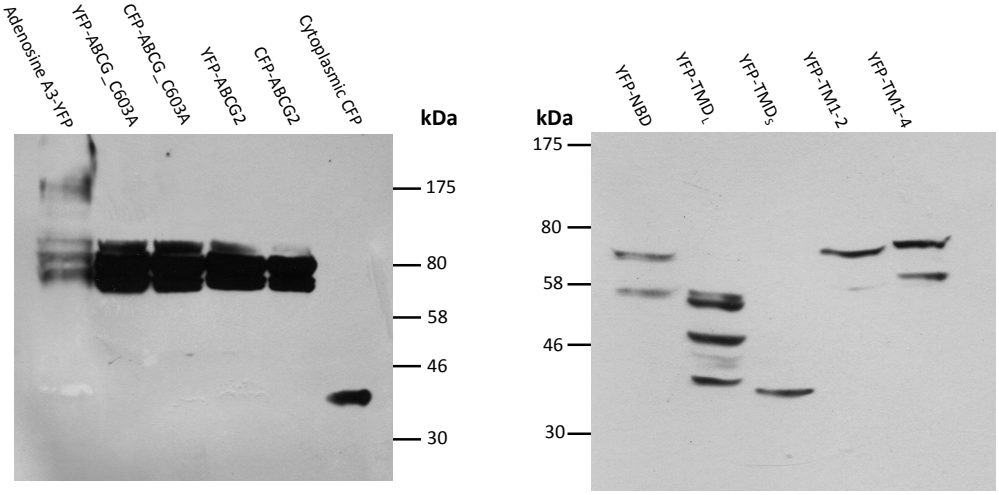

Figure 5.6: Western blot analysis of the DNA constructs employed in this FRET study. Approximately 20 µg of cell lysates were loaded onto each lane in the SDS-PAGE gels (with the exception of cytoplasmic CFP, loaded with 4-5 µg). Proteins were transferred onto nitrocellulose membrane and probed using primary monoclonal anti-GFP mouse IgGκ antibody and secondary polyclonal rabbit anti-mouse IgG antibody conjugated with horseradish peroxidase, prior to chemiluminescence detection. Representative western blot of 3 independent experiments was shown.

Additionally, Figure 5.6 (right panel) shows the expression of the YFP-tagged truncated ABCG2 proteins. As expected, YFP-TM1-4 migrated at the highest molecular weight, approximately 78 kDa (predicted to be 87 kDa using Compute pI/MW tool (Wilkins et al., 1999)), closely followed by YFP-TM-1-2 and YFP-NBD at approximately 75 kDa and 70 kDa (predicted be 80 kDa and 71 kDa). The extended YFP-TMD_L (predicted to be 70 kDa) migrated with multiple bands at molecular weights of approximately 55, 47, 43 kDa, larger than the shorter YFP-TMD_S, approximately 40 kDa (predicted to be 60 kDa). The expression of these truncated constructs will be discussed alongside the roles of ABCG2 domains in oligomerisation later in this chapter.

5.2.2 Function of CFP- and YFP-ABCG2

An adapted MX accumulation assay (compared to chapter 4) was employed to verify the function of the CFP- and YFP- tagged ABCG2, specifically in transiently expressing cells. Using a fluorescence imaging platereader (IX Micro) combined with a cell scoring algorithm, this assay allows the accumulation of MX (ABCG2 substrate) to be measured selectively in cells only expressing YFP-ABCG2 or CFP-ABCG2. The accumulation of MX (4 μM) was measured in the presence and absence of Ko143 (ABCG2 inhibitor), to confirm the function of CFP-ABCG2 and YFP-ABCG2. Figures 5.7 and S5.2 (Appendix) show the fluorescence images acquired for CFP-ABCG2 and YFP-ABCG2 expressing HEK293T cells in 96 well plates, respectively. Figure 5.7A (with the enlarged overlay in 5.7B) shows that the increase in MX accumulation (Cy5 channel) was notable in cells expressing CFP-ABCG2 (FITC channel) in the presence of Ko143 inhibitor from 0 to 60 min. The same was also observed in the cells expressing YFP-ABCG2 (Figure S5.2A in Appendix).

The average MX intracellular intensities in cells expressing CFP-ABCG2 or YFP-ABCG2 were subsequently obtained by subjecting the three channel fluorescence images to the multiwavelength cell scoring algorithm as described in detail in section 2.4.2. Briefly this algorithm in MetaXpress calculated the average intensities of both the ABCG2 fluorescent fusion protein and MX associated with individual cells. Subsequently the cell data were filtered using a threshold for YFP or CFP intensity using AcuityXpress to isolate the average intensity for MX in transfected cells only. Each set of data was normalised using the highest intensity as 100 % and lowest intensity as 0 % (in the whole data set), enabling multiple data sets to be pooled together for each cell line and the resultant accumulation curves of CFP-ABCG2 (Figure 5.8A) and YFP-ABCG2 (Figure 5.8B) in the presence and absence of Ko143 are shown in Figure 5.8. Two-way ANOVA analysis indicated significant increases ($p < 0.05$) in the % accumulation of MX in the presence of Ko143 after 20 min in CFP-ABCG2 expressing cells and after 30 min in YFP-ABCG2 expressing cells,

compared to MX alone – demonstrating that each fluorescent protein tagged ABCG2 construct was functional.

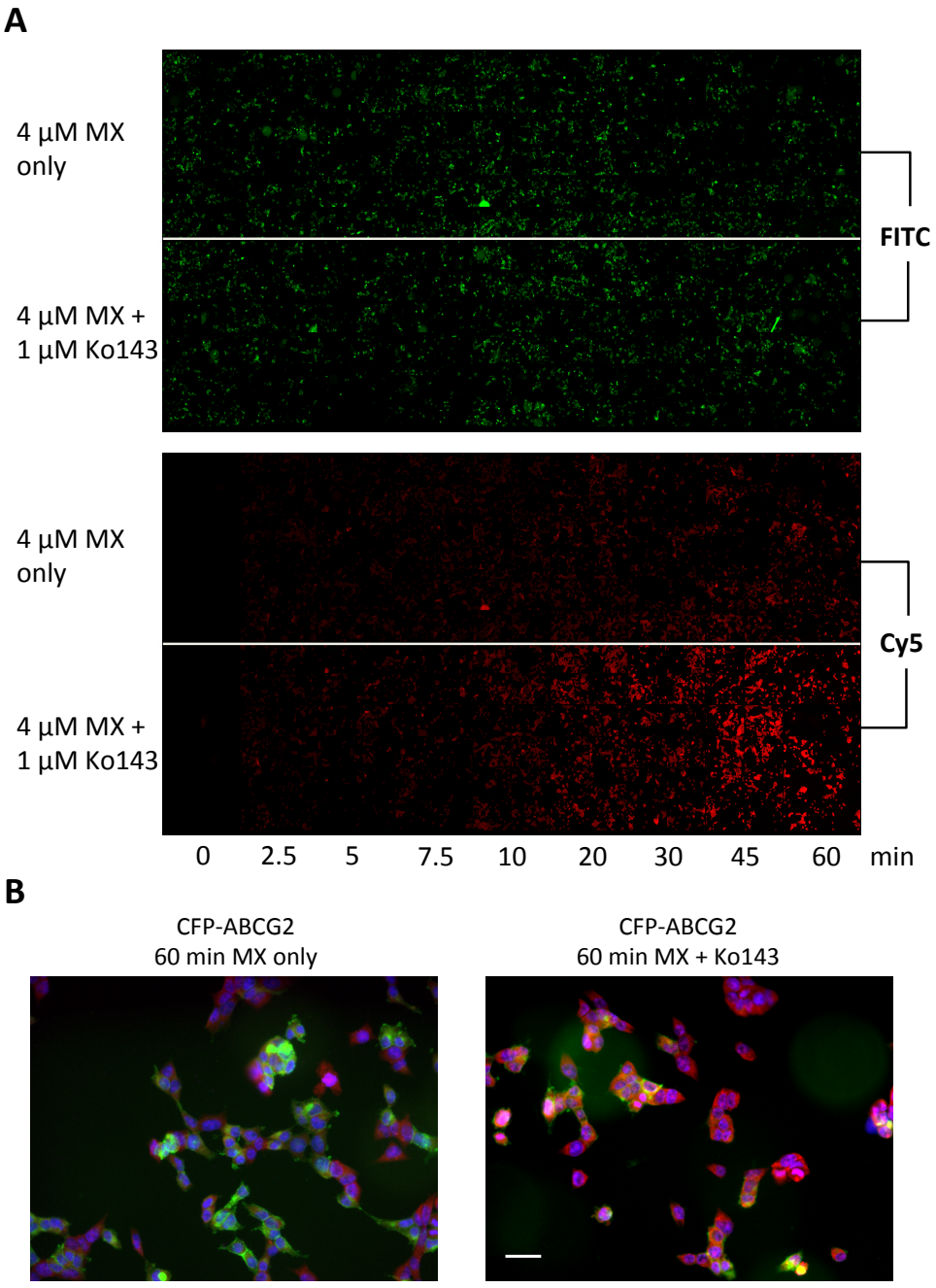

Figure 5.7: Fluorescence images acquired during the accumulation assay in HEK293T cells transiently expressing CFP-ABCG2. A – Fluorescence images of CFP-ABCG2 expressing cells (FITC channel, green, top) and the corresponding mitoxantrone (MX) accumulation (Cy5 channel, red, bottom) in a 96-well plate incubated with either 4 µM MX only or 4 µM MX + 1 µM Ko143, from 0 to 60 min at 37 °C. Images were acquired from 6 x 9 wells (4 sites each well). Nucleus staining was not indicated in this panel. **B –** Overlay images showing the nucleus stain (DAPI channel, blue), CFP-ABCG2 (FITC channel, green), and MX (Cy5 channel, red) acquired at 60 min incubation with either MX only (right) or MX + Ko143 (left). Scale bar = 20 µm.

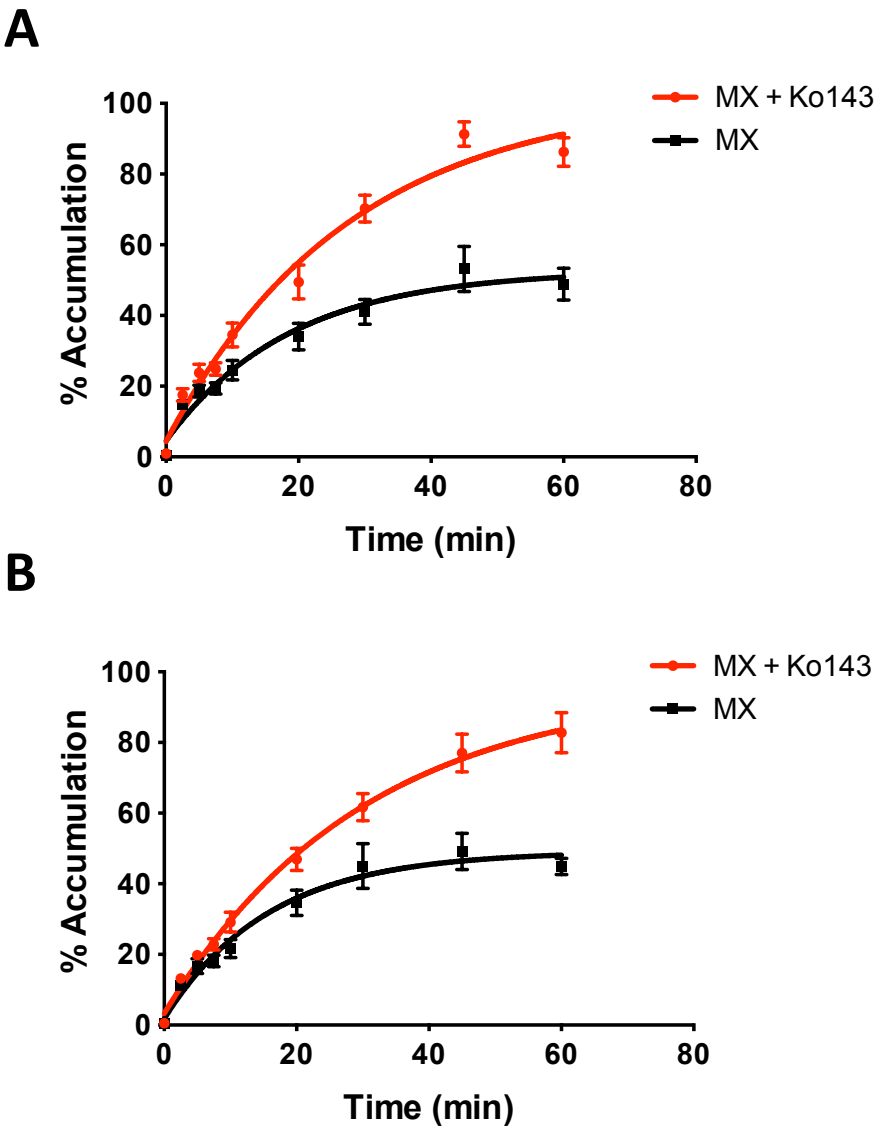

Figure 5.8: CFP-ABCG2 and YFP-ABCG2 are functional mitoxantrone (MX) exporters when expressed transiently in HEK293T cells. Normalised % MX accumulation in CFP-ABCG2 (**A**) and YFP-ABCG2 (**B**) expressing cells in the presence and absence of Ko143 at various time points. 4 µM MX and 1 µM Ko143 were used for the experiments. Data were pooled from 3 independent experiments (at least 20,000 cells were analysed) for each cell line, and presented as the mean ± SEM % accumulation. Images acquired using IX Micro platereader, shown in Figures 5.7 and S5.2, were subjected to multiwavelength cell scoring analysis and cell selection based on fluorescent protein intensity to obtain the average MX intensities in cells only expressing CFP-ABCG2 or YFP-ABCG2 (section 2.4.2). Two-way ANOVA analysis (Bonferroni post test) indicated significant increases ($p < 0.05$) in % MX accumulation upon addition of Ko143 after 20 min for CFP-ABCG2 data, and after 30 min for YFP-ABCG2 data. Data were fitted using one-phase association curve in GraphPad Prism 6.0. Half times of the accumulation curves were reported at 19 (MX + Ko143) and 13 min (MX), and 21 min (MX + Ko143) and 11 min (MX), for CFP-ABCG2 and YFP-ABCG2 respectively.

5.3 FRET acquisitiond data analysis

As briefly mentioned earlier, the key experimental limitations in FRET experiments arise because of inadequate control of acceptor and donor signal bleed-throughs. In this section, we discuss how the FRET acquisition and data analysis methods manage these limitations. First, the acceptor signal bleed-through area (Figure 5.9) indicates a small wavelength range where 458 nm laser based excitation of CFP could potentially also lead to unwanted excitation of YFP. To resolve this, the 405 nm laser was employed for CFP excitation. This should result in reduced YFP excitation, compared to the 458 nm laser, which is typical for CFP excitation elsewhere (Karpova et al., 2003). Additionally, AcPb FRET was employed in this study, and so only the intensity of the donor (CFP) was taken into account. Hence, the potential excitation of YFP by the 405nm laser should have minimal effect on the calculation of FRET efficiency.

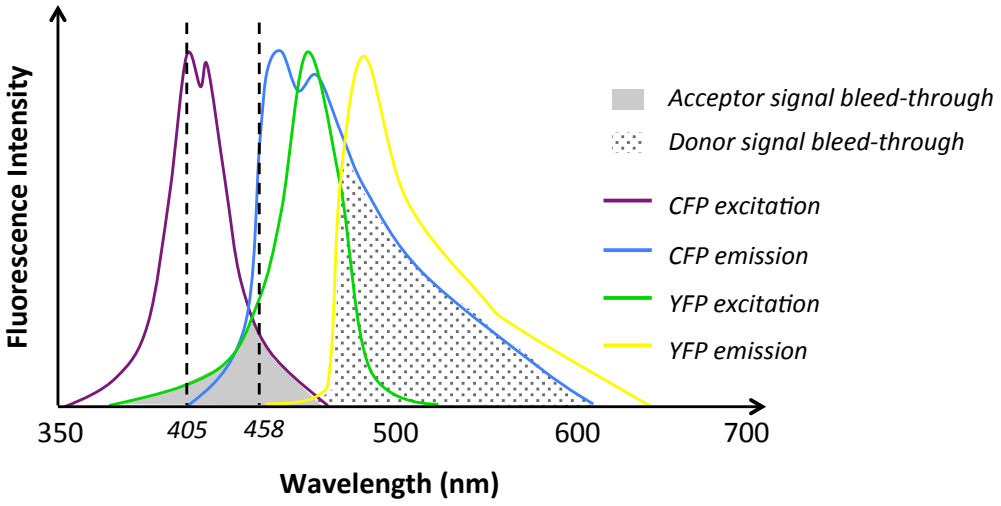

Figure 5.9: Limitations of FRET due to signal bleed-throughs caused by the overlapping of CFP and YFP excitation and emission spectra. Acceptor signal bleed-through highlights the overlapping area of CFP and YFP excitation spectra, where the laser excitation for CFP could lead to direct YFP excitation. Donor signal bleed-through highlights the overlapping area of CFP and YFP emission spectra, where acceptor emission could be detected along with CFP emission detection, and vice versa.

Another limitation highlighted in Figure 5.9 is the donor signal bleed-through caused by overlapping of the emission spectra of CFP and YFP, resulting in potential overestimation of CFP emission in AcPb FRET studies if left uncorrected. In this study, a spectral imaging method (Zimmermann et al., 2002) was employed to resolve this limitation using a linear unmixing algorithm, as described in Figure 5.10. Figure 5.10A first shows the mixed intensity plot, which represents a combination of fluorescence emission from both CFP-ABCG2 and YFP-ABCG2 in the region of interest (ROI, red). To fully account for the intensity of CFP-ABCG2, this mixed intensity plot in Figure 5.10A had to be resolved. The reference emission spectra of CFP-ABCG2 and YFP-ABCG2 (Figure 5.10B) were previously collected under identical conditions in single transfected cells. Using these reference spectra and the linear unmixing algorithm in Zen 2010, the CFP and YFP intensities in the mixed intensity plot of Figure 5.10A can be resolved as shown in Figure 5.10C. The total intensity discarded during the unmixing process by the algorithm was represented in the residual channel. Finally, the FRET efficiency, F_E, was determined as % increase in CFP intensities before and after YFP photobleaching.

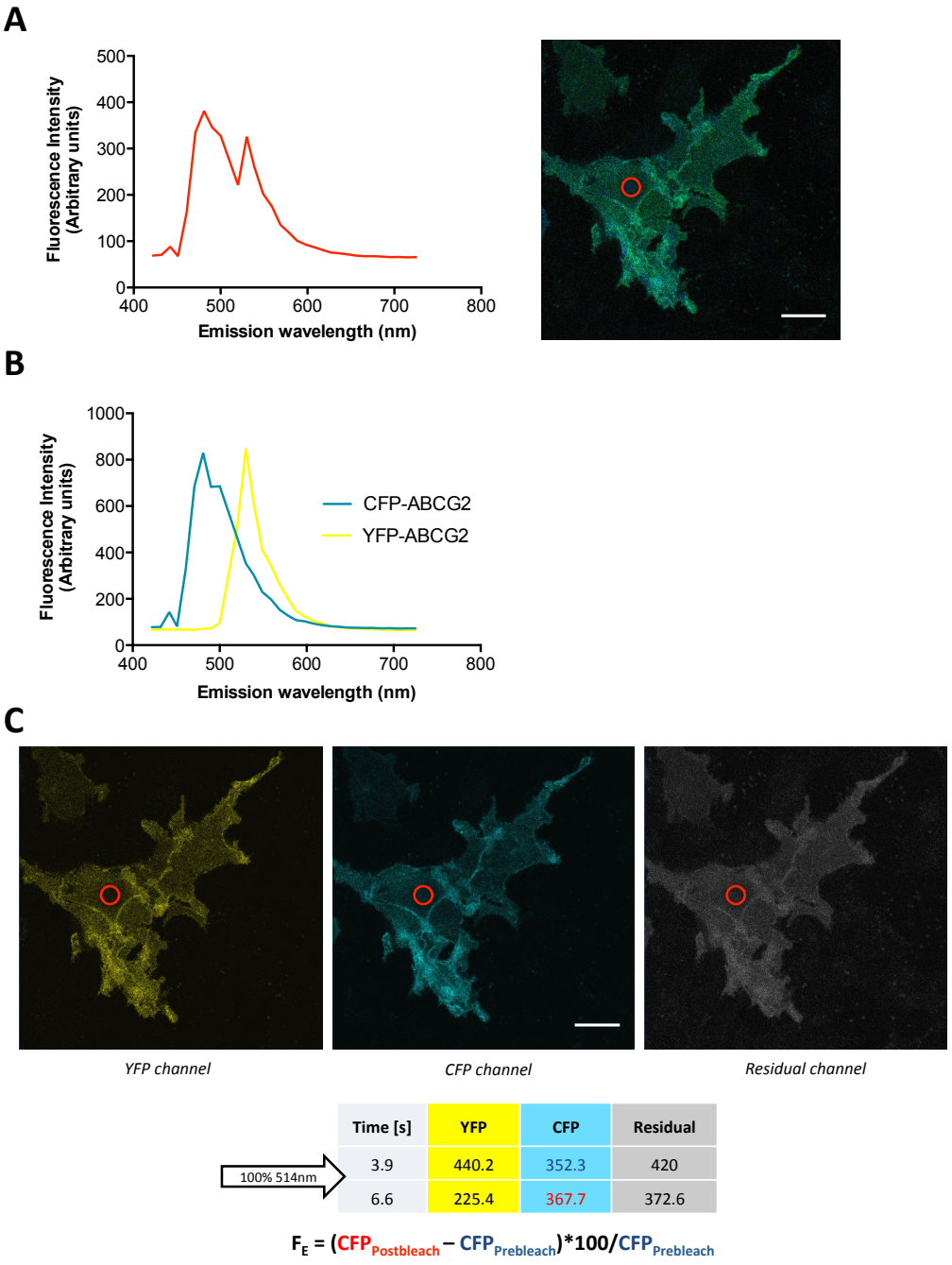

Figure 5.10: FRET spectral unmixing data analysis. A – Left panel: Mixed intensity plot of the ROI (region of interest) across the lambda emission scan (417-730 nm) collected immediately after YFP photobleaching, representing a combination of fluorescence emission from CFP and YFP. Right panel: ROI is represented as a red circle in the corresponding confocal image of cells expressing CFP-ABCG2 + YFP-ABCG2. **B –** Reference emission spectra of CFP-ABCG2 and YFP-ABCG2 collected separately from single transfected cells under identical conditions. **C –** Resolved CFP and YFP images and intensities from the same data set in panel A, using the linear unmixing algorithm in Zen 2010 and the reference spectra in B. The total intensity discarded during the separation process was represented in the residual channel. FRET efficiency (F_E) was finally calculated using the equation shown in the figure. Scale bar = 20 µm.

5.4 FRET method optimisation

5.4.1 Effects of using different lambda scan bandwidths

The emission lambda scans displayed in Figures 5.10A and 5.10B above are critical determinants of the linear unmixing algorithm. Optimisation of this acquisition step involved collecting the lambda scans at different bandwidths, as schematically represented in Figure 5.11A. Collecting the lambda spectrum at every 10 nm will occupy all the channels within the photomultiplier tube detector and could potentially lead to increased noise being generated (Zimmermann et al., 2003), potentially resulting in an increase in residuals. Although collecting the lambda spectrum at every 20 nm could generate less noise, it may in turn lead to a reduction in accuracy in the linear unmixing process. Figure 5.11B shows the resolved images (CFP, YFP, and residual) of two different data sets with emission spectra collected at every 10 and 20 nm. No visible difference in the residuals was observed.

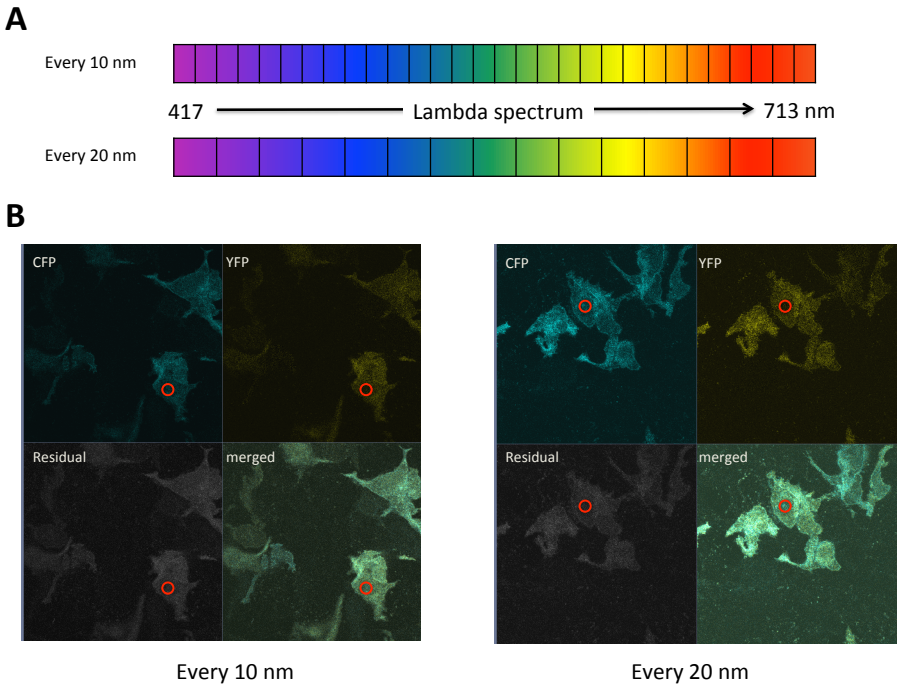

Figure 5.11: Differences between collecting the emission spectra at every 10 or 20 nm. A – Schematic representation of emission lambda spectra collected at every 10 and 20 nm**. B –** Resolved images (from linear unmixing; CFP, YFP, residual, and merged) from data sets (CFP-ABCG2 + YFP-ABCG2 expressing cells) with lambda spectra collected at every 10 and 20 nm. Red circle: region of interest (ROI).

Figure 5.12 shows the subsequent FRET efficiency obtained in cells expressing the different fluorescent fusion proteins obtained with lambda spectra collected at every 10 or 20 nm. Controls were investigated along with CFP-ABCG2 + YFP-ABCG2 expressing cells to optimise for "pseudo-FRET" and non-specific FRET in the plasma membrane (see section 5.5.1 later). No significant difference in FRET efficiency was observed between the two acquisition settings and subsequent emission lambda spectra were collected at every 10 nm prior to the linear unmixing process.

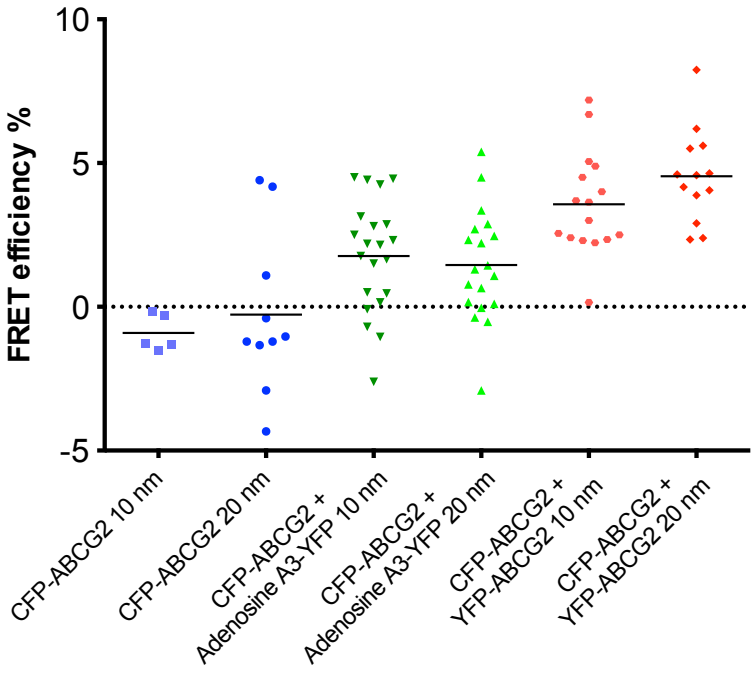

Figure 5.12: Comparing the differences in FRET efficiency % when the lambda emission spectra were collected at every 10 nm or every 20 nm. Data were collected from HEK293T cells transiently expressing CFP-ABCG2 alone, CFP-ABCG2 + Adenosine A3-YFP, and CFP-ABCG2 + YFP-ABCG2 in a single experiment. Lambda emission spectra were collected with 10 nm or 20 nm bandwidth as indicated. No significant difference was noted when comparing the two different acquisition settings. Statistical significance was assessed using one-way ANOVA analysis followed by Bonferroni multiple comparisons test.

5.4.2 Effects of YFP excitation on FRET efficiency

Another parameter optimised in this study was the presence or absence of YFP excitation during FRET acquisition. A spectral imaging acceptor photobleaching FRET method published recently (Broussard et al., 2013) suggests that YFP should not be excited during FRET acquisition. However,

direct YFP excitation would aid confirmation of YFP photobleaching during data acquisition. Hence, effects of presence or absence of YFP excitation on FRET efficiency was determined. For reliable comparison, parallel FRET experiments were conducted in cells expressing the same fluorescent proteins as Figure 5.12 above. Data were collected in the presence or absence of YFP excitation (using 2 % or 0.2 % 514 nm laser) and the resultant FRET efficiencies were shown in Figure 5.13. In the absence of YFP excitation, CFP-ABCG2 + YFP-ABCG2 and CFP-ABCG2 + Adenosine A3-YFP produced marginally lower FRET efficiencies when compared to the data sets obtained in the presence of YFP excitation. Overall, no obvious difference was observed using the two different acquisition settings and the subsequent FRET experiments were conducted in the presence of YFP excitation to ensure photobleaching of YFP during the FRET experiments.

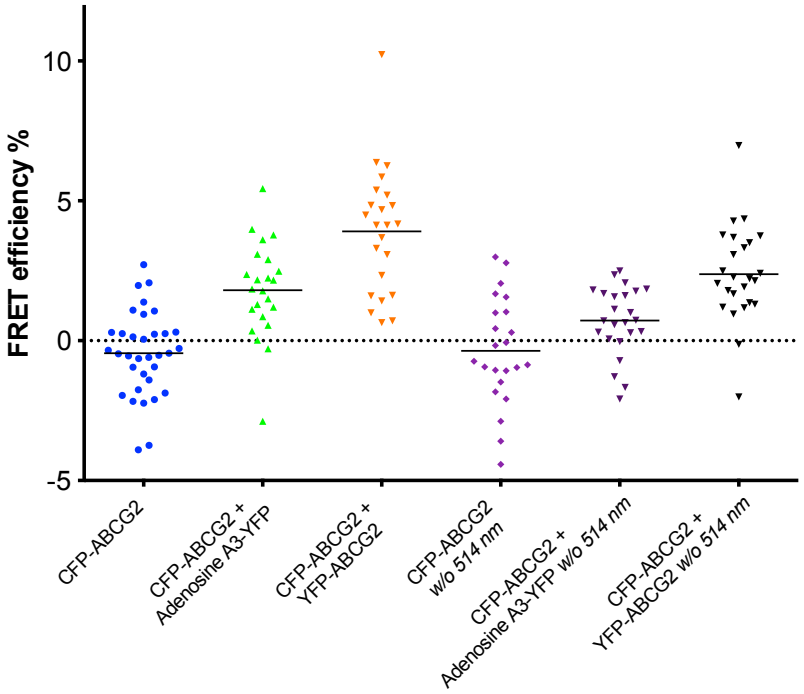

Figure 5.13: Effects of YFP excitation during data acquisition on the FRET efficiencies. FRET efficiencies (% mean) of CFP-ABCG2, CFP-ABCG2 + Adenosine A3-YFP, CFP-ABCG2 + YFP-ABCG2 obtained from data collected in the presence (2 % 514 nm) or absence (0.2 % 514 nm) of YFP excitation (parallel data sets). Data collected with 0.2 % 514 nm laser are indicated with *"w/o 514 nm"*. A minimum of 20 cells was examined from two independent experiments for each data set.

5.5 Oligomerisation of ABCG2 in live cells demonstrated by FRET microscopy

To establish the oligomerisation of ABCG2, the FRET efficiency of CFP-ABCG2 + YFP-ABCG2 was compared against three controls – CFP-ABCG2 alone, cytoplasmic CFP + YFP-ABCG2, and CFP-ABCG2 + Adenosine A3-YFP, when expressed in live HEK293T cells. Figure 5.14 below shows that CFP-ABCG2 alone produced no FRET efficiency (0.2 ± 0.2 %), whereas the other controls, cytoplasmic CFP + YFP-ABCG2 and CFP-ABCG2 + Adenosine A3-YFP yielded little FRET efficiency – 1.3 ± 0.2 % and 2.1 ± 0.3 % respectively. In contrast, CFP-ABCG2 + YFP-ABCG2 produced FRET efficiency of 4.6 ± 0.3 %, which is significantly higher ($p < 0.05$) compared to the three different controls, implying close interactions of ABCG2 molecules and potential ABCG2 oligomerisation in live cells.

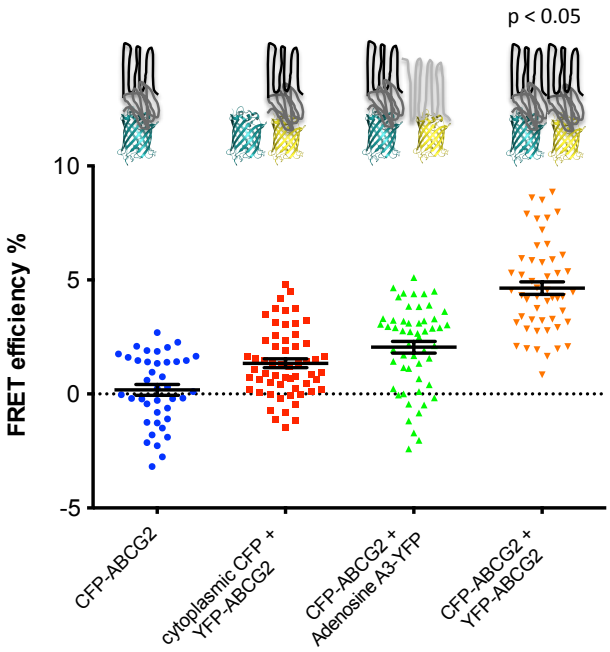

Figure 5.14: Increased FRET efficiency demonstrates oligomerisation of ABCG2. FRET efficiency (% mean ± SEM) of controls CFP-ABCG2 alone, cytoplasmic CFP + YFP-ABCG2, and CFP-ABCG2 + Adenosine A3-YFP, compared to CFP-ABCG2 + YFP-ABCG2. Schematics of the respective FRET pairs are shown in the figure. Data were acquired with 4 % 405 nm laser and 2 % 514 nm laser for CFP and YFP excitation respectively. A minimum of 40 cells was examined in four independent experiments for each data set. Significantly higher FRET in CFP-ABCG2 + YFP-ABCG2 ($p < 0.05$) compared to the controls was observed, determined using one-way ANOVA analysis followed by Bonferroni multiple comparisons test.

5.5.1 Effects of expression levels on FRET efficiency

It was reported that changes in the relative densities of acceptor and donor fluorophores can have false positive effects on FRET (Fung and Stryer, 1978). Using the data sets obtained from Figure 5.14, the effects of YFP/CFP expression ratios on FRET efficiencies were analysed retrospectively. Figure 5.15A indicates that the YFP/CFP expression ratios had no effect on the negligible FRET of cytoplasmic CFP + YFP-ABCG2 and the specific FRET of CFP-ABCG2 + YFP-ABCG2. Linear regression analysis suggested that the slopes did not deviate significantly from zero. In contrast, the FRET efficiency of CFP-ABCG2 + Adenosine A3-YFP increased as the YFP/CFP expression ratios increased, and regression analysis suggested a significantly non-zero slope, indicating the FRET observed between adenosine A3 and ABCG2 is non-specific and driven by protein expression levels, rather than by genuine interactions. Figure 5.15B also compares the overall expression ratios of the three different FRET pairs in Figure 5.14. There was no significant difference ($p > 0.05$) when comparing the expression ratios between the CFP-ABCG2 + Adenosine A3-YFP and CFP-ABCG2 + YFP-ABCG2. The expression ratios of cytoplasmic CFP + YFP-ABCG2 were shown to be significantly lower ($p < 0.05$) when compared to CFP-ABCG2 + YFP-ABCG2.

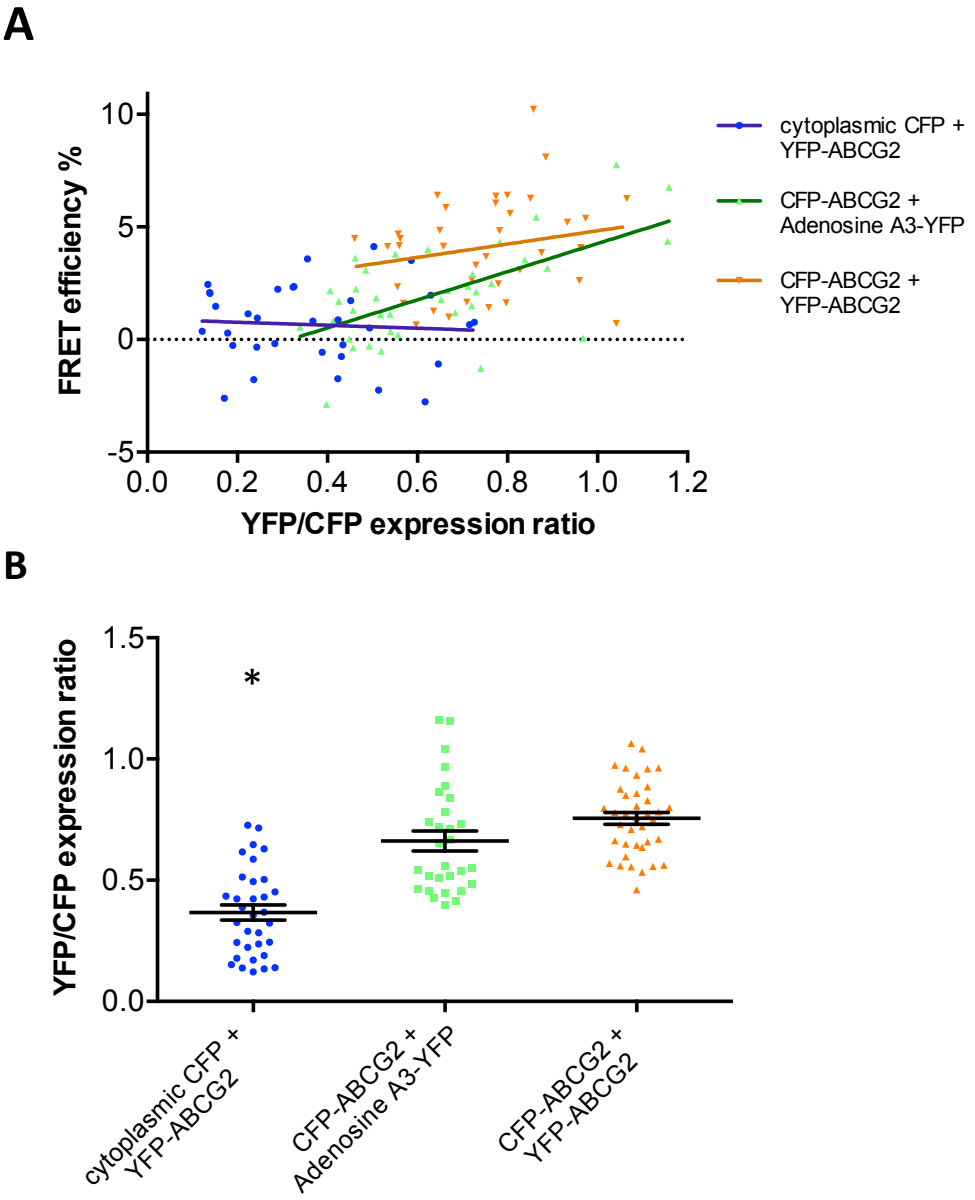

Figure 5.15: Effects of expression levels on FRET of ABCG2. A – Effects of YFP/CFP expression ratios on FRET efficiencies of the controls and ABCG2 FRET pairs, using data displayed in Figure 5.14. YFP/CFP expression ratios were generated using the pre-photobleaching fluorescence intensities of CFP and YFP after linear unmixing. Linear regression analysis for each data set in Graphpad Prism 6.0 showed that only the slope of CFP-ABCG2 + Adenosine A3-YFP (green) was significantly non-zero ($p < 0.001$, $R^2 = 0.38$). **B –** Distributions of YFP/CFP expression ratios (mean ± SEM) for the identical FRET data sets. Statistical significance (*, $p < 0.05$, when compared to CFP-ABCG2 + YFP-ABCG2) was assessed using one-way ANOVA analysis followed by Bonferroni multiple comparisons test.

5.5.2 Effects of substrate and inhibitors on ABCG2 FRET

Although the addition of substrate was found to have no effect on the diffusion of ABCG2 measured using FRAP (section 4.4.1), FRET was employed here to determine more specifically the effects of substrate or inhibitors on the oligomerisation of ABCG2 in live cells. A ligand induced change in oligomerisation state, or in the relative orientation of the protomers within the ABCG2 complex, might result in a change in FRET signal directly monitoring this interaction. However, Figure 5.16 below shows that there was no detectable change ($p > 0.05$) in the FRET of ABCG2 in the presence of substrate (4 µM mitoxantrone) or inhibitors (1 µM Ko143 or 4 µM chrysin), when compared to the equivalent amount of DMSO.

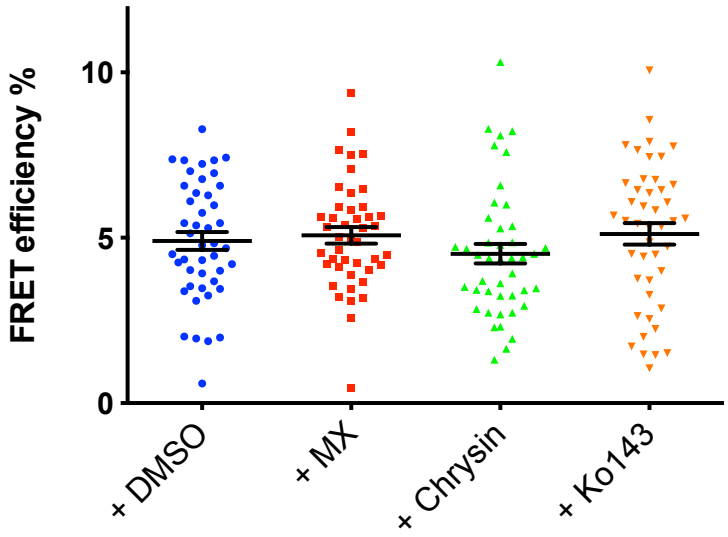

Figure 5.16: Effects of substrate and inhibitors on FRET of ABCG2. FRET efficiency (% mean ± SEM) of CFP-ABCG2 + YFP-ABCG2 expressed in live HEK293T cells acquired in the presence of 4 µM mitoxantrone (MX; substrate), 4 µM chrysin (inhibitor), 1 µM Ko143 (inhibitor), and the equivalent amount of DMSO (0.1 % (v/v); solvent for the drugs). Cells were incubated with the different compounds for at least 20 min before any data were collected. No significant difference in FRET efficiency ($p > 0.05$) was observed in the different treatments shown in the figure. A minimum of 30 cells was examined in three independent experiments for each data set. Statistical significance was assessed using one-way ANOVA analysis followed by Bonferroni multiple comparisons test.

5.5.3 Investigating the potential roles of different domains in ABCG2 oligomerisation

Upon successfully demonstrating oligomerisation of ABCG2 in live cells, attempts were made in this study to establish the roles of different ABCG2 domains in its oligomerisation using AcPb FRET. C603A mutants of CFP- and YFP-tagged ABCG2 were first generated to determine its importance in ABCG2 oligomerisation. Figure 5.17 shows that CFP-ABCG2_C603A + YFP-ABCG2_C603A yielded indifferent FRET efficiencies when compared to CFP-ABCG2 + YFP-ABCG2 wild type, $p > 0.05$, suggesting no effect of C603A in ABCG2 oligomerisation.

Various truncated ABCG2 constructs were also generated as summarised in Figure 5.3. These truncated constructs include the nucleotide binding domain (YFP-NBD), two versions of transmembrane domains (YFP-TMD_S and YFP-TMD_L), and two versions of nucleotide binding domain with part of the transmembrane helices (YFP-TM1-2 and YFP-TM1-4). When comparing across the truncated ABCG2 mutants, significant increases ($p < 0.05$) were observed in the FRET efficiencies of YFP-TMD_L and YFP-TMD_S compared to YFP-NBD, YFP-TM1-2, and YFP-TM1-4, when paired with CFP-ABCG2 (Figure 5.17). However, all the YFP-fused truncated ABCG2 proteins yielded significantly lower FRET efficiencies when compared to the full length protein, YFP-ABCG2 ($p < 0.05$), and the FRET efficiencies were similar to that of adenosine A3-YFP control (Figure 5.14).

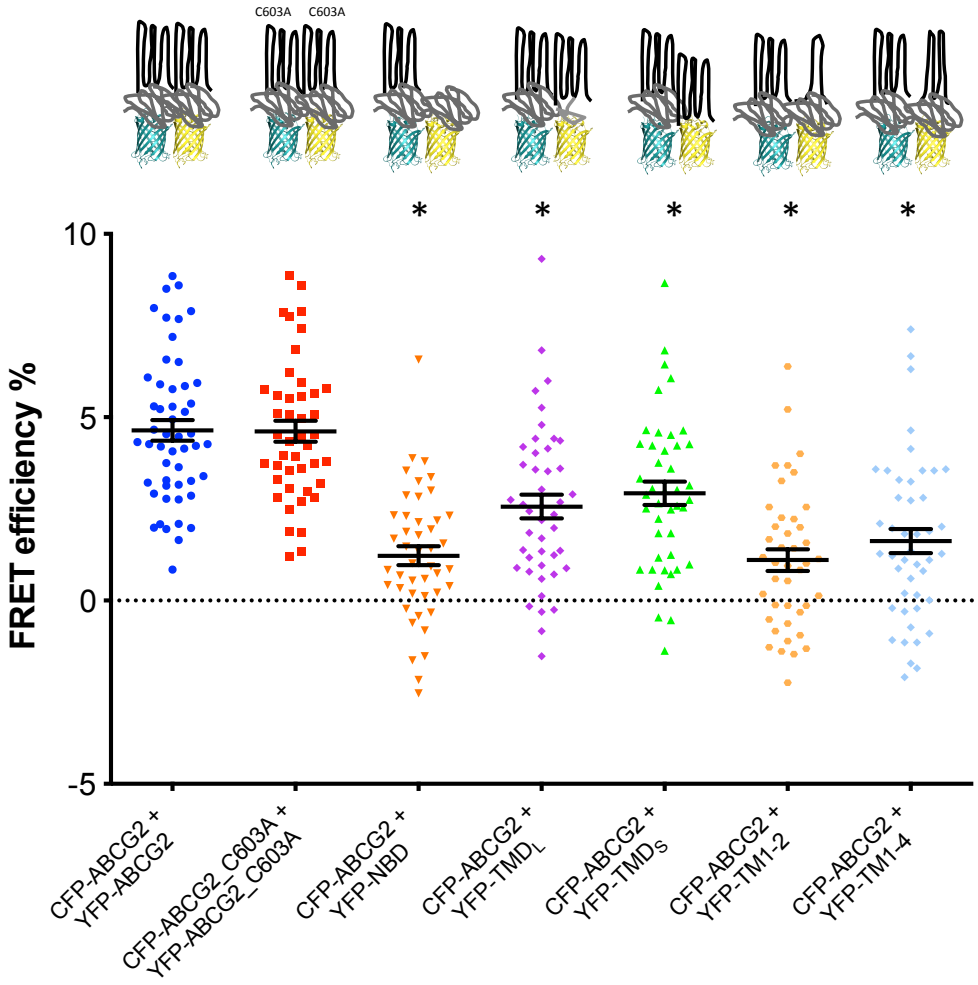

Figure 5.17: Transmembrane domain, rather than C603 disulphide bonds or the NBD, contributes to the oligomerisation of ABCG2. FRET efficiencies (% mean ± SEM) of the C603A mutant and various truncated ABCG2 proteins compared to those of full length ABCG2 wild type (data set from figure 5.14). A minimum of 40 cells was examined from three independent experiments for each data set (except for CFP-ABCG2 + YFP-ABCG2, four experiments). Statistical significance (*, $p < 0.05$, compared to CFP-ABCG2 + YFP-ABCG2) was assessed using one-way ANOVA analysis followed by Bonferroni multiple comparisons test.

For further verification of the roles of these truncated proteins in oligomerisation, cell lysates from single transfections were analysed with SDS-PAGE and western blotting under non-reducing conditions. Figure 5.18 indicates that YFP-ABCG2 wild type migrated as higher order oligomers (> 175 kDa) as well as monomers (approximate 90 kDa). The C603A mutation resulted in reduced detection of the oligomeric band and majority of the YFP-ABCG2_C603A migrated as the monomeric form. Finally, there was also some indication of aggregate formation in YFP-TMD_L whilst the YFP-TMD_S, YFP-

TM1-2, and YFP-TM1-4 migrated at molecular weights identical to the reducing western blot analysis (Figure 5.6).

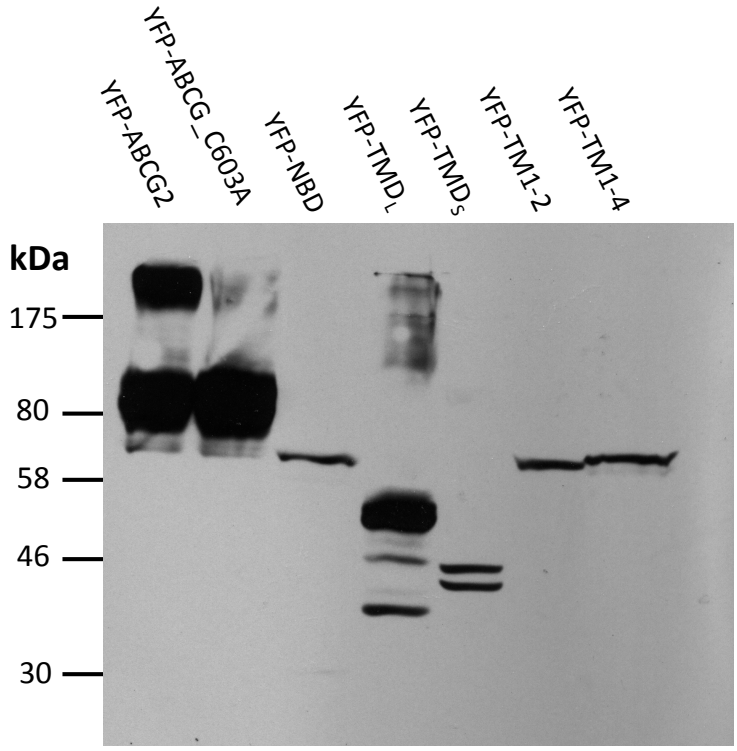

Figure 5.18: Non-reducing western blot analysis demonstrates the expression and capacity for oligomerisation of the YFP-fused ABCG2 proteins. Approximately 20 µg of cell lysates were loaded onto each lane in the SDS-PAGE under non-reducing condition. Proteins were transferred onto nitrocellulose membrane and probed using primary monoclonal anti-GFP mouse IgGκ antibody and secondary polyclonal rabbit anti-mouse IgG antibody conjugated with horseradish peroxidase, prior to chemiluminescence detection. Representative western blot of 2 independent experiments was shown.

5.6 Discussion

5.6.1 Establishing the oligomerisation of ABCG2 in live cells

In this chapter, ABCG2 oligomerisation in live cells was demonstrated using FRET microscopy. Several controls afforded confidence in this conclusion. For example, the absence of any "FRET" efficiency using CFP-ABCG2 alone (Figure 5.14) eliminated the possibility of "pseudo-FRET" behaviour, which can be produced by CFP in the presence of high power 514 nm laser excitation (Karpova et al., 2003). Cytoplasmic CFP + YFP-ABCG2 FRET pair controlled for non-specific FRET between the cytoplasmic CFP and YFP-ABCG2 molecules

due to random collision. The membrane adenosine A3-YFP was employed to take into account of any FRET efficiency yielded due to non-specific interaction with CFP-ABCG2 as a result of random collision in the membrane. Figure 5.14 demonstrates specific ABCG2-ABCG2 interactions as CFP-ABCG2 + YFP-ABCG2 yielded significantly higher FRET efficiency compared to these controls. Ni et al. have also previously demonstrated increased FRET efficiency in cells co-expressing CFP-ABCG2 and YFP-ABCG2 in a FRET experiment (Ni et al., 2010), but using fixed rather than living cells. There were also limitations to the control for "pseudo-FRET" behaviour (cytoplasmic CFP), which did not reflect the microenvironment of membrane CFP-ABCG2. Additionally, potential non-specific FRET between unrelated membrane proteins was not determined. We showed that such non-specific interactions could be relevant depending on donor/acceptor ratio (Figure 5.15), and due to the increased density of donor and acceptor molecules restricted to the plasma membrane. Ni et al. also did not address the donor bleed-through issue (highlighted Figure 5.9), where overlapping of the emission spectra of CFP and YFP could result in overestimation of CFP emission and inaccuracy in FRET efficiency calculation. In contrast, suitable membrane protein controls and spectral imaging FRET methods were employed in this study to overcome these limitations and provided clear demonstration of ABCG2 oligomerisation in live cells.

5.6.2 Simultaneous YFP excitation does not affect measured FRET efficiency

Direct YFP excitation during FRET acquisition might lead to reduced FRET efficiency because the FRET-induced excitation of YFP (by CFP emission) could be affected while YFP was already directly excited. This was not supported by the FRET measurements obtained with or without YFP excitation (Figure 5.13). Indeed, Figure 5.13 shows the opposite effect, in which FRET efficiencies of CFP-ABCG2 + Adenosine A3-YFP and CFP-ABCG2 + YFP-ABCG2 were slightly lower when data were collected without YFP excitation. It is possible that the sensitivity of the spectral imaging technique was reduced in

the absence of YFP excitation due to the very low or non-detectable YFP fluorescence signal, when YFP was not directly excited. This could be explained by the limited ability of the linear unmixing algorithm to resolve low level fluorescence signals as suggested in (Zimmermann et al., 2003). Hence, the presence of YFP excitation during FRET acquisition was shown to be beneficial by increasing the sensitivity of the spectral imaging technique. Further FRET experiments were therefore conducted in the presence of YFP excitation for this reason and to aid confirmation of YFP photobleaching during data acquisition.

5.6.3 Expression levels did not affect FRET of ABCG2

Fung and Stryer demonstrated that the surface density of the donor and acceptor molecules has a prominent effect on FRET studies (Fung and Stryer, 1978). This is because random collision between acceptor and donor molecules could result in false positive FRET when there is an increase in surface density. In a study of GPI-anchored proteins and cholera toxin B-subunit interaction, Kenworthy et al. reported an acceptor density dependent increase in FRET efficiency (Kenworthy et al., 2000). Berney and Danuser also reported an increase in FRET efficiency as the acceptor/donor ratios increased in a quantitative study comparing PEG-biotin/streptavidin complexes against simulated results (Berney and Danuser, 2003). In our study an increase in YFP/CFP ratio was only shown to have a significant influence on FRET efficiency between CFP-ABCG2 and adenosine A3-YFP, presumably as a result of random, non-specific collisions between the FRET partners. As expected, no FRET was observed between cytoplasmic CFP and YFP-ABCG2 due to the differences in subcellular localisation of these proteins. Finally, Figure 5.15 shows that the increased FRET efficiency in CFP-ABCG2 + YFP-ABCG2 was independent of the concentrations of donor and acceptor, supporting specific ABCG2-ABCG2 interactions.

5.6.4 No effect on FRET of ABCG2 in the presence of substrate

The presence of substrate or inhibitors did not affect FRET between the ABCG2 partners. This implies that ABCG2 molecules are likely to exist as functional oligomers in HEK293T cells and presence of ligands is unlikely to induce significant conformational changes that may affect the orientation of fluorescent proteins attached to the NBDs. As ABCG2 was highly expressed in this system, it is plausible that this does not represent ABCG2 at normal physiological level. However, ABCG2 is also known to be overexpressed in cancer cells (Kerr et al., 2011) and the findings in this study could imply that ABCG2 exist as functional oligomers in cancer cells to confer chemoresistance. Recently, heparin and low molecular weight heparin have been shown to affect ABCG2 function (Chen et al., 2014; Niu et al., 2012). With molecular weights of at least 8 kDa (low molecular weight heparin) or up to 40 kDa (heparin), these large polysaccharides could be screened for physical disruption of the oligomeric formation of ABCG2 using this FRET technique in the near future.

5.6.5 Roles of different domains in the oligomerisation of ABCG2

In this chapter, we show that although C603A mutation reduced the disulphide bond formation between ABCG2 molecules (Figure 5.18), it did not affect the oligomerisation of ABCG2 (Figure 5.17). This coincides with our results in chapter 4 where it was shown to be non-detrimental to the function and FRAP of ABCG2. The NBD alone construct also did not produce significant FRET signal (Figure 5.17), supporting the importance of the TMD in oligomerisation of ABCG2. However, the determination of roles of the different transmembrane helices in the oligomerisation of ABCG2 was difficult, as the other truncated ABCG2 proteins were not localised at the plasma membrane. The increase in FRET (of YFP-TMD_S and YFP-TMD_L) could be due to potential differences in expression levels. Our results here did not agree with the studies performed by Zhang's lab, who also investigated the roles of different domains in the oligomerisation of ABCG2, using various

biochemical assays, e.g. gel filtration, western blotting, and co-immunoprecipitation as summarised in section 1.6 (Mo et al., 2012; Xu et al., 2007). Both studies presented evidence to suggest that ABCG2 functions as oligomers through unique interactions located in the transmembrane helices 5 and 6 (TM5-6). In the studies, although it was claimed that the myc-tagged truncated ABCG2 proteins, specifically the NBD-TM1-2, NBD-TM1-4, TMD and TM5-6, were able to reach the plasma membrane when expressed in mammalian cells, the confocal (Xu et al., 2007) and fluorescence (Mo et al., 2012) images presented were inconclusive. The use of an intracellular epitope (N-terminal myc-tag) for immunofluorescence detection of membrane localisation further undermines the suggestion that the images show successful membrane trafficking of the truncated ABCG2 mutants (Mo et al., 2012). Therefore, the suggestion of TM5-6 being responsible for the oligomerisation of ABCG2 remains debatable and the investigation is currently impractical due to the trafficking issues of the truncated ABCG2 proteins.

5.6.6 Conclusion

A robust spectral imaging FRET method was established in this study, and the oligomerisation of ABCG2 in live cells was demonstrated, providing further confirmation that ABCG2 exists and functions as oligomers. Novel evidence showing the lack of effect of ligands (substrate and inhibitors) and the C603A mutation on ABCG2 oligomerisation in live cells was also presented. In an attempt to establish the domains responsible for ABCG2 oligomerisation, the discovery of possible misfolding and intracellular localisation of truncated ABCG2 proteins did not agree with the studies elsewhere. The trafficking issues of the truncated ABCG2 proteins rendered the determination of ABCG2 oligomerisation domains impractical thus far. However, we demonstrated the importance of TMD in the oligomerisation of ABCG2 as NBD alone yielded minimal FRET efficiency. Also, results in this chapter provided guidance for possible use of smaller truncations at the N- or C-terminus ends of ABCG2 in

the near future for identification of key sequences responsible for the folding and localisation of ABCG2.

It is conceivable that although FRET results support close interaction between YFP-ABCG2 and CFP-ABCG2, it is unclear if the translation and insertion at the endoplasmic reticulum results in the assembly of ABCG2 dimers from the same mRNA (e.g. CFP-ABCG2 may interact with CFP-ABCG2) before they reach the plasma membrane. However, the FRET technique cannot demonstrate higher order structures beyond ABCG2 dimers, such as tetramers. Thus, the main question of this study remained unanswered and higher resolution techniques, including FCS (fluorescence correlation spectroscopy) and TIRF (total internal reflection fluorescence) microscopy, were subsequently employed to resolve the oligomeric state of ABCG2. These will be presented in the following chapters.

Chapter 6 Fluorescence fluctuation measurements to study the diffusion and oligomerisation of ABCG2

In the previous chapters (4 and 5), membrane diffusion and oligomerisation of ABCG2 were studied using FRAP and FRET microscopy techniques. Both methods utilised the photobleaching of fluorescent proteins and measured the ensemble fluorescence intensities within a region of interest in the plasma membrane. They provided robust characterisation of ABCG2 diffusion and oligomerisation as a population at "single cell" level. However, for a better understanding of ABCG2 diffusion and oligomerisation as individual fluorescent complexes, more sensitive techniques are required. Hence, fluorescence correlation spectroscopy (FCS) and photon counting histogram (PCH) analysis were employed to study the diffusion and oligomerisation of ABCG2 at "single molecule" resolution. In this chapter, the background and theory behind FCS and PCH analysis is described. This is followed by a discussion of constructs characterisation before the FCS experiments were performed. The data acquisition for the FCS experiments is then presented along with the diffusion results of ABCG2. Finally, brightness analysis and oligomerisation of ABCG2 is discussed in the latter sections of this chapter.

6.1 Background and theory – FCS and PCH

6.1.1 Fluorescence correlation spectroscopy (FCS)

Background

FCS is an established biophysical technique now routinely used to measure the kinetic (diffusion) and molecular brightness (in combination with PCH analysis) parameters of fluorescent particles in solutions or living cells. This technique was first introduced in the 1970s in a study of the binding kinetics of ethidium bromide (Magde et al., 1972). The authors distinguished between

the free and DNA-bound ethidium bromide by demonstrating the differences in diffusion rates of the fluorescent particles using FCS (Elson, 2011; Magde et al., 1972). The rapid development of FCS occurred in the 1990s when the use of laser excitation and a confocal pinhole in FCS was introduced, which increased the signal-to-noise ratio of the system and improved the FCS experimental setup (Rigler et al., 1993), enabling increased application of the technique in biological samples.

Instrumentation and theory

Figure 6.1 below shows the basic instrumentation and principles of FCS (Briddon and Hill, 2007; Vukojević et al., 2005). A schematic representation of a typical FCS instrumental setup is shown in Figure 6.1A – identical to the set up for a confocal scanning laser microscope (section 1.7). In confocal microscopy, the confocal pinhole rejects out-of-focus emission light to produce high quality images. In FCS, the confocal pinhole provides a well defined small detection volume of 20-50 fL (highlighted in red, Figure 6.1A) for high resolution measurements. As the excited fluorescent molecules (green, Figure 6.1A) diffuse through the detection volume, light is transmitted to the detector (e.g. avalanche[2] photodiode or photomultiplier tubes). Over a specified time period, the number of pulses detected is recorded as fluctuations in fluorescence intensities, as represented in Figure 6.1B. The fluorescence fluctuation measurement is then subjected to statistical analysis using a normalised autocorrelation function:

$$G(\tau) = 1 + \langle \delta I(t) \, . \, \delta I(t+\tau) \rangle / \langle I \rangle^2$$

This function describes the decay of fluorescence intensity fluctuation as the average (represented by the symbol "<…>") of correlation between the fluctuations at a particular time point, δI(t), and the fluctuations measured at a later time point, δI(t+τ), normalised to the square of mean intensity, <I> (Briddon and Hill, 2007; Elson, 2011; Vukojević et al., 2005). By fitting the

[2] Avalanche is a process that incorporates internal gain (which is important for improving signal detected) in conventional photodiode, through an increase in the amount of charge using higher electric fields in a semiconductor.

experimentally determined autocorrelation curve (Figure 6.1C, black) to a model (Figure 6.1C, red) that describes the "ideal" diffusion behaviour of the fluorescent molecules (e.g. 2D or 3D diffusion), the average number of particles within the detection volume (*N*) and the average dwell time (τ_D) can be obtained, see section 2.9. The dwell time is determined as the midpoint of the fluctuation decay in the autocorrelation function (Figure 6.1C), and describes the time over which the fluorescent molecule stays in the confocal volume. The diffusion coefficient (*D*) of the fluorescent molecule of interest can be then determined using the following equation:

$$D = w^2_{xy} / 4.\tau_D$$

The concentration of the fluorescent molecules can also be calculated from *N* and known dimensions of the detection volume (Figure 6.1A), usually determined through calibration measurements of a dye with known diffusion properties. In situations where there is a mixture of fast and slow diffusing species, the respective autocorrelation curves are simply additive and can be fitted by multicomponent models to extract the relevant dwell times and the proportions for each species (Briddon et al., 2004), see section 6.4 for example. Hence, FCS allows the determination of diffusion of fluorescent molecules using autocorrelation analysis of the temporal changes in the fluorescence intensity fluctuations.

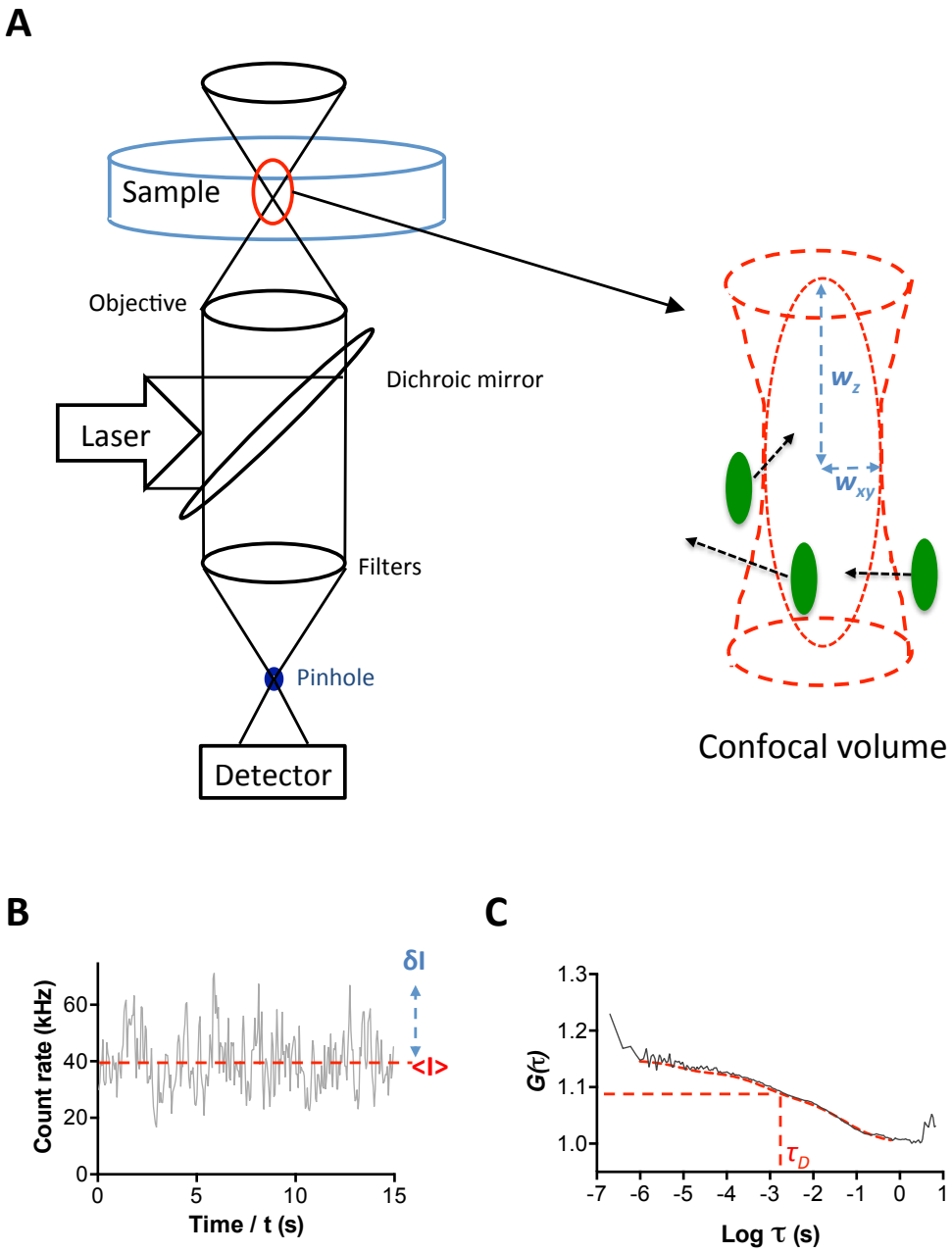

Figure 6.1: Schematic representation of basic FCS instrumentation and autocorrelation analysis. FCS instrumentation (**A**) is schematically represented and the confocal volume (or detection volume) is highlighted in red. The axial (w_z) and radial (w_{xy}) dimensions of the confocal volume are highlighted in the insert. The sensitivity of the detector is key in detecting the number of pulses emitted from the confocal volume. As the fluorescent molecules (green) diffuse through the confocal volume, the number of pulses detected is recorded as fluctuations in the fluorescent intensities over time, t (**B**). Fluorescence intensity fluctuations (δI) from the mean intensity <I> at each time point are compared with the δI at a range of later time points (δI(t+τ)) to produce the autocorrelation curve (black, **C**) normalised to $\langle I \rangle^2$. Fitting of the experimental autocorrelation curve with a theoretical model (red, **C**) allows the determination of kinetic parameters of the fluorescent particles, such as their dwell time within the confocal volume, τ_D, and average number of particles, *N*.

Application

Due to its non-invasive nature, the applications of FCS in live cells are found to be particularly appealing (Briddon and Hill, 2007; Chiantia et al., 2009; Macháň and Wohland, 2014). Coupled with its ability to produce quantitative mobility information at "single molecule" resolution, FCS has been employed in recent years to investigate membrane structural information, protein-DNA binding, and receptor binding affinities, using either fluorophore-labelling or GFP fusion techniques. For example, Briddon et al. identified the free and receptor bound antagonists of adenosine A_1 receptor within the confocal volume by demonstrating different dwell times obtained with FCS measurements (Briddon et al., 2004). Recently, the pharmacology of the human adenosine A_3 receptor antagonists was also successfully characterised using allosteric ligands and numerous comparisons of FCS analysis. The authors demonstrated that residence time of fluorescent antagonist was significantly reduced by the binding of allosteric ligand at the A_3 receptor dimer interface (Corriden et al., 2014). Additionally, measuring the diffusion coefficients of agonist-occupied adenosine A_3 receptors at equilibrium using FCS presented evidence of heterogeneous membrane complexes of adenosine A_3 receptors in the plasma membrane (Cordeaux et al., 2008). By combining FCS with super resolution stimulation emission detection (STED) microscopy to further reduce the detection volume, Eggeling et al. revealed that sphingolipids and GPI-anchored proteins were transiently trapped in small cholesterol-mediated complexes (Eggeling et al., 2009).

6.1.2 Photon counting histogram (PCH) analysis – theory and application

Photon counting histogram (PCH) was first described in 1999 as an alternative intensity distribution analysis of the FCS data sets to determine the molecular brightness of the fluorescent species of interest (Chen et al., 1999b). Instead of describing the time dependent fluorescence fluctuation decay (autocorrelation analysis), PCH analyses the frequency distribution of the fluorescence fluctuation amplitudes within the FCS traces which are divided

into bins of specified sampling time. This analysis allows the determination of average number of fluorescent particles ($\tilde{N}$) in the detection volume and their molecular brightness (ε), which is the average number of photons detected per molecule per sampling time (Chen et al., 1999a). The original PCH analysis (Chen et al., 1999b) was derived from a convolution of the Mandel's formula (Mandel, 1958) and the 3D Gaussian approximation of the point spread function (PSF) (Rigler et al., 1993). PCH analysis describes the statistics of photon detection (Figure 6.2) within a specified sampling time, which produces a super-Poisson distribution, schematically represented in Figure 6.2A (black dots). The super-Poisson distribution can be fitted with a theoretical PCH model (3D or 2D, 1- or 2-component), as shown in Figure 6.2A (red curve), to determine the $\tilde{N}$ and ε. In an open volume where the fluorescent particles can diffuse in and out of the confocal volume, the average number of photon counts (<k>) is related to the molecular brightness of the fluorescent particle (ε) and the average number of particles detected ($\tilde{N}$) where: (Chen et al., 1999b)

$$<k> = \varepsilon \, . \, \tilde{N}$$

The initial PCH models (Chen et al., 1999b) were derived based on two photon excitation systems. In this study, a single photon excitation system was employed and the PCH analysis was performed using an adapted PCH model that accounts for the deviation from the Gaussian confocal volume arising from single photon excitation, using a correction factor (see also sections 2.9.3 and 6.6) (Huang et al., 2004).

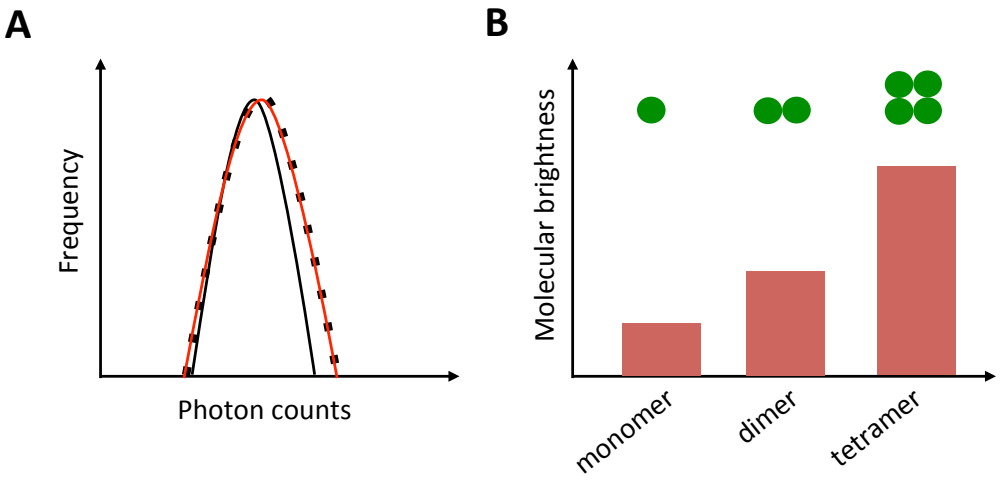

Figure 6.2: Schematic representation of PCH theory and application. A – Statistics of photon detection in PCH analysis. Black curve: Poisson statistics of the photon detection process from a light source with constant intensity. Black dots: Broadening of the Poisson curve (super-Poisson) due to fluctuations of the light source and varying positions of fluorescent molecules detected within the confocal volume. Red curve: PCH model fitting to the experimental data to determine the molecular brightness (ε) and average number of fluorescent particles within the confocal volume ($\tilde{N}$). **B –** Oligomeric states of fluorescent species can be predicted by the differences in molecular brightness determined from PCH analysis.

In summary, PCH analysis provides an account of the molecular brightness of the fluorescent species by analysing the distribution of fluorescence fluctuation amplitudes within a specified sampling time. It was first suggested to be a valuable technique for resolving various fluorescent species of different oligomeric states due to its ability to detect changes in molecular brightness (Chen et al., 1999a; Müller et al., 2000), Figure 6.2B. The same group of authors later characterised the molecular brightness of GFP in live cells for the first time (Chen et al., 2002) and also successfully demonstrated a two-fold difference in molecular brightness between dimeric GFP-GFP and monomeric GFP (Chen et al., 2003). Since then, other research groups have also reported PCH applications in the oligomerisation studies of other protein molecules in living cells. Malengo et al. first reported that it was possible to estimate the molecular brightness of membrane protein when applying PCH analysis in the study of GPI-anchored urokinase plasminogen activator receptors (Malengo et al., 2008). Wolf-Ringwall et al. also demonstrated aggregation of luteinising hormone membrane receptors upon treatment

with human chorionic gonadotropin using PCH analysis (Wolf-Ringwall et al., 2011). Recently, PCH was also employed to determine the oligomerisation of various GPCRs such as the serotonin, muscarinic and dopamine receptors (Herrick-Davis et al., 2012, 2013) and to establish the regulation of apical sorting and clustering of p75 neurotrophin receptors (Youker et al., 2013).

The main aim of this study is to characterise the oligomerisation of ABCG2. Whilst FRET microscopy in chapter 5 earlier demonstrated oligomerisation of ABCG2 as large populations, the oligomeric state of ABCG2 remained unidentified. In this chapter, FCS was first used to determine the diffusion of ABCG2 using autocorrelation analysis. The same FCS data sets were then subjected to PCH analysis to determine the oligomeric state of ABCG2 at high resolution (approximate detection radius of 150 nm) by comparing its molecular brightness against other control proteins. The characterisation of constructs and generation of low expressing stable clones is first discussed before the FCS and PCH experimental results are presented.

6.2 Construct characterisation and clonal selection for FCS and PCH studies

Four control constructs were generated in this study as comparison for the study of diffusion and oligomerisation of ABCG2 using FCS and PCH analysis. These constructs are schematically summarised in Figure 6.3 below. SfGFP and tandem-sfGFP constructs (two molecules of sfGFP joined together by a two amino acid linker Leu-Glu, formed by the *XhoI* restriction site), both containing the A206K mutation to reduce dimerisation of fluorescent proteins (Zacharias et al., 2002), were kindly provided by Marleen Groenen, University of Nottingham. These constructs were devised as controls in PCH brightness analysis as described later (section 6.5). In addition, other membrane integral controls were selected for comparison with the membrane localised sfGFP-ABCG2. These included the CD28-sfGFP and CD86-sfGFP, which were

generated from templates obtained from Professor Simon Davies, University of Oxford, and were used as controls for oligomeric (CD28) and monomeric (CD86) behaviour (James et al., 2006, 2007) in FCS and PCH experiments.

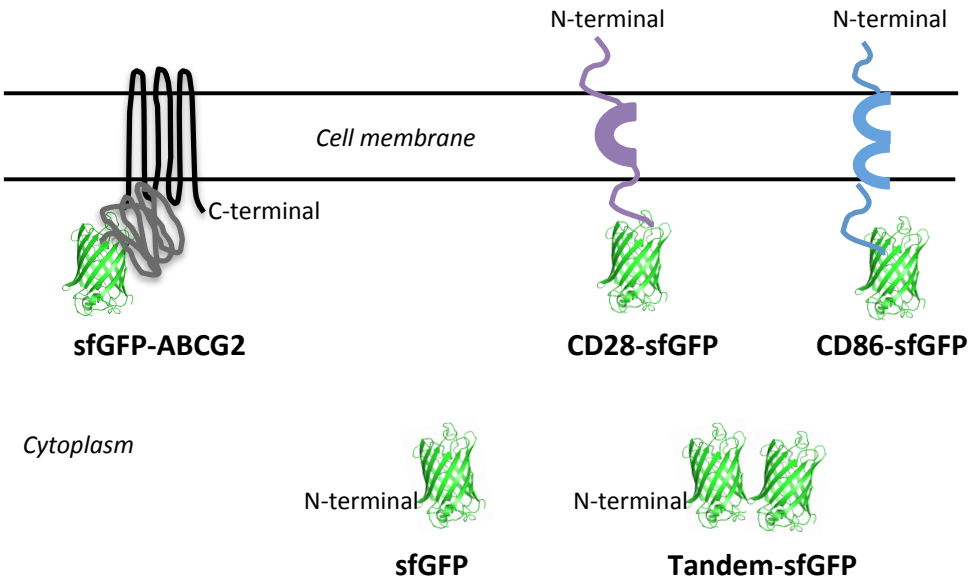

Figure 6.3: Schematic summary of the constructs generated for FCS and PCH experiments. SfGFP and tandem-sfGFP were cytoplasmic controls were employed to validate the PCH analysis methods. CD28-sfGFP and CD86-sfGFP were employed as membrane oligomer and monomer controls for comparison against the diffusion coefficient and molecular brightness obtained for sfGFP-ABCG2.

6.2.1 Characterisation of sfGFP and tandem-sfGFP constructs

SfGFP and tandem-sfGFP constructs were transiently transfected into HEK293T cells and their localisation and expression were confirmed with confocal imaging and western blot analysis (Figure 6.4). As expected, confocal images in Figure 6.4A show that both proteins were localised in the cytoplasm. Western blot analysis in Figure 6.4B shows that sfGFP and tandem-sfGFP migrated at expected molecular weight of 27 kDa and 54 kDa respectively (predicted using Compute pI/MW tool (Wilkins et al., 1999)).

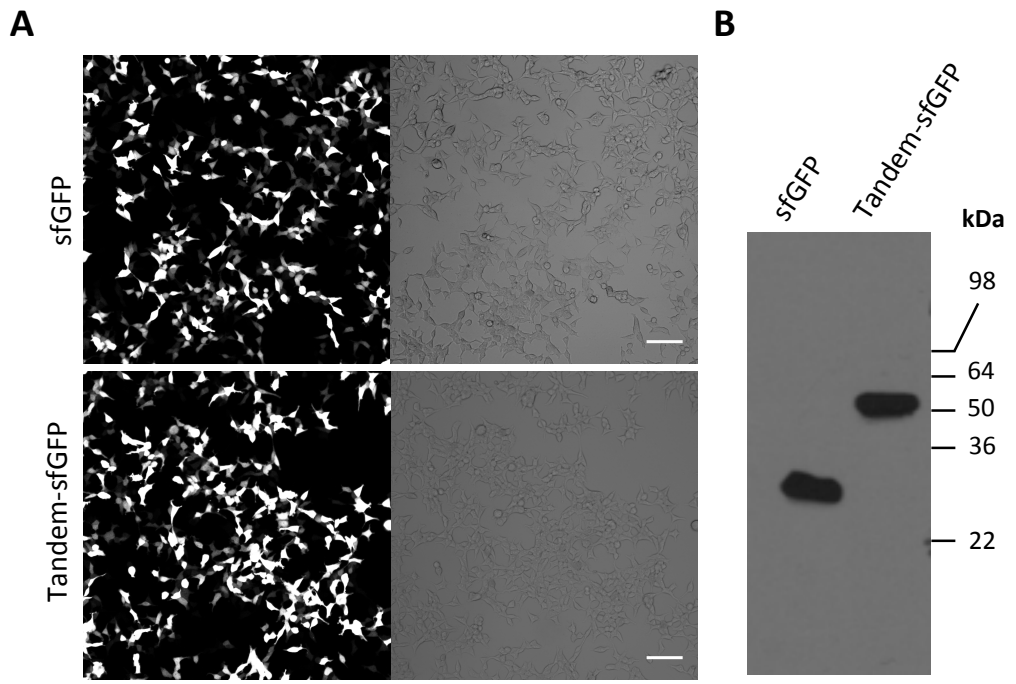

Figure 6.4: Localisation and expression of sfGFP and tandem-sfGFP. A – Confocal (and phase) images of HEK293T cells transiently transfected with sfGFP (top panel) and tandem-sfGFP (bottom panel) show that sfGFP and tandem-sfGFP were localised within the cell cytoplasm. Cells were seeded on 6-well plates and live cells were imaged with a LSM710 microscope equipped with a 10x objective. Scale bar = 100 µm. **B –** Western blot analysis of the corresponding transiently transfected cells in A. Approximately 20 µg of proteins were loaded onto each lane in the 12 % (w/v) polyacrylamide gel. Following electrophoresis and western transfer, the nitrocellulose membrane was probed using primary monoclonal anti-GFP mouse antibody and secondary polyclonal rabbit anti-mouse antibody conjugated with horseradish peroxidase, prior to chemiluminescent detection. Representative western blot of 3 independent experiments was shown.

6.2.2 Generation and characterisation of stable HEK293T clones expressing low levels of transfected protein

For the membrane proteins (CD28-sfGFP, CD86-sfGFP, sfGFP-ABCG2), it was necessary to obtain clones with low levels of expression to ensure optimal FCS data acquisition. The fluorescence fluctuations relative to the mean fluorescence intensity, which is critical to the analysis, are therefore greater when there is a lower expression of the fluorescent proteins (Chen et al., 1999a; Malengo et al., 2008). Hence, low expressing clones of CD86-sfGFP, CD28-sfGFP and sfGFP-ABCG2 were selected by dilution cloning (section 2.2.7). Figures 6.5 and 6.6 below show the confocal images of various clones of CD86-sfGFP and CD28-sfGFP grown from single cell colonies, with varying

degree of expression levels as indicated by the differences in GFP fluorescence intensity. The appropriate clones with low plasma membrane expression and healthy cell morphology for CD86-sfGFP and CD28-sfGFP were chosen sequentially as shown in the panels A and B. For the selection of low expressing sfGFP-ABCG2 stable clone (assisted by Deb Briggs, University of Nottingham), from a confluent 48-well plate, the clones (grown from single colonies) were gradually scaled up and seeded on coverslips, fixed and mounted on microscope slides for high resolution confocal imaging. Figure 6.7 shows the fixed stable clones expressing sfGFP-ABCG2 at different levels and the low expressing clone identified for further FCS experiments is highlighted.

For further confirmation of CD28-sfGFP and CD86-sfGFP expression, the low expressing stable clones were analysed by western blotting. Figure 6.8 shows western blot analysis derived from cell lysates of sfGFP-ABCG2, CD28-sfGFP, and CD86-sfGFP respectively. SfGFP-ABCG2 migrated at about 100 kDa with an additional lower molecular weight band of lower intensity indicative of glycosylation, corresponding to the previous western blot analysis of the mixed stable clone (section 4.2.1). The molecular weights of CD86-sfGFP and CD28-sfGFP were predicted to be 58 kDa and 48 kDa respectively (Wilkins et al., 1999). However, as seen in Figure 6.8, CD86-sfGFP migrated with molecular weight close to 100 kDa whilst the CD28-sfGFP migrated as a large smeared band with molecular weight of approximately 55-75 kDa. The broad band for CD28-sfGFP and increase in observed molecular weights for CD28-sfGFP and CD86-sfGFP may arise from glycosylation of CD28 and CD86, as reported in similar observations elsewhere (Corcoran et al., 2011; Hutchcroft et al., 1996), although this could also reflect the unpredictable migration of membrane proteins in SDS-PAGE analysis.

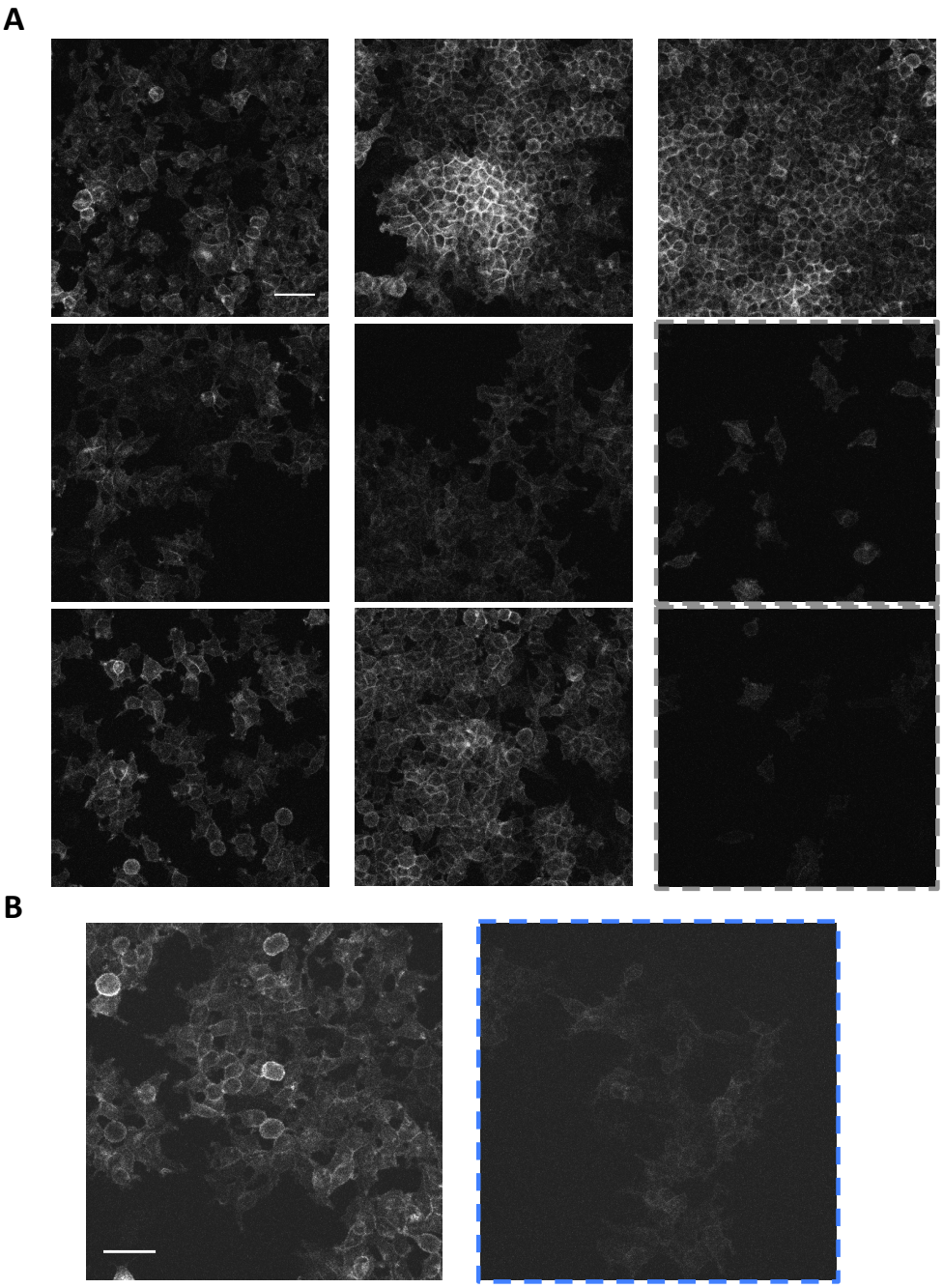

Figure 6.5: Selection of a low expressing CD86-sfGFP stably transfected HEK293T clone. Confocal images of live stable CD86-sfGFP expressing clones grown from single cell colonies. The low expressing clones (low and uniform fluorescence intensities) were initially identified and highlighted by grey dotted lines (**A**). The two clones identified were then left to grow and were observed again after 24-48 h. The stable clone highlighted in blue dotted line is the final low expressing stable CD86-sfGFP clone selected for FCS experiments (**B**). Confocal images were acquired with a modified Zeiss confocal system with a 20x objective. Brightness of the images in B was increased by 35 % for presentation purposes. Scale bar = 50 µm.

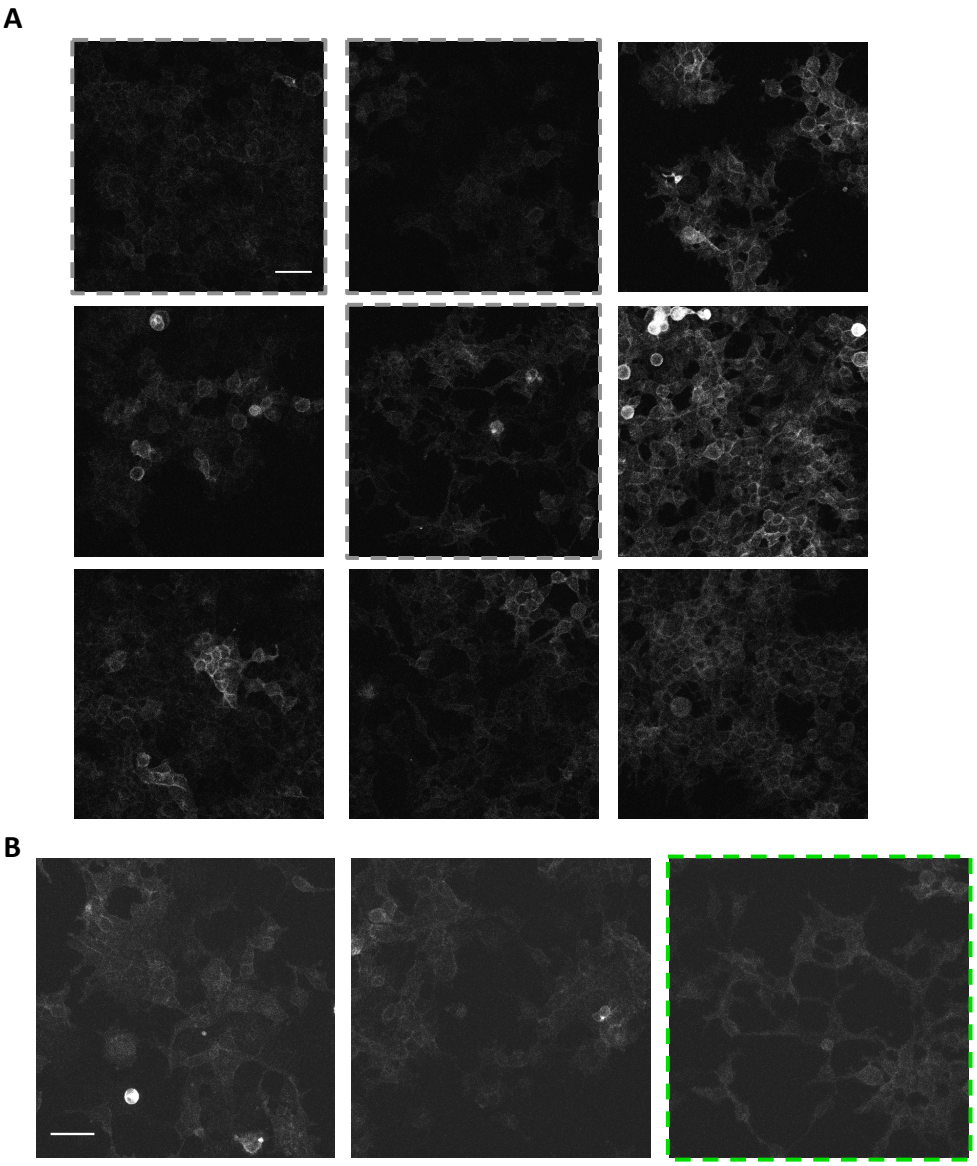

Figure 6.6: Selection of a low expressing CD28-sfGFP stably transfected HEK293T clone. Confocal images of live stable CD28-sfGFP expressing clones grown from single cell colonies. The low expressing clones (low and uniform fluorescence intensities) were initially identified and highlighted by grey dotted lines (**A**). The three clones identified were then left to grow and were observed again after 24-48 h. The stable clone highlighted in green dotted line is the final low expressing stable CD28-sfGFP clone selected for FCS experiments (**B**). Confocal images were acquired with a modified Zeiss confocal system with a 20x objective. Brightness of the images in B was increased by 35 % for presentation purposes. Scale bar = 50 µm.

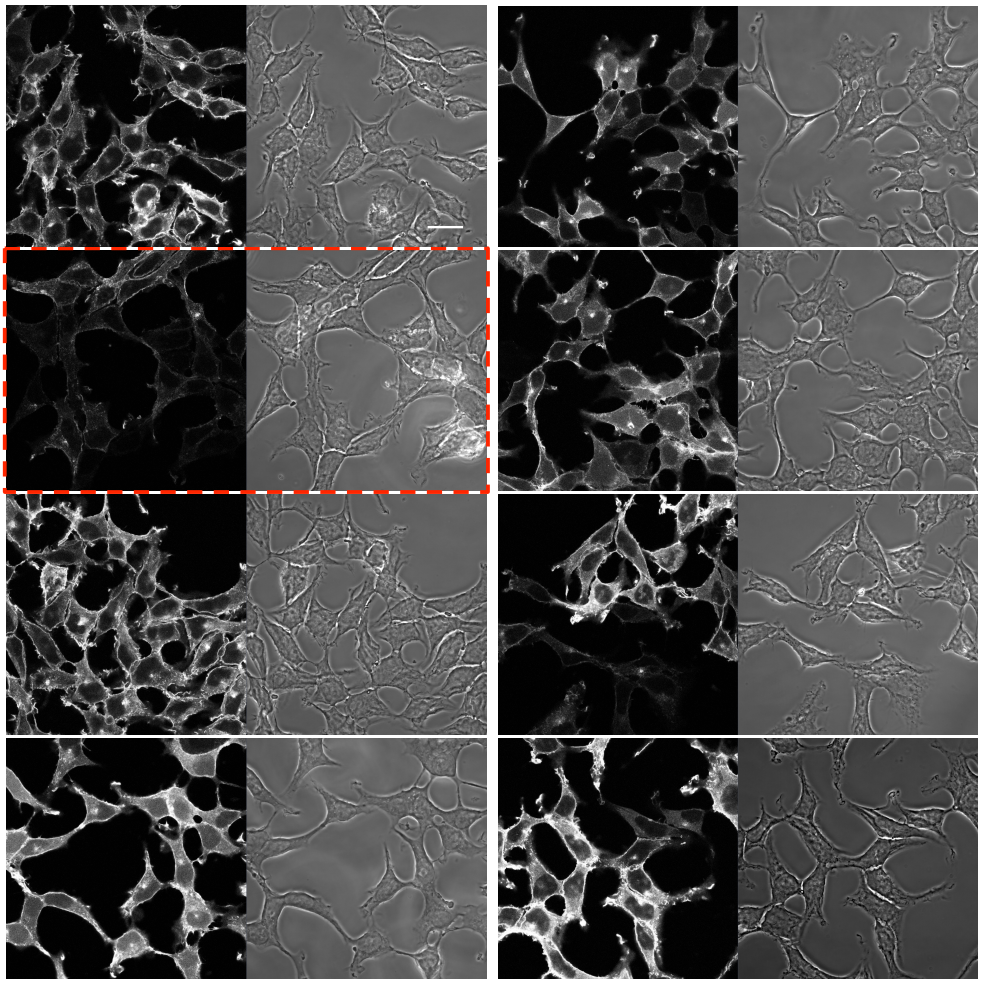

Figure 6.7: Selection of a low expressing sfGFP-ABCG2 stably transfected HEK293T clone. Confocal (and phase) images of fixed stable sfGFP-ABCG2 clones grown from single cell colonies. The low expressing stable sfGFP-ABCG2 clone selected is highlighted in the figure (red dotted lines). Images were acquired with a 63x oil objective (LSM710). Scale bar = 20 µm.

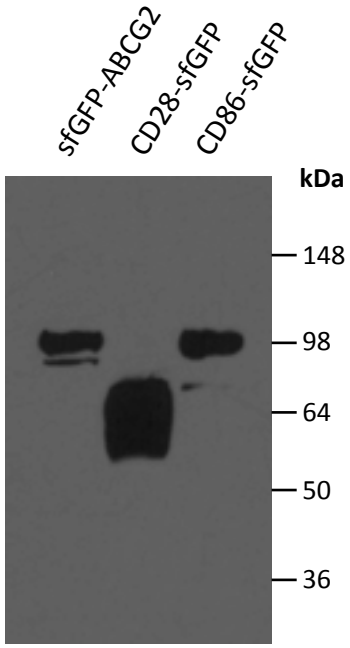

Figure 6.8: Western blot analysis indicating the observed molecular weights of sfGFP-ABCG2, CD28-sfGFP and CD86-sfGFP. Approximately 20 µg of proteins were loaded onto each lane in the 8 % (w/v) polyacrylamide gels (reducing conditions). Following electrophoresis and transfer, nitrocellulose membrane was probed using primary monoclonal anti-GFP mouse antibody and secondary polyclonal rabbit anti-mouse antibody conjugated with horseradish peroxidase, before chemiluminescent detection. Representative western blot of 3 independent experiments was shown.

6.3 FCS data acquisition

Before the FCS traces were collected, Rhodamine 6G calibration was performed to position the pinhole and identify the dimensions of the confocal volume on the day of the experiment (section 2.9.2). The cell acquisition conditions were also optimised and described in this section. For plasma membrane localised proteins, the confocal volume was positioned at the upper plasma membrane of the cell, as shown schematically in Figure 6.9A. By performing *z*-intensity scans, peaks of fluorescence intensities corresponding to the lower (LM) and upper (UM) plasma membranes were revealed (example shown in Figure 6.9B). The confocal volume was then positioned at the upper plasma membrane, highlighted in red. Previous studies have suggested that positioning of the confocal volume at the upper or lower plasma membrane had no effect on the diffusion of fluorescently labelled cholera toxin B in rat basophilic leukaemia cells (Bacia et al., 2004). The upper

plasma membrane was preferred (to the lower plasma membrane) in this study to minimise the effects of glass surface on the membrane dynamics (Wawrezinieck et al., 2005). For sfGFP and tandem-sfGFP (localised to the cytoplasm), the confocal volume was positioned in the middle of a broad cytoplasmic intensity peak upon performing *z*-intensity scan.

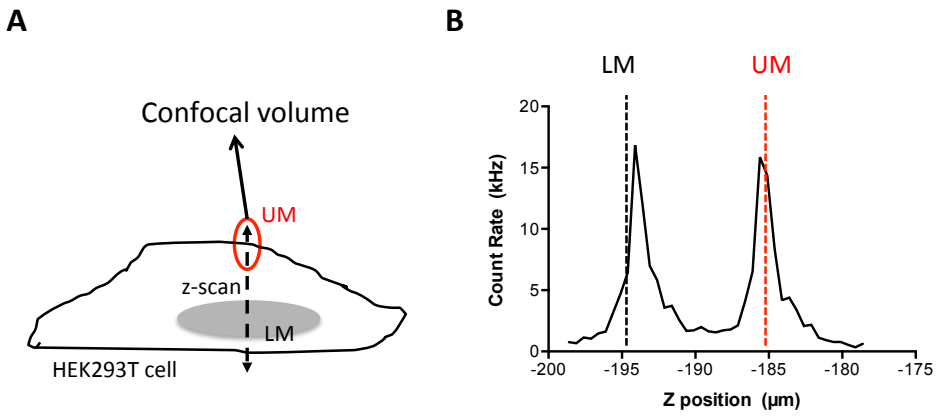

Figure 6.9: Positioning of the confocal volume in FCS experiments. For FCS acquisition of the membrane proteins in this study, confocal volume was positioned at the upper plasma membrane of HEK293T cell (schematic representation in **A**). This was determined by performing a *z*-intensity scan (example from sfGFP-ABCG2 transfected clone shown in **B**), which shows the intensity (count rate) peaks for the lower (LM) and upper (UM) plasma membranes.

Initially a number of experiments were performed to optimise the FCS traces obtained for autocorrelation analysis. A "pre-bleach" step was required prior to recording the measurements; for FCS analysis, the mean intensity <I> needs to be stable over the period of acquisition. This is because systemic or long lasting fluctuations in <I> during acquisition, possibly due to the presence of immobile fluorescent particles within the confocal volume, will lead to unusable autocorrelation curves, in which an asymptote is not observed as $G(\tau)$ approaches 1.0. Therefore, the pre-bleach step is required to ablate the fluorescence of these immobile particles. The laser power chosen here needs to be optimised as insufficient pre-bleach will contribute to inappropriate traces, and too much pre-bleach will also affect the FCS traces or subsequent analysis. Additionally, the laser power employed for acquisition which is too high will result in photobleaching of the particles during the acquisition period. Figure 6.10 shows examples of FCS traces (A-D)

and the corresponding autocorrelation decay curves (E-G), obtained under different acquisition conditions in cells expressing sfGFP-ABCG2. Figure 6.10A shows that increased laser power during acquisition resulted in continuous photobleaching in the FCS trace (and decay in <I>), yielding an inappropriate autocorrelation curve that did not reach asymptote (Figure 6.10E). Figures 6.10B and 6.10F show that insufficient pre-bleach conditions yielded low fluorescence fluctuation and low autocorrelation amplitude, likely to be due to presence of the immobile particles in combination with high concentration of sfGFP-ABCG2 in the plasma membrane. Increased pre-bleach (0.55 kW/cm^2 for 10 s) and using lower acquisition laser power improved the FCS traces with higher autocorrelation amplitude produced, Figures 6.10C and 6.10G. Despite this, the autocorrelation curve in Figure 6.10G was still unsuitable for further analysis, as the fluorescence fluctuation decay did not reach asymptote when $G(\tau)$ approaches 1.0, likely to be due to the increased mean intensity <I> resulting from high concentrations of sfGFP-ABCG2 molecules.

Chen et al. reported that a low concentration of fluorescent molecules was beneficial in FCS data acquisition (Chen et al., 1999a) as the curve amplitude $G(0)$ is proportional to $1/N$. Other studies of membrane proteins have also recommended that generating of low expressing stable clones (Malengo et al., 2008) or selecting cells within a certain range of fluorescent intensities (Herrick-Davis et al., 2012) were essential in FCS data acquisition. The fluorescence intensities (count rate, kHz) recorded for the FCS traces described thus far were all higher than 200 kHz, despite increased pre-bleach (Figure 6.10C). Herrick-Davis et al. selected low expressing cells with count rate of < 150 kHz (Herrick-Davis et al., 2012), suggesting that such data selection is important in FCS acquisition. Therefore, to obtain suitable FCS traces, the display range of the camera was adjusted during cell selection (with constant exposure time at 200 ms) to allow selection of low expressing cells through their lack of image saturation. Typically this identification step leads to FCS traces with a mean count rate of less than 100 kHz. Example of a

suitable FCS trace obtained using the optimised conditions (described in section 2.9.1) is shown in Figures 6.10D and 6.10H.

6.4 Diffusion of ABCG2 measured by FCS at "single molecule level"

Using the optimised acquisition conditions, suitable fluorescence fluctuation traces were collected from HEK293T cells stably expressing low levels of CD86-sfGFP, CD28-sfGFP and sfGFP-ABCG2, with examples shown in Figure 6.11 below (left panels), and cells transiently expressing free sfGFP or tandem-sfGFP (example traces shown in Figure S6.1A).

Figure 6.11 (right panels) shows the corresponding autocorrelation decay curves reached asymptote as $G(\tau)$ approached 1.0 (see Figure 6.10). This allowed for accurate autocorrelation curve fitting with the two-component 2D diffusion model (shown as black dotted lines, Figure 6.11). During data analysis, FCS traces were rejected if the autocorrelation curve did not reach an asymptote. This could be caused by sudden increase in concentrations of fluorescent proteins during data collection due to clustering of fluorescent molecules within the plasma membrane or random movement of the plasma membrane. Overall, 60 % of the recordings (captured with 3 x 15 traces) containing at least 1 x 15 s trace were suitable for the final autocorrelation and PCH analysis, with the remainder largely rejected due to the failure of the autocorrelation fit $G(\tau)$ to reach an asymptote of 1.0. The diffusion times (τ_{D1} and τ_{D2}) and the total number of particles (N_1 and N_2) detected within the confocal volume were obtained from the two-component 2D diffusion autocorrelation analysis. The two-component model was chosen to account for a fast autocorrelation component (τ_{D1}, typically less than 0.8 ms) caused by additional fluctuations due the photophysics of GFP (Briddon et al., 2011, 2004; Herrick-Davis et al., 2012) whilst the 2D diffusion model was employed to describe the restricted 2D diffusion of membrane proteins. Using the

known radial dimensions of the confocal volume (w_{xy}) obtained from Rhodamine 6G calibration experiments (section 2.9.2), the diffusion coefficients (*D*) and concentrations (*C*) of CD86-sfGFP, CD28-sfGFP, and sfGFP-ABCG2 were determined with the τ_{D2} and N_2 values. The *D* and *C* values obtained from the example traces are also indicated in Figure 6.11. For sfGFP and tandem-sfGFP (examples shown in Figure S6.1A), a single-component 3D diffusion model was chosen to fit the autocorrelation curves because the two-component model did not separate the close overlap between GFP photophysics (τ_{D1}) and dwell time (τ_{D2}) components. Additionally, the 3D diffusion model is more appropriate for describing diffusion within the cytoplasm.

The diffusion coefficients for the membrane proteins (CD86-sfGFP, CD28-sfGFP, sfGFP-ABCG2) are presented as log *D* (for linear transformation) in Figure 6.12A below. The diffusion coefficients obtained for CD86-sfGFP (*D* = 0.29 ± 0.17 μms^{-1}) and CD28-sfGFP (*D* = 0.27 ± 0.15 μms^{-1}) were approximately two to three times higher, compared to sfGFP-ABCG2 (*D* = 0.11 ± 0.03 μms^{-1}). In contrast, the sfGFP and tandem-sfGFP localised to the cytoplasm showed substantially faster mobility with *D* of 21.26 ± 0.67 μms^{-1} and 35.59 ± 5.12 μms^{-1} respectively (Figure S6.1B in Appendix), using a single-component 3D diffusion model for autocorrelation analysis. The average concentrations (*C*) of the particles detected within the confocal volume are shown in Figures 6.12B and S6.1C. Among the membrane proteins, CD86-sfGFP was found to have the highest concentration whilst the concentrations of sfGFP-ABCG2 and CD28-sfGFP in the plasma membrane were lower.

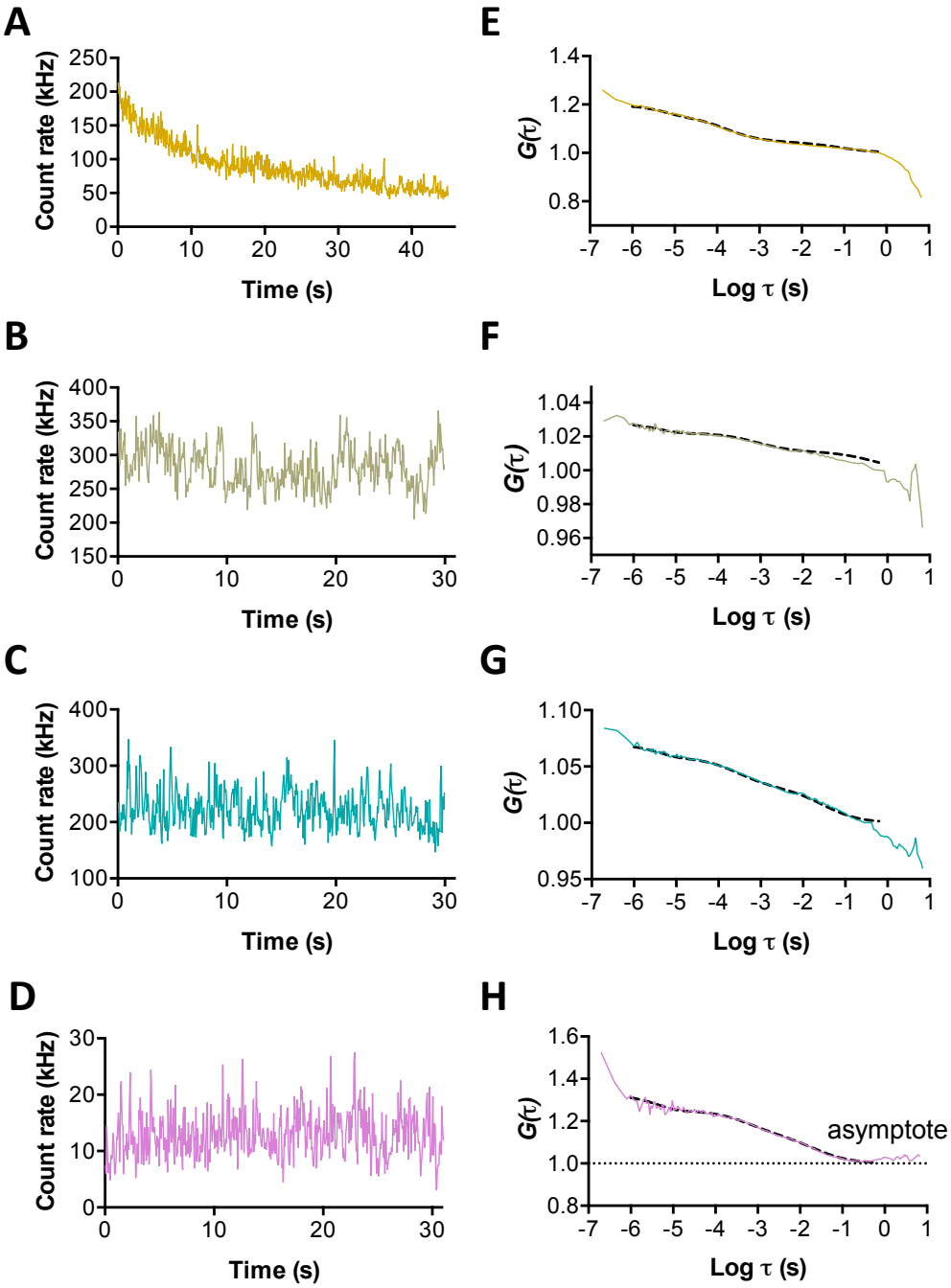

Figure 6.10: FCS traces and autocorrelation curves obtained with various acquisition/photobleaching conditions. Fluorescence fluctuation trace and autocorrelation curve obtained with low photobleaching conditions (0.12 kW/cm^2, 3 s) and high acquisition laser power (1.85 kW/cm^2) (**A and D**). Fluorescence fluctuation trace and autocorrelation curve obtained using low photobleaching conditions (0.12 kW/cm^2, 3 s) and lower acquisition laser power (0.24 kW/cm^2) (**B and E**). Fluorescence fluctuation trace and autocorrelation curve obtained with increased photobleaching conditions (0.55 kW/cm^2, 10 s) and 0.24 kW/cm^2 acquisition laser power (**C and F**). Suitable fluorescence fluctuation trace obtained with the optimised acquisition conditions described in section 2.9.1 after the selection of low expressing cells (**D and H**). Example traces were obtained from FCS experiments performed on sfGFP-ABCG2 expressing cells.

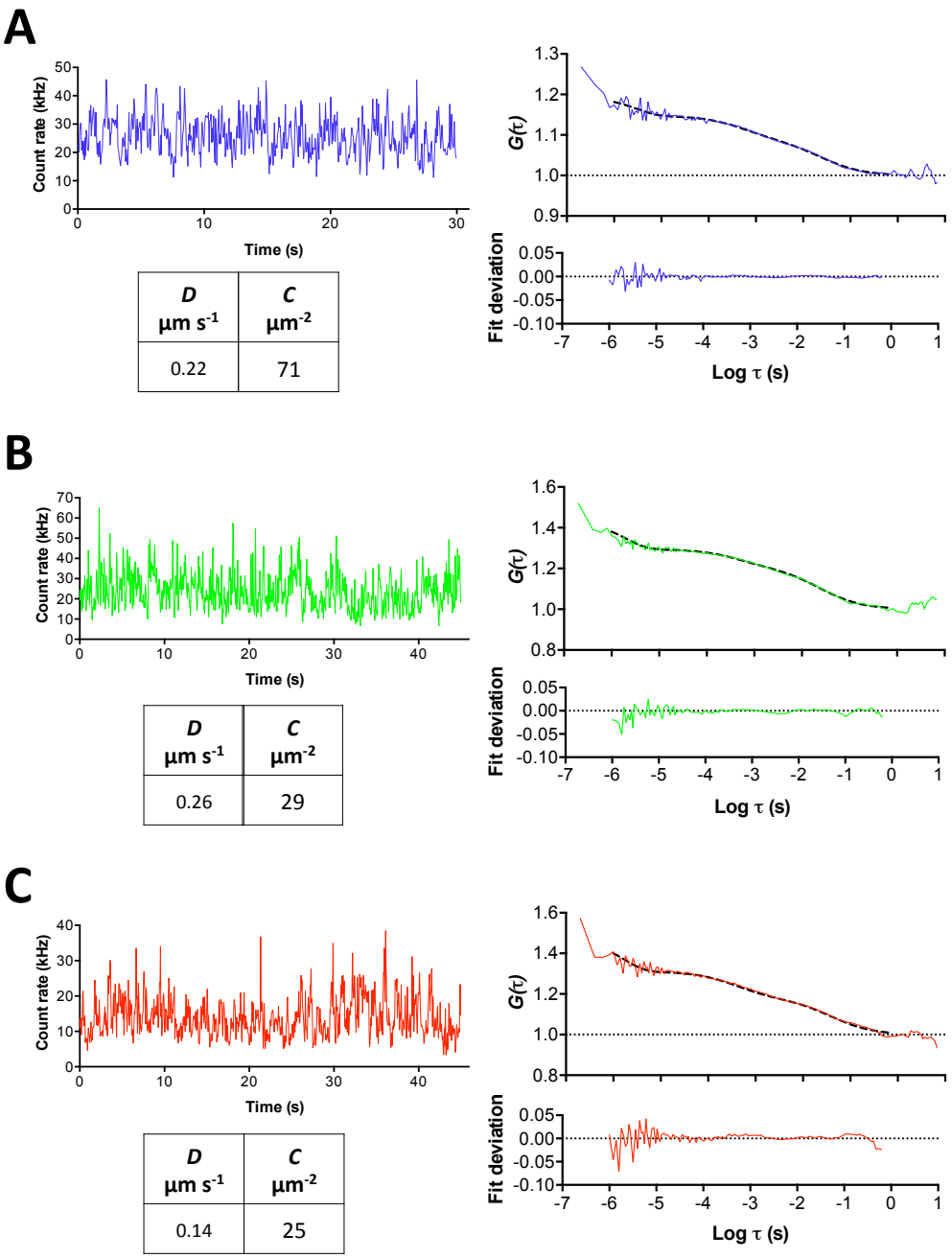

Figure 6.11: Examples of FCS traces and autocorrelation curves for A – CD86-sfGFP, B – CD28-sfGFP, and C – sfGFP-ABCG2. Fluorescence fluctuation traces (measured as count rate over time) are shown in the top left panels of A, B and C. Data fitting of the autocorrelation curves with a two-component 2D diffusion model (black dotted line) is shown in the right panels. The deviations of the experiment data from the fitted model are shown below the autocorrelation curves. The diffusion coefficients (*D*) and concentrations (*C,* number of molecules per μm^2) determined from the examples are also indicated in the figure tables.

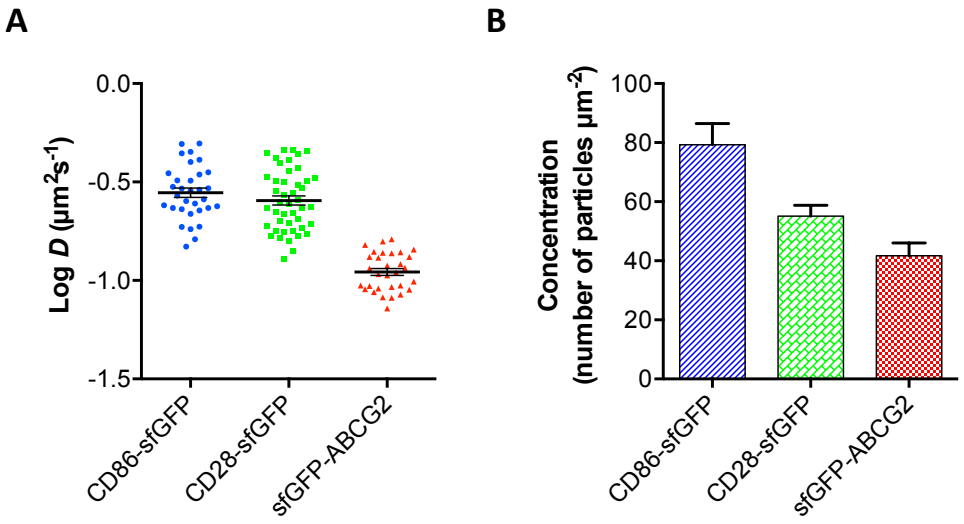

Figure 6.12: Diffusion coefficients (*D*) and membrane concentration (*C*) of sfGFP-ABCG2 compared to the membrane protein controls. A – Log *D* (mean ± SEM) and **B** – concentration (number of particles per μm^2, mean ± SEM) of sfGFP-ABCG2 compared to the controls. **A and B –** Results were obtained using the second component τ_{D2} (dwell time) and N_2 values from the two-component 2D diffusion autocorrelation analysis. Data were collected from at least 30 cells over 4 independent experiments.

6.5 Estimation of molecular brightness of controls cytoplasmic sfGFP and tandem-sfGFP using PCH analysis

To assess the ability of PCH analysis to discriminate fluorescent species according to their molecular brightness, an assessment of the brightness of cytoplasmic sfGFP and tandem-sfGFP (2x GFP) was first performed using 1-component PCH model fitting (Figure 6.13). The molecular brightness of tandem-sfGFP (15809 ± 484 cpm s^{-1}, counts per molecule per second) was found to be approximately twice the brightness of sfGFP (8506 ± 145 cpm s^{-1}). Thus PCH analysis distinguished dimeric and monomeric GFP variants through the expected doubling in molecular brightness. Application of a 2-component PCH model to the same data sets (Figure S6.2 in Appendix) resulted in only a small proportion of component 2 from the total species; and in this model the two fold change in brightness was retained (in components 1 and 2) for the tandem-sfGFP dimer compared to the monomeric variant.

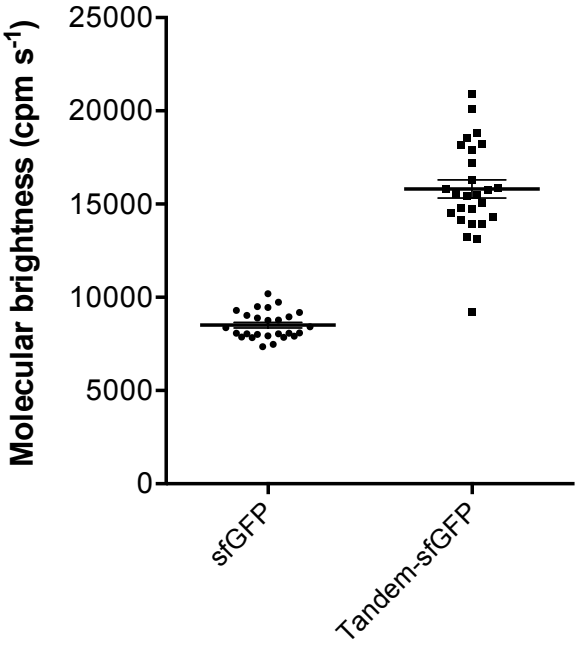

Figure 6.13: Validation of PCH analysis methods. Molecular brightness (mean ± SEM, cpm s^{-1} – counts per molecule per second) of sfGFP or tandem-sfGFP was determined as an assessment of the PCH analysis methods. Data were collected from at least 25 cells over 3 independent experiments.

6.6 Oligomerisation of ABCG2 demonstrated by PCH analysis

6.6.1 PCH analysis – binning time and data fitting

The same experimental data sets used to calculate the FCS autocorrelation results (section 6.4) were subjected to further PCH analysis to determine the molecular brightness parameters and gain insights into the oligomeric state of ABCG2. When optimising the PCH model for fitting of the experimental distributions, the influence of binning time (section 2.9.3) on the photon count histogram was first examined. Figure 6.14 shows the differences in PCH distributions (red dots) for an example sfGFP-ABCG2 data set, analysed using various binning times (0.01 ms to 5 ms) as indicated in the *x*-axes. The two extreme binning times, 0.01 ms and 5 ms, resulted in too few (0.01 ms) or too many (5 ms) counts associated with each bin in the PCH distributions (red dots). 1 ms was subsequently chosen as the binning time for PCH analysis to account for the fast autocorrelation component due to GFP photophysics

(< 0.8 ms) and ensure that the proteins of interest remained within the detection volume during the sampling period (i.e. dwell time, τ_{D2} > 1 ms) (Kilpatrick et al., 2012; Macdonald et al., 2013). Although the different binning times produced qualitatively different distributions in Figure 6.14, the effect on PCH analysis was less significant. Figure S6.3 shows that the different binning times (apart from 5 ms) had minimal impact on the molecular brightness of CD86-sfGFP and the normalised brightness of CD28-sfGFP and sfGFP-ABCG2.

Figure 6.15 shows the PCH distributions obtained from an example data set of sfGFP-ABCG2 fitted with a single-component or 2-component PCH models using 1 ms as the binning time. The reduced chi^2 value obtained from the model fitting provided an indication of the goodness of fit for each model. The average number of fluorescent molecules ($\tilde{N}$) and molecular brightness (ε) obtained from the PCH model fitting are also shown in the tables in the figure. For the 2-component PCH model analysis (Figure 6.15B), the $\tilde{N}$ and ε values for components 1 (C1) and 2 (C2) were obtained. Further examples of PCH analysis for CD86-sfGFP and CD28-sfGFP can be found in the Appendix, Figures S6.4 and S6.5 respectively. It was observed that the 2-component PCH model was the better fit for sfGFP-ABCG2 and CD28-sfGFP data sets whilst the 1-component PCH model was shown to be a sufficient fit for the CD86-sfGFP data sets, also indicated in the improvements in the reduced chi^2 values in Figure S6.6. Despite this, both models were employed for final brightness analysis to demonstrate any differences in using the two models.

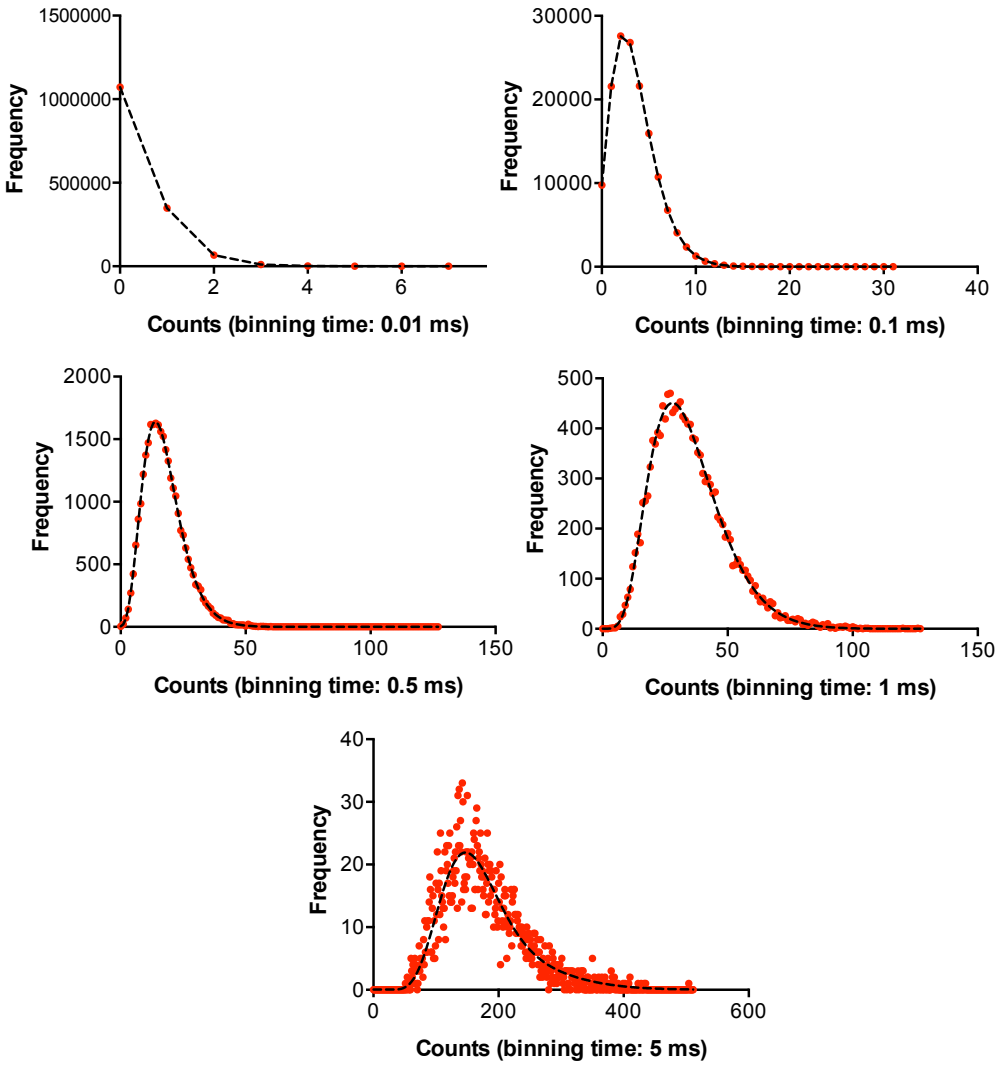

Figure 6.14: Effects of binning time on PCH distributions. PCH distributions (red dots) of an example sfGFP-ABCG2 data set (fitted with 2-component PCH model, black dotted lines) obtained using various binning times (0.01 ms, 0.1 ms, 0.5 ms, 1 ms, and 5 ms) as indicated along the *x*-axes.

A

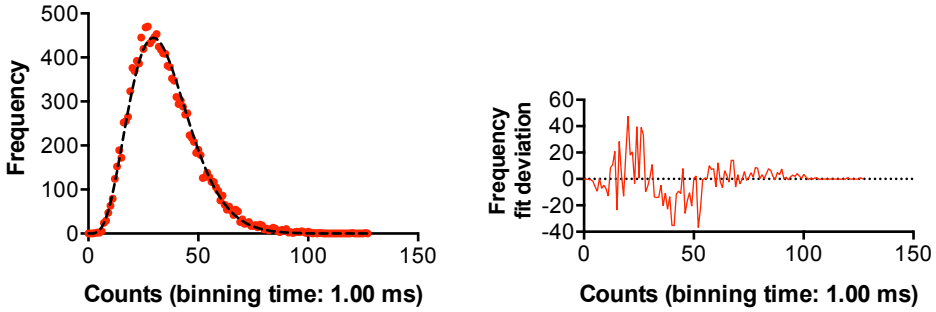

Counts per molecule (kHz)	C1 No. of molecules	C1 Brightness (cpm s^{-1})	First order correction	Reduced chi ^{2}
6.54	7.4	15255	0.16	1.73

B

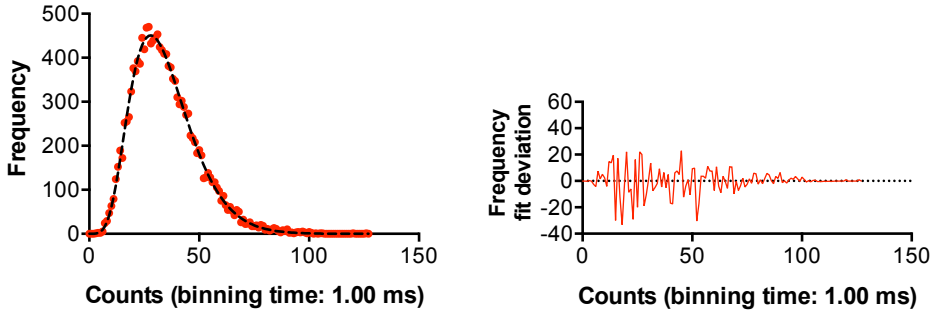

Counts per molecule (kHz)	C1 No. of molecules	C2 No. of molecules	C1 Brightness (cpm s^{-1})	C2 Brightness (cpm s^{-1})	First order correction	Reduced chi ^{2}
6.54	7.4	3.0	6063	23021	0.16	1.04

Figure 6.15: Example of PCH analysis from sfGFP-ABCG2 data set. 1-component (**A**) and 2-component (**B**) 3D PCH models were used for the fitting of the PCH distributions obtained from one of the FCS traces of sfGFP-ABCG2, using 1 ms binning time. The fit deviations and reduced chi^2 values provide an indication of goodness of fit for the different PCH models. The average number of molecules and brightness values for component 1 (C1) and component 2 (C2, for 2-component analysis in B) are also shown in the tables. The applied first order correction was determined from calibration experiments to correct for single photon excitation employed (section 2.9.3). PCH analysis was performed in Zen 2010.

6.6.2 1-component PCH analysis supports oligomerisation of ABCG2

Figure 6.16 compares the molecular brightness (ε) of sfGFP-ABCG2 against the monomer (CD86-sfGFP) and oligomer (CD28-sfGFP) controls obtained from 1-component PCH analysis of the FCS data sets. Figure 6.16A shows that the average molecular brightness of sfGFP-ABCG2 was 17298 ± 766 cpm s^{-1}

compared to those of CD28-sfGFP (21246 ± 1219 cpm s^{-1}) and CD86-sfGFP (12828 ± 889 cpm s^{-1}). These initial PCH results suggested that the sfGFP-ABCG2 fluorescent species exhibited mean ε higher than the monomeric control CD86-sfGFP, $p < 0.05$, and it was not significantly different from the oligomeric control CD28-sfGFP, $p > 0.05$. To control for the variability in absolute molecular brightness values between experiments, the molecular brightness of CD28-sfGFP or sfGFP-ABCG2 was normalised against the average brightness of CD86-sfGFP in each experimental day. Figure 6.16B shows that CD28-sfGFP and sfGFP-ABCG2 have approximately 1.7- and 1.4-fold higher ε relative to CD86-sfGFP respectively (one-sample t-test analysis shows both data sets were significantly different from 1, $p < 0.05$), indicating that both CD28-sfGFP and sfGFP-ABCG2 form higher order oligomers (for example, dimers) compared to CD86-sfGFP.

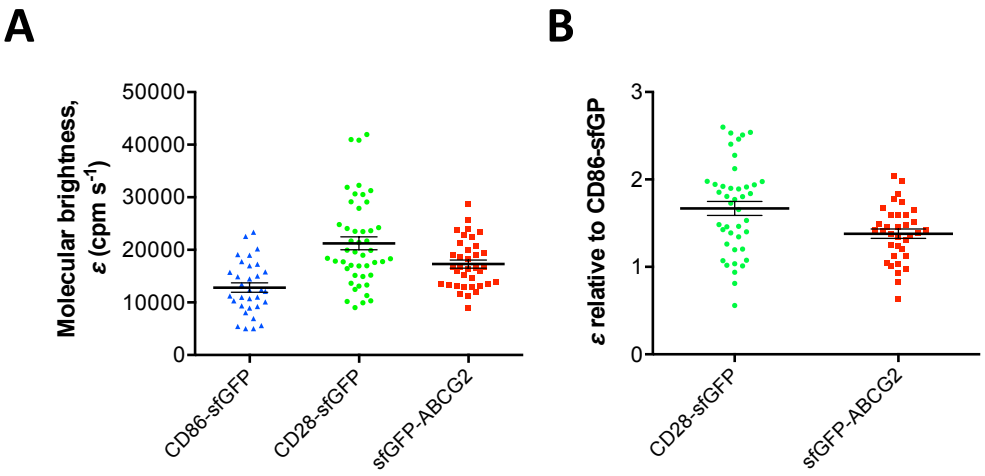

Figure 6.16: Increased molecular brightness (ε) of sfGFP-ABCG2 indicating possible oligomeric formation. Molecular brightness (mean ± SEM) of CD86-sfGFP, CD28-sfGFP, and sfGFP-ABCG2 obtained using 1-component PCH analysis showing increased molecular brightness of sfGFP-ABCG2 and CD28-sfGFP compared to CD86-sfGFP, $p < 0.05$ (**A**). Relative brightness of CD28-sfGFP and sfGFP-ABCG2 (mean ± SEM) normalised to the average ε of CD86-sfGFP in each experiment (**B**). Data were collected from at least 30 cells over 4 independent experiments. Statistical significance in A was assessed using non-parametric Kruskal-Wallis analysis followed by Dunnett's multiple comparisons test in GraphPad Prism 6.0. The mean values in B were found to be significantly different from 1.0 ($p < 0.05$) when assessed using one-sample t-test in GraphPad Prism 6.0.

6.6.3 High order oligomeric structure in ABCG2 indicated by 2-component PCH analysis

The 1.7- and 1.4-fold increase in molecular brightness observed for CD28-sfGFP and sfGFP-ABCG2 (Figure 6.16) could potentially reflect a mixture of oligomeric species of differing brightness, e.g. mixture of monomers and dimers in CD28-sfGFP and sfGFP-ABCG2. It was first verified that fitting of the CD86-sfGFP data sets with 2-component PCH model could not determine a different component as the molecular brightness for C1 (component 1) and C2 (component 2) of CD86-sfGFP were found to be identical (Figure S6.7 in Appendix). Also, as indicated in section 6.6.1 and Figure S6.6, the 2-component PCH model was found to be the more appropriate fit for the CD28-sfGFP (Figure S6.4) and sfGFP-ABCG2 (Figure 6.15) data sets. Therefore, the average molecular brightness of CD86-sfGFP (1-component analysis) obtained from each experimental day was used for normalisation of the molecular brightness of C1 and C2 for CD28-sfGFP and sfGFP-ABCG2 obtained by 2-component PCH analysis, shown in Figure 6.17.

This revealed a second component, C2, with higher molecular brightness for CD28-sfGFP and sfGFP-ABCG2 as shown in Figure 6.17A. In CD28-sfGFP and sfGFP-ABCG2, C1 represented 71 % and 67 % whilst C2 represented 29 % and 33 % of the total particles detected, respectively (Figure 6.17B). This suggests that the C2s identified from the 2-component analysis of CD28-sfGFP and sfGFP-ABCG2 were present at a significant portion. The ε of C1 for CD28-sfGFP or sfGFP-ABCG2 was found to be similar to the molecular brightness of CD86-sfGFP (ε ratios of 0.9 and 0.7 respectively) whilst the ε of C2 for CD28-sfGFP and sfGFP-ABCG2 were each 2-3 fold higher than the ε of CD86-sfGFP.

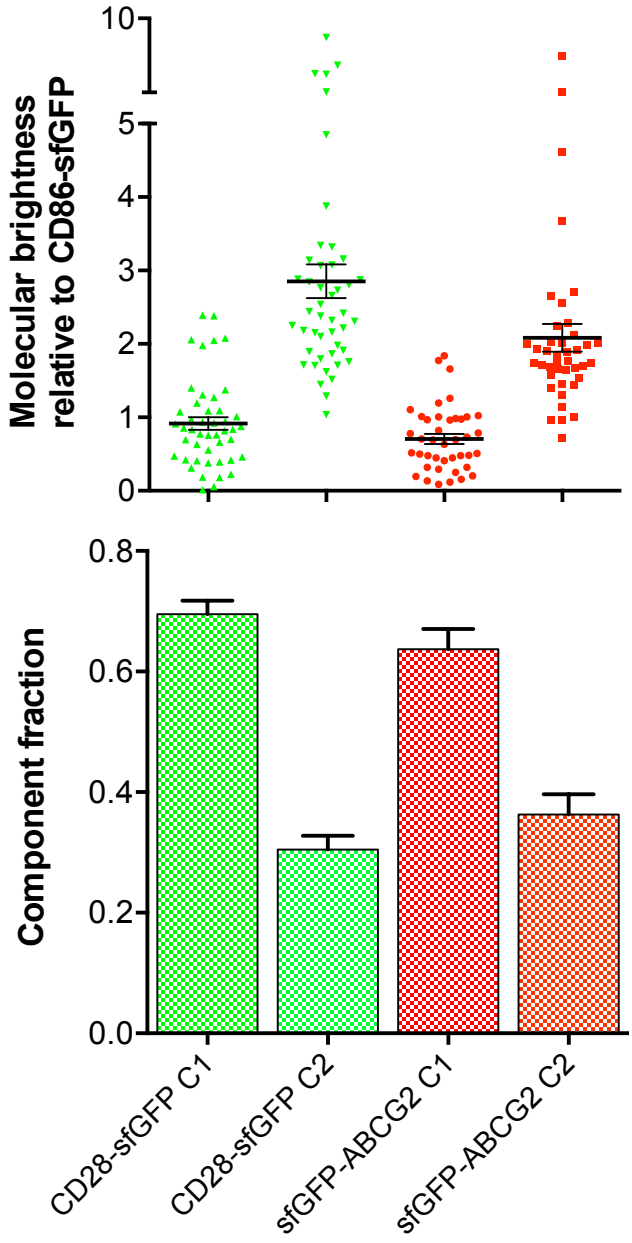

Figure 6.17: Presence of multiple species and higher oligomeric states in sfGFP-ABCG2 and CD28-sfGFP revealed by 2-component PCH analysis. Top panel: Molecular brightness (mean ± SEM) of component 1 (C1) and component 2 (C2) of CD28-sfGFP and sfGFP-ABCG2 normalised to the average molecular brightness of CD86-sfGFP obtained with 1-component PCH analysis. No significant difference was detected when comparing the relative molecular brightness of C2 for CD28-sfGFP and C2 for sfGFP-ABCG2, $p > 0.05$. Statistical significance was assessed using non-parametric Kruskal-Wallis analysis followed by Dunnett's multiple comparisons test in GraphPad Prism 6.0. Bottom panel: Component fractions of C1 and C2 obtained for CD28-sfGFP and sfGFP-ABCG2. 2-component analysis was performed in Zen 2010. Data were collected from at least 30 cells over 4 independent experiments.

6.6.4 Ratio of C2: C1 supports tetrameric formation for ABCG2 and CD28

As a separate indicator of the oligomeric state represented by C2 components for CD28-sfGFP and sfGFP-ABCG2, in which the C1 component was interpreted as the "unit" brightness for each protein. The C2: C1 molecular brightness ratios were then calculated using the paired C1 and C2 molecular brightness values obtained within the data sets. Figure 6.18 shows that mean C2: C1 ratios of 4.0 and 3.9 were obtained for the CD28-sfGFP and sfGFP-ABCG2 data sets, respectively. Assuming that component 1 is a monomer (with similar brightness to CD86-sfGFP as shown above), this 4x increase in molecular brightness of C2 supports tetrameric organisation of ABCG2, and the oligomer control CD28.

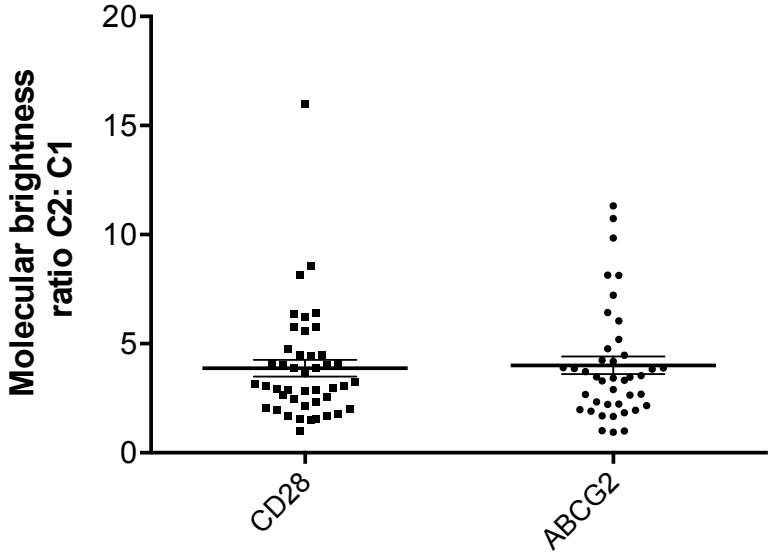

Figure 6.18: Molecular brightness ratios indicate possible tetrameric formation in ABCG2 and CD28. Molecular brightness of component 2 (C2) for CD28-sfGFP and sfGFP-ABCG2 were ratioed against the corresponding molecular brightness of component 1 (C1), paired values. Mean ± SEM of the data sets are shown. Data were collected from at least 30 cells over 4 independent experiments.

6.7 Discussion

6.7.1 Establishing diffusion coefficient of ABCG2 at "single molecule" level

The autocorrelation analysis combined with FCS measurements in this chapter provided detailed characterisation of ABCG2 diffusion in the plasma membrane at high spatial resolution, with an approximate sampling radius of 150 nm. The diffusion coefficients of membrane proteins obtained from the autocorrelation analysis (0.1-0.3 $\mu m^2 s^{-1}$) were comparable to the diffusion coefficients obtained in chapter 4 using FRAP microscopy (0.1-0.5 $\mu m^2 s^{-1}$). As FRAP measures particle diffusion over a much larger area (radius of 2 µm) compared to FCS, a reduction in diffusion coefficient measured using FRAP could suggest limited long-range diffusion of the membrane proteins and free diffusion of proteins could be restricted to small domains within the plasma membrane (Cezanne et al., 2004; Kilpatrick et al., 2012). This was not observed in this study, indicating that the diffusion of ABCG2 is not subjected to different short- or long-range diffusion constraints. Two recent studies reported similar diffusion coefficients (0.1-0.2 $\mu m^2 s^{-1}$) for GFP tagged adenosine A3 receptors and fluorescent proteins tagged NPY receptors, using similar FCS experimental set up (Corriden et al., 2014; Kilpatrick et al., 2012). This was expected, as the molecular weights of these receptors and ABCG2 are known to be similar (within a two-fold difference). Other FCS studies also reported diffusion coefficients of membrane proteins at similar range – 0.1 to 0.3 $\mu m^2 s^{-1}$ for interleukin-4 membrane receptors (Weidemann et al., 2011), and 0.5 to 0.8 $\mu m^2 s^{-1}$ for various GPCRs including the same fluorescent protein tagged controls CD86 and CD28 (Herrick-Davis et al., 2013). Together, these results confirmed the reliability of the FCS set up and autocorrelation analysis for the membrane proteins in this study. The 100-fold increase in *D* reported for the sfGFP and tandem-sfGFP in Figure S6.1 was not surprising as the values were within reasonable range when compared against other studies of GFP diffusion in nucleus (approximately 50 $\mu m^2 s^{-1}$) and cytoplasm (approximately 90 $\mu m^2 s^{-1}$) (Dross et al., 2009; Petrášek and Schwille, 2008). The 3D diffusion measurements of sfGFP and tandem-sfGFP were also

expected to be dissimilar compared to the restricted 2D membrane diffusion of ABCG2, CD28, and CD86.

6.7.2 Oligomerisation of ABCG2 demonstrated by FCS and PCH analysis

FCS diffusion results indicate likely oligomerisation of ABCG2

When investigating oligomeric EGFP mobility in live cell nuclei, Dross et al. reported similar changes in *D* as observed in Figure S6.1, in which a two-fold reduction in *D* was observed when comparing EGFP dimers against single EGFP (Dross et al., 2009). This consistent observation is surprising because according to the Stokes-Einstein formula, a two-fold decrease in *D* can only be achieved by an eight-fold increase in protein radius for freely diffusible spherical proteins (Lippincott-Schwartz et al., 2001). Figure 6.4 shows that there was only two-fold increase in molecular weight comparing sfGFP with tandem-sfGFP and the A206K sfGFP variant was employed to prevent self-association of GFP (Zacharias et al., 2002). This suggests that an eight-fold increase in protein size is unlikely. Hence, this 2x difference in *D* observed might imply that diffusion measurements obtained using FCS live cell experiments are very sensitive to changes in molecular weight in cell cytoplasm. As discussed in section 4.5.4 about the membrane proteins, proteins in cytoplasm could also exhibit anomalous diffusion due to the complex environment (Regner et al., 2013) and this may also account for the sizeable unexpected reduction in *D* of tandem-sfGFP compared to sfGFP.

The *D* of sfGFP-ABCG2 is approximately $^{1}/_{3}$ of CD86-sfGFP. As both molecules have similar molecular weight (approximately 100 kDa), this might suggest that sfGFP-ABCG2 exists as higher order oligomers (possibly more than 2-fold increase in size) compared to CD86-sfGFP. Although this proposition of ABCG2 oligomeric state using the *D* is plausible, it is important to consider the environmental factors that could affect the diffusion of membrane proteins as summarised in chapter 4 (sections 4.5.3 and 4.5.4). Most importantly, the

membrane topology of CD86 is different compared to ABCG2, with CD86 having fewer transmembrane segments than ABCG2 (1 compared to 6), and this could also affect the diffusion of the membrane proteins (Saxton and Jacobson, 1997). Therefore, it is difficult to interpret the oligomerisation of cellular proteins based on the changes in *D* and their predicted molecular weights, due to potential effects of other factors on the diffusion of proteins.

PCH analysis shows ABCG2 exists as higher order oligomeric species

As the diffusion coefficient analysis alone was not sufficient for the characterisation of ABCG2 oligomerisation, PCH analysis was employed in this chapter to provide a more insightful demonstration of protein oligomerisation (Müller et al., 2000). The two-fluorophore species (tandem-sfGFP) was first established to have double the molecular brightness compared to the single-fluorophore species (sfGFP), as reported elsewhere (Chen et al., 2003). The 1-component PCH analysis (Figure 6.16) suggests that CD28 and ABCG2 could exist as dimers, on the assumption that that CD86 is a monomer, as determined using several methods (Dorsch et al., 2009; Herrick-Davis et al., 2013; Zhang et al., 2003). In a similar manner, Herrick-Davis et al. also reported dimer formation of various GPCRs (muscarinic, dopamine, 5-HT receptorss and β2-adrenoceptors) when their molecular brightness were compared to those of CD28 and CD86 using a 1-component PCH analysis (Herrick-Davis et al., 2013). The lower than expected increase in molecular brightness observed for CD28 and ABCG2 compared to CD86 (1.7- and 1.4-fold instead of 2-fold) could be attributed to the higher expression of CD86 (higher concentrations shown in Figure 6.12) leading to increased chances of aggregation and therefore higher average molecular brightness obtained (Chen et al., 2003). This observation (lower than expected increase in molecular brightness) could also suggest existence of single-fluorophore species within CD28 and ABCG2, possibly caused by existence of non-fluorescent sfGFP (see later). 2-component PCH analysis suggests that the latter is likely since a second component was not detected in the CD86 data sets but was seen in the CD28 and ABCG2 data sets (Figures 6.17 and S6.7). In

line with this argument, the 2-component PCH model was also shown to be a better fit for the CD28 and ABCG2 data sets (Figure S6.6A). The same 2-component PCH model was also employed elsewhere to demonstrate aggregation of NPY receptor and β-arrestin complexes (Kilpatrick et al., 2012). The results in Figure 6.17 suggest the presence of more than 1 fluorescent species within the CD28 and ABCG2 samples and that the second component could exist as higher order oligomer states, with 2- to 3-fold higher molecular brightness compared to CD86. In fact, analysis of the C2: C1 ratios of CD28 and ABCG2, in which C1 is interpreted as a "monomeric unit" for each protein, indicates that both CD28 and ABCG2 might exist as tetramers (Figure 6.18). The detection of monomeric fluorescent species in ABCG2 (C1 of 2-component PCH analysis) was unexpected as the known minimal functional unit for ABCG2 is a dimer. The biological significance of this is still unclear, however, this could also be due to the existence of non-fluorescent sfGFP molecules resulting lower than expect brightness for multiple fluorophore particles (see next section).

An in-depth review of the evidence on ABCG2 oligomerisation thus far is presented in section 1.6. In short, studies have suggested that ABCG2 should function at least as a dimer, and could exist as tetramers and higher order oligomers. This evidence was obtained using biochemical studies such as non-reducing SDS-PAGE analysis (Litman et al., 2002), gel filtration chromatography (Xu et al., 2004), and electron microscopy analysis of purified proteins (Dezi et al., 2010; McDevitt et al., 2006) in yeast and mammalian cells. Fluorescence microscopy studies (FRET and BiFC) on ABCG2 expressed in mammalian cells suggested oligomerisation of ABCG2 but did not produce any indication on the oligomeric state of ABCG2 (Haider et al., 2011; Ni et al., 2010), see chapter 5. Results in this chapter present a novel finding where for the first time, higher order oligomeric state of ABCG2 were demonstrated in live cell experiments. Although CD28 was thought to exist as dimer (Dorsch et al., 2009), the suggestion of CD28 existing as an exclusive dimer has not been

conclusive in other studies (Greene et al., 1996; James et al., 2007; Lazar-Molnar et al., 2006; Tacke et al., 1997), and higher order oligomer formation of CD28 is plausible. Hence, the results in this chapter suggesting potential tetrameric organisation of CD28 are not unreasonable. The oligomeric states of ABCG2 and CD28 were further investigated using TIRF stepwise photobleaching method in chapter 7 and extensive discussions will be presented in section 7.5.1.

6.7.3 Experimental limitations

Criteria for autocorrelation analysis

To ensure robust autocorrelation analysis, only appropriate measurements were analysed (e.g. *G(τ)* reach an asymptote of 1.0), see examples in section 6.4. The measurements that did not meet the required criteria are likely to be caused by potential clustering of the fluorescent proteins or continuous photobleaching during data collection. Further analysis of the traces shows that rejected traces were highest in the CD86-sfGFP data set. Figure 6.12 shows that CD86-sfGFP has the highest concentrations compared to CD28-sfGFP and sfGFP-ABCG2. This could explain the increased likelihood of clustering of CD86-sfGFP fluorescent molecules detected during data acquisition and the difficulty in selection of low expressing cells during the experiments. The final results presented were obtained from the accepted measurements that allow accurate analysis with the FCS and PCH models.

Effects of binning time on PCH analysis

The effects of binning time on PCH analysis were also investigated in this study to ensure that 1 ms was a suitable binning time of choice. The PCH theory assumes that the particles remained within the detection volume during the sampling/binning time. If the binning time size is too large, it could lead to under-sampling (e.g. 5 ms binning time sampling of a 10 s trace would result in 2000 total bins compared to 10000 bins for 1 ms binning time, Figure 6.14). The binning time chosen should be faster than the dwell time (τ_D) of

the fluorescent protein of interest as PCH models assume that the fluorescent proteins are immobile during the sampling period (Macdonald et al., 2013; Perroud et al., 2005). However, if the binning time size chosen is too small, the signal-to-noise ratio of the analysis will be reduced, and fewer photons are collected per bin, Figure 6.14 (Wu and Müller, 2005). Larger binning time size is however beneficial to reduce the molecular brightness contribution from fluctuations of the fast-moving component (τ_{D1}) caused by GFP photophysics, and to ensure that the molecular brightness was mostly contributed by the slow-moving component (τ_{D2}), which is the membrane fluorescent protein of interest (Kilpatrick et al., 2012). The large differences (more than 100-fold) in dwell times between the proteins in the cytoplasm (sfGFP and tandem-sfGFP) and the membrane proteins (CD86-sfGFP, CD28-sfGFP and sfGFP-ABCG2) meant that it was impossible to use a binning time that is suitable for both. Additionally, dwell times of sfGFP and tandem-sfGFP (approximately 0.15-0.5 ms) were identical to those of τ_{D1} photophysics (approximately 0.3-0.8 ms) and two-component autocorrelation analysis could not separate the two in the sfGFP and tandem-sfGFP data sets. The final binning time chosen for all the PCH analysis in this study was 1 ms, which was only appropriate for the membrane proteins of interest. Therefore, the PCH results of sfGFP and tandem-sfGFP in Figures 6.13 and S6.2 were subject to an under-sampling effect. Nonetheless, analysing these data sets with faster binning time (0.1 ms) did not alter the conclusions of a 2-fold increase in molecular brightness of tandem-sfGFP compared to sfGFP (data not shown).

Adequacy of PCH models and other presence of other artefacts in PCH analysis

In this study, the 1-component and 2-component 3D PCH models available in Zen 2010 were employed to analyse the FCS traces. Although the same PCH models were employed previously to determine the molecular brightness of membrane proteins (Herrick-Davis et al., 2013; Kilpatrick et al., 2012; Youker et al., 2013), there are deficiencies in these models and these can lead to ambiguity in the molecular brightness results. First, the molecular brightness

values of the membrane proteins with 2D diffusion were obtained from 3D PCH models and this could introduce inaccuracy or errors when fitting the experimental distributions. The potential use of 2D models in PCH analysis is currently under development and could be employed as the model of choice in the future for PCH analysis of membrane proteins when they become readily available (Anikovsky et al., 2011). Second, although it has "single molecule" resolution, FCS measures the fluctuations of a number of particles during the data acquisition and the average ensemble molecular brightness of the particles in the confocal volume was obtained, instead of the molecular brightness of the individual fluorescent particles. The 2-component PCH model is also unlikely to resolve brightness of multiple components accurately when there are more than 2 fluorescent species involved. A global analysis was previously employed to analyse sample with more than 2 fluorophore species but was found to be insufficient to describe the model experiment (Müller et al., 2000), and a suitable multiple component PCH analysis is yet to be established. The degree of variability in the PCH data sets shown in Figures 6.16 and 6.17, particularly CD28 and ABCG2, could indicate possible presence of multiple oligomeric species detected in the sample.

Additionally, the properties of the fluorophore, which are detectable by the highly sensitive nature of the FCS, could also introduce systemic errors in this study and these could not be accounted for appropriately in the models employed. These factors could contribute to the presence of apparently monomeric fluorescent species found in the CD28 and ABCG2 data sets from the 2-component PCH analysis (Figure 6.17) and this will also be discussed in section 7.5.3 later. Several factors have been suggested to lead to non-fluorescent proteins and underestimation of the oligomeric state of fluorescent particles using PCH analysis: (Chen et al., 2010)

1. Quenching caused by changes in microenvironment (e.g. pH and fusion protein)
2. Presence of long-lived dark state of the fluorophore

3. Incomplete fluorescent protein maturation

For example, the same group of authors reported that the red fluorescent protein (mRFP1) has a higher portion of long-lived dark state than EGFP (Hillesheim et al., 2006), making mRFP less suitable for brightness measurements (Chen et al., 2003). However, these authors also observed lower than expected brightness for the EGFP dimer controls on some occasions (less than two times brightness compared to single EGFP), and suggested that non-fluorescent EGFP is possible due to incomplete maturation of the fluorescent protein (Chen et al., 2010). Interestingly, the authors also suggested that dimerisation of EGFP-fusion proteins could also lead to reduction in brightness, possibly due to quenching of the fluorophores (Chen et al., 2010). Overall, the limits to which the PCH models can resolve multiple fluorescent species and the presence of non-fluorescent GFP are likely to affect the molecular brightness results. Therefore, the molecular brightness ratios among the fusion membrane proteins (with similar microenvironments) were regarded as the key results for the final interpretation whilst the molecular brightness of sfGFP and tandem-sfGFP were only used for validation of the PCH analysis. Also, although the molecular brightness ratios provided good quantitative indicators of ABCG2 oligomerisation in living cells for the first time, the interpretation of the results relies on the assumptions of the "unit" brightness component (C1), which was assumed to be a monomer on the basis of the expected behaviour of CD86.

6.7.4 Concluding remarks

In conclusion, by employing "single molecule" resolution FCS measurements, the diffusion and molecular brightness results here presented novel evidence of multiple ABCG2 oligomeric species, including tetrameric formation, in live cells. Although PCH results indicate that ABCG2 could exist as tetramers, these conclusions depend on key assumptions, such as the brightness of a "monomeric unit", and the observation that CD28 may form higher order

oligomers (compared to dimers as suggested previously). The current PCH models are limited to separating a maximum of two fluorescent species components and will require further fine-tuning and modifications. Additionally, this technique measures the average molecular brightness of a number of particles at “single molecule” level but does not identify the molecular brightness of the individual fluorescent particles. Therefore, total internal reflection fluorescence (TIRF) microscopy in combination with stepwise photobleaching analysis was employed in the next chapter to establish the oligomeric state of ABCG2 by resolving some of the limitations of PCH analysis.

Chapter 7 Total internal reflection fluorescence microscopy and stepwise photobleaching analysis to resolve the oligomerisation of ABCG2

In the previous chapter, brightness analysis of FCS measurements (PCH) indicated tetrameric formation of ABCG2 in live cells. This suggestion was potentially limited by factors such as the appropriate reference controls to clearly define monomer and dimer species and the non-optimal PCH models used to estimate average molecular brightness albeit at "single molecule" resolution. Therefore, an imaging technique that allows single particle imaging of fluorescently labelled ABCG2 is desirable, to provide a clear illustration of ABCG2 oligomerisation. In this chapter, the combination of total internal reflection fluorescence (TIRF) microscopy and stepwise photobleaching analysis to elucidate the oligomerisation of ABCG2 will be presented. The theories and applications of TIRF microscopy and stepwise photobleaching analysis will be first described, followed by an explanation of the automated step detection algorithm to analyse the acquired TIRF videos. Finally, statistical modelling of the final photobleaching step distributions to determine the oligomeric state of ABCG2 will be discussed.

7.1 Background and theory – TIRF microscopy and stepwise photobleaching analysis

David Axelrod first combined total internal reflection fluorescence (TIRF) illumination and cellular microscopy in the 1980s and provided means of selective visualisation of fluorophores close to the excitation surface in cellular environment (Axelrod, 1981). TIRF microscopy excites fluorophores through the generation of an evanescent field resulting in a thin layer of

excitation of the sample. This enables fluorescence detection of in-focus fluorophores within a limited *z*-axis depth, with reduced "out-of-focus" contribution from fluorophores above or below this region. Since its establishment, TIRF microscopy has been widely applied in biochemistry and cell biology and some of these applications will be discussed in the following sections.

7.1.1 Evanescent field theory

The principle of TIRF illumination is based on the production of an evanescent field generated by refraction of the excitation light arriving at the plane of incidence between two mediums of different refractive indices (*n*). Figure 7.1 below provides an illustration of this phenomenon as the excitation light (purple) propagates from the glass (higher refractive index) to the aqueous medium (lower refractive index). Refraction is governed by Snell's law where:

$$n_1 * sin\,\theta_1 = n_2 * sin\,\theta_2$$

As light propagates through a medium of higher refractive index (n_1) into a medium of lower refractive index (n_2) the angle of the subsequent refracted beam (ϑ_2) is affected by the initial angle of incidence (ϑ_1), see Figure 7.1. If ϑ_1 reaches a "critical angle" (ϑ_c), the refraction direction of the excitation light becomes parallel to the plane of incidence, and ϑ_2 = 90° (i.e. sin ϑ_2 = 1). Hence, the ϑ_c is given the by the simplified Snell's function:

$$\theta_c = sin^{-1}\left(\frac{n_2}{n_1}\right)$$

When $\vartheta_1 > \vartheta_c$ (also known as the supercritical angles), the excitation light is completely reflected back into the medium of high refractive index (the glass, as shown in Figure 7.1). This is known as total internal reflection (TIR). Although light does not then propagate through the aqueous medium, this phenomenon results in the generation of an electromagnetic field in the aqueous medium adjacent to the plane of incidence, also known as the evanescent field (Figure 7.1). The intensity of this evanescent field decreases

exponentially as it propagates into the aqueous medium, thereby generating a thin layer of excitation (approximate 100 nm) of the sample above the plane of incidence (Axelrod, 2001; Mattheyses et al., 2010).

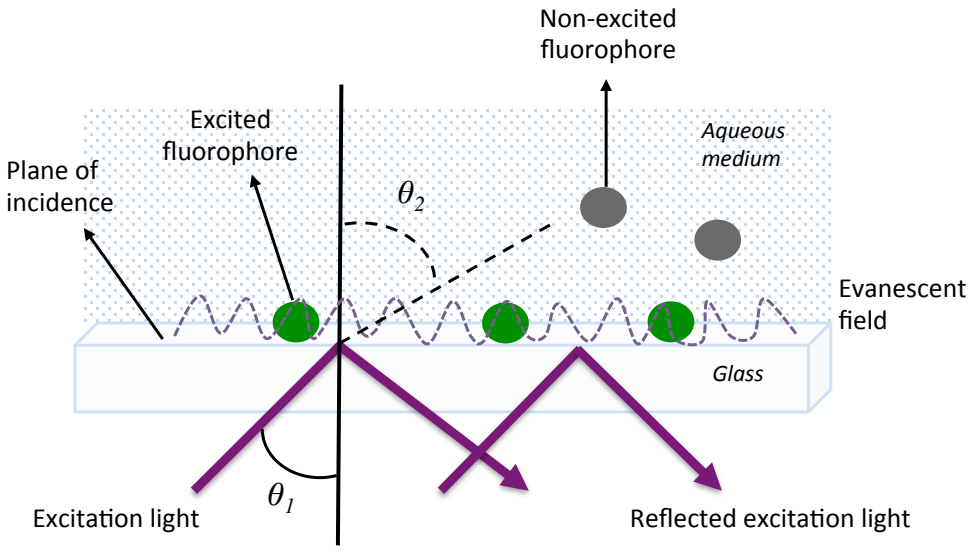

Figure 7.1: Schematic illustration of the generation of an evanescent field through the total internal reflection phenomenon. As the excitation light propagates from a high refractive index medium (glass) into the lower refractive index medium (aqueous medium) at an angle of incidence (ϑ_1) larger than the 'critical angle', excitation light is reflected back into the glass medium. This total internal reflection phenomenon generates an evanescent field of excitation at the glass-aqueous medium interface, yielding a thin layer of excitation, an advantage exploited in TIRF microscopy for single particle imaging. Figure adapted from *Nikon MicroscropyU* (Ross, S.T., Schwartz, S., Fellers, T.J., and Davidson, M.W. TIRF microscopy: Introduction and application, http://www.microscopyu.com, accessed 15/11/2014).

7.1.2 TIRF microscopy instrumentation

Most commercial or "home made" TIRF systems employ lasers as the source of excitation and a high numerical aperture objective to achieve large incident angles (ϑ_1) required for the TIR phenomenon as illustrated in Figure 7.1 above. This is also known as the through-the-objective TIRF illumination method (Mattheyses et al., 2010). Figure 7.2 below compares the differences between the TIRF and epifluorescence illumination methods, in which the reduced depth of excitation generated in TIRF is desirable, approximately 100 nm in TIRF compared to > 800 nm in epifluorescence. The modifications of the entry position of the excitation beam and utilisation of a high numerical aperture objective are the main differences between the two illumination

methods. In TIRF, the excitation beam (purple lines and arrows in Figure 7.2A) is positioned away from the optical axis at the back focal plane of the objective and the incident angle is increased as the excitation beam is positioned further away from the optical axis. The numerical aperture (NA) of an objective describes its ability to gather light and the maximum angle at which the excitation light can emerge from the objective. This is described by the following equation:

$$\mathrm{NA} = n * \sin\theta$$

Where n is the refractive index of the sample and ϑ is the angle of the refracted beam measured from the optical axis. According to Snell's Law (see above), for TIR to occur, the NA of the objective must be greater than the refractive index of the sample (so ϑ > 90°). The refractive indices for water and cytoplasm are 1.33 and 1.38 respectively; hence, the common objectives employed in TIRF microscopy have an NA of at least 1.45 (Axelrod, 2001; Mattheyses et al., 2010). The radial position of the excitation beam and the numerical aperture of the objective employed are therefore established as the vital components in TIRF microscopy.

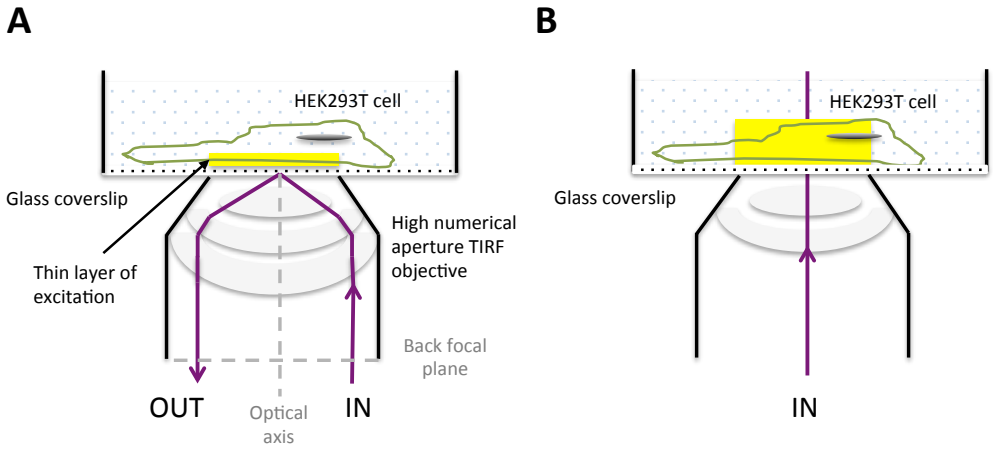

Figure 7.2: Schematic representations to compare TIRF and epifluorescence illumination methods. A – TIRF illumination of the sample (e.g. HEK293T cell) is achieved using a high numerical aperture objective and by positioning the excitation beam away from the optical axis at the back focal plane of the objective. A thin layer of excitation (yellow) is produced at the lower plasma membrane just above the coverslip. **B –** Standard epifluorescence illumination of the HEK293T cell produces increased excitation depth in the cell (yellow), compared to TIRF illumination.

7.1.3 Single particle imaging in TIRF and stepwise photobleaching analysis

The ability of TIRF microscopy to produce selective excitation at the glass coverslip, as shown in Figures 7.1 and 7.2A, is beneficial for high resolution investigation of cellular trafficking and accurate determination of protein kinetics at the cell surface. In the early 2000s, Axelrod summarised several key applications of TIRF microscopy in biochemistry and cell biology, such as visualisation of single fluorescent particles, tracking of secretory granules in cells, and determination of micro-morphological structures and dynamics in living cells (Axelrod, 2001). One of the foremost applications in TIRF microscopy routinely employed today is the detection of single fluorescent particles in the plasma membrane. Sako et al. first described the use of single particle TIRF imaging to visualise and detect the dimerisation of the epidermal growth factor receptor (EGFR) in combination with FRET measurements. The EGFR molecules were labelled using Cy3 and Cy5 fluorophores and they were visualised as single fluorescent spots in the plasma membrane of A431 carcinoma cells (Sako et al., 2000). Iino et al. then demonstrated the oligomerisation of GFP-tagged E-cadherin molecules using single particle TIRF imaging methods by analysing the intensities and diffusion of the fluorescent spots (Iino et al., 2001).

The single fluorescent spots resolved by TIRF microscopy on the plasma membrane could represent single fluorescent molecules, or more importantly oligomers of a fluorescent species. Therefore, photobleaching of these spots over time should occur in a number of discrete steps, allowing the potential of this technique to determine the molecular composition of the fluorescent spots. Mashanov et al. were the first to demonstrate this by reporting single step photobleaching behaviour of immobilised single GFP molecules (Mashanov et al., 2003). Subsequently, a variation in photobleaching step behaviour of GFP tagged MotB molecules was observed in a study where the total of number of GFP-MotB molecules per motor was estimated by dividing

the total intensity of individual fluorescent spots by the average intensity of an untagged GFP molecule (Leake et al., 2006).

Accurate determination of oligomeric organisation using this photobleaching technique requires first the identification of fluorescence intensities of many individual fluorescent spots over time and second the identification of the "photobleaching steps" extracted from background photobleaching or fluorescence decay. Ulbrich and Isacoff addressed these by developing a novel TIRF imaging and stepwise photobleaching method to determine the subunit composition of glutamate NMDA receptors in *Xenopus laevis* oocytes. The GFP-tagged NMDA receptors were immobile when expressed in *X. laevis*, and this allowed for feasible spot selection and fluorescence intensity determination over time. Additionally, low expression of GFP-tagged NMDA receptors can be easily achieved by controlling the expression levels in *X. laevis*. Low-pass and high-pass filters were applied to the final images to remove the background fluorescence and Poisson noise within the fluorescence intensity traces for final extraction of photobleaching steps (Ulbrich and Isacoff, 2007). Figure 7.3 below shows a schematic representation of this method where photobleaching of single fluorescent spots can reveal the oligomeric state of fluorescent proteins of interest in a stepwise manner.

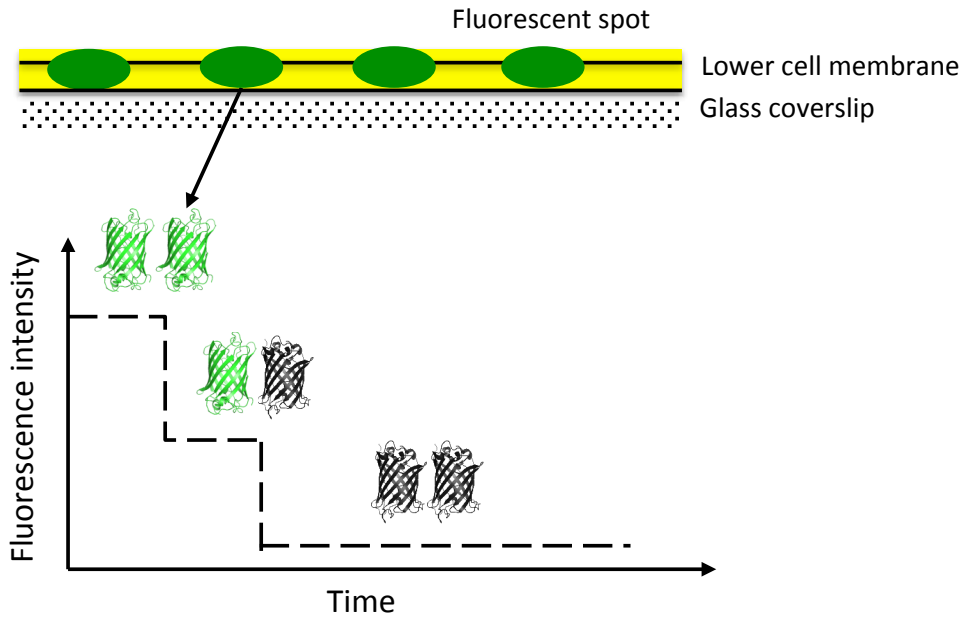

Figure 7.3: Illustrative representation of single particle TIRF imaging in combination with stepwise photobleaching analysis to determine the oligomeric state of fluorescent membrane proteins.

This method has since then become popular and employed in no less than 50 different studies (see recent mini-review by (Arant and Ulbrich, 2014)). It is of no surprise that due to the ability of TIRF to directly illuminate the lower plasma membrane in the sample, most of these studies were perform to investigate fluorescently labelled membrane proteins expressed in *X. laevis* oocytes or mammalian cells. Within their research groups, M. H. Ulbrich and E. Y. Isacoff have successfully identified the subunit compositions of the voltage-sensing phosphatase (Kohout et al., 2008), the potassium channel complex of KCNQ1 and KCNE1 (Nakajo et al., 2010), the acid sensing heteromeric complex (Yu et al., 2012), and the organisation of glutamate receptors such as the NMDA receptors (Ulbrich and Isacoff, 2007, 2008), the kainate receptors (Reiner et al., 2012), and the AMPA receptors (Hastie et al., 2013). Various other research groups have also applied the stepwise photobleaching analysis method in mammalian cells to determine the subunit organisation of membrane proteins (see Table 7.1 below). The protein subunit organisation of functional ion channel complexes has been extensively studied using the TIRF stepwise photobleaching method in

mammalian cells. For example, results from Ji et al. and Demuro et al. together have successfully resolved the subunit organisation of STIM (stromal interaction molecule) and Orai proteins in the formation of functional store-operated calcium channels in resting and activated states (Demuro et al., 2011; Ji et al., 2008). This technique was also employed to determine the changes in the oligomerisation of tumour growth factor β receptor and ABCA1 cholesterol transporter in the presence of ligands/substrates (Nagata et al., 2013; Zhang et al., 2009b, 2010). In the studies of CFTR (cystic fibrosis transmembrane regulator) and SERT (serotonin transporter) oligomerisation, the authors employed stepwise bleaching analysis as a complementary method to supplement their conclusions obtained from brightness/intensity analyses (Anderluh et al., 2014; Haggie and Verkman, 2008).

Although the underlying theory is identical, the means of applying spot bleaching methods vary considerably among the studies listed in Table 7.1. For example, McGuire et al. demonstrated the oligomeric state of two well known receptors (GluK2 and glycine-α receptors) in mammalian HEK293 cells using a fully automated system (PIF algorithm) for unbiased selection of fluorescent spots and detection of photobleaching steps developed in-house. This method has a potential advantage over the majority of the TIRF stepwise photobleaching studies where spot selection and analysis of photobleaching steps were performed manually (Arant and Ulbrich, 2014).

Table 7.1: Subunit and complex organisation of the proteins investigated using single particle TIRF imaging and stepwise bleaching analysis. "Monomeric" denotes the presence of A206K mutation in the GFP variant employed by the authors to reduce dimerisation of GFP.

Protein complex/subunits investigated	Fluorescent proteins/Dye used	Expression systems	References
Calcium channels (Orai 1)	EGFP	Fixed HEK293 cells	(Ji et al., 2008)
Calcium channels (Orai 1 and 3)	EGFP	Fixed and live HEK293 cells	(Demuro et al., 2011)
CaCC, calcium activated chloride channels	EGFP	Fixed HEK293 cells	(Ohshiro et al., 2014)
Potassium channels (K2P1) Potassium channels (Kv2.1) Potassium channels (I_{Ks})	EGFP	Live CHO cells	(Plant et al., 2010) (Plant et al., 2011) (Plant et al., 2014)
TRP channel (TRPM8)	EGFP	Live HEK293 or F11 cells	(Veliz et al., 2010)
Glutamine receptor (GluK2) Glycine α1 receptor	Monomeric sfGFP	Fixed HEK293 cells	(McGuire et al., 2012)
ABCA1 cholesterol transporter	Monomeric EGFP	Live HeLa cells	(Nagata et al., 2013)
ABCC7/CFTR, Cystic fibrosis transmembrane regulatory	EGFP	Live COS7 and CHO cells	(Haggie and Verkman, 2008)
SERT, Serotonin transporter	Monomeric EGFP	Live HEK293 cells	(Anderluh et al., 2014)
TGFβ receptors type 1,2, and 3	EGFP, DBCO545	Live HeLa, MCF7 cells and cardiomyocytes	(Cheng et al., 2014; He et al., 2011; W. Zhang et al., 2010; W. Zhang et al., 2009)
Toll-like receptor 4	EGFP	Fixed DC2.4 (dendritic cells)	(Wang and Yang, 2014a)
Insulin receptor	EGFP	Fixed MDA-MB-231 cells	(Wang and Yang, 2014b)
Prestin (membrane motor protein)	EGFP	Membranes of lysed HEK293 cells	(Hallworth and Nichols, 2012)

7.1.4 Aims of current study

In chapter 6, stable low expressing clones of HEK293T cells expressing sfGFP-ABCG2 and CD28-sfGFP were generated and characterised. PCH analysis indicated that both ABCG2 and CD28 could potentially exist as dimers or higher order tetramers. However, the results were limited by several factors and the suggestions remained inconclusive. The same cell lines were further investigated in this chapter using single particle TIRF imaging and stepwise photobleaching analysis to establish the oligomeric organisation of ABCG2.

7.2 TIRF imaging and photobleaching

In contrast to PCH analysis (which was performed on data obtained from live cells), it was necessary to perform TIRF imaging using fixed cells to ensure fluorescent spots remained stationary throughout the acquisition period. Figure 7.4 below shows the images of a HEK293T cell expressing sfGFP-ABCG2, acquired using epifluorescence illumination at the equatorial level (Figure 7.4A) and TIRF illumination at the lower plasma membrane (Figure 7.4B). Low expressing cells were chosen (see section 2.10.1) to ensure that the individual fluorescent spots were visibly separated in the TIRF images (Figure 7.4B). Figure 7.4C shows progressive photobleaching of the same cell under TIRF illumination at high laser power. Images were captured at 10 Hz (100 ms per frame), and complete photobleaching was observed after 15 s. TIRF videos obtained in Zen 2012 were subsequently converted to 8-bit *TIF* videos as described in section 2.10.1 before they were analysed using the PIF algorithm (developed by McGuire et al).

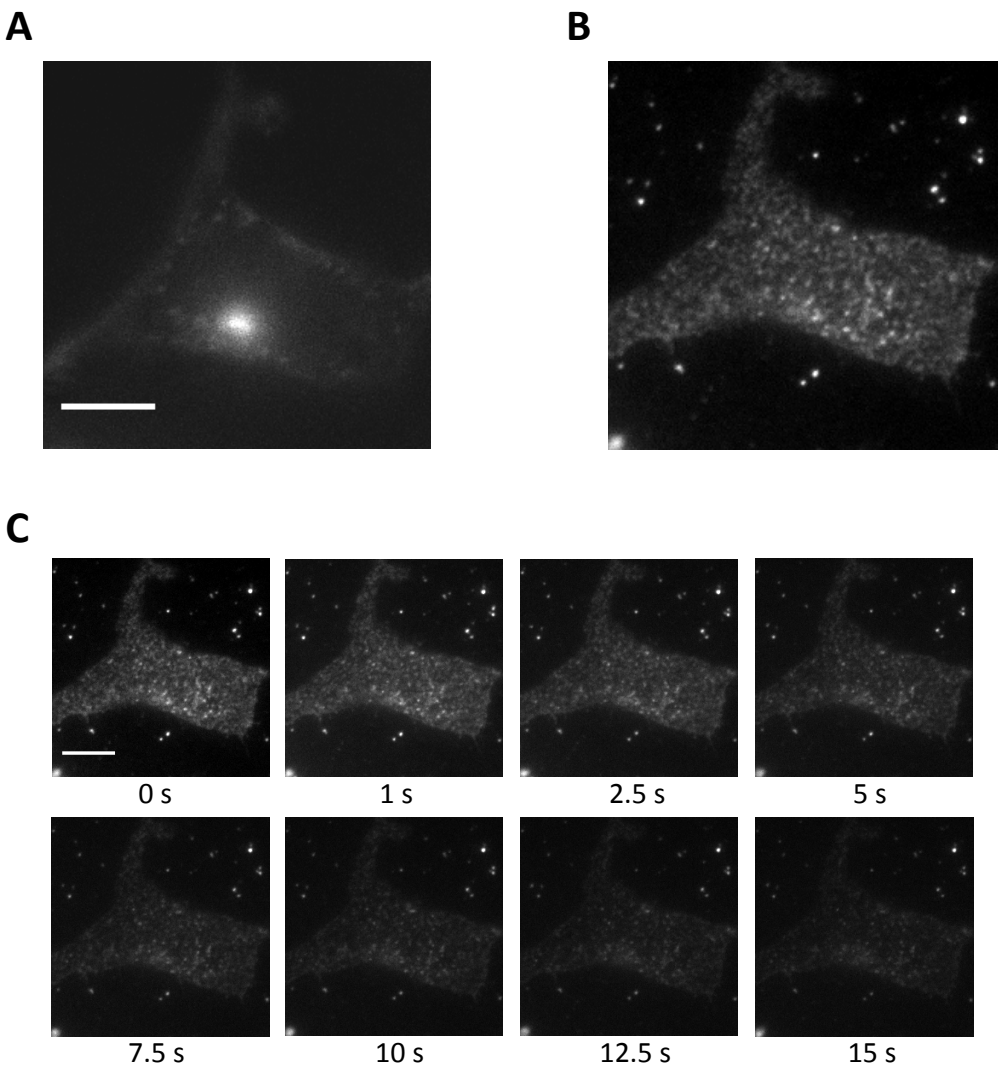

Figure 7.4: Epifluorescence and TIRF imaging of a fixed HEK293T cell expressing sfGFP-ABCG2. A – Epifluorescence image of the cell at equatorial focal plane acquired using standard acquisition laser power. **B –** TIRF image of the cell at lower plasma membrane focal plane acquired using high laser power, prior to photobleaching. **C –** Photobleaching images of cell in B from 0 to 15 s under TIRF configuration. **A and C –** Scale bar = 10 µm

7.3 Stepwise photobleaching analysis

The fully automated PIF algorithm was subsequently employed to perform stepwise photobleaching analysis on the TIRF videos acquired as described above (McGuire et al., 2012). The algorithm first identifies the stationary fluorescent spots, calculates their fluorescence intensities over time, and finally detects the number of discrete photobleaching steps in the spot fluorescence intensity traces. Figure 7.5 below provides an illustration of the analysis of a TIRF photobleaching video using the PIF algorithm. First, the

region of interest (ROI) was drawn manually in the software (Figure 7.5A). The algorithm parameters for subsequent analysis were then specified. Table 7.2 below provides a summary of the key parameters and these were described in detail in section 2.10.2. Several parameters were pre-determined by performing analysis of the intensity distributions prior to data collection as discussed in the following sections. The individual fluorescent spots were then identified. Figure 7.5B shows a screen shot of the spots selected (red) within the sample image at 0 s. The fluorescence intensity traces were calculated for the individual fluorescent spots, as described in section 2.10.2. Figure 7.5C shows an example of a raw fluorescence intensity trace from one of the fluorescent spots detected within the cell. The background fluorescence intensity within the raw traces was subsequently removed using a LoG filter, revealing the photobleaching steps and allowing for the final step detection process by the algorithm, as illustrated Figure 7.5D below.

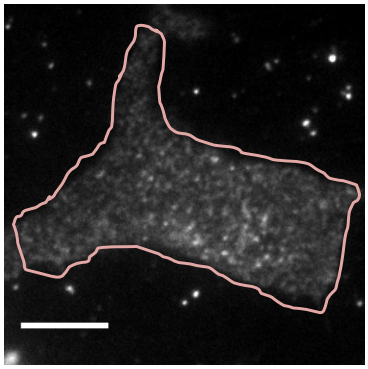

A. Define region of interest

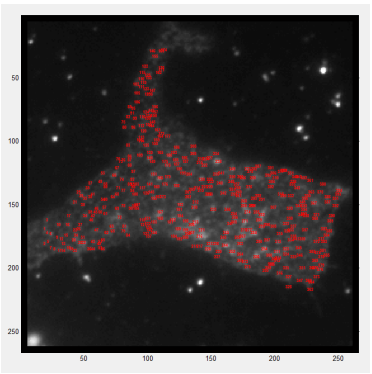

B. Spot selection

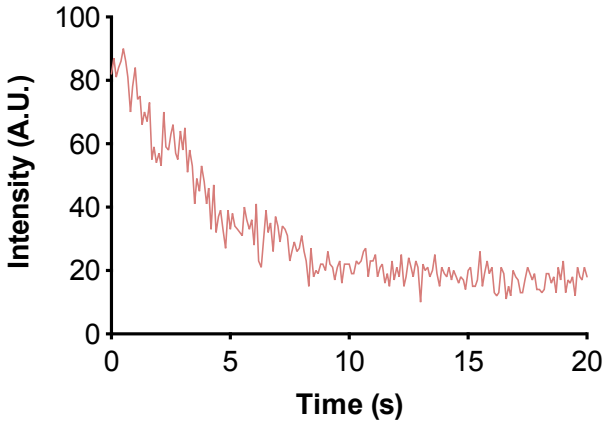

C. Fluorescence intensity trace calculation

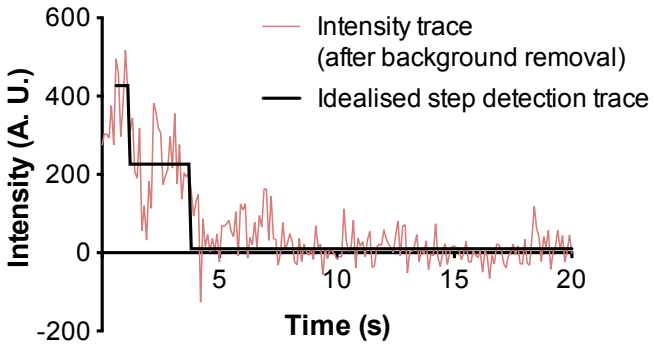

D. Background removal and step detection

Figure 7.5: Automated PIF algorithm used for stepwise photobleaching analysis of the TIRF videos. Example analysis of the TIRF data in Figure 7.4 is shown here. **A –** Manual definition of the region of interest (ROI). The whole cell region was chosen as the ROI. Scale bar = 10 µm. **B –** Automated spot selection performed by PIF algorithm based on the chosen parameters, see section 2.10.2. **C –** Example fluorescence intensity trace calculated from one of the fluorescent spots selected in in panel B. **D –** Trace filtration and photobleaching step detection. Background fluorescence was removed using LoG filter and the intensity here was calculated using a reference theoretical estimation (section 2.10.2). Hence, the absolute fluorescence intensities in C and D are not comparable. Photobleaching step detection within the fluorescence intensity traces was also shown in the example trace.

Table 7.2: Key parameters defined for stepwise photobleaching analysis of the TIRF videos using PIF algorithm. The parameters that required pre-determination ('max no of neighbours', 'minimum amplitude', 'fixed sigma' and 'min. step amplitude') were highlighted in blue, respectively. The other parameter highlighted in purple, 'step/noise ratio (SNR)', will be discussed further in section 7.5.4. See section 2.10.2 for a full description of the algorithm parameters.

General parameters	Spot detection	Filter	Step detection	Accepted/ Rejected
Time per frame 100 ms Starting frame no. 1 No. of average frames for image display 20 No. of average frames for baseline estimation 20	*Max. no. of neighbours* 2 *Minimum amplitude* 150 δF/F 10%	**Background removal** ☑ Fix filter size ☑ *Fixed sigma* 1.6 ☑ Symmetric filter Intensity calculation ☑ Theo. LoG intensity **Trace filter** ☐ Chung-Kennedy ☐ if SNR < 1.8	**1st approx. step detection** First SNR 0.75 Progress fraction 10 Progress fraction 1000 Min step length 3 Amp. Tolerance 0.6 *Min. step amplitude* 75	Proximity sigma 1.25 Counter fit/fit 1 Reduced chi^2 max. 1.5 Max. step amplitude 900 *Step/noise ratio (SNR) >* 1.6

7.3.1 Algorithm optimisation: pixel size of fluorescent spots

The first parameter that required determination prior to the individual cell analysis is the size of the fluorescent spots in the TIRF images, which is defined by the acquisition system. This is represented as the 'max no of neighbours' in the algorithm (see Table 7.2). In McGuire et al, a camera with a pixel size of 24 µm and a 60x TIRF objective were employed for acquisition, yielding fluorescent spots with the size of 3 x 3 pixels. This results in a 'max no of neighbours' of 1, indicating that the centre pixels of the selected fluorescent spots have a maximum of one neighbouring pixel. However, a different acquisition system (with a camera of 16 µm pixel size and a 100x TIRF objective) was employed in this study. Therefore, this parameter was determined by careful examination of the TIRF images generated. Figure 7.6 shows a magnified pixel-by-pixel image (from the example cell shown in Figure 7.4B). Fluorescent spot selections using two different spot sizes, 5 x 5 pixels (Figure 7.6A) and 3 x 3 pixels (Figure 7.6B), were compared. This comparison indicated that most fluorescent spots were adequately selected with 5 x 5 pixels. The 'max no of neighbours' parameter was therefore set to 2, allowing two neighbouring pixels from the centre pixels for the selected spots, as also recommended by the PIF algorithm authors for equivalent TIRF acquisition set ups. Figure 7.6A also shows possible overlapping of fluorescent spots (orange and light blue dotted lines) within the TIRF image that would be rejected by the spot selection algorithm if they were too close to each other. This rejection is based on the 'proximity sigma' parameter (Table 7.2), described in more detail in section 2.10.2 '*Fluorescent spots selection and fluorescence intensity calculation*'.

A

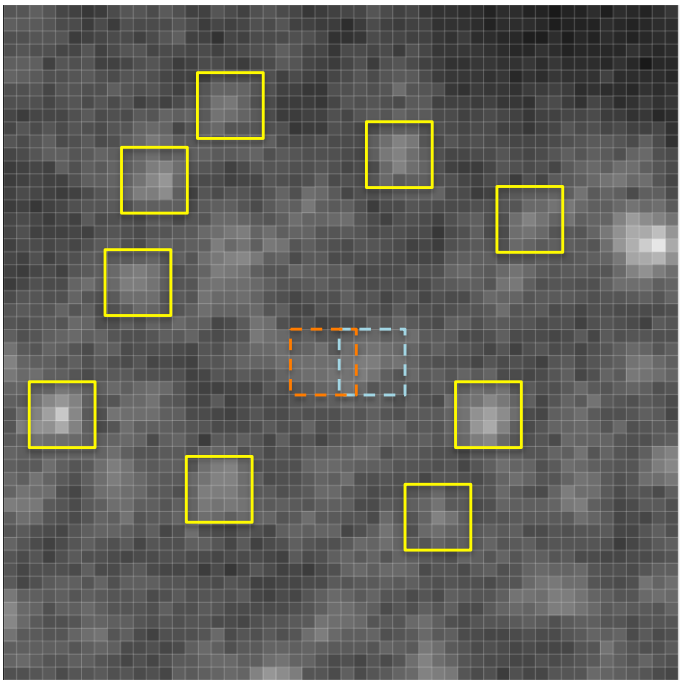

B

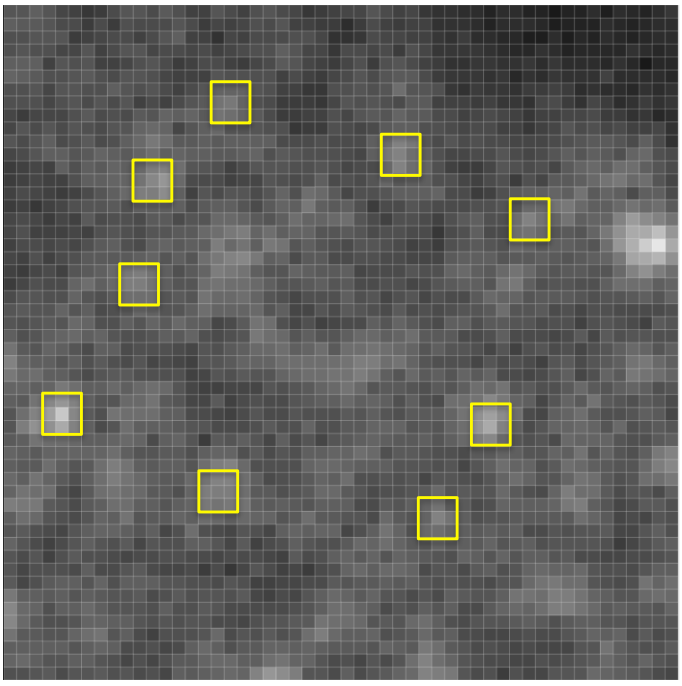

Figure 7.6: Magnified pixel-by-pixel of raw TIRF images for the determination of fluorescent spots size. Magnified images generated from TIRF example data shown in Figure 7.4. Fluorescent spots were selected manually using two different sizes, 5 x 5 pixels (**A**) or 3 x 3 pixels (**B**), to confirm the appropriate 'max no of neighbours' parameter for the PIF algorithm analysis. Each small square in the TIRF images represents a single pixel and each yellow box represents the selection of fluorescent spots using the two different sizes. Potential overlapping of fluorescent spots was shown in A as orange and blue dotted lines.

7.3.2 Algorithm determination: Determination of analysis parameters using spot fluorescence intensity and photobleaching step distribution histograms

Three other parameters have to be determined for each TIRF video (highlighted in blue in Table 7.2) prior to analysis, comprising:

1. 'Minimum amplitude'. This parameter defines the threshold fluorescence intensity for a spot to be selected.
2. 'Fixed sigma'. The sigma parameter describes the point-spread function of the fluorescent spot and fixing this parameter is advantageous to enable LoG trace filtration for background removal (section 2.10.2).
3. 'Min step amplitude'. This parameter determines the minimum change in fluorescence intensity amplitude for a photobleaching step to be detected.

The first two parameters were determined by performing an initial intensity scan in the software. The resulting frequency distributions for the fluorescence intensity and sigma of the fluorescent spots are plotted as histograms in Figures 7.7A and 7.7B. The lowest high frequency of fluorescence intensity observed was set as the 'minimum amplitude' threshold for spot selection, e.g. '150' in Figure 7.7A. For sigma, the most common value observed was used as the 'fixed sigma' as the reference point for background removal by the LoG filter, e.g. '1.6' in Figure 7.7B. The 'minimum step amplitude' was determined from the step size frequency histogram as shown in Figure 7.7C after performing a full stepwise photobleaching analysis with the software when the 'min step amplitude' was set to zero. As before, the lowest common fluorescence intensity observed was employed as the 'min step amplitude', e.g. '75' in Figure 7.7C. The three parameters described in this section were individually determined for each TIRF video. Typically, the 'minimum amplitude threshold' was found to be 100-150, the 'fixed sigma' was determined as 1.6-1.8, and the 'minimum step amplitude' was determined between 50-100, for all the TIRF videos analysed in this study.

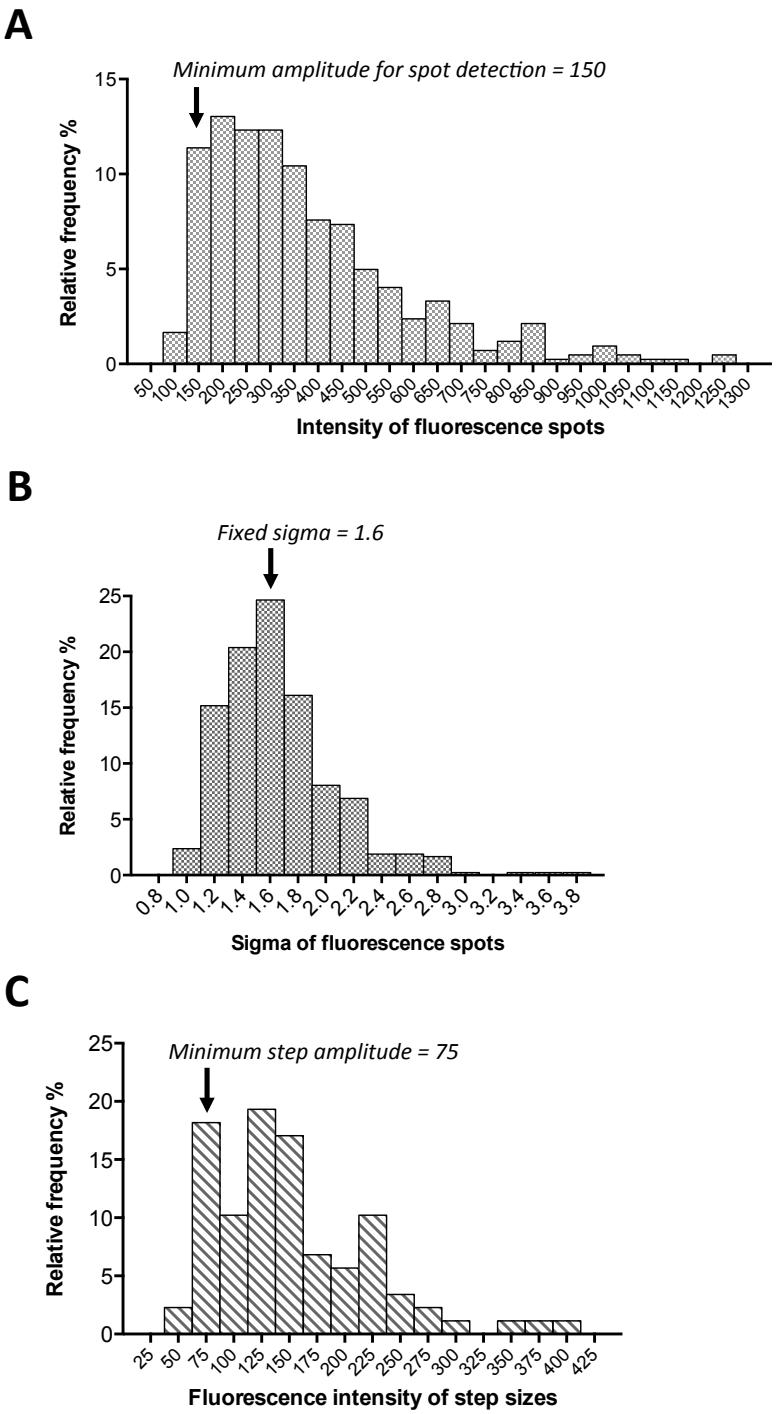

Figure 7.7: Determination of various parameters for stepwise photobleaching analysis using PIF algorithm. Distributions of the fluorescence intensity amplitudes (**A**), sigma (**B**), and fluorescence intensity step sizes (**C**) to determine the minimum amplitude threshold for spot detection (**A**), the sigma for background removal using LoG filter (**B**), and the minimum step amplitude for photobleaching step detection (**C**), respectively. Example optimisation analyses shown here were performed on the TIRF data obtained in Figure 7.4.

7.4 Determination of ABCG2 oligomeric state in HEK293T cell membranes, compared to CD28 and ABCC4

Following optimisation of the analysis parameters, the number of photobleaching steps of the fluorescent spots in each TIRF video was determined. Figure 7.8 below shows a magnified section of the TIRF image of Figure 7.4B and example analyses of four representative spots from the sfGFP-ABCG2 expressing cell, in which 2, 3 or 4 photobleaching steps were identified. The photobleaching step frequency histogram obtained from one experiment was also shown in Figure 7.8. The frequency histogram does not unambiguously reveal the oligomeric organisation as increased frequency was detected for various photobleaching steps (instead of a single distinct photobleaching step), Figure 7.8. This is caused by the presence of non-fluorescent sfGFP molecules and potential overlapping spots. The use of binomial models was therefore necessary to determine the oligomeric organisation of ABCG2. A simple schematic representation of how the non-fluorescent sfGFP molecules could affect a tetramer and a dimer complex is shown in Figure 7.9. The consequence of this is a reduced number of photobleaching steps detected corresponding to the number of fluorescent sfGFP molecules. The second consideration is that a small percentage of overlapping fluorescent spots could be detected, especially in high expressing mammalian expression systems such as the HEK293T cells, and this results in higher than expected number of photobleaching steps. To account for the two events, double binomial distributions were used; with variable proportions set to model different percentages of spot overlap (see next section and section 2.10.3).

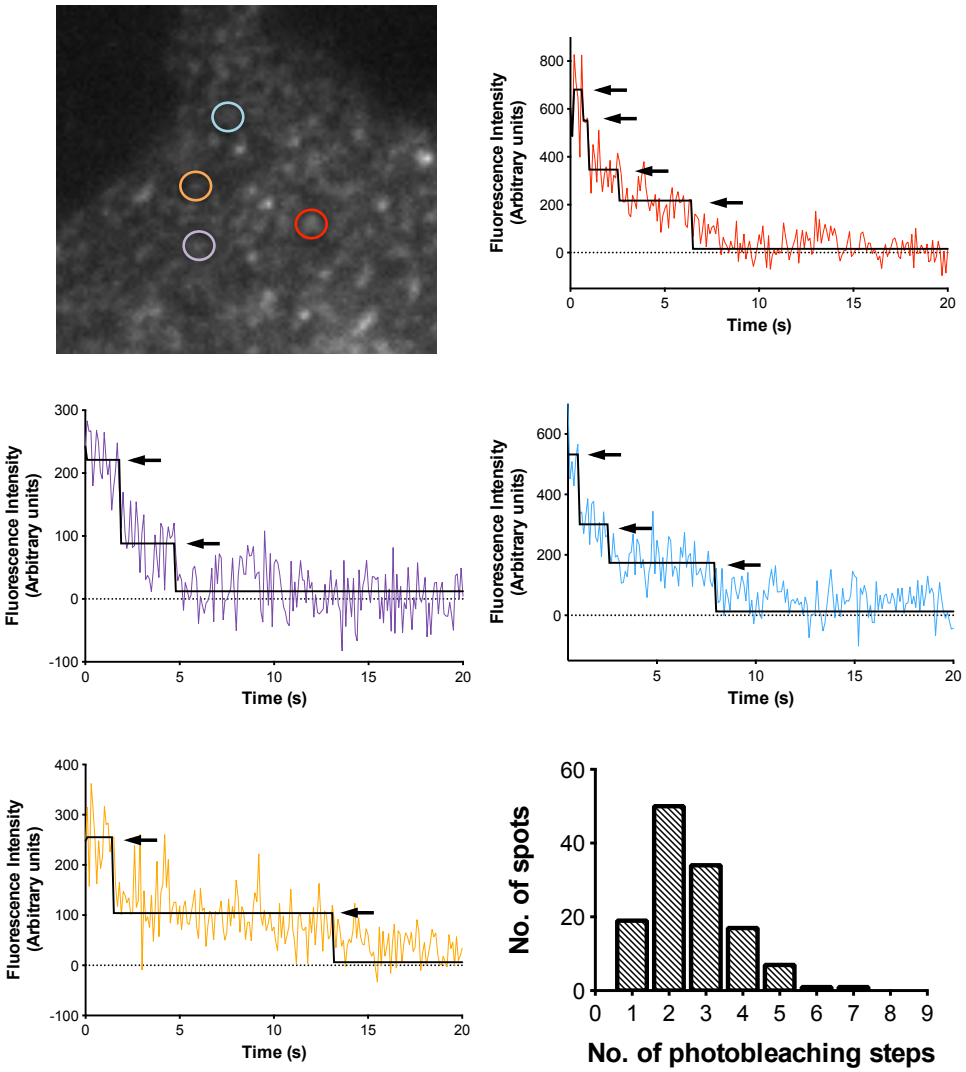

Figure 7.8: Examples of photobleaching step detection analysis in sfGFP-ABCG2 expressing cell. Four selected fluorescent spots are highlighted with coloured circles in the magnified TIRF image of a cell expressing sfGFP-ABCG2. Fluorescence intensity plots show the corresponding intensity traces (LoG corrected for background) of the highlighted fluorescent spots (according to colours). The arrows indicate the number of photobleaching steps determined by the final idealised step detection traces (black curves) of the fluorescent spots. The photobleaching step frequency histogram obtained from one experimental day is also shown (bottom right panel).

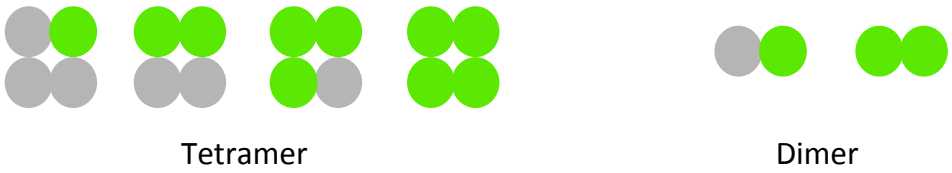

Figure 7.9: Effects of non-fluorescent GFP molecules. Schematic representations of fluorescent tetramer and dimer complexes that might be detected in the presence of non-fluorescent sfGFP labelled subunits (grey). The lower than expected number of photobleaching steps will resemble the number of fluorescent sfGFP molecules (green) within the complexes.

7.4.1 SfGFP-ABCG2 photobleaching step frequency histogram is best fit by a tetrameric model

To determine the most appropriate oligomeric model, optimal % for fluorescent GFP, various binomial fits assuming 10 % spot overlap were compared against the actual sfGFP-ABCG2 photobleaching step frequency histogram using a goodness of fit test (described in section 2.10.3). Dimer, trimer, tetramer and pentamer models of different probability of fluorescent sfGFP (when p = 0.50, 0.55, or 0.60) were investigated as shown in Figure 7.10. The tetrameric model was deemed as most appropriate to describe the sfGFP-ABCG2 photobleaching step frequency histogram. This was confirmed by calculating the reduced chi-square values (R-values) of the different models (Table S7.1 in Appendix). Lower R-value indicates reduced difference between the expected frequencies and the observed data, implying better data fitting using the associated binomial models.

7.4.2 Single oligomeric model analysis suggests tetrameric organisation of sfGFP-ABCG2

For the study of sfGFP-ABCG2 oligomerisation, photobleaching step frequency histograms obtained using the PIF analysis for sfGFP-ABCG2 (analysing the low expressing HEK293T stable clone described in chapter 6), were compared against the CD28-sfGFP reference control (using low expressing HEK293T stable clone, chapter 6) and the full-length ABC transporter ABCC4-sfGFP (transiently expressed in HEK293T cells, chapter 4). Examples of PIF stepwise photobleaching analysis for CD28-sfGFP and ABCC4-sfGFP are shown in Figures S7.1 and S7.2 in Appendix respectively. In addition, the effects of substrate incubation with 4 µM mitoxantrone (MX) for 30 min, on the sfGFP-ABCG2 photobleaching step frequency histogram was also studied. In each case, the frequency histogram shown represents combined analysis of over 30 cells and at least four independent experiments.

Photobleaching step frequency histograms obtained for sfGFP-ABCG2, sfGFP-ABCG2 in the presence of MX, CD28-sfGFP, and ABCC4-sfGFP were modelled with the respective best fit binomial distribution, as indicated in Figure 7.11. MX incubation did not affect the photobleaching step frequency histogram of sfGFP-ABCG2 (Figure 7.11A versus Figure 7.11B), modelled optimally based on a tetrameric model (Table S7.1). However, the frequency histograms of CD28-sfGFP (Figure 7.11C) and ABCC4-sfGFP (Figure 7.11D) were different compared to sfGFP-ABCG2, indicating potentially altered subunit organisation. Determination of the most appropriate distribution by goodness of fit (as for ABCG2; Table S7.1) suggested that these proteins existed as lower order oligomers, with a trimer model reported as the optimal fit. The same probability of fluorescent sfGFP ($p = 0.55$) was employed for all the oligomeric binomial models shown in Figure 7.11.

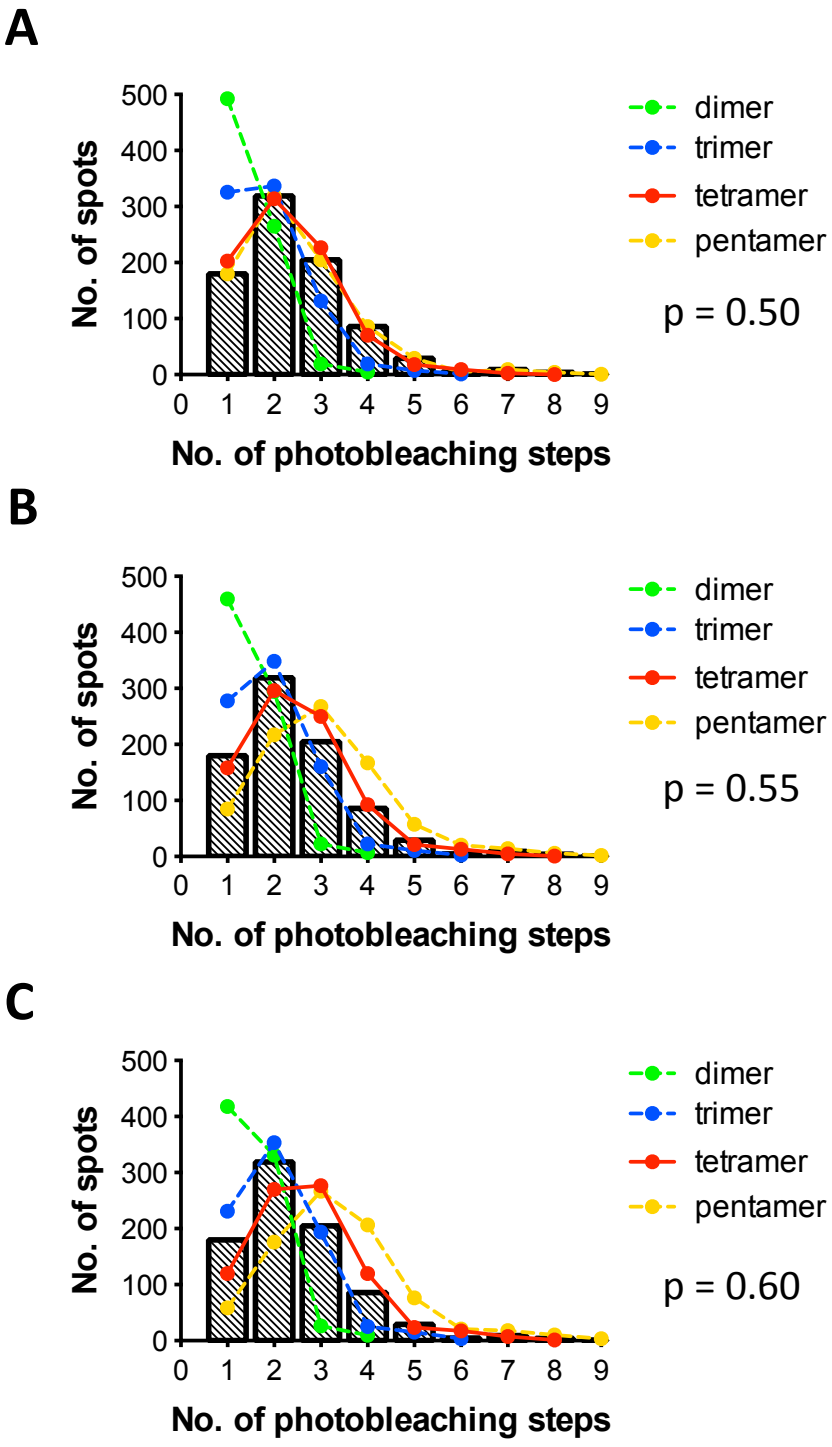

Figure 7.10: Fitting of the photobleaching step frequency histogram of sfGFP-ABCG2 data set with different oligomeric models. The dimer, trimer, tetramer, and pentamer models were calculated using probability of fluorescent GFP of 0.50 (**A**), 0.55 (**B**), and 0.60 (**C**). Overlaying the various oligomeric models (assuming 10% fluorescent spot overlapping) against the sfGFP-ABCG2 data set shows that the tetramer models in all three panels were the best fit for the frequency histogram of sfGFP-ABCG2.

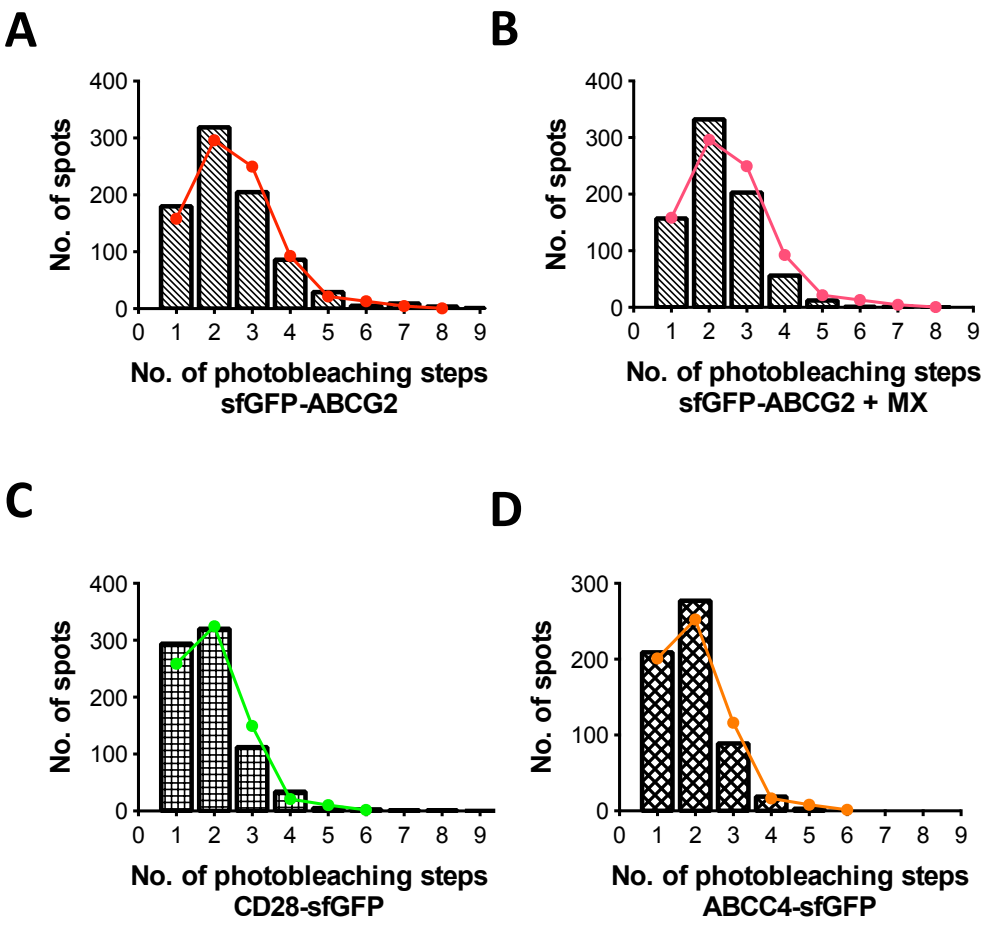

Figure 7.11: Determination of oligomerisation of ABCG2 using photobleaching step frequency histograms and oligomeric modelling. Frequency histograms (total number of fluorescent spots) of the number of photobleaching steps acquired for sfGFP-ABCG2 (**A**), sfGFP-ABCG2 in the presence of 4 µM mitoxantrone, 30 min (**B**), CD28-sfGFP (**C**), and ABCC4-sfGFP (**D**). The double binomial oligomeric models that best described the photobleaching step histograms are also shown as curves with coloured dots and lines in the respective figures. The frequency histogram of sfGFP-ABCG2 in **A** (and in the presence of MX in **B**) was best described using the tetramer model whilst the histograms of CD28-sfGFP (**C**) and ABCC4-sfGFP (**D**) were best fitted by a trimer model. Oligomeric models with p = 0.55, and 10% overlapping spots were employed. Data were collected from over 30 cells (at least 600 spots) for each sample and 5 independent experiments (4 independent experiments for sfGFP-ABCG2 + MX).

7.4.3 Multiple component oligomeric model suggests that sfGFP-ABCG2 exists predominantly as tetramers

The models based on a single population of oligomeric composition (sections 7.4.1 and 7.4.2) provided adequate fit to the sfGFP-ABCG2 data. However, it is also possible that the fluorescent proteins studied exist in a mixture of different oligomers (for example dimers and tetramers). This can be modelled

using a more complex binomial fit, in which the dimer and tetramer binomial models shown earlier are combined together using various dimer: tetramer (D/T) ratios. Figure 7.12 shows the dimer/tetramer model when fitted to the frequency histograms of sfGFP-ABCG2, CD28-sfGFP and ABCC4-sfGFP. Figure 7.12A shows that the photobleaching step frequency histogram of sfGFP-ABCG2 was best fitted using a dimer/tetramer model consisting of only 10% dimer and 90% tetramer (teal curve) yielding an R-value (reduced chi^2 value) of 5 from goodness of fit test, again indicating that sfGFP-ABCG2 exists predominantly as tetramers. For CD28-sfGFP, the photobleaching step frequency histogram (Figure 7.12B) was best fitted with a dimer/tetramer model with equal % of each oligomer state (i.e. 1: 1 D/T ratio, blue curve), and it yielded an R-value of 2, 2.5-fold smaller than the trimer model (R-value of 5 from Table S7.1). In contrast, the 1: 1 D/T ratio oligomeric model did not improve the fitting of the frequency histogram of ABCC4-sfGFP, producing an R-value of 5, compared to 3 when the trimer model was used (Table S7.1).

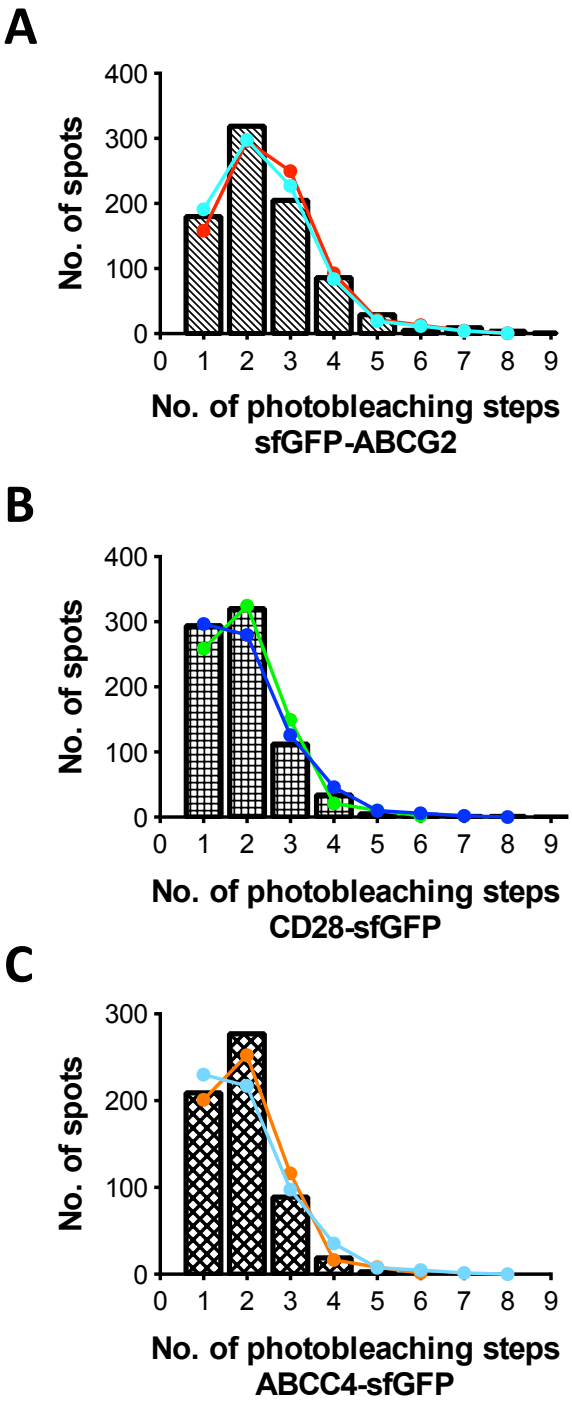

Figure 7.12: Multiple component oligomeric models to determine mixture of oligomeric species in sfGFP-ABCG2 and CD28-sfGFP. Photobleaching step frequency histograms of sfGFP-ABCG2 (**A**), CD28-sfGFP (**B**) and ABCC4-sfGFP (**C**). The single oligomeric models that best fit the data sets are shown, i.e. the tetramer model for sfGFP-ABCG2 (red) and trimer model for CD28-sfGFP (green) and ABCC4-sfGFP (orange) along with the dimer/tetramer models – 1: 9 dimer: tetramer ratio for sfGFP-ABCG2 (teal), and 1: 1 dimer: tetramer ratio for CD28-sfGFP (blue) and ABCC4-sfGFP (light blue). Oligomeric models with p = 0.55, and 10% overlapping spots were employed. Data were collected from over 30 cells (at least 700 spots) for each sample and 5 independent experiments.

7.4.4 Photobleaching step distribution variation among experimental data sets

In Figures 7.11 and 7.12 above, the frequency histograms were presented using the total number of fluorescent spots combined from all experiments. This is a comprehensive view of the overall photobleaching step distributions and ensured that the distributions were not affected by any experiments where there was lower than usual number of fluorescent spots analysed. However, it might also mask potential variability that could occur between the individual experiments. As the number of cells and the number of fluorescent spots accepted for each experiment were different, a single experiment with high number of fluorescent spots accepted could skew the overall frequency histograms significantly. To analyse the extent of experimental variability, Figure 7.13 shows the histograms calculated from the average normalised distribution of sfGFP-ABCG2 and CD28-sfGFP fitted to the expected dimer/tetramer oligomeric models. This confirms that the distributions of the average data obtained were fairly represented by the pooled histogram data based on the total number of fluorescent spots (Figures 7.11 and 7.12). Therefore, the variability between the independent experiments was not a factor that could influence the final interpretations obtained based on the frequency analysis of the total number of fluorescent spots.

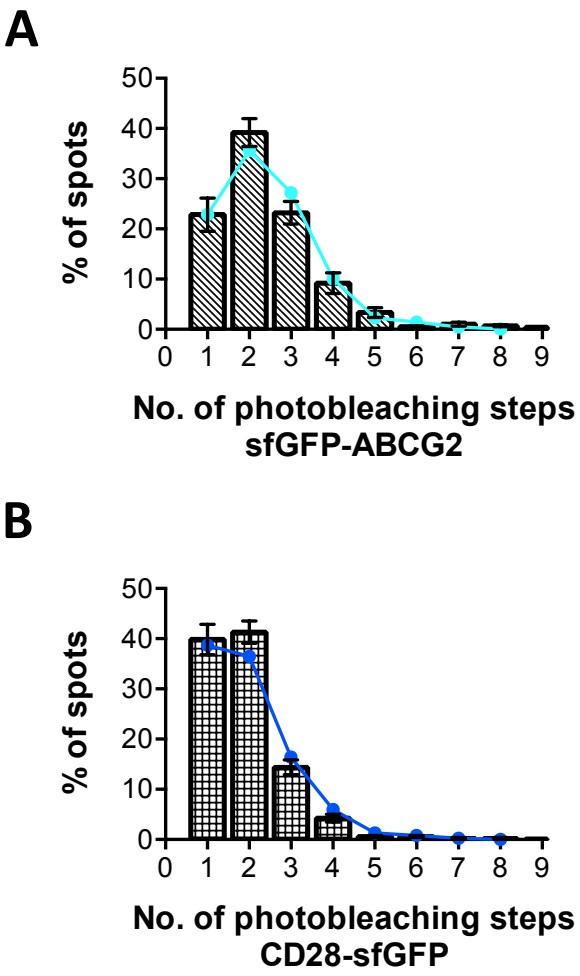

Figure 7.13: Normalised average photobleaching step frequency histograms to examine the variability between experiments. Mean ± SEM of the % of fluorescent spots and the number of photobleaching steps for sfGFP-ABCG2 (**A**) and CD28-sfGFP (**B**). The appropriate dimer: tetramer models (dimer: tetramer ratios of 1: 9 for sfGFP-ABCG2 (teal) and 1: 1 for CD28-sfGFP (blue)) employed to fit the histograms are shown. Average data were generated from normalising the photobleaching step frequencies of 5 independent experiments; over 30 cells and at least 700 spots were examined.

7.5 Discussion

7.5.1 Single particle TIRF imaging and binomial distribution analysis demonstrate that ABCG2 exist as a tetramer in mammalian cell membrane

TIRF imaging and stepwise photobleaching analysis of cells expressing sfGFP-ABCG2 have successfully indicated higher order oligomeric organisation of ABCG2 molecules in the plasma membrane. We concluded that ABCG2 molecules organised predominantly as tetramers, with 10 % existing as dimers. In contrast the CD28 frequency histogram is best described by the dual oligomeric model, which assumed an even mix of dimers and tetramers.

The general consensus of a minimal functional unit for ABCG2 is thought to be a dimer (section 1.6) because it only contains a single NBD and at least two NBDs are required for ATP hydrolysis and substrate transport in ABC transporters. It has been demonstrated by several studies that ABCG2 are likely to form dimers or higher order oligomers (Bhatia et al., 2005; Haider et al., 2011; Henriksen et al., 2005b; Kage et al., 2005; Ni et al., 2010). However, current evidence regarding precise ABCG2 subunit organisation is often inconclusive and/or limited by the use of denatured ABCG2 protein samples, as reviewed in section 1.6. For example, fluorescence-based techniques on mammalian cells such as FRET (Ni et al., 2010) and our data in chapter 5, and bimolecular fluorescence complementation (BiFC) (Haider et al., 2011) using mammalian cells cannot distinguish between dimerisation and higher order oligomerisation. PFO (perfluoro-octanoic acid)-PAGE and gel filtration chromatography analyses indicated that ABCG2 molecules could organise as a dodecameric complex (Xu et al., 2004). Additionally, using SDS-PAGE and electron microscopy analysis of purified ABCG2, Dezi et al. suggested that tetrameric organisation could be at least one of the oligomeric states of ABCG2 present in the native membrane (Dezi et al., 2010), but did not rule out the existence of other oligomeric states reported elsewhere. In this study, we resolved that tetrameric organisation is the predominant oligomeric form

of ABCG2 when investigated in intact mammalian cells. The implication of the tetrameric organisation of ABCG2 on its functionality or mechanism is yet to be established, but it is possible that the higher order tetrameric organisation enhances the structural stability of ABCG2 complex in the membrane (Ali and Imperiali, 2005; Cymer and Schneider, 2012), see chapter 8 for further discussion.

The presence of substrate (mitoxantrone) did not alter the oligomerisation of ABCG2, unlike the dynamic organisation of ABCA1 transporters, where dimer-monomer inter-conversion was observed upon binding of apolipoprotein A-1 during the generation of HDL (Nagata et al., 2013). However, it is also possible that the potential substrate specific alteration of ABCG2 organisation may not have been detected as TIRF imaging was performed after the cells were fixed.

CD28-sfGFP was employed in this study as a control to predict the characteristics of an oligomeric protein in the plasma membrane using this technique. CD28 is a T-lymphocyte receptor that binds to co-stimulatory molecules such as CD80 and CD86 to regulate T cell stimulation (Aruffo and Seed, 1987; Greene et al., 1996) and it is widely thought to form homodimeric complexes through disulphide interactions (Lazar-Molnar et al., 2006). However, Greene et al. could not rule out presence of tetrameric species in their CD28 samples prepared from gel permeation chromatography (Greene et al., 1996). This is a limitation that could explain the binding heterogeneity observed in their experiment as suggested in a review (Collins et al., 2002). FRET experiments reported that removal of intermolecular disulphide interaction (mutation of cysteine-123 residue) did not affect the oligomerisation of CD28 at the plasma membrane (Lazar-Molnar et al., 2006), suggesting that other domains could contribute to the CD28 dimeric interactions. These other domains may also play further roles in the formation of higher order CD28 oligomers. Furthermore, a non-reducing radioimmunoprecipitation assay of CD28 showed that higher order oligomeric

formation (than dimer) was possible (Tacke et al., 1997). Although inconclusive, results from brightness analysis in chapter 6 also suggested that CD28 could form higher order oligomers (e.g. tetramers). Therefore, the suggestion presented in Figure 7.12 above indicating that CD28 exists as even mixture of dimers and tetramers in the plasma membrane of HEK293T cells is realistic and also more likely than a homogeneous population of trimers (Figure 7.11).

ABCC4 is a less well-characterised ABC transporter thought to be involved in the regulation of cAMP (Copsel et al., 2011), the transport of antiviral agents, and offering protective function for multiple organs against toxic compounds (Abla et al., 2008). Although it is known to have two NBDs and two transmembrane domains (TMDs), its oligomeric structure remains unknown. Results in Figure 7.11 indicate that ABCC4 molecules could organise as trimers, and the use of dimer/tetramer model did not improve the fitting of the ABCC4 frequency histogram (Figure 7.12). The CFTR, also known as ABCC7, belongs to the same ABCC protein subfamily, and contains identical number of NBDs and TMDs as ABCC4. Its oligomerisation has been studied more extensively, and contradictory evidence has been reported. Multiple electron microscopy studies suggested that ABCC7 molecules organised as dimeric complexes (Cant et al., 2014; L. Zhang et al., 2009) whilst TIRF imaging and intensity analysis suggested that ABCC7 should exist only as monomers (Haggie and Verkman, 2008). The oligomeric structure of ABCC4 therefore cannot be proposed based solely on our TIRF stepwise photobleaching experiments. The likelihood of ABCC4 molecules existing as trimers or as a mixture of dimers and tetramers cannot be ruled out. Regardless of these uncertainties, the full length ABC transporter, ABCC4, was clearly shown to exist as lower order oligomeric structure compared to the half transporter, ABCG2.

7.5.2 Critical appraisal of TIRF stepwise photobleaching method

The combination method of TIRF imaging and stepwise photobleaching employed here offers several advantages and limitations when compared to other studies.

First, it is highly advantageous when compared to the oligomerisation studies of ABCG2 performed previously (see above and section 1.6). Our fluorescence technique allows the estimate of precise stoichiometry ABCG2 oligomeric organisation, in contrast to the FRET and BiFC methods or the biochemistry techniques (e.g. co-immunoprecipitation and gel electrophoresis). Second, ABCG2 was expressed and investigated in mammalian cells. Although the cells were chemically fixed prior to image acquisition, ABCG2 remained in the plasma membrane during acquisition. It is therefore more likely to represent its native state, when compared to biochemical and electron microscopy studies in which ABCG2 protein samples were purified and removed from the plasma membrane. Furthermore, accurate analysis of the electron microscopy data relies on homology modelling of electron map using current available ABC transporter structures, most of which have low sequence similarities compared to ABCG2 (see section 1.4).

Using the fully automated PIF algorithm, this method provided means of impartial data analysis (spot selection and step detection) and strong statistical power in which a large number of spots were investigated. This is advantageous compared to the TIRF stepwise photobleaching studies performed on ABCC7 (Haggie and Verkman, 2008) and ABCA1 (Nagata et al., 2013), where manual step detection was performed (see Table 7.1). However, the PFA fixation in our method could result in the quenching of GFP fluorescence (Brewis et al., 2000; Ganguly et al., 2011) and undesired protein-protein crosslinking. Despite this, immobilisation of the fluorescent spots was

necessary for accurate tracking of the fluorescent spots over time and determination of the number of photobleaching steps, as suggested in (Arant and Ulbrich, 2014). This disadvantage in our study is complemented by the oligomerisation results from brightness analysis of FCS measurements obtained from live cells, where tetrameric organisation of ABCG2 was also indicated (see chapter 6).

Another limitation within the TIRF stepwise photobleaching technique is that each fluorescent spot was assumed to represent a single protein complex (or oligomer). However, the size of the fluorescent spots detected in this study is in fact limited by Abbé diffraction limit, which is approximately 100 nm for the wavelengths employed here. Each fluorescent spot could therefore comprise of more than a single protein complex and this assumption was modelled as the 10% overlapping fluorescent spots in the binomial distributions (see next section). Again, this limitation is somewhat complemented by the PCH analysis in chapter 6 as the molecular brightness data were generated from "single molecule" statistical analysis of FCS measurements.

7.5.3 Assumptions in the binomial fitting of histograms

Two key assumptions were required for generating the binomial oligomeric models to fit the frequency histogram, for which the experimental data are difficult to obtain.

First, it was assumed that there were 10 % overlapping fluorescent spots in the TIRF videos. Although most of the closely located fluorescent spots were rejected during the spot selection process (see section 2.10.2 and Figure 7.6A), it is not inconceivable that two protein complexes could be too close to each other and detected as a single fluorescent spot, because of Abbé limit as discussed above. Overlapping of fluorescent spots will result in higher than

expected oligomer and number of photobleaching steps. Another theory is that this assumption could also imply the existence of higher order oligomeric states, e.g. 10 % of ABCG2 could exist as octameric complex. This supports the biochemical evidence presented in (McDevitt et al., 2006) where a tetrameric dimer complex was suggested. However, we could not resolve these two theories with the necessary justification at the time.

Another influential factor when calculating the oligomeric models was the probability of fluorescent sfGFP molecules. This was estimated at 0.55 in this study. It is comparable to the 53 % reported in (McGuire et al., 2012), in which identical methods, e.g. fixed HEK293T cells and monomeric sfGFP as the fluorescent tag, were employed. However, the exact reason for the presence of a proportion of non-fluorescent GFP is thus far unclear. It was suggested by Ulbrich and Isacoff in their pioneer publication (Ulbrich and Isacoff, 2007) that this phenomenon is similar to that of the DsRed (Garcia-Parajo et al., 2001) where a certain fraction of the GFP molecules existed in a non-fluorescent "dark" state and resulted in a lower than expected number of photobleaching steps observed. Table 7.3 below summarises the probability of fluorescent GFP reported in the literature thus far. McGuire et al. explained that the low maturation rate (probability of fluorescent GFP) observed in their studies (0.53), compared to those reported by Ulbrich and Isacoff (0.8), was due to the higher temperature (37°C) in which the HEK293T cells were grown, as compared to the lower temperature (18°C) for *X. laevis* oocytes. The reasoning behind this suggestion was unclear, as the EGFP variant was shown to have improved chromophore maturation at high temperature (Macdonald et al., 2012; Patterson et al., 1997). The description of this probability as the "maturation rate" of GFP by McGuire et al. was probably unsuitable, and the reason for the differences in the probability of fluorescent GFP could not be accurately explained. However, other studies have also reported lower than 0.8 probability of fluorescent GFP using mammalian or oocyte expression systems (Coste et al., 2012; Nagata et al., 2013; Nakajo et al., 2010), see Table

7.3. Quenching of GFP fluorescence emission caused by cell fixation with paraformaldehyde (Brewis et al., 2000; Ganguly et al., 2011) may explain the lower % of fluorescent sfGFP molecules observed in this study compared to the 66 % reported in live HeLa cells (Nagata et al., 2013). This quenching caused by cell fixation could also explain the inconsistency observed in chapter 6, where the assumption of a proportion of non-fluorescent sfGFP was not required in the PCH analysis of live cell data, and a 1.8-fold increase in molecular brightness was observed in tandem-sfGFP, compared to monomeric sfGFP. Finally, considering all the above arguments, it is reasonable to conclude that the probability value is likely to be multifactorial depending on cell types, fluorophores and measurement conditions.

Table 7.3: Summary of the expression systems, fluorescent proteins employed and probability of fluorescent GFP reported in various TIRF stepwise photobleaching studies.

Expression system	Fluorescent protein	Methods of determination and probability of fluorescent GFP	References
X. laevis oocytes (live)	Monomeric EGFP or EGFP	Best fit model, 0.8	(Reiner et al., 2012; Ulbrich and Isacoff, 2007)
X. laevis oocytes (live)	Monomeric EGFP	Best fit model, 0.64	(Nakajo et al., 2010)
HEK293 (membrane from lyse cells)	EGFP	Best fit model, 0.67	(Hallworth and Nichols, 2012)
HEK293 cells (fixed)	Monomeric sfGFP	Best fit model, 0.53	(McGuire et al., 2012)
HEK293 cells (fixed)	EGFP	Best fit assumption, 0.8	(Ji et al., 2008)
Hela cells (live)	Monomeric EGFP	Fluorophore labelling and co-localisation, 0.66	(Nagata et al., 2013)
HEK293 cells (fixed)	Monomeric EGFP	Best fit model, 0.75	(Ohshiro et al., 2014)
HEK293 cells (live)	GFP	Best fit assumption, 0.8	(Plant et al., 2014, 2011)
HEK239 cells (live)	GFP	Best fit model, 0.9	(Anderluh et al., 2014)
HEK293 cells (fixed)	GFP	Best fit assumption, 0.8	(W. Zhang et al., 2009)

Finally, the use of single or multiple oligomeric models could also affect the final interpretation of the frequency histograms. For ABCG2, there was no

such problem as both models predicted a predominant tetrameric organisation. In contrast, it was less conclusive for CD28 and ABCC4 as it was difficult to distinguish a best fit between the trimer and the 1: 1 dimer/tetramer models. For CD28, the use of 1: 1 dimer/tetramer model to describe the frequency histogram is deemed to be more plausible based on other supporting evidence from the literature. However, the lack of literature evidence for the oligomerisation of ABCC4 means that accurate determination is not possible at this stage (see section 7.5.1).

7.5.4 Excluded traces to compensate for experimental limitations

The other potential limiting factor in the final analysis was the high number of traces rejected. Only cells with higher than 20 % accepted traces were accounted for in the final frequency step histograms, and approximately 60 % of the cells analysed in this study were excluded from the final analysis. The two main criteria that resulted in the rejection of the traces were 1) the inadequate spot separation and 2) the low step to noise ratios yielded in the step detection traces.

The uncontrolled increased expression of membrane localised fluorescent proteins in HEK293T cells results in difficulty in obtaining cells with clear spot separation. For example, despite selection of a low expressing clone of CD86-sfGFP (monomeric control), the cells were inappropriate for this analysis. The majority of the TIRF images acquired for CD86-sfGFP cells were inadequate for further stepwise photobleaching analysis due to poor spot separation (spots not visibly separated by eye) in the TIRF images, shown in Figure S7.3 in Appendix. This could be due to the higher expression of CD86 compared to CD28 and ABCG2 at the plasma membrane. The use of a fully automated algorithm to analyse every single spot detected and setting rejection criteria within the software was therefore critical for compensating for this limitation.

Additionally, the mammalian cells were also known to produce higher background autofluorescence noise compared to *X. laevis* oocytes (McGuire et al., 2012). The use of SNRs as a rejection criterion allowed the photobleaching steps to be clearly distinguished from the background noise due to random fluorescence fluctuations produced in mammalian cells. By setting a minimum step to noise ratio as threshold, traces with high background noise were rejected and excluded from the final analysis. Although a high SNR threshold is preferred to ensure that good quality traces were analysed, it would in turn cause an increase in traces rejected (see Figure S7.4A in Appendix). The SNR in this study was chosen as 1.6 based on the results and suggestions in (McGuire et al., 2012), and to ensure sufficient traces were accepted for final analysis (see Figure S7.4 in Appendix for further explanation). In summary, the high number of traces rejected in this study was necessary to compensate the experimental limitations caused by the mammalian expression system.

7.5.5 Concluding remarks

Single particle TIRF imaging and stepwise photobleaching analysis employed in this study, for the first time, has provided strong evidence of tetrameric organisation of ABCG2 in mammalian plasma membrane. In comparison, the control CD28 protein organisation was optimally modelled as a mixture of dimers and tetramers, and the full length transporter ABCC4 is likely to exist as lower oligomeric state compared to the half transporter ABCG2. Further studies on the importance of tetrameric organisation on ABCG2 function could potentially lead to new strategies in drug development for targetting ABCG2 oligomerisation.

Chapter 8 Final discussion and future perspectives

8.1 Key findings

The use of several fluorescence techniques to investigate ABCG2 expressed in mammalian cells has enabled comprehensive characterisation of ABCG2 organisation within living and fixed mammalian cell membranes. Overall, the findings in this study can be categorised into three sections – function and localisation, membrane dynamics, and oligomerisation.

Using confocal imaging and fluorescence accumulation assays, we first established that N-terminus tagging of ABCG2 with fluorescent proteins was not detrimental to its localisation and function, as previously suggested in (Haider et al., 2011; Ni et al., 2010). We also verified that C603A and T362A point mutations did not affect the function of ABCG2. It is therefore unlikely that the intermolecular disulphide bridge involving the Cys-603 residue or the phosphorylation of ABCG2 by Pim-1 kinase at the Thr-362 residue (Xie et al., 2007) has a significant impact on the drug exporter function over the time frame of our experiments. The localisation results of truncated YFP-tagged ABCG2 mutants suggested that the NBD (or at least part of the N-terminus of ABCG2) and the transmembrane helices 5-6 could be proposed as important for successful folding and membrane trafficking of ABCG2.

The pioneer investigation of membrane dynamics of ABCG2 using two different techniques (FRAP and FCS) for the first time successfully characterised the membrane diffusion of ABCG2 in live cells. The slower diffusion of ABCG2 suggests that it forms larger complexes or is restricted by more membrane component interactions (increased number of transmembrane helices), compared to the study controls (membrane

localised sfGFPs and CD28 and CD86 glycoproteins). We showed that C603A and T362A mutations did not affect the diffusion of ABCG2 measured using FRAP. We also presented evidence that suggests ABCG2 diffusion was not affected by the presence of ligands (transport substrates and inhibitors) and cell cytoskeleton disruption.

The primary objective of this study was to resolve the uncertain evidence regarding oligomeric organisation of ABCG2, using fluorescence techniques. Using three different fluorescence techniques that were carefully controlled, we provided evidence for ABCG2 oligomerisation in live cells and indications of its precise oligomeric organisation. We showed that the transmembrane domain of ABCG2 is most likely to be important in the oligomerisation of ABCG2. However, it was challenging to establish the exact domains within ABCG2 that are important for its oligomerisation using FRET microscopy, since the truncated mutants were not localised at the plasma membrane. Nonetheless, two complementary fluorescence techniques successfully demonstrated tetrameric organisation of ABCG2. PCH analysis indicated 4-fold increase in the average molecular brightness of ABCG2 (compared to its "monomeric unit") in live cells, while TIRF stepwise photobleaching analysis in fixed cells also suggested that the photobleaching step frequency histogram of ABCG2 (obtained from individual fluorescent spots) was best described using tetrameric models. Furthermore, we also demonstrated that presence of ligands did not alter the subunit organisation of ABCG2 oligomers in live or fixed cells.

8.2 General advantages and limitations of experimental methods

The pros and cons of each of the individual fluorescence techniques have already been discussed in the respective results chapters. Here, we highlight

several general advantages and limitations of these experiments, comparing across the fluorescence techniques.

First, fusion of ABCG2 to a fluorescent protein has allowed the visualisation of ABCG2 and direct investigation of ABCG2 behaviour in live/fixed cells by studying the genetically fused fluorescent protein. The use of HEK293T cells as the expression system (instead of yeast or bacteria) with identical translation and membrane trafficking machinery should also generate ABCG2 that closely resembles the physiological state of the protein. The main advantage of using fluorescent protein tagging with genetic fusion is that the cell is in theory, likely to produce a 1: 1 ratio of fluorescent protein and ABCG2 molecules, unlike other fluorescent labelling methods (e.g. antibodies or SNAP labels) which have concerns regarding the tagging efficacy and feasibility of antibody treatments in live cells. As discussed in section 7.5.3, although "dark" fluorophores were not detected in the PCH analysis (chapter 6), statistical modelling of photobleaching step frequency histograms (chapter 7) suggested that only 55 % of the GFP molecules are fluorescent. The presence of non-fluorescent GFP molecules could be explained by the incomplete maturation of GFP chromophore (section 1.7) or quenching of GFP due to treatment of the cells, e.g. fixation.

Fluorescent protein tagging of the NBD of ABCG2 could also mask potential interactions of ABCG2 (with intracellular domains or other molecules) where the NBD was implicated in. This may affect some of our interpretations regarding the roles of NBD in ABCG2 oligomerisation and lack of interactions of ABCG2 with the cell cytoskeleton. However, it is unlikely that the "head-to-tail" dimer interactions of NBDs are disrupted since the fluorescent protein tagged ABCG2 remained functional. This limitation could be improved in future using small molecule fluorescence tagging of short epitope sequences, such as the 11-residue coenzyme A systems (Yin et al., 2005) and the biarsenical labelling of tetracysteine recognition sequences (6 to 8 residues;

(Adams et al., 2002)) to investigate the effects of fluorescent protein tagging in future studies. Expressing the recombinant proteins in HEK293T cells using strong a CMV promoter also resulted in high expression of fluorescent proteins. Although it may not present a fair reflection of ABCG2 at normal physiological levels, increased expression of ABCG2 is common in cancer cells (e.g. multiple myeloma (Turner et al., 2006)). This potential limitation was also minimised by the selection of low expressing clonal cell lines in certain experiments.

A brief comparison of the four techniques employed in this study is summarised in Table 8.1. Although the mobility measurements obtained from different spatial resolution techniques (FRAP and FCS) presented novel observations of ABCG2 diffusion in the plasma membrane, they are poor indicators of oligomerisation since the diffusion coefficient is relatively insensitive to molecular weight changes and it can be markedly affected by other factors (e.g. interactions with other membrane proteins or cell cytoskeleton) as discussed in chapter 4. FRET studies demonstrated at least a dimer formation of ABCG2 but they could not distinguish potential higher order oligomerisation. In contrast, PCH analysis (based on single particle statistics) was able to demonstrate higher order oligomer ABCG2 formation by detecting more than 2-fold increase in ABCG2 molecular brightness, when compared against CD86 monomer control and the C1 “monomeric unit” of ABCG2 (2-component PCH analysis). However, current PCH models are limited to distinguishing two different fluorescent species and are derived based on a 3D fluctuation model. Accurate determination of the oligomeric organisation using PCH analysis also relies on the knowledge of the true brightness of a “monomer” for comparison, and accurate determination of this can be difficult (chapter 6). Equally, TIRF stepwise photobleaching analysis also provided evidence of higher order oligomeric organisation of ABCG2 (more than dimer). Although this method did not rely on the knowledge of the brightness of a “monomeric unit”, the cells had to be fixed for immobilisation

of fluorescent spots and statistical modelling of the photobleaching step frequency histograms required other assumptions to be made, in particular that not all the genetically tagged GFP was fluorescent. Of these methods, TIRF stepwise photobleaching was able to provide strongest evidence for tetrameric organisation of ABCG2 and model the possible heterogeneity in the oligomerisation of ABCG2 (e.g. dimer: tetramer ratios of 1: 9 for ABCG2 and 1: 1 for CD28), whilst methods such as FRET and PCH (1-component model) assume "homogeneous" ABCG2 oligomers. Despite the different pitfalls, the techniques (especially PCH analysis and TIRF stepwise photobleaching) have generated complementary results that suggested predominant tetrameric organisation of ABCG2 molecules.

Table 8.1: Comparison of the fluorescence techniques employed in this study.

	FRAP	**FRET**	**FCS/PCH**	**TIRF stepwise photobleaching**
Live cell application	Yes	Yes	Yes	Yes/No
Stable/ transient cells	Stable	Transient	Stable	Stable or transient
Single wavelength detection	Yes	No	Yes	Yes
Final measurements	Fluorescence recovery	Increase in donor fluorescence signal	Fluorescence fluctuation/ molecular brightness	Number of photobleaching steps
Measurement types	Ensemble	Ensemble	Single molecule resolution	Single particle
Detection of dimers	No	Yes	Yes	Yes
Identification of oligomeric state	No	No	Possible indication	Yes

8.3 Future perspectives

8.3.1 Significance of ABCG2 tetrameric organisation

It was established that the minimum functional unit of an ABC transporter contains two NBDs. Therefore, as a "half transporter", it is safe to assume that formation of ABCG2 dimers is required for its function (Bhatia et al., 2005). Here, we demonstrated that ABCG2 is most likely to adopt a tetrameric organisation in the plasma membrane. The questions that are yet to be addressed are: 1) the importance of tetrameric organisation of ABCG2 and 2) potential approaches to prevent the oligomerisation of ABCG2.

The majority of cellular proteins (over 35 %) exist as symmetrical oligomers, in particular dimers and tetramers (Goodsell and Olson, 2000). Despite most of the proteins in the Protein Data Bank being reported as monomers, this may be a reflection of experimental limitations that favour determination of monomeric protein structures (Jones and Thornton, 1996). If dimeric ABCG2 is the minimal functional unit (as suggested in (Bhatia et al., 2005) and others), could the tetrameric organisation of ABCG2 be also important for its function (e.g. ATP hydrolysis and substrate transport)? Or could it have a different role *in vivo*? Evidence of dimerisation of the "full length" ABC transporters (e.g. ABCB1 (Boscoboinik et al., 1990; Poruchynsky and Ling, 1994) and ABCC1 (Rosenberg et al., 2001)) suggest that ABC transporters may indeed require more than 2 NBDs and 2 TMDs as a functional unit for ATP hydrolysis and substrate transport. However, there is no direct evidence to support this suggestion thus far. Larger protein complexes can be more resistant to degradation and denaturation (Ali and Imperiali, 2005) and examples elsewhere have proposed that oligomerisation can be important in the structural stability of membrane proteins (Cymer and Schneider, 2012). Therefore, it could also be argued that the tetrameric formation of ABCG2 is important for the structural stability of the protein whilst the dimeric ABCG2 remains as the key functional component within the complex.

The difficulty in the disruption of oligomerisation in ABCG2 is the main reason for the lack of understanding in this area. How do membrane proteins such as ABCG2 form oligomers? The evidence presented in this study implied that the nucleotide binding domain is unlikely to be important in ABCG2 oligomerisation. Truncated TMDs of ABCG2 resulted in poor membrane localisation, hampering the efforts for the accurate determination of domains responsible for ABCG2 oligomerisation (chapter 5). Although it was previously suggested that the transmembrane helices 5 and 6 are important in the oligomerisation of ABCG2 (Xu et al., 2007), we cannot rule out the possible roles of multiple interacting sites in other transmembrane helices that may be responsible for the formation of an oligomer with a complementary geometrical shape (Ali and Imperiali, 2005). A crystal structure or reliable homology model that shows the binding interfaces between ABCG2 molecules is much desired to resolve potential interacting sites in the TMD. This is also challenging at present because unlike ABCB1, ABCG2 has very low sequence similarities in comparison to the X-ray crystal structures presented thus far (e.g. for the bacterial Sav1866 transporter). Nevertheless, the findings and fluorescence methods presented in this study can form a reliable foundation for any future studies on the oligomerisation of ABCG2.

In past two decades, protein-protein interactions have become a therapeutic target in the clinic. Small molecules of approximately 0.5 kDa have been developed and showed promise in the inhibition of various protein-protein interactions (Arkin et al., 2014). A recent macrocylic class of compounds (Ensemblins) that inhibits the interaction between interleukin-17 and its receptor has been reported, representing one of the major breakthroughs in the search of protein-protein interaction inhibitors (Mullard, 2012). The wide substrate specificity of ABCG2 indicates that some of these newly developed compounds may even be applicable in the inhibition of ABCG2-ABCG2 interactions. Therefore, it is possible that as the drug design strategy and understanding of ABCG2 oligomerisation progress, the use of small molecules

(with good efficacy and sufficient bioavailability) to target protein-protein interactions mediating the oligomerisation of ABCG2 may one day become a therapy option in multidrug resistance of cancers.

8.3.2 Establishing the pharmacology of ABCG2

Aside from oligomerisation, current knowledge on ABCG2 pharmacology is also lacking. Up to now, only one pharmacology study of substrate binding affinity in ABCG2 has been reported (Clark et al., 2006). Stable HEK293T clones (with varying expression levels) of sfGFP-tagged ABCG2 and various fluorescence techniques employed in this study present an opportunity to extend the knowledge of ABCG2 in this area. Pharmacology studies can be designed using the fluorescence accumulation assays employed in this study, although this may require new synthetic fluorescent ligands such as the BODIPY fluorescent dye conjugated compounds (Loudet and Burgess, 2007). A reverse of the accumulation assay set up can be exploited to study the rate of efflux in ABCG2, providing further insights to the pharmacology of ABCG2. A preliminary experiment of this efflux assay was successfully implemented and could be used as guidance for further experiments. Furthermore, FCS has also been routinely employed to study the pharmacology of adenosine receptors (Briddon and Hill, 2007; Briddon et al., 2004; Corriden et al., 2014) and slight modification of current FCS methods may allow quantitative determination of binding and dissociation rates of ABCG2 ligands at “single molecule” resolution.

8.3.3 Potential new imaging methods to study ABCG2

Finally, true “single molecule” imaging that allows investigation of ABCG2 at single protein complex level was not achieved. Spatial resolution in fluorescence microscopy (e.g. TIRF single particle imaging) was limited to a minimum pixel size of 100 nm (in *x* and *y*) due to Abbé diffraction limit, which is at least 10 fold greater than the approximate diameter of a protein

molecule. Recently, commercial super resolution microscope systems employing techniques such as photoactivation localisation microscopy (PALM) and stochastic optical reconstruction microscopy (STORM) have become available to biologists, allowing nanoscale imaging of proteins dynamics in living cells (Godin et al., 2014), providing opportunity for true "single molecule" investigations in the future. Second, the recent development of intravital microscopy allows high resolution *in situ* fluorescence imaging in live animals, achieved through the use of multiphoton excitation techniques and far red fluorophores to overcome loss of fluorescent signal due to light scattering and reduced absorption associated with tissue depth. This technique may provide further opportunity to investigate the dynamics and oligomerisation of ABCG2 in its natural environment and the determination of importance of ABCG2 tetrameric organisation using *in situ* fluorescence studies (Ellenbroek and van Rheenen, 2014).

References

Abla, N., Chinn, L.W., Nakamura, T., Liu, L., Huang, C.C., Johns, S.J., Kawamoto, M., Stryke, D., Taylor, T.R., Ferrin, T.E., et al. (2008). The human multidrug resistance protein 4 (MRP4, ABCC4): Functional analysis of a highly polymorphic gene. Journal of Pharmacology and Experimental Therapeutics *325*, 859–868.

Abolhoda, A., Wilson, A.E., Ross, H., Danenberg, P.V., Burt, M., and Scotto, K.W. (1999). Rapid activation of MDR1 gene expression in human metastatic sarcoma after in vivo exposure to doxorubicin. Clinical Cancer Research *5*, 3352–3356.

Adams, C.L., Chen, Y.T., Smith, S.J., and Nelson, W.J. (1998). Mechanisms of epithelial cell-cell adhesion and cell compaction revealed by high-resolution tracking of E-cadherin-green fluorescent protein. Journal of Cell Biology *142*, 1105–1119.

Adams, S.R., Campbell, R.E., Gross, L.A., Martin, B.R., Walkup, G.K., Yao, Y., Llopis, J., and Tsien, R.Y. (2002). New biarsenical ligands and tetracysteine motifs for protein labeling in vitro and in vivo: Synthesis and biological applications. Journal of the American Chemical Society *124*, 6063–6076.

Agrawal, S., Reemtsma, K., Bagiella, E., Oluwole, S.F., and Braunstein, N.S. (2004). Role of TAP-1 and/or TAP-2 antigen presentation defects in tumorigenicity of mouse melanoma. Cellular Immunology *228*, 130–137.

Aguilar-Bryan, L., Nichols, C.G., Wechsler, S.W., Clement, J.P., Boyd, A.E., González, G., Herrera-Sosa, H., Nguy, K., Bryan, J., and Nelson, D.A. (1995). Cloning of the beta cell high-affinity sulfonylurea receptor: a regulator of insulin secretion. Science *268*, 423–426.

Aguilar-Bryan, L., Clement, J.P., Gonzalez, G., Kunjilwar, K., Babenko, A., and Bryan, J. (1998). Toward understanding the assembly and structure of KATP channels. Physiological Reviews *78*, 227–245.

Alfred H, S. (1999). P-Glycoprotein, a gatekeeper in the blood–brain barrier. Advanced Drug Delivery Reviews *36*, 179–194.

Ali, M.H., and Imperiali, B. (2005). Protein oligomerization: How and why. Bioorganic & Medicinal Chemistry *13*, 5013–5020.

Allen, J.D., van Loevezijn, A., Lakhai, J.M., van der Valk, M., van Tellingen, O., Reid, G., Schellens, J.H.M., Koomen, G.-J., and Schinkel, A.H. (2002). Potent and specific inhibition of the breast cancer resistance protein multidrug transporter in vitro and in mouse intestine by a novel analogue of Fumitremorgin C. Molecular Cancer Therapeutics *1*, 417–425.

Aller, S.G., Yu, J., Ward, A., Weng, Y., Chittaboina, S., Zhuo, R., Harrell, P.M., Trinh, Y.T., Zhang, Q., Urbatsch, I.L., et al. (2009). Structure of P-glycoprotein reveals a molecular basis for poly-specific drug binding. Science *323*, 1718–1722.

Altschul, S.F., Gish, W., Miller, W., Myers, E.W., and Lipman, D.J. (1990). Basic local alignment search tool. Journal of Molelcular Biology *215*, 403–410.

Ambudkar, S.V., Kim, I.-W., Xia, D., and Sauna, Z.E. (2006). The A-loop, a novel conserved aromatic acid subdomain upstream of the Walker A motif in ABC transporters, is critical for ATP binding. FEBS Letters *580*, 1049–1055.

Anderluh, A., Klotzsch, E., Reismann, A.W.A.F., Brameshuber, M., Kudlacek, O., Newman, A.H., Sitte, H.H., and Schutz, G.J. (2014). Single molecule analysis reveals coexistence of stable serotonin transporter monomers and oligomers in the live cell plasma membrane. Journal of Biological Chemistry *289*, 4387–4394.

Andersson, C., Dragomir, A., Hjelte, L., and Roomans, G.M. (2002). Cystic fibrosis transmembrane conductance regulator (CFTR) activity in nasal epithelial cells from cystic fibrosis patients with severe genotypes. Clinical Science *103*, 417–424.

Anikovsky, M., Wiltshire, Z.D., Weisshart, K., and Petersen, N.O. (2011). Photon counting histogram analysis for two-dimensional systems. ChemPhysChem *12*, 2439–2448.

Arant, R.J., and Ulbrich, M.H. (2014). Deciphering the subunit composition of multimeric proteins by counting photobleaching steps. ChemPhysChem *15*, 600–605.

Arkin, M.R., Tang, Y., and Wells, J.A. (2014). Small-molecule inhibitors of protein-protein interactions: Progressing toward the reality. Chemistry & Biology *21*, 1102–1114.

Aruffo, A., and Seed, B. (1987). Molecular cloning of a CD28 cDNA by a high-efficiency COS cell expression system. Proceedings of the National Academy of Sciences *84*, 8573–8577.

Axelrod, D. (1981). Cell-substrate contacts illuminated by total internal reflection fluorescence. The Journal of Cell Biology *89*, 141–145.

Axelrod, D. (2001). Total internal reflection fluorescence microscopy in cell biology: Total internal reflection fluorescence. Traffic *2*, 764–774.

Axelrod, D., Koppel, D.E., Schlessinger, J., Elson, E., and Webb, W.W. (1976). Mobility measurement by analysis of fluorescence photobleaching recovery kinetics. Biophysical Journal *16*, 1055–1069.

Azzaria, M., Schurr, E., and Gros, P. (1989). Discrete mutations introduced in the predicted nucleotide-binding sites of the mdr1 gene abolish its ability to confer multidrug resistance. Molecular and Cellular Biology *9*, 5289–5297.

Bacia, K., Scherfeld, D., Kahya, N., and Schwille, P. (2004). Fluorescence correlation spectroscopy relates rafts in model and native membranes. Biophysical Journal *87*, 1034–1043.

Bakos, E., Klein, I., Welker, E., Szabó, K., Müller, M., Sarkadi, B., and Váradi, A. (1997). Characterization of the human multidrug resistance protein containing mutations in the ATP-binding cassette signature region. Biochemical Journal *323 (Pt 3)*, 777–783.

Becker, J.-P., Depret, G., Van Bambeke, F., Tulkens, P.M., and Prévost, M. (2009). Molecular models of human P-glycoprotein in two different catalytic states. BMC Structural Biology *9*, 3.

Benderra, Z., Faussat, A.-M., Sayada, L., Perrot, J.-Y., Chaoui, D., Marie, J.-P., and Legrand, O. (2004). Breast cancer resistance protein and P-glycoprotein in 149 adult acute myeloid leukemias. Clinical Cancer Research *10*, 7896–7902.

Benderra, Z., Faussat, A.M., Sayada, L., Perrot, J.-Y., Tang, R., Chaoui, D., Morjani, H., Marzac, C., Marie, J.-P., and Legrand, O. (2005). MRP3, BCRP, and P-glycoprotein activities are prognostic factors in adult acute myeloid leukemia. Clinical Cancer Research *11*, 7764–7772.

Berge, K.E., Tian, H., Graf, G.A., Yu, L., Grishin, N.V., Schultz, J., Kwiterovich, P., Shan, B., Barnes, R., and Hobbs, H.H. (2000). Accumulation of dietary cholesterol in sitosterolemia caused by mutations in adjacent ABC transporters. Science *290*, 1771–1775.

Berney, C., and Danuser, G. (2003). FRET or No FRET: A quantitative comparison. Biophysical Journal *84*, 3992–4010.

Bernsel, A., Viklund, H., Hennerdal, A., and Elofsson, A. (2009). TOPCONS: Consensus prediction of membrane protein topology. Nucleic Acids Research 37, W465–W468.

Bhatia, A., Schafer, H., and Hrycyna, C. (2005). Oligomerization of the human ABC transporter ABCG2: Evaluation of the native protein and chimeric dimers. Biochemistry *44*, 10893–10904.

Boscoboinik, D., Debanne, M.T., Stafford, A.R., Jung, C.Y., Gupta, R.S., and Epand, R.M. (1990). Dimerization of the P-glycoprotein in membranes. Biochimica et Biophysica Acta (BBA) - Biomembranes *1027*, 225–228.

Boussif, O., Lezoualc'h, F., Zanta, M.A., Mergny, M.D., Scherman, D., Demeneix, B., and Behr, J.P. (1995). A versatile vector for gene and oligonucleotide transfer into cells in culture and in vivo: Polyethylenimine. Proceedings of the National Academy of Sciences *92*, 7297–7301.

Brewis, N., Phelan, A., Webb, J., Drew, J., Elliott, G., and O'Hare, P. (2000). Evaluation of VP22 spread in tissue culture. Journal of Virology *74*, 1051–1056.

Briddon, S.J., and Hill, S.J. (2007). Pharmacology under the microscope: the use of fluorescence correlation spectroscopy to determine the properties of ligand–receptor complexes. Trends in Pharmacological Sciences *28*, 637–645.

Briddon, S.J., Kellam, B., and Hill, S.J. (2011). Design and use of fluorescent ligands to study ligand–receptor interactions in dingle living cells. In Receptor Signal Transduction Protocols, G.B. Willars, and R.A.J. Challiss, eds. (Totowa, NJ: Humana Press), pp. 211–236.

Briddon, S.J., Middleton, R.J., Cordeaux, Y., Flavin, F.M., Weinstein, J.A., George, M.W., Kellam, B., and Hill, S.J. (2004). Quantitative analysis of the formation and diffusion of A1-adenosine receptor-antagonist complexes in single living cells. Proceedings of the National Academy of Sciences *101*, 4673–4678.

Brown, C.R., Hong-Brown, L.Q., Biwersi, J., Verkman, A.S., and Welch, W.J. (1996). Chemical chaperones correct the mutant phenotype of the delta F508 cystic fibrosis transmembrane conductance regulator protein. Cell Stress Chaperones *1*, 117–125.

Broussard, J.A., Rappaz, B., Webb, D.J., and Brown, C.M. (2013). Fluorescence resonance energy transfer microscopy as demonstrated by measuring the activation of the serine/threonine kinase Akt. Nature Protocols *8*, 265–281.

Brunham, L.R., Kruit, J.K., Iqbal, J., Fievet, C., Timmins, J.M., Pape, T.D., Coburn, B.A., Bissada, N., Staels, B., Groen, A.K., et al. (2006). Intestinal ABCA1 directly contributes to HDL biogenesis in vivo. Journal of Clinical Investigation *116*, 1052–1062.

Burer, H., Foekens, J.A., Look, M.P., Meijer-van Gelder, M.E., Klijn, J.G.M., Wiemer, E.A.C., Stoter, G., and Nooter, K. (2003). RNA expression of breast cancer resistance protein, lung resistance-related protein, multidrug resistance-associated proteins 1 and 2, and multidrug resistance gene 1 in breast cancer: Correlation with chemotherapeutic response. Clinical Cancer Research *9*, 827–836.

Busnelli, M., Mauri, M., Parenti, M., and Chini, B. (2013). Chapter Seventeen - Analysis of GPCR dimerization using acceptor photobleaching resonance energy transfer techniques. In Methods in Enzymology, P. Michael Conn, ed. (Academic Press), pp. 311–327.

Callaghan, R., and Riordan, J.R. (1993). Synthetic and natural opiates interact with P-glycoprotein in multidrug-resistant cells. Journal Biological Chemistry *268*, 16059–16064.

Cant, N., Pollock, N., and Ford, R.C. (2014). CFTR structure and cystic fibrosis. International Journal of Biochemistry & Cell Biology *52*, 15–25.

Carrier, I., Urbatsch, I.L., Senior, A.E., and Gros, P. (2007). Mutational analysis of conserved aromatic residues in the A-loop of the ABC transporter ABCB1A (mouse Mdr3). FEBS Letters *581*, 301–308.

Cascorbi, I. (2011). P-glycoprotein: Tissue distribution, substrates, and functional consequences of genetic variations. In Drug Transporters, M.F. Fromm, and R.B. Kim, eds. (Berlin, Heidelberg: Springer Berlin Heidelberg), pp. 261–283.

Casella, J.F., Flanagan, M.D., and Lin, S. (1981). Cytochalasin D inhibits actin polymerization and induces depolymerization of actin filaments formed during platelet shape change. Nature *293*, 302–305.

Cezanne, L., Lecat, S., Lagane, B., Millot, C., Vollmer, J.-Y., Matthes, H., Galzi, J.-L., and Lopez, A. (2004). Dynamic confinement of NK2 receptors in the plasma membrane: Improved FRAP analysis and biological relevance. Journal of Biological Chemistry *279*, 45057–45067.

Chalfie, M., Tu, Y., Euskirchen, G., Ward, W., and Prasher, D. (1994). Green fluorescent protein as a marker for gene expression. Science *263*, 802–805.

Chang, G. (2003). RETRACTED: Structure of MsbA from Vibrio cholera: A multidrug resistance ABC transporter homolog in a closed conformation. Journal of Molecular Biology *330*, 419–430.

Charrier, C., Ehrensperger, M.-V., Dahan, M., Lévi, S., and Triller, A. (2006). Cytoskeleton regulation of glycine receptor number at synapses and diffusion in the plasma membrane. Journal of Neuroscience *26*, 8502–8511.

Chen, J., Lu, G., Lin, J., Davidson, A.L., and Quiocho, F.A. (2003). A tweezers-like motion of the ATP-binding cassette dimer in an ABC transport cycle. Molecular Cell *12*, 651–661.

Chen, Y., Johnson, J., Macdonald, P., Wu, B., and Müller, J.D. (2010). Observing protein interactions and their stoichiometry in living cells by brightness analysis of fluorescence fluctuation experiments. In Methods in Enzymology, (Elsevier), pp. 345–363.

Chen, Y., Müller, J.D., Berland, K.M., and Gratton, E. (1999b). Fluorescence fluctuation spectroscopy. Methods *19*, 234–252.

Chen, Y., Müller, J.D., Ruan, Q., and Gratton, E. (2002). Molecular brightness characterization of EGFP in vivo by fluorescence fluctuation spectroscopy. Biophysical Journal *82*, 133–144.

Chen, Y., Müller, J.D., So, P.T.C., and Gratton, E. (1999a). The photon counting histogram in fluorescence fluctuation spectroscopy. Biophysical Journal *77*, 553–567.

Chen, Y., Wei, L.-N., and Müller, J.D. (2003). Probing protein oligomerization in living cells with fluorescence fluctuation spectroscopy. Proceedings of the National Academy of Sciences *100*, 15492–15497.

Chen, Y., Scully, M., Petralia, G., and Kakkar, A. (2014). Binding and inhibition of drug transport proteins by heparin: A potential drug transporter modulator capable of reducing multidrug resistance in human cancer cells. Cancer Biology & Therapy *15*, 135–145.

Cheng, M., Zhang, W., Yuan, J., Luo, W., Li, N., Lin, S., Yang, Y., Fang, X., and Chen, P.R. (2014). Single-molecule dynamics of site-specific labeled transforming growth factor type II receptors on living cells. Chemical Communications *50*, 14724–14727.

Chiantia, S., Ries, J., and Schwille, P. (2009). Fluorescence correlation spectroscopy in membrane structure elucidation. Biochimica et Biophysica Acta (BBA) - Biomembranes *1788*, 225–233.

Choudhury, H.G., Tong, Z., Mathavan, I., Li, Y., Iwata, S., Zirah, S., Rebuffat, S., van Veen, H.W., and Beis, K. (2014). Structure of an antibacterial peptide ATP-binding cassette transporter in a novel outward occluded state. Proceedings of the National Academy of Sciences *111*, 9145–9150.

Cisternino, S., Mercier, C., Bourasset, F., Roux, F., and Scherrmann, J.-M. (2004). Expression, up-regulation, and transport activity of the multidrug-Resistance protein Abcg2 at the mouse blood-brain barrier. Cancer Research *64*, 3296–3301.

Clark, R., Kerr, I.D., and Callaghan, R. (2006). Multiple drugbinding sites on the R482G isoform of the ABCG2 transporter. British Journal of Pharmacology *149*, 506–515.

Clegg, R.M. (1995). Fluorescence resonance energy transfer. Current Opinion in Biotechnology *6*, 103–110.

Clement, J.P., Kunjilwar, K., Gonzalez, G., Schwanstecher, M., Panten, U., Aguilar-Bryan, L., and Bryan, J. (1997). Association and stoichiometry of K(ATP) channel subunits. Neuron *18*, 827–838.

Cody, C.W., Prasher, D.C., Westler, W.M., Prendergast, F.G., and Ward, W.W. (1993). Chemical structure of the hexapeptide chromophore of the Aequorea green-fluorescent protein. Biochemistry *32*, 1212–1218.

Cole, N.B., Smith, C.L., Sciaky, N., Terasaki, M., Edidin, M., and Lippincott-Schwartz, J. (1996). Diffusional mobility of Golgi proteins in membranes of living cells. Science *273*, 797–801.

Cole, S.P.C. (2014). Targeting multidrug resistance protein 1 (MRP1, ABCC1): Past, present, and future. Annual Review of Pharmacology Toxicology *54*, 95–117.

Cole, S.P.C., and Deeley, R.G. (2006). Transport of glutathione and glutathione conjugates by MRP1. Trends in Pharmacological Sciences *27*, 438–446.

Cole, S.P., Bhardwaj, G., Gerlach, J.H., Mackie, J.E., Grant, C.E., Almquist, K.C., Stewart, A.J., Kurz, E.U., Duncan, A.M., and Deeley, R.G. (1992). Overexpression of a transporter gene in a multidrug-resistant human lung cancer cell line. Science *258*, 1650–1654.

Collins, A.V., Brodie, D.W., Gilbert, R.J.C., Iaboni, A., Manso-Sancho, R., Walse, B., Stuart, D.I., van der Merwe, P.A., and Davis, S.J. (2002). The interaction properties of costimulatory molecules revisited. Immunity *17*, 201–210.

Copsel, S., Garcia, C., Diez, F., Vermeulem, M., Baldi, A., Bianciotti, L.G., Russel, F.G.M., Shayo, C., and Davio, C. (2011). Multidrug resistance protein 4 (MRP4/ABCC4) regulates cAMP cellular levels and controls human leukemia cell proliferation and differentiation. Journal of Biological Chemistry *286*, 6979–6988.

Corcoran, K., Jabbour, M., Bhagwandin, C., Deymier, M.J., Theisen, D.L., and Lybarger, L. (2011). Ubiquitin-mediated regulation of CD86 protein expression by the ubiquitin ligase membrane-associated RING-CH-1 (MARCH1). Journal of Biological Chemistry *286*, 37168–37180.

Cordeaux, Y., Briddon, S.J., Alexander, S.P.H., Kellam, B., and Hill, S.J. (2008). Agonist-occupied A3 adenosine receptors exist within heterogeneous complexes in membrane microdomains of individual living cells. FASEB Journal *22*, 850–860.

Cordon-Cardo, C., O'Brien, J.P., Casals, D., Rittman-Grauer, L., Biedler, J.L., Melamed, M.R., and Bertino, J.R. (1989). Multidrug-resistance gene (P-glycoprotein) is expressed by endothelial cells at blood-brain barrier sites. Proceedings of the National Academy of Sciences *86*, 695–698.

Cormack, B.P., Valdivia, R.H., and Falkow, S. (1996). FACS-optimized mutants of the green fluorescent protein (GFP). Gene *173*, 33–38.

Corriden, R., Kilpatrick, L.E., Kellam, B., Briddon, S.J., and Hill, S.J. (2014). Kinetic analysis of antagonist-occupied adenosine-A3 receptors within membrane microdomains of individual cells provides evidence of receptor dimerization and allosterism. FASEB Journal *28*, 4211–4222.

Coste, B., Xiao, B., Santos, J.S., Syeda, R., Grandl, J., Spencer, K.S., Kim, S.E., Schmidt, M., Mathur, J., Dubin, A.E., et al. (2012). Piezo proteins are pore-forming subunits of mechanically activated channels. Nature *483*, 176–181.

Cotten, J.F., and Welsh, M.J. (1998). Covalent modification of the nucleotide binding domains of cystic fibrosis transmembrane conductance regulator. Journal of Biological Chemistry *273*, 31873–31879.

Cotten, J.F., Ostedgaard, L.S., Carson, M.R., and Welsh, M.J. (1996). Effect of cystic fibrosis-associated mutations in the fourth intracellular loop of cystic fibrosis transmembrane conductance regulator. Journal of Biological Chemistry *271*, 21279–21284.

Crameri, A., Whitehorn, E.A., Tate, E., and Stemmer, W.P. (1996). Improved green fluorescent protein by molecular evolution using DNA shuffling. Nature Biotechnology *14*, 315–319.

Currier, S.J., Kane, S.E., Willingham, M.C., Cardarelli, C.O., Pastan, I., and Gottesman, M.M. (1992). Identification of residues in the first cytoplasmic loop of P-glycoprotein involved in the function of chimeric human MDR1-MDR2 transporters. Journal of Biological Chemistry *267*, 25153–25159.

Cutting, G.R. (2005). Modifier genetics: Cystic fibrosis. Annual Review of Genomics and Human Genetics *6*, 237–260.

Cymer, F., and Schneider, D. (2012). Oligomerization of polytopic α-helical membrane proteins: causes and consequences. Biological Chemistry *393*, 1215–1230.

Dassa, E. (2011). Natural history of ABC systems: Not only transporters. Essays in Biochemistry *50*, 19–42.

Davidson, A.L., and Sharma, S. (1997). Mutation of a single MalK subunit severely impairs maltose transport activity in Escherichia coli. Journal of Bacteriology *179*, 5458–5464.

Davidson, A.L., Shuman, H.A., and Nikaido, H. (1992). Mechanism of maltose transport in Escherichia coli: Transmembrane signaling by periplasmic binding proteins. Proceedings of the National Academy of Sciences *89*, 2360–2364.

Davidson, A.L., Dassa, E., Orelle, C., and Chen, J. (2008). Structure, function, and evolution of bacterial ATP-binding cassette systems. Microbiology and Molecular Biology Reviews *72*, 317–364.

Dawson, R.J.P., and Locher, K.P. (2006). Structure of a bacterial multidrug ABC transporter. Nature *443*, 180–185.

Dawson, R.J.P., and Locher, K.P. (2007). Structure of the multidrug ABC transporter Sav1866 from Staphylococcus aureus in complex with AMP-PNP. FEBS Letters *581*, 935–938.

Dean, M., White, M.B., Amos, J., Gerrard, B., Stewart, C., Khaw, K.T., and Leppert, M. (1990). Multiple mutations in highly conserved residues are found in mildly affected cystic fibrosis patients. Cell *61*, 863–870.

Dean, M., Hamon, Y., and Chimini, G. (2001). The human ATP-binding cassette (ABC) transporter superfamily. Journal of Lipid Research *42*, 1007–1017.

Decottignies, A., and Goffeau, A. (1997). Complete inventory of the yeast ABC proteins. Nature Genetics *15*, 137–145.

Deeley, R.G., Westlake, C., and Cole, S.P.C. (2006). Transmembrane transport of endo- and xenobiotics by mammalian ATP-binding cassette multidrug resistance proteins. Physiological Reviews *86*, 849–899.

Dehghan, A., Köttgen, A., Yang, Q., Hwang, S.-J., Kao, W.L., Rivadeneira, F., Boerwinkle, E., Levy, D., Hofman, A., Astor, B.C., et al. (2008). Association of three genetic loci with

uric acid concentration and risk of gout: a genome-wide association study. Lancet *372*, 1953–1961.

Demuro, A., Penna, A., Safrina, O., Yeromin, A.V., Amcheslavsky, A., Cahalan, M.D., and Parker, I. (2011). Subunit stoichiometry of human Orai1 and Orai3 channels in closed and open states. Proceedings of the National Academy of Sciences *108*, 17832–17837.

Denny, J. (2006). Molecular Mechanisms, Biological Actions, and Neuropharmacology of the Growth-Associated Protein GAP-43. Current Neuropharmacology *4*, 293–304.

Dezi, M., Fribourg, P.-F., Di Cicco, A., Arnaud, O., Marco, S., Falson, P., Di Pietro, A., and Lévy, D. (2010). The multidrug resistance half-transporter ABCG2 is purified as a tetramer upon selective extraction from membranes. Biochimica et Biophysica Acta (BBA) - Biomembranes *1798*, 2094–2101.

Dhanasekaran, S.M., Barrette, T.R., Ghosh, D., Shah, R., Varambally, S., Kurachi, K., Pienta, K.J., Rubin, M.A., and Chinnaiyan, A.M. (2001). Delineation of prognostic biomarkers in prostate cancer. Nature *412*, 822–826.

Diestra, J.E., Scheffer, G.L., Català, I., Maliepaard, M., Schellens, J.H.M., Scheper, R.J., Germà-Lluch, J.R., and Izquierdo, M.A. (2002). Frequent expression of the multi-drug resistance-associated protein BCRP/MXR/ABCP/ABCG2 in human tumours detected by the BXP-21 monoclonal antibody in paraffin-embedded material. The Journal of Pathology *198*, 213–219.

Diop, N.K., and Hrycyna, C.A. (2005). N-Linked glycosylation of the human ABC transporter ABCG2 on asparagine 596 is not essential for expression, transport activity, or trafficking to the plasma membrane. Biochemistry *44*, 5420–5429.

Dixon, P.H., Weerasekera, N., Linton, K.J., Donaldson, O., Chambers, J., Egginton, E., Weaver, J., Nelson-Piercy, C., de Swiet, M., Warnes, G., et al. (2000). Heterozygous MDR3 missense mutation associated with intrahepatic cholestasis of pregnancy: evidence for a defect in protein trafficking. Human Molecular Genetics *9*, 1209–1217.

Dohse, M., Scharenberg, C., Shukla, S., Robey, R.W., Volkmann, T., Deeken, J.F., Brendel, C., Ambudkar, S.V., Neubauer, A., and Bates, S.E. (2010). Comparison of ATP-binding cassette transporter interactions with the tyrosine kinase inhibitors imatinib, nilotinib, and dasatinib. Drug Metabolism and Disposition *38*, 1371–1380.

Dorsch, S., Klotz, K.-N., Engelhardt, S., Lohse, M.J., and Bunemann, M. (2009). Analysis of receptor oligomerization by FRAP microscopy. Nature Methods *6*, 225–230.

Doyle, L.A., Yang, W., Abruzzo, L.V., Krogmann, T., Gao, Y., Rishi, A.K., and Ross, D.D. (1998). A multidrug resistance transporter from human MCF-7 breast cancer cells. Proceedings of the National Academy of Sciences *95*, 15665–15670.

Drake, F.H., Zimmerman, J.P., McCabe, F.L., Bartus, H.F., Per, S.R., Sullivan, D.M., Ross, W.E., Mattern, M.R., Johnson, R.K., and Crooke, S.T. (1987). Purification of topoisomerase II from amsacrine-resistant P388 leukemia cells. Evidence for two forms of the enzyme. Journal of Biological Chemistry *262*, 16739–16747.

Dross, N., Spriet, C., Zwerger, M., Müller, G., Waldeck, W., and Langowski, J. (2009). Mapping eGFP oligomer mobility in living cell nuclei. PLoS ONE *4*, e5041.

Dunne, M.J., Kane, C., Shepherd, R.M., Sanchez, J.A., James, R.F.L., Johnson, P.R.V., Aynsley-Green, A., Lu, S., Clement, J.P., Lindley, K.J., et al. (1997). Familial persistent hyperinsulinemic hypoglycemia of infancy and mutations in the sulfonylurea receptor. New England Journal of Medicine *336*, 703–706.

Edidin, M. (1991). Differences between the lateral organization of conventional and inositol phospholipid-anchored membrane proteins. A further definition of micrometer scale membrane domains. The Journal of Cell Biology *112*, 1143–1150.

Edidin, M., Zúñiga, M.C., and Sheetz, M.P. (1994). Truncation mutants define and locate cytoplasmic barriers to lateral mobility of membrane glycoproteins. Proceedings of the National Academy of Sciences *91*, 3378–3382.

Eggeling, C., Ringemann, C., Medda, R., Schwarzmann, G., Sandhoff, K., Polyakova, S., Belov, V.N., Hein, B., von Middendorff, C., Schönle, A., et al. (2009). Direct observation of the nanoscale dynamics of membrane lipids in a living cell. Nature *457*, 1159–1162.

Eisenblätter, T., Hüwel, S., and Galla, H.-J. (2003). Characterisation of the brain multidrug resistance protein (BMDP/ABCG2/BCRP) expressed at the blood–brain barrier. Brain Research *971*, 221–231.

Ejendal, K.F.K., Diop, N.K., Schweiger, L.C., and Hrycyna, C.A. (2006). The nature of amino acid 482 of human ABCG2 affects substrate transport and ATP hydrolysis but not substrate binding. Protein Science *15*, 1597–1607.

Elson, E.L. (2011). Fluorescence correlation spectroscopy: Past, present, future. Biophysical Journal *101*, 2855–2870.

Erkens, G.B., Berntsson, R.P.-A., Fulyani, F., Majsnerowska, M., Vujičić-Žagar, A., Ter Beek, J., Poolman, B., and Slotboom, D.J. (2011). The structural basis of modularity in ECF-type ABC transporters. Nature Structural & Molecular Biology *18*, 755–760.

Faraone, D., Aguzzi, M.S., Ragone, G., Russo, K., Capogrossi, M.C., and Facchiano, A. (2006). Heterodimerization of FGF-receptor 1 and PDGF-receptor-alpha: A novel mechanism underlying the inhibitory effect of PDGF-BB on FGF-2 in human cells. Blood *107*, 1896–1902.

Feder, T.J., Brust-Mascher, I., Slattery, J.P., Baird, B., and Webb, W.W. (1996). Constrained diffusion or immobile fraction on cell surfaces: A new interpretation. Biophysical Journal *70*, 2767–2773.

Fernandez, S.M., and Berlin, R.D. (1976). Cell surface distribution of lectin receptors determined by resonance energy transfer. Nature *264*, 411–415.

Fetsch, E.E., and Davidson, A.L. (2002). Vanadate-catalyzed photocleavage of the signature motif of an ATP-binding cassette (ABC) transporter. Proceedings of the National Academy of Sciences *99*, 9685–9690.

Förster, T. (2012). Energy migration and fluorescence. Journal of Biomedical Optics *17*, 011002.

Fox, E., and Bates, S.E. (2007). Tariquidar (XR9576): A P-glycoprotein drug efflux pump inhibitor. Expert Review of Anticancer Therapy *7*, 447–459.

Frick, M., Schmidt, K., and Nichols, B.J. (2007). Modulation of lateral diffusion in the plasma membrane by protein density. Current Biology *17*, 462–467.

Frizzell, R.A. (1999). Ten years with CFTR. Physiological Reviews *79*, S1–S2.

Fung, B.K.-K., and Stryer, L. (1978). Surface density determination in membranes by fluorescence energy transfer. Biochemistry *17*, 5241–5248.

Gadola, S.D., Moins-Teisserenc, H.T., Trowsdale, J., Gross, W.L., and Cerundolo, V. (2000). TAP deficiency syndrome. Clinical and Experimental Immunology *121*, 173–178.

Galimberti, S., Guerrini, F., Palumbo, G.A., Consoli, U., Fazzi, R., Morabito, F., Santini, V., and Petrini, M. (2004). Evaluation of BCRP and MDR-1 co-expression by quantitative molecular assessment in AML patients. Leukemia Research *28*, 367–372.

Ganguly, S., Clayton, A.H.A., and Chattopadhyay, A. (2011). Fixation alters fluorescence lifetime and anisotropy of cells expressing EYFP-tagged serotonin1A receptor. Biochemical and Biophysical Research Communications *405*, 234–237.

Garcia-Parajo, M.F., Koopman, M., van Dijk, E.M.H.P., Subramaniam, V., and van Hulst, N.F. (2001). The nature of fluorescence emission in the red fluorescent protein DsRed,

revealed by single-molecule detection. Proceedings of the National Academy of Sciences *98*, 14392–14397.

Gedeon, C., Behravan, J., Koren, G., and Piquette-Miller, M. (2006). Transport of glyburide by placental ABC transporters: Implications in fetal drug exposure. Placenta *27*, 1096–1102.

Ghosh, R.N., and Webb, W.W. (1994). Automated detection and tracking of individual and clustered cell surface low density lipoprotein receptor molecules. Biophysical Journal *66*, 1301–1318.

Giacomini, K.M., Huang, S.-M., Tweedie, D.J., Benet, L.Z., Brouwer, K.L.R., Chu, X., Dahlin, A., Evers, R., Fischer, V., Hillgren, K.M., et al. (2010). Membrane transporters in drug development. Nature Reviews Drug Discovery *9*, 215–236.

Godin, A.G., Lounis, B., and Cognet, L. (2014). Super-resolution microscopy approaches for live cell imaging. Biophysical Journal *107*, 1777–1784.

Goksel, D.L., Fischbach, K., Duggirala, R., Mitchell, B.D., Aguilar-Bryan, L., Blangero, J., Stern, M.P., and O'Connell, P. (1998). Variant in sulfonylurea receptor-1 gene is associated with high insulin concentrations in non-diabetic Mexican Americans: SUR-1 gene variant and hyperinsulinemia. Human Genetics *103*, 280–285.

Gottesman, M.M., and Pastan, I. (1993). Biochemistry of multidrug resistance mediated by the multidrug transporter. Annual Review of Biochemistry *62*, 385–427.

Graf, G.A., Yu, L., Li, W.-P., Gerard, R., Tuma, P.L., Cohen, J.C., and Hobbs, H.H. (2003). ABCG5 and ABCG8 are obligate heterodimers for protein trafficking and biliary cholesterol excretion. Journal of Biological Chemistry *278*, 48275–48282.

Greene, J.L., Leytze, G.M., Emswiler, J., Peach, R., Bajorath, J., Cosand, W., and Linsley, P.S. (1996). Covalent dimerization of CD28/CTLA-4 and oligomerization of CD80/CD86 regulate T cell costimulatory interactions. Journal of Biological Chemistry *271*, 26762–26771.

Gutmann, H., Hruz, P., Zimmermann, C., Beglinger, C., and Drewe, J. (2005). Distribution of breast cancer resistance protein (BCRP/ABCG2) mRNA expression along the human GI tract. Biochemical Pharmacology *70*, 695–699.

Haber, M., Smith, J., Bordow, S.B., Flemming, C., Cohn, S.L., London, W.B., Marshall, G.M., and Norris, M.D. (2006). Association of high-level MRP1 expression with poor clinical outcome in a large prospective study of primary neuroblastoma. Journal of Clinical Oncology *24*, 1546–1553.

Haggie, P.M., and Verkman, A.S. (2008). Monomeric CFTR in plasma membranes in live cells revealed by single molecule fluorescence imaging. Journal of Biological Chemistry *283*, 23510–23513.

Haider, A.J., Briggs, D., Self, T.J., Chilvers, H.L., Holliday, N.D., and Kerr, I.D. (2011). Dimerization of ABCG2 analysed by bimolecular fluorescence complementation. PLoS ONE *6*, e25818.

Hallworth, R., and Nichols, M.G. (2012). Prestin in HEK cells is an obligate tetramer. Journal of Neurophysiology *107*, 5–11.

Hancock, J.F., Paterson, H., and Marshall, C.J. (1990). A polybasic domain or palmitoylation is required in addition to the CAAX motif to localize p21ras to the plasma membrane. Cell *63*, 133–139.

Hanson, P.I., and Whiteheart, S.W. (2005). AAA+ proteins: Have engine, will work. Nature Reviews Molecular Cell Biology *6*, 519–529.

Hastie, P., Ulbrich, M.H., Wang, H.-L., Arant, R.J., Lau, A.G., Zhang, Z., Isacoff, E.Y., and Chen, L. (2013). AMPA receptor/TARP stoichiometry visualized by single-molecule subunit counting. Proceedings of the National Academy of Sciences *110*, 5163–5168.

Hazai, E., and Bikádi, Z. (2008). Homology modeling of breast cancer resistance protein (ABCG2). Journal of Structural Biology *162*, 63–74.

He, K., Fu, Y., Zhang, W., Yuan, J., Li, Z., Lv, Z., Zhang, Y., and Fang, X. (2011). Single-molecule imaging revealed enhanced dimerization of transforming growth factor β type II receptors in hypertrophic cardiomyocytes. Biochemical and Biophysical Research Communications *407*, 313–317.

Hebbeln, P., Rodionov, D.A., Alfandega, A., and Eitinger, T. (2007). Biotin uptake in prokaryotes by solute transporters with an optional ATP-binding cassette-containing module. Proceedings of the National Academy of Sciences *104*, 2909–2914.

Heim, R., and Tsien, R.Y. (1996). Engineering green fluorescent protein for improved brightness, longer wavelengths and fluorescence resonance energy transfer. Current Biology *6*, 178–182.

Heim, R., Prasher, D.C., and Tsien, R.Y. (1994). Wavelength mutations and posttranslational autoxidation of green fluorescent protein. Proceedings of the National Academy of Sciences *91*, 12501–12504.

Heim, R., Cubitt, A.B., and Tsien, R.Y. (1995). Improved green fluorescence. Nature *373*, 663–664.

Van Helvoort, A., Smith, A.J., Sprong, H., Fritzsche, I., Schinkel, A.H., Borst, P., and van Meer, G. (1996). MDR1 P-glycoprotein is a lipid translocase of broad specificity, while MDR3 P-glycoprotein specifically translocates phosphatidylcholine. Cell *87*, 507–517.

Henriksen, U., Gether, U., and Litman, T. (2005a). Effect of Walker A mutation (K86M) on oligomerization and surface targeting of the multidrug resistance transporter ABCG2. Journal of Cell Science *118*, 1417–1426.

Henriksen, U., Fog, J.U., Litman, T., and Gether, U. (2005b). Identification of intra- and intermolecular disulfide bridges in the multidrug resistance transporter ABCG2. Journal of Biological Chemistry *280*, 36926–36934.

Herrick-Davis, K., Grinde, E., Cowan, A., and Mazurkiewicz, J.E. (2013). Fluorescence correlation spectroscopy analysis of serotonin, adrenergic, muscarinic, and dopamine receptor dimerization: The oligomer number puzzle. Molecular Pharmacology *84*, 630–642.

Herrick-Davis, K., Grinde, E., Lindsley, T., Cowan, A., and Mazurkiewicz, J.E. (2012). Oligomer size of the serotonin 5-hydroxytryptamine 2C (5-HT2C) receptor revealed by fluorescence correlation spectroscopy with photon counting histogram analysis: Evidence for homodimers without monomers or tetramers. Journal of Biological Chemistry *287*, 23604–23614.

Herwaarden, A.E. va., Wagenaar, E., Karnekamp, B., Merino, G., Jonker, J.W., and Schinkel, A.H. (2006). Breast cancer resistance protein (Bcrp1/Abcg2) reduces systemic exposure of the dietary carcinogens aflatoxin B1, IQ and Trp-P-1 but also mediates their secretion into breast milk. Carcinogenesis *27*, 123–130.

Hewitt, E.W., and Lehner, P.J. (2003). The ABC-transporter signature motif is required for peptide translocation but not peptide binding by TAP. European Journal of Immunology *33*, 422–427.

Higgins, C.F. (1992). ABC transporters: From microorganisms to man. Annual Review of Cell Biology *8*, 67–113.

Higgins, C.F., and Gottesman, M.M. (1992). Is the multidrug transporter a flippase? Trends in Biochemical Sciences *17*, 18–21.

Higgins, C.F., and Linton, K.J. (2004). The ATP switch model for ABC transporters. Nature Structural & Molecular Biology *11*, 918–926.

Higgins, C.F., Hiles, I.D., Salmond, G.P.C., Gill, D.R., Downie, J.A., Evans, I.J., Holland, I.B., Gray, L., Buckel, S.D., Bell, A.W., et al. (1986). A family of related ATP-binding subunits coupled to many distinct biological processes in bacteria. Nature *323*, 448–450.

Hillebrand, M., Verrier, S.E., Ohlenbusch, A., Schafer, A., Soling, H.-D., Wouters, F.S., and Gartner, J. (2007). Live cell FRET microscopy: Homo- and heterodimerisation of two human peroxisomal ABC transporters, the adrenoleukodystrophy protein (ALDP, ABCD1) and PMP70 (ABCD3). Journal of Biological Chemistry *282*, 26997–27005.

Hillesheim, L.N., Chen, Y., and Müller, J.D. (2006). Dual-color photon counting histogram analysis of mRFP1 and EGFP in living cells. Biophysical Journal *91*, 4273–4284.

Hirsch-Reinshagen, V., Burgess, B.L., and Wellington, C.L. (2008). Why lipids are important for Alzheimer disease? Molecular and Cellular Biochemistry *326*, 121–129.

Hohl, M., Briand, C., Grütter, M.G., and Seeger, M.A. (2012). Crystal structure of a heterodimeric ABC transporter in its inward-facing conformation. Nature Structural & Molecular Biology *19*, 395–402.

Honjo, Y., Hrycyna, C.A., Yan, Q.W., Medina-Pérez, W.Y., Robey, R.W., van de Laar, A., Litman, T., Dean, M., and Bates, S.E. (2001). Acquired mutations in the MXR/BCRP/ABCP gene alter substrate specificity in MXR/BCRP/ABCP-overexpressing cells. Cancer Research *61*, 6635–6639.

Hopfner, K.P., Karcher, A., Shin, D.S., Craig, L., Arthur, L.M., Carney, J.P., and Tainer, J.A. (2000). Structural biology of Rad50 ATPase: ATP-driven conformational control in DNA double-strand break repair and the ABC-ATPase superfamily. Cell *101*, 789–800.

Hou, Y., Li, C.-Z., Palaniyandi, K., Magtibay, P.M., Homolya, L., Sarkadi, B., and Chang, X. (2009). Effects of putative catalytic base mutation E211Q on ABCG2-mediated methotrexate transport. Biochemistry *48*, 9122–9131.

Huang, B., Perroud, T.D., and Zare, R.N. (2004). Photon counting histogram: One-photon Eecitation. ChemPhysChem *5*, 1523–1531.

Hummel, I., Klappe, K., Ercan, C., and Kok, J.W. (2011). Multidrug resistance-related protein 1 (MRP1) function and localization depend on cortical actin. Molecular Pharmacology *79*, 229–240.

Hung, L.W., Wang, I.X., Nikaido, K., Liu, P.Q., Ames, G.F., and Kim, S.H. (1998). Crystal structure of the ATP-binding subunit of an ABC transporter. Nature *396*, 703–707.

Hutchcroft, J.E., Tsai, B., and Bierer, B.E. (1996). Differential phosphorylation of the T lymphocyte costimulatory receptor CD28. Activation-dependent changes and regulation by protein kinase C. Journal of Biological Chemistry *271*, 13362–13370.

Hyde, S.C., Emsley, P., Hartshorn, M.J., Mimmack, M.M., Gileadi, U., Pearce, S.R., Gallagher, M.P., Gill, D.R., Hubbard, R.E., and Higgins, C.F. (1990). Structural model of ATP-binding proteing associated with cystic fibrosis, multidrug resistance and bacterial transport. Nature *346*, 362–365.

Iino, R., Koyama, I., and Kusumi, A. (2001). Single molecule imaging of green fluorescent proteins in living cells: E-cadherin forms oligomers on the free cell surface. Biophysical Journal *80*, 2667–2677.

Inagaki, N., Gonoi, T., Clement, J.P., Wang, C.Z., Aguilar-Bryan, L., Bryan, J., and Seino, S. (1996). A family of sulfonylurea receptors determines the pharmacological properties of ATP-sensitive K+ channels. Neuron *16*, 1011–1017.

Inagaki, N., Gonoi, T., and Seino, S. (1997). Subunit stoichiometry of the pancreatic β-cell ATP-sensitive K+ channel. FEBS Letters *409*, 232–236.

James, J.R., Oliveira, M.I., Carmo, A.M., Iaboni, A., and Davis, S.J. (2006). A rigorous experimental framework for detecting protein oligomerization using bioluminescence resonance energy transfer. Nature Methods *3*, 1001–1006.

James, J.R., White, S.S., Clarke, R.W., Johansen, A.M., Dunne, P.D., Sleep, D.L., Fitzgerald, W.J., Davis, S.J., and Klenerman, D. (2007). Single-molecule level analysis of the subunit composition of the T cell receptor on live T cells. Proceedings of the National Academy of Sciences *104*, 17662–17667.

Janas, E. (2003). The ATP hydrolysis cycle of the nucleotide-binding domain of the mitochondrial ATP-binding cassette transporter Mdl1p. Journal of Biological Chemistry *278*, 26862–26869.

Jares-Erijman, E.A., and Jovin, T.M. (2003). FRET imaging. Nature Biotechnology *21*, 1387–1395.

Ji, W., Xu, P., Li, Z., Lu, J., Liu, L., Zhan, Y., Chen, Y., Hille, B., Xu, T., and Chen, L. (2008). Functional stoichiometry of the unitary calcium-release-activated calcium channel. Proceedings of the National Academy of Sciences *105*, 13668–13673.

Jin, M.S., Oldham, M.L., Zhang, Q., and Chen, J. (2012). Crystal structure of the multidrug transporter P-glycoprotein from Caenorhabditis elegans. Nature *490*, 566–569.

Jones, P.M., and George, A.M. (1999). Subunit interactions in ABC transporters: Towards a functional architecture. FEMS Microbiology Letters *179*, 187–202.

Jones, P.M., and George, A.M. (2002). Mechanism of ABC transporters: A molecular dynamics simulation of a well characterized nucleotide-binding subunit. Proceedings of the National Academy of Sciences *99*, 12639–12644.

Jones, P.M., and George, A.M. (2004). The ABC transporter structure and mechanism: perspectives on recent research. Cellular and Molecular Life Sciences *61*, 682–699.

Jones, P.M., and George, A.M. (2012). Role of the D-loops in allosteric control of ATP hydrolysis in an ABC transporter. Journal of Physical Chemistry A *116*, 3004–3013.

Jones, S., and Thornton, J.M. (1996). Principles of protein-protein interactions. Proceedings of the National Academy of Sciences *93*, 13–20.

Jonker, J.W., Smit, J.W., Brinkhuis, R.F., Maliepaard, M., Beijnen, J.H., Schellens, J.H.M., and Schinkel, A.H. (2000). Role of breast cancer resistance protein in the bioavailability and fetal penetration of topotecan. Journal of the National Cancer Institute *92*, 1651–1656.

Jonker, J.W., Merino, G., Musters, S., van Herwaarden, A.E., Bolscher, E., Wagenaar, E., Mesman, E., Dale, T.C., and Schinkel, A.H. (2005). The breast cancer resistance protein BCRP (ABCG2) concentrates drugs and carcinogenic xenotoxins into milk. Nature Medicine *11*, 127–129.

Juliano, R.L., and Ling, V. (1976). A surface glycoprotein modulating drug permeability in Chinese hamster ovary cell mutants. Biochimica et Biophysica Acta *455*, 152–162.

Kaether, C., and Gerdes, H.-H. (1995). Visualization of protein transport along the secretory pathway using green fluorescent protein. FEBS Letters *369*, 267–271.

Kage, K., Fujita, T., and Sugimoto, Y. (2005). Role of Cys-603 in dimer/oligomer formation of the breast cancer resistance protein BCRP/ABCG2. Cancer Science *96*, 866–872.

Kälin, N., Claass, A., Sommer, M., Puchelle, E., and Tümmler, B. (1999). DeltaF508 CFTR protein expression in tissues from patients with cystic fibrosis. Journal of Clinical Investigation *103*, 1379–1389.

Kaminski, W.E., Piehler, A., and Wenzel, J.J. (2006). ABC A-subfamily transporters: Structure, function and disease. Biochimica et Biophysica Acta (BBA) - Molecular Basis of Disease *1762*, 510–524.

Kane, C., Shepherd, R.M., Squires, P.E., Johnson, P.R.V., James, R.F.L., Milla, P.J., Aynsley-Green, A., Lindley, K.J., and Dunne, M.J. (1996). Loss of functional KATP channels in

pancreatic β–cells causes persistent hyperinsulinemic hypoglycemia of infancy. Nature Medicine *2*, 1344–1347.

Kanzaki, A., Toi, M., Nakayama, K., Bando, H., Mutoh, M., Uchida, T., Fukumoto, M., and Takebayashi, Y. (2001). Expression of multidrug resistance-related transporters in human breast carcinoma. Japanese Journal of Cancer Research *92*, 452–458.

Karpova, T.S., Baumann, C.T., He, L., Wu, X., Grammer, A., Lipsky, P., Hager, G.L., and McNally, J.G. (2003). Fluorescence resonance energy transfer from cyan to yellow fluorescent protein detected by acceptor photobleaching using confocal microscopy and a single laser. Journal of Microscopy *209*, 56–70.

Kaya, A.İ., Uğur, Ö., Altuntaş, O., Sayar, K., and Onaran, H.O. (2011). Long and short distance movements of β2-adrenoceptor in cell membrane assessed by photoconvertible fluorescent protein dendra2–β2-adrenoceptor fusion. Biochimica et Biophysica Acta (BBA) - Molecular Cell Research *1813*, 1511–1524.

Kenworthy, A.K., Nichols, B.J., Remmert, C.L., Hendrix, G.M., Kumar, M., Zimmerberg, J., and Lippincott-Schwartz, J. (2004). Dynamics of putative raft-associated proteins at the cell surface. Journal of Cell Biology *165*, 735–746.

Kenworthy, A.K., Petranova, N., and Edidin, M. (2000). High-resolution FRET microscopy of cholera toxin B-subunit and GPI-anchored proteins in cell plasma membranes. Molecular Biology of the Cell *11*, 1645–1655.

Kerr, I.D., Haider, A.J., and Gelissen, I.C. (2011). The ABCG family of membrane-associated transporters: You don't have to be big to be mighty. British Journal of Pharmacology *164*, 1767–1779.

Kerr, I.D., Jones, P.M., and George, A.M. (2010). Multidrug efflux pumps: The structures of prokaryotic ATP-binding cassette transporter efflux pumps and implications for our understanding of eukaryotic P-glycoproteins and homologues. FEBS Journal *277*, 550–563.

Keskitalo, J.E., Zolk, O., Fromm, M.F., Kurkinen, K.J., Neuvonen, P.J., and Niemi, M. (2009). ABCG2 polymorphism markedly affects the pharmacokinetics of atorvastatin and rosuvastatin. Clinical Pharmacology & Therapeutics *86*, 197–203.

Kilpatrick, L.E., Briddon, S.J., and Holliday, N.D. (2012). Fluorescence correlation spectroscopy, combined with bimolecular fluorescence complementation, reveals the effects of β-arrestin complexes and endocytic targeting on the membrane mobility of neuropeptide Y receptors. Biochimica et Biophysica Acta (BBA) - Molecular Cell Research *1823*, 1068–1081.

Kim, I.-W., Peng, X.-H., Sauna, Z.E., FitzGerald, P.C., Xia, D., Müller, M., Nandigama, K., and Ambudkar, S.V. (2006). The conserved tyrosine residues 401 and 1044 in ATP sites of human P-glycoprotein are critical for ATP binding and hydrolysis: Evidence for a conserved subdomain, the A-Loop in the ATP-binding cassette. Biochemistry *45*, 7605–7616.

Kim, W.S., Hill, A.F., Fitzgerald, M.L., Freeman, M.W., Evin, G., and Garner, B. (2011). Wild type and Tangier disease ABCA1 mutants modulate cellular amyloid-β production independent of cholesterol efflux activity. Journal of Alzheimer's Disease *27*, 441–452.

Kim, Y.H., Ishii, G., Goto, K., Ota, S., Kubota, K., Murata, Y., Mishima, M., Saijo, N., Nishiwaki, Y., and Ochiai, A. (2009). Expression of breast cancer resistance protein is associated with a poor clinical outcome in patients with small-cell lung cancer. Lung Cancer *65*, 105–111.

Kohout, S.C., Ulbrich, M.H., Bell, S.C., and Isacoff, E.Y. (2008). Subunit organization and functional transitions in Ci-VSP. Nature Structural & Molecular Biology *15*, 106–108.

Van der Kolk, D.M., Vellenga, E., Scheffer, G.L., Müller, M., Bates, S.E., Scheper, R.J., and de Vries, E.G.E. (2002). Expression and activity of breast cancer resistance protein (BCRP) in de novo and relapsed acute myeloid leukemia. Blood *99*, 3763–3770.

Kondo, C., Suzuki, H., Itoda, M., Ozawa, S., Sawada, J., Kobayashi, D., Ieiri, I., Mine, K., Ohtsubo, K., and Sugiyama, Y. (2004). Functional analysis of SNPs variants of BCRP/ABCG2. Pharmaceutical Research *21*, 1895–1903.

Koppel, D.E., Sheetz, M.P., and Schindler, M. (1981). Matrix control of protein diffusion in biological membranes. Proceedings of the National Academy of Sciences *78*, 3576–3580.

Kosztyu, P., Bukvova, R., Dolezel, P., and Mlejnek, P. (2014). Resistance to daunorubicin, imatinib, or nilotinib depends on expression levels of ABCB1 and ABCG2 in human leukemia cells. Chemico-Biological Interactions *219*, 203–210.

Krishna, R., and Mayer, L.D. (2000). Multidrug resistance (MDR) in cancer. Mechanisms, reversal using modulators of MDR and the role of MDR modulators in influencing the pharmacokinetics of anticancer drugs. European Journal of Pharmaceutical Sciences *11*, 265–283.

Krishnan, N., Pan, H., Buckley, D.J., and Buckley, A. (2003). Prolactin-regulated pim-1 transcription: identification of critical promoter elements and Akt signaling. Endocrine *20*, 123–130.

Laemmli, U.K. (1970). Cleavage of structural proteins during the assembly of the head of bacteriophage T4. Nature *227*, 680–685.

Langmann, T., Klucken, J., Reil, M., Liebisch, G., Luciani, M.-F., Chimini, G., Kaminski, W.E., and Schmitz, G. (1999). Molecular cloning of the human ATP-Binding cassette transporter 1 (hABC1): Evidence for sterol-dependent regulation in macrophages. Biochemical and Biophysical Research Communications *257*, 29–33.

Lawson, J., O'Mara, M.L., and Kerr, I.. (2008). Structure-based interpretation of the mutagenesis database for the nucleotide binding domains of P-glycoprotein. Biochimica et Biophysica Acta (BBA) - Biomembranes *1778*, 376–391.

Lazar-Molnar, E., Almo, S.C., and Nathenson, S.G. (2006). The interchain disulfide linkage is not a prerequisite but enhances CD28 costimulatory function. Cellular Immunology *244*, 125–129.

Leake, M.C., Chandler, J.H., Wadhams, G.H., Bai, F., Berry, R.M., and Armitage, J.P. (2006). Stoichiometry and turnover in single, functioning membrane protein complexes. Nature *443*, 355–358.

Lee, M.H., Lu, K., Hazard, S., Yu, H., Shulenin, S., Hidaka, H., Kojima, H., Allikmets, R., Sakuma, N., Pegoraro, R., et al. (2001). Identification of a gene, ABCG5, important in the regulation of dietary cholesterol absorption. Nature Genetics *27*, 79–83.

Leier, I., Jedlitschky, G., Buchholz, U., Cole, S.P., Deeley, R.G., and Keppler, D. (1994). The MRP gene encodes an ATP-dependent export pump for leukotriene C4 and structurally related conjugates. Journal of Biological Chemistry *269*, 27807–27810.

Leith, C.P., Kopecky, K.J., Godwin, J., McConnell, T., Slovak, M.L., Chen, I.M., Head, D.R., Appelbaum, F.R., and Willman, C.L. (1997). Acute myeloid leukemia in the elderly: Assessment of multidrug resistance (MDR1) and cytogenetics distinguishes biologic subgroups with remarkably distinct responses to standard chemotherapy. A Southwest Oncology Group study. Blood *89*, 3323–3329.

Lemmon, M.A., Treutlein, H.R., Adams, P.D., Brünger, A.T., and Engelman, D.M. (1994). A dimerization motif for transmembrane alpha-helices. Nature Structural Biology *1*, 157–163.

Lerner-Marmarosh, N., Gimi, K., Urbatsch, I.L., Gros, P., and Senior, A.E. (1999). Large scale purification of detergent-soluble P-glycoprotein from Pichia pastoris cells and characterization of nucleotide binding properties of wild-type, Walker A, and Walker B mutant proteins. Journal of Biological Chemistry *274*, 34711–34718.

Leslie, E.M., Deeley, R.G., and Cole, S.P.C. (2005). Multidrug resistance proteins: Role of P-glycoprotein, MRP1, MRP2, and BCRP (ABCG2) in tissue defense. Toxicology and Applied Pharmacology *204*, 216–237.

Li, J., Jaimes, K.F., and Aller, S.G. (2014). Refined structures of mouse P-glycoprotein. Protein Science *23*, 34–46.

Linton, K.J. (2007). Structure and Function of ABC Transporters. Physiology *22*, 122–130.

Linton, K.J., and Higgins, C.F. (1998). The Escherichia coli ATP-binding cassette (ABC) proteins. Molecular Microbiology *28*, 5–13.

Lippincott-Schwartz, J., Snapp, E., and Kenworthy, A. (2001). Studying protein dynamics in living cells. Nature Reviews Molecular Cell Biology *2*, 444–456.

Litman, T., Jensen, U., Hansen, A., Covitz, K.-M., Zhan, Z., Fetsch, P., Abati, A., Hansen, P.R., Horn, T., Skovsgaard, T., et al. (2002). Use of peptide antibodies to probe for the mitoxantrone resistance-associated protein MXR/BCRP/ABCP/ABCG2. Biochimica et Biophysica Acta *1565*, 6–16.

Liu, Y., Yang, Y., Qi, J., Peng, H., and Zhang, J. (2008). Effect of cysteine mutagenesis on the function and disulfide bond formation of human ABCG2. Journal of Pharmacology and Experimental Therapeutics *326*, 33–40.

Locher, K.P., Lee, A.T., and Rees, D.C. (2002). The E. coli BtuCD structure: a framework for ABC transporter architecture and mechanism. Science *296*, 1091–1098.

Loo, T.W., and Clarke, D.M. (1995). Membrane topology of a cysteine-less mutant of human P-glycoprotein. Journal of Biological Chemistry *270*, 843–848.

Loo, T.W., and Clarke, D.M. (2000). Identification of residues within the drug-binding domain of the human multidrug resistance P-glycoprotein by cysteine-scanning mutagenesis and reaction with dibromobimane. Journal of Biological Chemistry *275*, 39272–39278.

Loo, T.W., Bartlett, M.C., and Clarke, D.M. (2004). The drug-binding pocket of the human multidrug resistance P-glycoprotein is accessible to the aqueous medium. Biochemistry *43*, 12081–12089.

Loo, T.W., Bartlett, M.C., and Clarke, D.M. (2006). Transmembrane segment 1 of human P-glycoprotein contributes to the drug-binding pocket. Biochemical Journal *396*, 537–545.

Loudet, A., and Burgess, K. (2007). BODIPY dyes and their derivatives: Syntheses and spectroscopic properties. Chemical Reviews *107*, 4891–4932.

Lowry, O.H., Rosebrough, N.J., Farr, A.L., and Randall, R.J. (1951). Protein measurement with the Folin phenol reagent. Journal of Biological Chemistry *193*, 265–275.

Lukacs, G.L., Chang, X.B., Bear, C., Kartner, N., Mohamed, A., Riordan, J.R., and Grinstein, S. (1993). The delta F508 mutation decreases the stability of cystic fibrosis transmembrane conductance regulator in the plasma membrane. Determination of functional half-lives on transfected cells. Journal of Biological Chemistry *268*, 21592–21598.

Macdonald, P.J., Chen, Y., and Müller, J.D. (2012). Chromophore maturation and fluorescence fluctuation spectroscopy of fluorescent proteins in a cell-free expression system. Analytical Biochemistry *421*, 291–298.

Macdonald, P.J., Johnson, J., Smith, E., Chen, Y., and Müller, J.D. (2013). Brightness analysis. In Methods in Enzymology, (Elsevier), pp. 71–98.

Macháň, R., and Wohland, T. (2014). Recent applications of fluorescence correlation spectroscopy in live systems. FEBS Letters *588*, 3571–3584.

Magde, D., Elson, E., and Webb, W. (1972). Thermodynamic fluctuations in a reacting system — Measurement by fluorescence correlation spectroscopy. Physical Review Letters *29*, 705–708.

Malengo, G., Andolfo, A., Sidenius, N., Gratton, E., Zamai, M., and Caiolfa, V.R. (2008). Fluorescence correlation spectroscopy and photon counting histogram on membrane proteins: Functional dynamics of the glycosylphosphatidylinositol-anchored urokinase plasminogen activator receptor. Journal of Biomedical Optics *13*, 031215.

Maliepaard, M., Scheffer, G., Faneyte, I., van Gastelen, M., Pijnenborg, A., Schinkel, A., van De Vijver, M., Scheper, R., and Schellens, J. (2001). Subcellular localization and distribution of the breast cancer resistance protein transporter in normal human tissues. Cancer Research *61*, 3458–3464.

Mandel, L. (1958). Fluctuations of photon beams and their correlations. Proceedings of the Physical Society *72*, 1037–1048.

Mao, Q., and Unadkat, J. (2005). Role of the breast cancer resistance protein (ABCG2) in drug transport. AAPS Journal *7*, E118–E133.

Marie, J.P., Zittoun, R., and Sikic, B.I. (1991). Multidrug resistance (mdr1) gene expression in adult acute leukemias: Correlations with treatment outcome and in vitro drug sensitivity. Blood *78*, 586–592.

Martin, C., Higgins, C.F., and Callaghan, R. (2001). The vinblastine binding site adopts high- and low-affinity conformations during a transport cycle of P-glycoprotein. Biochemistry *40*, 15733–15742.

Mashanov, G.I., Tacon, D., Knight, A.E., Peckham, M., and Molloy, J.E. (2003). Visualizing single molecules inside living cells using total internal reflection fluorescence microscopy. Methods *29*, 142–152.

Matte, A., and Delbaere, L.T. (2010). ATP-binding Motifs. In Encyclopedia of Life Sciences, John Wiley & Sons, Ltd, ed. (Chichester, UK: John Wiley & Sons, Ltd).

Mattheyses, A.L., Simon, S.M., and Rappoport, J.Z. (2010). Imaging with total internal reflection fluorescence microscopy for the cell biologist. Journal of Cell Science *123*, 3621–3628.

McDevitt, C., Collins, R., Conway, M., Modok, S., Storm, J., Kerr, I., Ford, R., and Callaghan, R. (2006). Purification and 3D structural analysis of oligomeric human multidrug transporter ABCG2. Structure *14*, 1623–1632.

McDevitt, C.A., Shintre, C.A., Grossmann, J.G., Pollock, N.L., Prince, S.M., Callaghan, R., and Ford, R.C. (2008a). Structural insights into P-glycoprotein (ABCB1) by small angle X-ray scattering and electron crystallography. FEBS Letters. *582*, 2950–2956.

McDevitt, C.A., Crowley, E., Hobbs, G., Starr, K.J., Kerr, I.D., and Callaghan, R. (2008b). Is ATP binding responsible for initiating drug translocation by the multidrug transporter ABCG2? FEBS Journal *275*, 4354–4362.

McGuire, H., Aurousseau, M.R.P., Bowie, D., and Blunck, R. (2012). Automating single subunit counting of membrane proteins in mammalian cells. Journal of Biological Chemistry *287*, 35912–35921.

Merino, G., Alvarez, A.I., Pulido, M.M., Molina, A.J., Schinkel, A.H., and Prieto, J.G. (2006). Breast cancer resistance protein (BCRP/ABCG2) transports fluoroquinolone

antibiotics and affects their oral availability, pharmacokinetics, and milk secretion. Drug Metabolism and Disposition *34*, 690–695.

Merino, G., Jonker, J.W., Wagenaar, E., van Herwaarden, A.E., and Schinkel, A.H. (2005). The breast cancer resistance protein (BCRP/ABCG2) affects pharmacokinetics, hepatobiliary excretion, and milk secretion of the antibiotic nitrofurantoin. Molecular Pharmacology *67*, 1758–1764.

Meszaros, P., Hummel, I., Klappe, K., Draghiciu, O., Hoekstra, D., and Kok, J.W. (2013). The function of the ATP-binding cassette (ABC) transporter ABCB1 is not susceptible to actin disruption. Biochimica et Biophysica Acta (BBA) - Biomembranes *1828*, 340–351.

Metzler, R., and Klafter, J. (2000). The random walk's guide to anomalous diffusion: A fractional dynamics approach. Physics Reports *339*, 1–77.

Mikhailov, M.V., Campbell, J.D., de Wet, H., Shimomura, K., Zadek, B., Collins, R.F., Sansom, M.S., Ford, R.C., and Ashcroft, F.M. (2005). 3-D structural and functional characterization of the purified K_{ATP} channel complex Kir6.2-SUR1: 3D structure of the K_{ATP} channel. The EMBO Journal *24*, 4166–4175.

Miki, T., Nagashima, K., and Seino, S. (1999). The structure and function of the ATP-sensitive K+ channel in insulin-secreting pancreatic beta-cells. Journal of Molecular Endocrinology *22*, 113–123.

Minsky, M. (1988). Memoir on inventing the confocal scanning microscope. Scanning *10*, 128–138.

Miyawaki, A., Llopis, J., Heim, R., McCaffery, J.M., Adams, J.A., Ikura, M., and Tsien, R.Y. (1997). Fluorescent indicators for Ca2+ based on green fluorescent proteins and calmodulin. Nature *388*, 882–887.

Mizuarai, S., Aozasa, N., and Kotani, H. (2004). Single nucleotide polymorphisms result in impaired membrane localization and reduced atpase activity in multidrug transporter ABCG2. International Journal of Cancer *109*, 238–246.

Mo, W., Qi, J., and Zhang, J.-T. (2012). Different roles of TM5, TM6, and ECL3 in the oligomerization and function of human ABCG2. Biochemistry *51*, 3634–3641.

Molinski, S., Eckford, P.D.W., Pasyk, S., Ahmadi, S., Chin, S., and Bear, C.E. (2012). Functional rescue of F508del-CFTR using small molecule correctors. Frontiers in Pharmacology *3*, 160.

Momburg, F., Roelse, J., Howard, J.C., Butcher, G.W., Hämmerling, G.J., and Neefjes, J.J. (1994). Selectivity of MHC-encoded peptide transporters from human, mouse and rat. Nature *367*, 648–651.

Morin, J.G., and Hastings, J.W. (1971). Energy transfer in a bioluminescent system. Journal of Cellular Physiology *77*, 313–318.

Morisaki, K., Robey, R.W., Özvegy-Laczka, C., Honjo, Y., Polgar, O., Steadman, K., Sarkadi, B., and Bates, S.E. (2005). Single nucleotide polymorphisms modify the transporter activity of ABCG2. Cancer Chemotherapy and Pharmacology *56*, 161–172.

Mullard, A. (2012). Protein–protein interaction inhibitors get into the groove. Nature Reviews Drug Discovery *11*, 173–175.

Müller, J.D., Chen, Y., and Gratton, E. (2000). Resolving heterogeneity on the single molecular level with the photon-counting histogram. Biophysical Journal *78*, 474–486.

Müller, M., Bakos, E., Welker, E., Váradi, A., Germann, U.A., Gottesman, M.M., Morse, B.S., Roninson, I.B., and Sarkadi, B. (1996). Altered drug-stimulated ATPase activity in mutants of the human multidrug resistance protein. Journal of Biological Chemistry *271*, 1877–1883.

Mumenthaler, S.M., Ng, P.Y.B., Hodge, A., Bearss, D., Berk, G., Kanekal, S., Redkar, S., Taverna, P., Agus, D.B., and Jain, A. (2009). Pharmacologic inhibition of Pim kinases alters prostate cancer cell growth and resensitizes chemoresistant cells to taxanes. Molecular Cancer Therapeutics *8*, 2882–2893.

Nagai, T., Ibata, K., Park, E.S., Kubota, M., Mikoshiba, K., and Miyawaki, A. (2002). A variant of yellow fluorescent protein with fast and efficient maturation for cell-biological applications. Nature Biotechnology *20*, 87–90.

Nagata, K.O., Nakada, C., Kasai, R.S., Kusumi, A., and Ueda, K. (2013). ABCA1 dimer-monomer interconversion during HDL generation revealed by single-molecule imaging. Proceedings of the National Academy of Sciences *110*, 5034–5039.

Nakajo, K., Ulbrich, M.H., Kubo, Y., and Isacoff, E.Y. (2010). Stoichiometry of the KCNQ1 - KCNE1 ion channel complex. Proceedings of the National Academy of Sciences *107*, 18862–18867.

Neefjes, J.J., Momburg, F., and Hämmerling, G.J. (1993). Selective and ATP-dependent translocation of peptides by the MHC-encoded transporter. Science *261*, 769–771.

Ni, Z., Mark, M., Cai, X., and Mao, Q. (2010). Fluorescence resonance energy transfer (FRET) analysis demonstrates dimer/oligomer formation of the human breast cancer resistance protein (BCRP/ABCG2) in intact cells. International Journal of Biochemistry and Molecular Biology *1*, 1–11.

Nikaido, K., and Ames, G.F. (1999). One intact ATP-binding subunit is sufficient to support ATP hydrolysis and translocation in an ABC transporter, the histidine permease. Journal of Biological Chemistry *274*, 26727–26735.

Niu, Q., Wang, W., Li, Y., Ruden, D.M., Wang, F., Li, Y., Wang, F., Song, J., and Zheng, K. (2012). Low molecular weight heparin ablates lung cancer cisplatin-resistance by inducing proteasome-mediated ABCG2 protein degradation. PLoS ONE *7*, e41035.

Nobili, S., Landini, I., Giglioni, B., and Mini, E. (2006). Pharmacological strategies for overcoming multidrug resistance. Current Drug Targets *7*, 861–879.

Ohshiro, J., Yamamura, H., Saeki, T., Suzuki, Y., and Imaizumi, Y. (2014). The multiple expression of Ca2+-activated Cl− channels via homo- and hetero-dimer formation of TMEM16A splicing variants in murine portal vein. Biochemical and Biophysical Research Communications *443*, 518–523.

Oldham, M.L., Khare, D., Quiocho, F.A., Davidson, A.L., and Chen, J. (2007). Crystal structure of a catalytic intermediate of the maltose transporter. Nature *450*, 515–521.

Olsen, H., Nilsen, H., Hayes, B., Berg, P.R., Svendsen, M., Lien, S., and Meuwissen, T. (2007). Genetic support for a quantitative trait nucleotide in the ABCG2 gene affecting milk composition of dairy cattle. BMC Genetics *8*, 32.

O'Mara, M.L., and Tieleman, D.P. (2007). P-glycoprotein models of the apo and ATP-bound states based on homology with Sav1866 and MalK. FEBS Letters. *581*, 4217–4222.

Ormö, M., Cubitt, A.B., Kallio, K., Gross, L.A., Tsien, R.Y., and Remington, S.J. (1996). Crystal structure of the Aequorea victoria green fluorescent protein. Science *273*, 1392–1395.

Ostedgaard, L.S., Rogers, C.S., Dong, Q., Randak, C.O., Vermeer, D.W., Rokhlina, T., Karp, P.H., and Welsh, M.J. (2007). Processing and function of CFTR-DeltaF508 are species-dependent. Proceedings of the National Academy of Sciences *104*, 15370–15375.

Ozvegy, C., Váradi, A., and Sarkadi, B. (2002). Characterization of drug transport, ATP hydrolysis, and nucleotide trapping by the human ABCG2 multidrug transporter. Modulation of substrate specificity by a point mutation. Journal of Biological Chemistry *277*, 47980–47990.

Pajic, M., Murray, J., Marshall, G.M., Cole, S.P.C., Norris, M.D., and Haber, M. (2011). ABCC1 G2012T single nucleotide polymorphism is associated with patient outcome in primary neuroblastoma and altered stability of the ABCC1 gene transcript. Pharmacogenetics and Genomics *21*, 270–279.

Patowary, S., Alvarez-Curto, E., Xu, T.-R., Holz, J.D., Oliver, J.A., Milligan, G., and Raicu, V. (2013). The muscarinic M3 acetylcholine receptor exists as two differently sized complexes at the plasma membrane. Biochemical Journal *452*, 303–312.

Patterson, G.H., Knobel, S.M., Sharif, W.D., Kain, S.R., and Piston, D.W. (1997). Use of the green fluorescent protein and its mutants in quantitative fluorescence microscopy. Biophysical Journal *73*, 2782–2790.

Pedelacq, J.-D., Cabantous, S., Tran, T., Terwilliger, T.C., and Waldo, G.S. (2006). Engineering and characterization of a superfolder green fluorescent protein. Nature Biotechnology *24*, 79–88.

Pedemonte, N., Lukacs, G.L., Du, K., Caci, E., Zegarra-Moran, O., Galietta, L.J., and Verkman, A. (2005). Small-molecule correctors of defective ΔF508-CFTR cellular processing identified by high-throughput screening. Journal of Clinical Investigation *115*, 2564–2571.

Perroud, T.D., Huang, B., and Zare, R.N. (2005). Effect of bin time on the photon counting histogram for one-photon excitation. ChemPhysChem *6*, 905–912.

Petrášek, Z., and Schwille, P. (2008). Precise measurement of diffusion coefficients using scanning fluorescence correlation spectroscopy. Biophysical Journal *94*, 1437–1448.

Petronilli, V., and Ames, G.F. (1991). Binding protein-independent histidine permease mutants. Uncoupling of ATP hydrolysis from transmembrane signaling. Journal of Biological Chemistry *266*, 16293–16296.

Piston, D.W., and Kremers, G.-J. (2007). Fluorescent protein FRET: The good, the bad and the ugly. Trends in Biochemical Sciences *32*, 407–414.

Plant, L.D., Dementieva, I.S., Kollewe, A., Olikara, S., Marks, J.D., and Goldstein, S.A.N. (2010). One SUMO is sufficient to silence the dimeric potassium channel K2P1. Proceedings of the National Academy of Sciences *107*, 10743–10748.

Plant, L.D., Dowdell, E.J., Dementieva, I.S., Marks, J.D., and Goldstein, S.A.N. (2011). SUMO modification of cell surface Kv2.1 potassium channels regulates the activity of rat hippocampal neurons. The Journal of General Physiology *137*, 441–454.

Plant, L.D., Xiong, D., Dai, H., and Goldstein, S.A.N. (2014). Individual IKs channels at the surface of mammalian cells contain two KCNE1 accessory subunits. Proceedings of the National Academy of Sciences *111*, E1438–E1446.

Polak, M., and Cavé, H. (2007). Neonatal diabetes mellitus: A disease linked to multiple mechanisms. Orphanet Journal of Rare Diseases *2*, 12.

Polgar, O., Robey, R.W., Morisaki, K., Dean, M., Michejda, C., Sauna, Z.E., Ambudkar, S.V., Tarasova, N., and Bates, S.E. (2004). Mutational analysis of ABCG2: Role of the GXXXG motif. Biochemistry *43*, 9448–9456.

Polgar, O., Ierano, C., Tamaki, A., Stanley, B., Ward, Y., Xia, D., Tarasova, N., Robey, R.W., and Bates, S.E. (2010). Mutational analysis of threonine 402 adjacent to the GXXXG dimerization motif in transmembrane segment 1 of ABCG2. Biochemistry *49*, 2235–2245.

Pollex, E., Lubetsky, A., and Koren, G. (2008). The role of placental breast cancer resistance protein in the efflux of glyburide across the human placenta. Placenta *29*, 743–747.

Poruchynsky, M.S., and Ling, V. (1994). Detection of oligomeric and monomeric forms of P-glycoprotein in multidrug resistant cells. Biochemistry *33*, 4163–4174.

Prasher, D.C., Eckenrode, V.K., Ward, W.W., Prendergast, F.G., and Cormier, M.J. (1992). Primary structure of the Aequorea victoria green-fluorescent protein. Gene *111*, 229–233.

Procko, E., Ferrin-O'Connell, I., Ng, S.-L., and Gaudet, R. (2006). Distinct structural and functional properties of the ATPase sites in an asymmetric ABC transporter. Molecular Cell *24*, 51–62.

Quazi, F., and Molday, R.S. (2014). ATP-binding cassette transporter ABCA4 and chemical isomerization protect photoreceptor cells from the toxic accumulation of excess 11-cis-retinal. Proceedings of the National Academy of Sciences *111*, 5024–5029.

Ramachandra, M., Ambudkar, S.V., Chen, D., Hrycyna, C.A., Dey, S., Gottesman, M.M., and Pastan, I. (1998). Human P-glycoprotein exhibits reduced affinity for substrates during a catalytic transition state. Biochemistry *37*, 5010–5019.

Ramjeesingh, M., Li, C., Garami, E., Huan, L.J., Galley, K., Wang, Y., and Bear, C.E. (1999). Walker mutations reveal loose relationship between catalytic and channel-gating activities of purified CFTR (cystic fibrosis transmembrane conductance regulator). Biochemistry *38*, 1463–1468.

Reed, J.C. (1995). Regulation of apoptosis by bcl-2 family proteins and its role in cancer and chemoresistance. Current Opinion in Oncology *7*, 541–546.

Regner, B.M., Vučinić, D., Domnisoru, C., Bartol, T.M., Hetzer, M.W., Tartakovsky, D.M., and Sejnowski, T.J. (2013). Anomalous diffusion of single particles in cytoplasm. Biophysical Journal *104*, 1652–1660.

Reid, B.G., and Flynn, G.C. (1997). Chromophore formation in green fluorescent protein. Biochemistry *36*, 6786–6791.

Reiner, A., Arant, R.J., and Isacoff, E.Y. (2012). Assembly stoichiometry of the GluK2/GluK5 kainate receptor complex. Cell Reports *1*, 234–240.

Reits, E.A., Vos, J.C., Grommé, M., and Neefjes, J. (2000). The major substrates for TAP in vivo are derived from newly synthesized proteins. Nature *404*, 774–778.

Reits, E.A., and Neefjes, J.J. (2001). From fixed to FRAP: Measuring protein mobility and activity in living cells. Nature Cell Biology *3*, E145–E147.

Van Rheenen, J., Langeslag, M., and Jalink, K. (2004). Correcting confocal acquisition to optimize imaging of fluorescence resonance energy transfer by sensitized emission. Biophysical Journal *86*, 2517–2529.

Rhoades, E., Gussakovsky, E., and Haran, G. (2003). Watching proteins fold one molecule at a time. Proceedings of the National Academy of Sciences *100*, 3197–3202.

Rigler, R., Mets, Ü., Widengren, J., and Kask, P. (1993). Fluorescence correlation spectroscopy with high count rate and low background: Analysis of translational diffusion. European Biophysics Journal *22*, 169–175.

Riordan, J.R., Rommens, J.M., Kerem, B., Alon, N., Rozmahel, R., Grzelczak, Z., Zielenski, J., Lok, S., Plavsic, N., and Chou, J.L. (1989). Identification of the cystic fibrosis gene: Cloning and characterization of complementary DNA. Science *245*, 1066–1073.

Rizzo, M.A., Springer, G.H., Granada, B., and Piston, D.W. (2004). An improved cyan fluorescent protein variant useful for FRET. Nature Biotechnology *22*, 445–449.

Robey, R.W., Honjo, Y., Morisaki, K., Nadjem, T.A., Runge, S., Risbood, M., Poruchynsky, M.S., and Bates, S.E. (2003). Mutations at amino-acid 482 in the ABCG2 gene affect substrate and antagonist specificity. British Journal of Cancer *89*, 1971–1978.

Rodionov, D.A., Hebbeln, P., Eudes, A., ter Beek, J., Rodionova, I.A., Erkens, G.B., Slotboom, D.J., Gelfand, M.S., Osterman, A.L., Hanson, A.D., et al. (2009). A novel class of

modular transporters for vitamins in prokaryotes. Journal of Bacteriology *191*, 42–51.

Rosenberg, M.F., Kamis, A.B., Callaghan, R., Higgins, C.F., and Ford, R.C. (2003). Three-dimensional structures of the mammalian multidrug resistance P-glycoprotein demonstrate major conformational changes in the transmembrane domains upon nucleotide binding. Journal of Biological Chemistry *278*, 8294–8299.

Rosenberg, M.F., Bikadi, Z., Chan, J., Liu, X., Ni, Z., Cai, X., Ford, R.C., and Mao, Q. (2010). The human breast cancer resistance protein (BCRP/ABCG2) shows conformational changes with mitoxantrone. Structure *18*, 482–493.

Rosenberg, M.F., Mao, Q., Holzenburg, A., Ford, R.C., Deeley, R.G., and Cole, S.P. (2001). The structure of the multidrug resistance protein 1 (MRP1/ABCC1). Crystallization and single-particle analysis. Journal of Biological Chemistry *276*, 16076–16082.

Rothnie, A., Callaghan, R., Deeley, R.G., and Cole, S.P.C. (2006). Role of GSH in estrone sulfate binding and translocation by the multidrug resistance protein 1 (MRP1/ABCC1). Journal of Biological Chemistry *281*, 13906–13914.

Roy, R., Hohng, S., and Ha, T. (2008). A practical guide to single-molecule FRET. Nature Methods *5*, 507–516.

Russ, W.P., and Engelman, D.M. (2000). The GxxxG motif: A framework for transmembrane helix-helix association. Journal of Molecular Biology *296*, 911–919.

Sako, Y., Minoghchi, S., and Yanagida, T. (2000). Single-molecule imaging of EGFR signalling on the surface of living cells. Nature Cell Biology *2*, 168–172.

Sarankó, H., Tordai, H., Telbisz, Á., Özvegy-Laczka, C., Erdős, G., Sarkadi, B., and Hegedűs, T. (2013). Effects of the gout-causing Q141K polymorphism and a CFTR ΔF508 mimicking mutation on the processing and stability of the ABCG2 protein. Biochemical and Biophysical Research Communications *437*, 140–145.

Saris, C.J., Domen, J., and Berns, A. (1991). The pim-1 oncogene encodes two related protein-serine/threonine kinases by alternative initiation at AUG and CUG. EMBO Journal. *10*, 655–664.

Saxton, M.J. (1999). Chapter 8 Lateral diffusion of lipids and proteins. In membrane permeability 100 years since Ernest Overton, (Academic Press), pp. 229–282.

Saxton, M.J., and Jacobson, K. (1997). Single-particle tracking: Applications to membrane dynamics. Annual Review of Biophysics and Biomolecular Structure *26*, 373–399.

Schinkel, A.H. (1999). P-Glycoprotein, a gatekeeper in the blood-brain barrier. Advanced Drug Delivery Reviews *36*, 179–194.

Schinkel, A.H., Kemp, S., Dollé, M., Rudenko, G., and Wagenaar, E. (1993). N-glycosylation and deletion mutants of the human MDR1 P-glycoprotein. Journal of Biological Chemistry *268*, 7474–7481.

Schmitz, G., and Langmann, T. (2001). Structure, function and regulation of the ABC1 gene product. Current Opinion in Lipidology *12*, 129–140.

Schneider, C.A., Rasband, W.S., and Eliceiri, K.W. (2012). NIH Image to ImageJ: 25 years of image analysis. Nature Methods *9*, 671–675.

Schuler, B., and Eaton, W.A. (2008). Protein folding studied by single-molecule FRET. Current Opinion in Structural Biology *18*, 16–26.

Schultz, M.J., Wijnholds, J., Peppelenbosch, M.P., Vervoordeldonk, M.J., Speelman, P., van Deventer, S.J., Borst, P., and van der Poll, T. (2001). Mice lacking the multidrug resistance protein 1 are resistant to Streptococcus pneumoniae-induced pneumonia. Journal of Immunology *166*, 4059–4064.

Senes, A., Gerstein, M., and Engelman, D.M. (2000). Statistical analysis of amino acid patterns in transmembrane helices: The GxxxG motif occurs frequently and in association with beta-branched residues at neighboring positions. Journal of Molecular Biology *296*, 921–936.

Senior, A.E., al-Shawi, M.K., and Urbatsch, I.L. (1995). The catalytic cycle of P-glycoprotein. FEBS Letters. *377*, 285–289.

Shapiro, A.B., Corder, A.B., and Ling, V. (1997). P-glycoprotein-mediated Hoechst 33342 transport out of the lipid bilayer. European Journal of Biochemistry *250*, 115–121.

Sharom, F.J. (2011). The P-glycoprotein multidrug transporter. Essays in Biochemistry *50*, 161–178.

Sheppard, D.N., and Welsh, M.J. (1999). Structure and function of the CFTR chloride channel. Physiological Reviews *79*, S23–S45.

Shi, Z., Tiwari, A.K., Shukla, S., Robey, R.W., Singh, S., Kim, I.-W., Bates, S.E., Peng, X., Abraham, I., Ambudkar, S.V., et al. (2011). Sildenafil reverses ABCB1- and ABCG2-mediated chemotherapeutic drug resistance. Cancer Research. *71*, 3029–3041.

Shigeta, J., Katayama, K., Mitsuhashi, J., Noguchi, K., and Sugimoto, Y. (2010). BCRP/ABCG2 confers anticancer drug resistance without covalent dimerization. Cancer Science *101*, 1813–1821.

Shimomura, O. (1979). Structure of the chromophore of Aequorea green fluorescent protein. FEBS Letters *104*, 220–222.

Shimomura, O., Johnson, F.H., and Saiga, Y. (1962). Extraction, purification and properties of aequorin, a bioluminescent protein from the luminous hydromedusan, Aequorea. Journal of Cellular and Comparative Physiology *59*, 223–239.

Shintre, C.A., Pike, A.C.W., Li, Q., Kim, J.-I., Barr, A.J., Goubin, S., Shrestha, L., Yang, J., Berridge, G., Ross, J., et al. (2013). Structures of ABCB10, a human ATP-binding cassette transporter in apo- and nucleotide-bound states. Proceedings of the National Academy of Sciences. *110*, 9710–9715.

Shroyer, N.F., Lewis, R.A., Yatsenko, A.N., Wensel, T.G., and Lupski, J.R. (2001). Cosegregation and functional analysis of mutant ABCR (ABCA4) alleles in families that manifest both Stargardt disease and age-related macular degeneration. Human Molecular Genetics *10*, 2671–2678.

Shukla, S., Robey, R.W., Bates, S.E., and Ambudkar, S.V. (2006). The calcium channel blockers, 1,4-dihydropyridines, are substrates of the multidrug resistance-linked ABC drug transporter, ABCG2. Biochemistry *45*, 8940–8951.

Shyamala, V., Baichwal, V., Beall, E., and Ames, G.F. (1991). Structure-function analysis of the histidine permease and comparison with cystic fibrosis mutations. Journal of Biology Chemistry *266*, 18714–18719.

Shyng, S., and Nichols, C.G. (1997). Octameric stoichiometry of the KATP channel complex. Journal of General Physiology *110*, 655–664.

Sievers, F., Wilm, A., Dineen, D., Gibson, T.J., Karplus, K., Li, W., Lopez, R., McWilliam, H., Remmert, M., Söding, J., et al. (2011). Fast, scalable generation of high-quality protein multiple sequence alignments using Clustal Omega. Molecular Systems Biology *7*, 539.

Slot, A.J., Molinski, S.V., and Cole, S.P.C. (2011). Mammalian multidrug-resistance proteins (MRPs). Essays in Biochemistry *50*, 179–207.

Smit, L.S., Wilkinson, D.J., Mansoura, M.K., Collins, F.S., and Dawson, D.C. (1993). Functional roles of the nucleotide-binding folds in the activation of the cystic fibrosis transmembrane conductance regulator. Proceedings of the National Academy of Sciences *90*, 9963–9967.

Smith, P.C., Karpowich, N., Millen, L., Moody, J.E., Rosen, J., Thomas, P.J., and Hunt, J.F. (2002). ATP binding to the motor domain from an ABC transporter drives formation of a nucleotide sandwich dimer. Molecular Cell *10*, 139–149.

Sonveaux, N., Vigano, C., Shapiro, A.B., Ling, V., and Ruysschaert, J.M. (1999). Ligand-mediated tertiary structure changes of reconstituted P-glycoprotein. A tryptophan fluorescence quenching analysis. Journal of Biological Chemistry *274*, 17649–17654.

Sparreboom, A., Loos, W.J., Burger, H., Sissung, T.M., Verweij, J., Figg, W.D., Nooter, K., and Gelderblom, H. (2005). Effect of ABCG2 genotype on the oral vioavailability of topotecan. Cancer Biology & Therapy *4*, 650–653.

Sprague, B.L., and McNally, J.G. (2005). FRAP analysis of binding: Proper and fitting. Trends in Cell Biology *15*, 84–91.

Sprague, B.L., Pego, R.L., Stavreva, D.A., and McNally, J.G. (2004). Analysis of binding reactions by fluorescence recovery after photobleaching. Biophysical Journal *86*, 3473–3495.

Steinbach, D., and Legrand, O. (2007). ABC transporters and drug resistance in leukemia: Was P-gp nothing but the first head of the Hydra? Leukemia *21*, 1172–1176.

Stockner, T., de Vries, S.J., Bonvin, A.M.J.J., Ecker, G.F., and Chiba, P. (2009). Data-driven homology modelling of P-glycoprotein in the ATP-bound state indicates flexibility of the transmembrane domains. FEBS Journal *276*, 964–972.

Støy, J., Edghill, E.L., Flanagan, S.E., Ye, H., Paz, V.P., Pluzhnikov, A., Below, J.E., Hayes, M.G., Cox, N.J., Lipkind, G.M., et al. (2007). Insulin gene mutations as a cause of permanent neonatal diabetes. Proceedings of the National Academy of Sciences *104*, 15040–15044.

Stryer, L. (1978). Fluorescence energy transfer as a spectroscopic ruler. Annual Review of Biochemistry *47*, 819–846.

Szakács, G., Paterson, J.K., Ludwig, J.A., Booth-Genthe, C., and Gottesman, M.M. (2006). Targeting multidrug resistance in cancer. Nature Reviews Drug Discovery *5*, 219–234.

Szentpétery, Z., Sarkadi, B., Bakos, E., and Váradi, A. (2004). Functional studies on the MRP1 multidrug transporter: Characterization of ABC-signature mutant variants. Anticancer Research. *24*, 449–455.

Tacke, M., Hanke, G., Hanke, T., and Hünig, T. (1997). CD28-mediated induction of proliferation in resting T cells in vitro and in vivo without engagement of the T cell receptor: Evidence for functionally distinct forms of CD28. European Journal of Immunology *27*, 239–247.

Takada, T., Suzuki, H., Gotoh, Y., and Sugiyama, Y. (2005). Regulation of the cell surface expression of human BCRP/ABCG2 by the phosphorylation state of Akt in polarized cells. Drug Metabolism and Disposition *33*, 905–909.

Tamaki, A., Ierano, C., Szakacs, G., Robey, R.W., and Bates, S.E. (2011). The controversial role of ABC transporters in clinical oncology. Essays in Biochemistry *50*, 209–232.

Tertoolen, L.G., Blanchetot, C., Jiang, G., Overvoorde, J., Gadella, T.W., Jr, Hunter, T., and den Hertog, J. (2001). Dimerization of receptor protein-tyrosine phosphatase alpha in living cells. BMC Cell Biology *2*, 8.

Thomas, P.M., Cote, G.J., Wohllk, N., Haddad, B., Mathew, P.M., Rabl, W., Aguilar-Bryan, L., Gagel, R.F., and Bryan, J. (1995). Mutations in the sulfonylurea receptor gene in familial persistent hyperinsulinemic hypoglycemia of infancy. Science *268*, 426–429.

Timmins, J.M., Lee, J.-Y., Boudyguina, E., Kluckman, K.D., Brunham, L.R., Mulya, A., Gebre, A.K., Coutinho, J.M., Colvin, P.L., Smith, T.L., et al. (2005). Targeted inactivation of hepatic Abca1 causes profound hypoalphalipoproteinemia and kidney hypercatabolism of apoA-I. Journal of Clinical Investigation *115*, 1333–1342.

Tombline, G., Bartholomew, L., Gimi, K., Tyndall, G.A., and Senior, A.E. (2004). Synergy between conserved ABC signature Ser residues in P-glycoprotein catalysis. Journal of Biological Chemistry *279*, 5363–5373.

Tombline, G., Muharemagić, A., White, L.B., and Senior, A.E. (2005). Involvement of the "occluded nucleotide conformation" of P-glycoprotein in the catalytic pathway. Biochemistry *44*, 12879–12886.

Trock, B.J., Leonessa, F., and Clarke, R. (1997). Multidrug resistance in breast cancer: A meta-analysis of MDR1/gp170 expression and its possible functional significance. Journal of the National Cancer Institute *89*, 917–931.

Tsien, R.Y. (1998). The green fluorescent protein. Annual Review of Biochemistry *67*, 509–544.

Turner, J.G., Gump, J.L., Zhang, C., Cook, J.M., Marchion, D., Hazlehurst, L., Munster, P., Schell, M.J., Dalton, W.S., and Sullivan, D.M. (2006). ABCG2 expression, function, and promoter methylation in human multiple myeloma. Blood *108*, 3881–3889.

Ueda, K., Cardarelli, C., Gottesman, M.M., and Pastan, I. (1987). Expression of a full-length cDNA for the human "MDR1" gene confers resistance to colchicine, doxorubicin, and vinblastine. Proceedings of the National Academy of Sciences *84*, 3004–3008.

Uggla, B., Ståhl, E., Wågsäter, D., Paul, C., Karlsson, M.G., Sirsjö, A., and Tidefelt, U. (2005). BCRP mRNA expression v. clinical outcome in 40 adult AML patients. Leukemia Research *29*, 141–146.

Ulbrich, M.H., and Isacoff, E.Y. (2007). Subunit counting in membrane-bound proteins. Nature Methods *4*, 319–321.

Ulbrich, M.H., and Isacoff, E.Y. (2008). Rules of engagement for NMDA receptor subunits. Proceedings of the National Academy of Sciences *105*, 14163–14168.

Urbatsch, I.L., Gimi, K., Wilke-Mounts, S., and Senior, A.E. (2000). Investigation of the role of glutamine-471 and glutamine-1114 in the two catalytic sites of P-glycoprotein. Biochemistry *39*, 11921–11927.

Urbatsch, I.L., Tyndall, G.A., Tombline, G., and Senior, A.E. (2003). P-glycoprotein catalytic mechanism. Journal of Biological Chemistry *278*, 23171–23179.

Veliz, L.A., Toro, C.A., Vivar, J.P., Arias, L.A., Villegas, J., Castro, M.A., and Brauchi, S. (2010). Near-membrane dynamics and capture of TRPM8 channels within transient confinement domains. PLoS ONE *5*, e13290.

Vos, J.C., Reits, E.A.J., Wojcik-Jacobs, E., and Neefjes, J. (2000). Head–head/tail–tail relative orientation of the pore-forming domains of the heterodimeric ABC transporter TAP. Current Biology *10*, 1–7.

Vukojević, V., Pramanik, A., Yakovleva, T., Rigler, R., Terenius, L., and Bakalkin, G. (2005). Study of molecular events in cells by fluorescence correlation spectroscopy. Cellular and Molecular Life Sciences *62*, 535–550.

Wachter, R.M., Elsliger, M.-A., Kallio, K., Hanson, G.T., and Remington, S.J. (1998). Structural basis of spectral shifts in the yellow-emission variants of green fluorescent protein. Structure *6*, 1267–1277.

Walker, J.E., Saraste, M., Runswick, M.J., and Gay, N.J. (1982). Distantly related sequences in the alpha- and beta-subunits of ATP synthase, myosin, kinases and other ATP-requiring enzymes and a common nucleotide binding fold. EMBO Journal *1*, 945–951.

Wallace, W., Schaefer, L.H., and Swedlow, J.R. (2001). A workingperson's guide to deconvolution in light microscopy. BioTechniques *31*, 1076–1078, 1080, 1082 passim.

Wandel, C., Kim, R., Wood, M., and Wood, A. (2002). Interaction of morphine, fentanyl, sufentanil, alfentanil, and loperamide with the efflux drug transporter P-glycoprotein. Anesthesiology *96*, 913–920.

Wanders, R.J.A., Visser, W.F., Roermund, C.W.T., Kemp, S., and Waterham, H.R. (2006). The peroxisomal ABC transporter family. Pflügers Archiv - European Journal of Physiology *453*, 719–734.

Wang, F., and Yang, Y. (2014a). Identification of an antitumor immune response of polyhistidine through a toll-like receptor 4-dependent manner. Biochemical and Biophysical Research Communications *453*, 148–152.

Wang, F., and Yang, Y. (2014b). Quercetin suppresses insulin receptor signaling through inhibition of the insulin ligand–receptor binding and therefore impairs cancer cell proliferation. Biochemical and Biophysical Research Communications *452*, 1028–1033.

Wang, S., Makhina, E.N., Masia, R., Hyrc, K.L., Formanack, M.L., and Nichols, C.G. (2013). Domain organization of the ATP-sensitive potassium channel complex examined by fluorescence resonance energy transfer. Journal of Biological Chemistry *288*, 4378–4388.

Ward, A., Reyes, C.L., Yu, J., Roth, C.B., and Chang, G. (2007). Flexibility in the ABC transporter MsbA: Alternating access with a twist. Proceedings of the National Academy of Sciences *104*, 19005–19010.

Ward, A.B., Szewczyk, P., Grimard, V., Lee, C.-W., Martinez, L., Doshi, R., Caya, A., Villaluz, M., Pardon, E., Cregger, C., et al. (2013). Structures of P-glycoprotein reveal its conformational flexibility and an epitope on the nucleotide-binding domain. Proceedings of the National Academy of Sciences *110*, 13386–13391.

Wawrezinieck, L., Rigneault, H., Marguet, D., and Lenne, P.-F. (2005). Fluorescence correlation spectroscopy diffusion laws to probe the submicron cell membrane organization. Biophysical Journal *89*, 4029–4042.

Weidemann, T., Worch, R., Kurgonaite, K., Hintersteiner, M., Bökel, C., and Schwille, P. (2011). Single cell analysis of ligand binding and complex formation of interleukin-4 receptor subunits. Biophysical Journal *101*, 2360–2369.

Weiss, J., Rose, J., Storch, C.H., Ketabi-Kiyanvash, N., Sauer, A., Haefeli, W.E., and Efferth, T. (2006). Modulation of human BCRP (ABCG2) activity by anti-HIV drugs. Journal of Antimicrobial Chemotherapy *59*, 238–245.

White, J., and Stelzer, E. (1999). Photobleaching GFP reveals protein dynamics inside live cells. Trends in Cell Biology *9*, 61–65.

Wijnholds, J., Evers, R., van Leusden, M.R., Mol, C.A.A.M., Zaman, G.J.R., Mayer, U., Beijnen, J.H., Valk, M.V.D., Krimpenfort, P., and Borst, P. (1997). Increased sensitivity to anticancer drugs and decreased inflammatory response in mice lacking the multidrug resistance-associated protein. Nature Medicine *3*, 1275–1279.

Wilkins, M.R., Gasteiger, E., Bairoch, A., Sanchez, J.C., Williams, K.L., Appel, R.D., and Hochstrasser, D.F. (1999). Protein identification and analysis tools in the ExPASy server. Methods in Molecular Biology *112*, 531–552.

Wilund, K.R., Yu, L., Xu, F., Hobbs, H.H., and Cohen, J.C. (2004). High-level expression of ABCG5 and ABCG8 attenuates diet-induced hypercholesterolemia and atherosclerosis in Ldlr-/- mice. Journal of Lipid Research *45*, 1429–1436.

Winter, M.C., and Welsh, M.J. (1997). Stimulation of CFTR activity by its phosphorylated R domain. Nature *389*, 294–296.

Wolf-Ringwall, A.L., Winter, P.W., Liu, J., Van Orden, A.K., Roess, D.A., and Barisas, B.G. (2011). Restricted lateral diffusion of luteinizing hormone receptors in membrane microdomains. Journal of Biological Chemistry *286*, 29818–29827.

Wong, K., Ma, J., Rothnie, A., Biggin, P.C., and Kerr, I.D. (2014). Towards understanding promiscuity in multidrug efflux pumps. Trends in Biochemical Sciences *39*, 8–16.

Woodward, O.M., Köttgen, A., Coresh, J., Boerwinkle, E., Guggino, W.B., and Köttgen, M. (2009). Identification of a urate transporter, ABCG2, with a common functional polymorphism causing gout. Proceedings of the National Academy of Sciences *106*, 10338–10342.

Woodward, O.M., Köttgen, A., Coresh, J., Boerwinkle, E., Guggino, W.B., and Köttgen, M. (2009). Identification of a urate transporter, ABCG2, with a common functional polymorphism causing gout. Proceedings of the National Academy of Sciences.

Woodward, O.M., Tukaye, D.N., Cui, J., Greenwell, P., Constantoulakis, L.M., Parker, B.S., Rao, A., Köttgen, M., Maloney, P.C., and Guggino, W.B. (2013). Gout-causing Q141K mutation in ABCG2 leads to instability of the nucleotide-binding domain and can be corrected with small molecules. Proceedings of the National Academy of Sciences *110*, 5223–5228.

Wu, B., and Müller, J.D. (2005). Time-integrated fluorescence cumulant analysis in fluorescence fluctuation spectroscopy. Biophysical Journal *89*, 2721–2735.

Xia, C.Q., and Smith, P.G. (2012). Drug efflux transporters and multidrug resistance in acute leukemia: Therapeutic impact and novel approaches to mediation. Molecular Pharmacology *82*, 1008–1021.

Xie, Y., Xu, K., Linn, D.E., Yang, X., Guo, Z., Shimelis, H., Nakanishi, T., Ross, D.D., Chen, H., Fazli, L., et al. (2007). The 44-kDa Pim-1 kinase phosphorylates BCRP/ABCG2 and thereby promotes its multimerization and drug-resistant activity in human prostate cancer cells. Journal of Biological Chemistry *283*, 3349–3356.

Xu, J., Liu, Y., Yang, Y., Bates, S., and Zhang, J. (2004). Characterization of oligomeric human half-ABC transporter ATP-binding cassette G2. Journal of Biological Chemistry *279*, 19781–19789.

Xu, J., Peng, H., Chen, Q., Liu, Y., Dong, Z., and Zhang, J. (2007). Oligomerization domain of the multidrug resistance-associated transporter ABCG2 and its dominant inhibitory activity. Cancer Research *67*, 4373–4381.

Xu, K., Schwarz, P.M., and Ludueña, R.F. (2002). Interaction of nocodazole with tubulin isotypes. Drug Development Research *55*, 91–96.

Yang, F., Moss, L.G., and Phillips, G.N. (1996). The molecular structure of green fluorescent protein. Nature Biotechnology *14*, 1246–1251.

Yang, Y., Liu, Y., Dong, Z., Xu, J., Peng, H., Liu, Z., and Zhang, J.-T. (2007). Regulation of function by dimerization through the amino-terminal membrane-spanning domain of human ABCC1/MRP1. Journal of Biological Chemistry *282*, 8821–8830.

Yin, J., Straight, P.D., McLoughlin, S.M., Zhou, Z., Lin, A.J., Golan, D.E., Kelleher, N.L., Kolter, R., and Walsh, C.T. (2005). Genetically encoded short peptide tag for versatile protein labeling by Sfp phosphopantetheinyl transferase. Proceedings of the National Academy of Sciences *102*, 15815–15820.

Youker, R.T., Bruns, J.R., Costa, S.A., Rbaibi, Y., Lanni, F., Kashlan, O.B., Teng, H., and Weisz, O.A. (2013). Multiple motifs regulate apical sorting of p75 via a mechanism that involves dimerization and higher-order oligomerization. Molecular Biology of the Cell *24*, 1996–2007.

Yu, Y., Ulbrich, M.H., Li, M., Dobbins, S., Zhang, W.K., Tong, L., Isacoff, E.Y., and Yang, J. (2012). Molecular mechanism of the assembly of an acid-sensing receptor ion channel complex. Nature Communications *3*, 1252.

Yvan-Charvet, L., Pagler, T.A., Seimon, T.A., Thorp, E., Welch, C.L., Witztum, J.L., Tabas, I., and Tall, A.R. (2010). ABCA1 and ABCG1 protect against oxidative stress-induced macrophage apoptosis during efferocytosis. Circulation Research *106*, 1861–1869.

Zacharias, D.A., Violin, J.D., Newton, A.C., and Tsien, R.Y. (2002). Partitioning of lipid-modified monomeric GFPs into membrane microdomains of live cells. Science *296*, 913–916.

Zaitseva, J., Holland, I.B., and Schmitt, L. (2004). The role of CAPS buffer in expanding the crystallization space of the nucleotide-binding domain of the ABC transporter haemolysin B from Escherichia coli. Acta Crystallographica Section D: Biological Crystallography *60*, 1076–1084.

Zaitseva, J., Jenewein, S., Jumpertz, T., Holland, I.B., and Schmitt, L. (2005). H662 is the linchpin of ATP hydrolysis in the nucleotide-binding domain of the ABC transporter HlyB. EMBO Journal. *24*, 1901–1910.

Zarrabi, N., Ernst, S., Verhalen, B., Wilkens, S., and Börsch, M. (2014). Analyzing conformational dynamics of single P-glycoprotein transporters by Förster resonance energy transfer using hidden Markov models. Methods *66*, 168–179.

Zhang, L., Aleksandrov, L.A., Zhao, Z., Birtley, J.R., Riordan, J.R., and Ford, R.C. (2009). Architecture of the cystic fibrosis transmembrane conductance regulator protein and structural changes associated with phosphorylation and nucleotide binding. Journal of Structural Biology *167*, 242–251.

Zhang, P., Wang, J., and Shi, Y. (2010). Structure and mechanism of the S component of a bacterial ECF transporter. Nature *468*, 717–720.

Zhang, W., Mojsilovic-Petrovic, J., Andrade, M.F., Zhang, H., Ball, M., and Stanimirovic, D.B. (2003). The expression and functional characterization of ABCG2 in brain endothelial cells and vessels. FASEB Journal *17*, 2085–2087.

Zhang, W., Jiang, Y., Wang, Q., Ma, X., Xiao, Z., Zuo, W., Fang, X., and Chen, Y.-G. (2009). Single-molecule imaging reveals transforming growth factor- -induced type II receptor dimerization. Proceedings of the National Academy of Sciences *106*, 15679–15683.

Zhang, W., Yuan, J., Yang, Y., Xu, L., Wang, Q., Zuo, W., Fang, X., and Chen, Y.-G. (2010). Monomeric type I and type III transforming growth factor-β receptors and their dimerization revealed by single-molecule imaging. Cell Research *20*, 1216–1223.

Zhang, X., Schwartz, J.-C.D., Almo, S.C., and Nathenson, S.G. (2003). Crystal structure of the receptor-binding domain of human B7-2: Insights into organization and signaling. Proceedings of the National Academy of Sciences *100*, 2586–2591.

Zimmermann, T., Rietdorf, J., Girod, A., Georget, V., and Pepperkok, R. (2002). Spectral imaging and linear un-mixing enables improved FRET efficiency with a novel GFP2–YFP FRET pair. FEBS Letters *531*, 245–249.

Zimmermann, T., Rietdorf, J., and Pepperkok, R. (2003). Spectral imaging and its applications in live cell microscopy. FEBS Letters *546*, 87–92.

Zolotukhin, S., Potter, M., Hauswirth, W.W., Guy, J., and Muzyczka, N. (1996). A “humanized” green fluorescent protein cDNA adapted for high-level expression in mammalian cells. Journal of Virology *70*, 4646–4654.

Appendix

```
Sav1866             ------------------------------------------------------------
Human-ABCB1         --------------------------------MDLEGDRNGGAKKKNFFKLNNKSEKDKK
C.elegans-ABCB1     MLRNGSLRQSLRTLDSFSLAPEDVLKTAIKTVEDYEGDNIDSNG---EIKI---TRDAKE


Sav1866             ---------MIKRYLQFVKPYKYRIFATIIVGIIKFGIPMLIPLLIKYAIDGVINNHALT
Human-ABCB1         EKKPTVSVFSMFRYSNWLDKL-YMVVGTLAAIIHGAGLPLMMLVFGEM-TDIFANAGNLE
C.elegans-ABCB1     EVVNKVSIPQLYRYTTTLEKL-LLFIGTLVAVITGAGLPLMSILQGKV-SQAFINEQIVI
                              : **   :.     ...*: . *   *:*::  :  :   : . *   :

Sav1866             TDEKVHHLTIAIGIALFIFVIVRPPI----------------EFIRQYLAQWTSNKILYD
Human-ABCB1         DLMSNITNRSDINDTGFFMNLEEDMTRYAYYYSGIGAGVLVAAYIQVSFWCLAAGRQIHK
C.elegans-ABCB1     NNNGSTFLP--TGQNYTKTDFEHDVMNVVWSYAAMTVGMWAAGQITVTCYLYVAEQMNNR
                                       : .                       *       .: :

Sav1866             IRKKLYNHLQALSARFYANNQVGQVISRVINDVEQTKDFILTGLMNIWLDCITIIIALSI
Human-ABCB1         IRKQFFHAIMRQEIGWFDVHDVGELNTRLTDDVSKINEGIGDKIGMFFQSMATFFTGFIV
C.elegans-ABCB1     LRREFVKSILRQEISWFDTNHSGTLATKLFDNLERVKEGTGDKIGMAFQYLSQFITGFIV
                    :*::: . :   .  ::  .. * : ::: :::.: ::     :   :     :: .: :

Sav1866             MFFLDVKLTLAALFIFPFYILTVYVFFGRLRKLTRERSQALAEVQGFLHERVQGISVVKS
Human-ABCB1         GFTRGWKLTLVILAISPVLGLSAAVWAKILSSFTDKELLAYAKAGAVAEEVLAAIRTVIA
C.elegans-ABCB1     AFTHSWQLTLVMLAVTPIQALCGFAIAKSMSTFAIRETLRYAKAGKVVEETISSIRTVVS
                     *    :***. * : *.  *   .    : .:: ..    *:.  . .* : .* .* :

Sav1866             FAIEDNEAKNFDKKNTNFLTRALKHTRWNAYSFAAINTVTDIGPIIVIGVGAYLAISGSI
Human-ABCB1         FGGQKKELERYNKNLEEAKRIGIKKAITANISIGAAFLLIYASYALAFWYGTTLVLSGEY
C.elegans-ABCB1     LNGLRYELERYSTAVEEAKKAGVLKGLFLGISFGAMQASNFISFALAFYIGVGWVHDGSL
                    :     * :.:..   :    .: :      *:.*       .  :.:  *.  . .*.

Sav1866             TVGTLAAFVGYLELLFGPLRRL--VASFTTLTQSFASMDRVFQLIDEDYDIK--NGVGAQ
Human-ABCB1         SIGQVLTV--FFSVLIGAFSVGQASPSIEAFANARGAAYEIFKIIDNKPSIDSYSKSGHK
C.elegans-ABCB1     NFGDMLTT--FSSVMMGSMALGLAGPQLAVLGTAQGAASGIYEVLDRKPVIDSSSKAGRK
                    ..* : :   : .:::* :       .: .:  : .:   :::::*..  *.  .  * :

Sav1866             PIEIKQGRIDIDHVSFQYND-NEAPILKDINLSIEKGETVAFVGMSGGGKSTLINLIPRF
Human-ABCB1         PDNI-KGNLEFRNVHFSYPSRKEVKILKGLNLKVQSGQTVALVGNSGCGKSTTVQLMQRL
C.elegans-ABCB1     DMKI-KGDITVENVHFTYPSRPDVPILRGMNLRVNAGQTVALVGSSGCGKSTIISLLLRY
                      :* :* : . .* * * .  :. **: :** :: *:***:** ** **** :.*: *

Sav1866             YDVTSGQILIDGHNIKDFLTGSLRNQIGLVQQDNILFSDTVKENILLGRPTATDEEVVEA
Human-ABCB1         YDPTEGMVSVDGQDIRTINVRFLREIIGVVSQEPVLFATTIAENIRYGRENVTMDEIEKA
C.elegans-ABCB1     YDVLKGKITIDGVDVRDINLEFLRKNVAVVSQEPALFNCTIEENISLGKEGITREEMVAA
                    **  .* : :** ::: :    **: :.:*.*:  **  *: ***  *:   * :*:  *

Sav1866             AKMANAHDFIMNLPQGYDTEVGERGVKLSGGQKQRLSIARIFLNNPPILILDEATSALDL
Human-ABCB1         VKEANAYDFIMKLPHKFDTLVGERGAQLSGGQKQRIAIARALVRNPKILLLDEATSALDT
C.elegans-ABCB1     CKMANAEKFIKTLPNGYNTLVGDRGTQLSGGQKQRIAIARALVRNPKILLLDEATSALDA
                     * *** .** .**. ::* **:**.:********::*** ::.** **:*********

Sav1866             ESESIIQEALDVLSKDRTTLIVAHRLSTITHADKIVVIENGHIVETGTHRELIAKQGAYE
Human-ABCB1         ESEAVVQVALDKARKGRTTIVIAHRLSTVRNADVIAGFDDGVIVEKGNHDELMKEKGIYF
C.elegans-ABCB1     ESEGIVQQALDKAAKGRTTIIIAHRLSTIRNADLIISCKNGQVVEVGDHRALMAQQGLYY
                    ***.::* ***   * ***:::******: .** *   .:* :** * *  *: ::* *

Sav1866             HLYSIQNLMIKRYLQFVKPYKY----------------------------RIFATIIVG-
Human-ABCB1         KLVTMQTAGNEVELENAADESK--------SEIDALEMSSNDSRSSLIRKRSTRRSVRGS
C.elegans-ABCB1     DLVTAQTFTDAVDSAAEGKFSRENSVARQTSEHEGLSRQASEMDDIMNRVRS---STIGS
                    .* : *.             .                              *       *
```

Figure S1.1: Sequence alignment to map biochemically identified ABCB1 binding sites on X-ray crystal structures. Protein sequence of human ABCB1 was aligned against *S. aureus* Sav1866 and *C. elegans* ABCB1 using Clustal Omega (Sievers et al., 2011).

Figure S1.1 (continued)

```
Sav1866             ---------------------------------------IIKFGIPMLIPLLIK---YAID
Human-ABCB1         QAQDRKL-------------STKEALDE-SIPPVSFWRIMKLNLTEWPYFVVGVFCAIIN
C.elegans-ABCB1     ITNGPVIDEKEERIGKDALSRLKQELEENNAQKTNLFEILYHARPHALSLFIGMSTATIG
                                                      *:        :.:      *

Sav1866             GVIN------------NHALTTDEKVHHLTIAIGIALFIFVIVRPPIEFIRQYLAQ----
Human-ABCB1         GGLQPAFAIIFSKIIGVFTRI-DDPETKRQ--NSNLFSLLFLALGIISFITFFLQGFTFG
C.elegans-ABCB1     GFIYPTYSVFFTSFMNVFAG---NPADFLS--QGHFWALMFLVLAAAQGICSFLMTFFMG
                    * :              .:    :         .    ::.:.    . *  :*

Sav1866             WTSNKILYDIRKKLYNHLQALSARFYA--NNQVGQVISRVINDVEQTKDFILTGLMNIWL
Human-ABCB1         KAGEILTKRLRYMVFRSMLRQDVSWFDDPKNTTGALTTRLANDAAQVKGAIGSRLAVITQ
C.elegans-ABCB1     IASESLTRDLRNKLFRNVLSQHIGFFDSPQNASGKISTRLATDVPNLRTAIDFRFSTVIT
                     :.: :   :*  ::. :      ::   :*  * : :*: .*. : :  *   :  :

Sav1866             DCITIIIALSIMFFLDVKLTLAALFIFPFYILTVYVFFGRLRKLTRERSQALAEVQGFLH
Human-ABCB1         NIANLGTGIIISFIYGWQLTLLLLAIVPIIAIAGVVEMKMLSGQALKDKKELEGSGKIAT
C.elegans-ABCB1     TLVSMVAGIGLAFFYGWQMALLIIAILPIVAFGQYLRGRRFTGKNVKSASEFADSGKIAI
                       .:  .: : *:   :::*  : *.*:  :   :    :     :  . :     :

Sav1866             ERVQGISVVKSFAIEDNEAKNFDKKNTNFLTRALKHTRWNAYSFAAINTVTDIGPIIVIG
Human-ABCB1         EAIENFRTVVSLTQEQKFEHMYAQSLQVPYRNSLRKAHIFGITFSFTQAMMYFSYAGCFR
C.elegans-ABCB1     EAIENVRTVQALAREDTFYENFCEKLDIPHKEAIKEAFIQGLSYGCASSVLYLLNTCAYR
                    * :: . .* ::: *:.  . : :.      .:::.:   . ::.  .::  :

Sav1866             VGAYLAISGSITVGTLAAFVGYLELLFGPLRR-LVASF-TTLTQSFASMDRVFQLIDEDY
Human-ABCB1         FGAYLVAHKLM--SFEDVLLVFSAVVFGAMAVGQVSSFAPDYAKAKISAAHIIMIIEKTP
C.elegans-ABCB1     MGLALIITDPPTMQPMRVLRVMYAITISTSTLGFATSYFPEYAKATFAGGIIFGMLRKIS
                    .*  *            .:     : :.      .:*:    :::  :   :: :: :

Sav1866             DIK--NGVGAQPIEIKQGRIDIDHVSFQYND-NEAPILKDINLSIEKGETVAFVGMSGGG
Human-ABCB1         LIDSYSTEGLM-PNTLEGNVTFGEVVFNYPTRPDIPVLQGLSLEVKKGQTLALVGSSGCG
C.elegans-ABCB1     KIDSLSLAGE--KKKLYGKVIFKNVRFAYPERPEIEILKGLSFSVEPGQTLALVGPSGCG
                     *.  .  *    :   *.: : .* * *    :  :*: :.:.:: *:*:*:** ** *

Sav1866             KSTLINLIPRFYDVTSGQILIDGHNIKDFLTGSLRNQIGLVQQDNILFSDTVKENILLGR
Human-ABCB1         KSTVVQLLERFYDPLAGKVLLDGKEIKRLNVQWLRAHLGIVSQEPILFDCSIAENIAYGD
C.elegans-ABCB1     KSTVVALLERFYDTLGGEIFIDGSEIKTLNPEHTRSQIAIVSQEPTLFDCSIAENIIYGL
                    ***:: *: ****  .*::::** :** :     * ::.:*.*:  **. :: ***  *

Sav1866             PT--ATDEEVVEAAKMANAHDFIMNLPQGYDTEVGERGVKLSGGQKQRLSIARIFLNNPP
Human-ABCB1         NSRVVSQEEIVRAAKEANIHAFIESLPNKYSTKVGDKGTQLSGGQKQRIAIARALVRQPH
C.elegans-ABCB1     DPSSVTMAQVEEAARLANIHNFIAELPEGFETRVGDRGTQLSGGQKQRIAIARALVRNPK
                        .:  :: .**: ** * ** .**: :.*.**::*.:********::*** ::.:*

Sav1866             ILILDEATSALDLESESIIQEALDVLSKDRTTLIVAHRLSTITHADKIVVIENGHIVETG
Human-ABCB1         ILLLDEATSALDTESEKVVQEALDKAREGRTCIVIAHRLSTIQNADLIVVFQNGRVKEHG
C.elegans-ABCB1     ILLLDEATSALDTESEKVVQEALDRAREGRTCIVIAHRLNTVMNADCIAVVSNGTIIEKG
                    **:********* ***.::*****   : ** :::****.*: .** *.*..** : * *

Sav1866             THRELIAKQGAYEHLYSIQNL----
Human-ABCB1         THQQLLAQKGIYFSMVSVQAGTKRQ
C.elegans-ABCB1     THTQLMSEKGAYYKLTQKQMTEKK-
                    ** :*::::* *  : . *
```

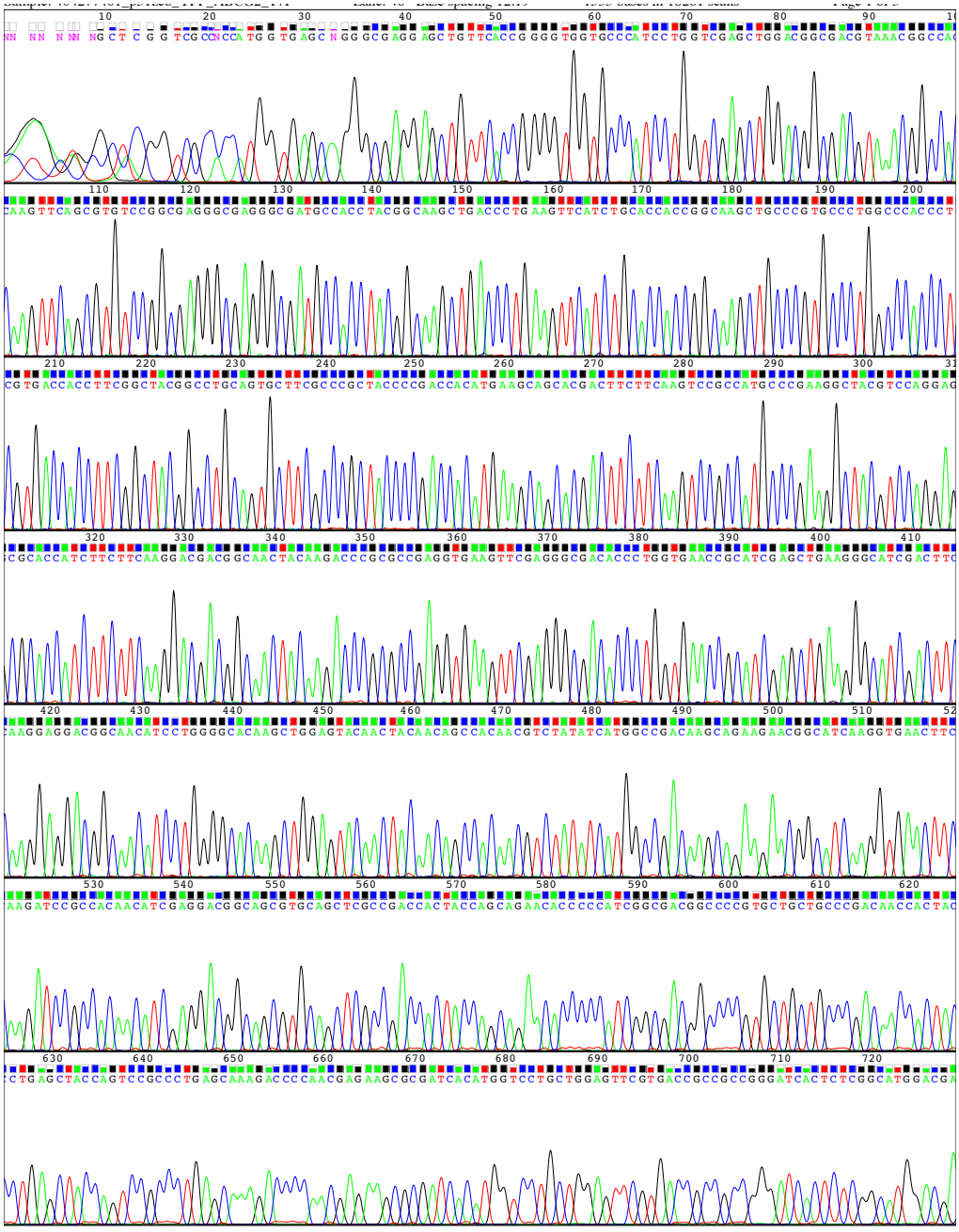

Figure S3.1: Sequencing data (DNA chromatogram) of YFP-ABCG2 obtained using T7F primer.

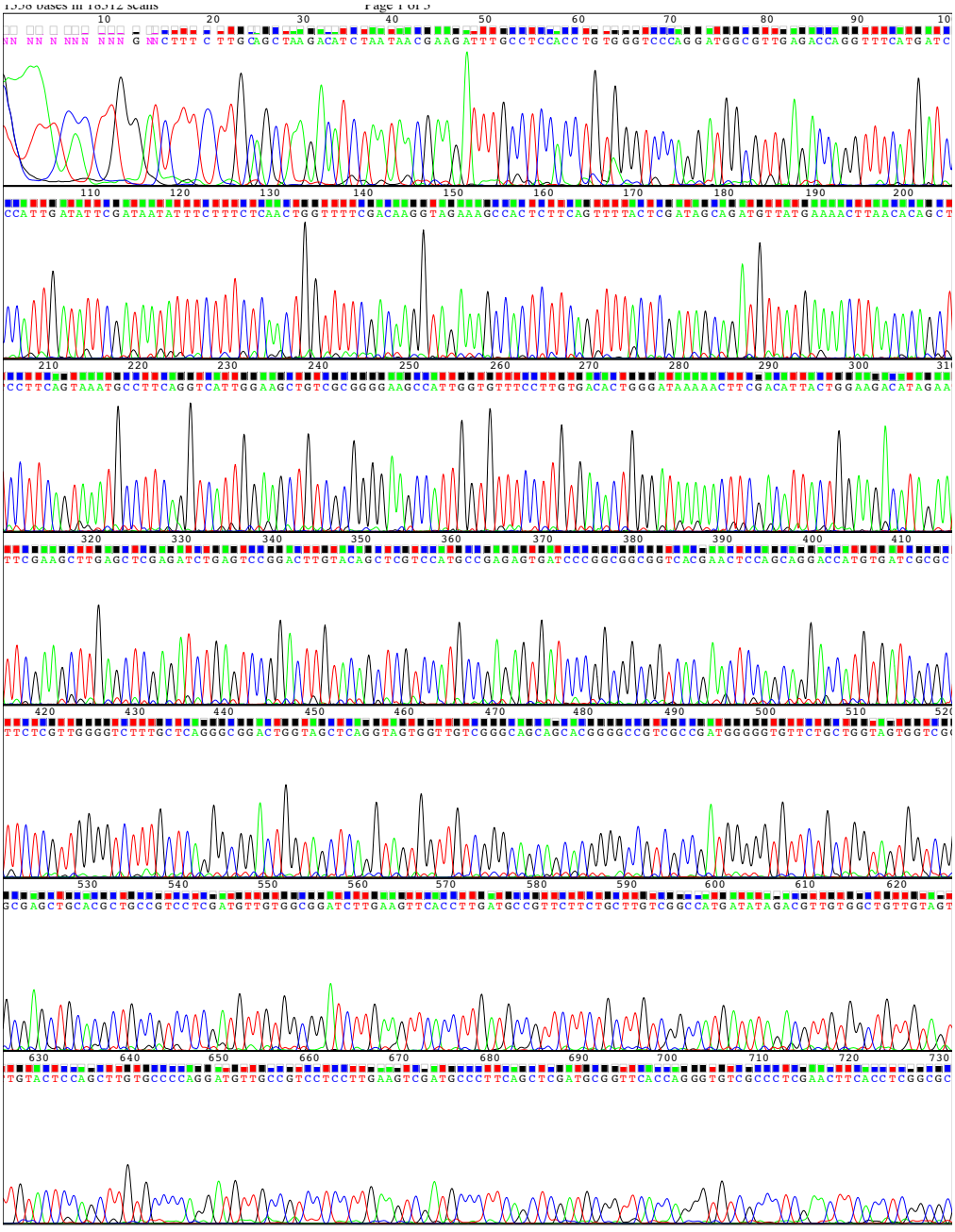

Figure S3.2: Sequencing data (DNA chromatogram) of YFP-ABCG2 obtained using SeqR1 primer.

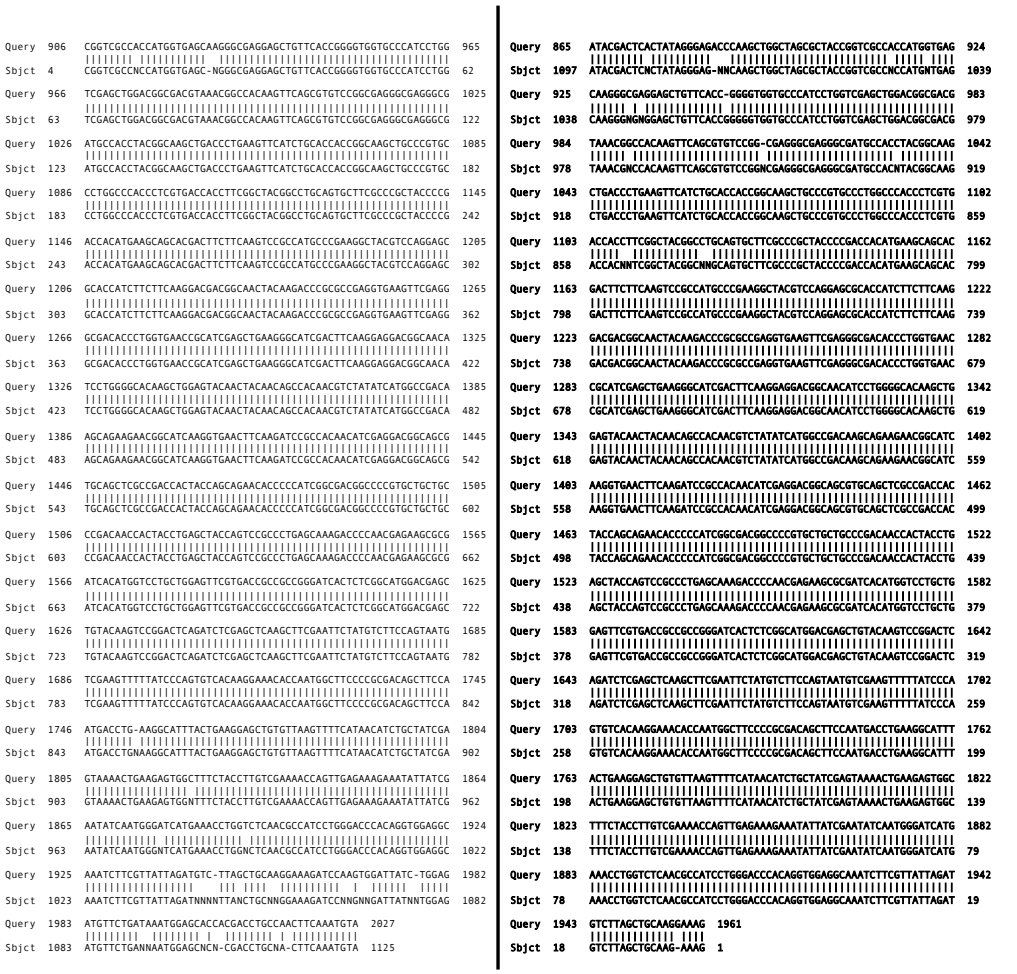

Figure S3.3: Examples of sequence alignment in YFP-ABCG2. DNA Sequencing data (Sbjct) obtained for YFP-ABCG2 using T7F and SeqR1 primers were aligned against the predicted sequences (Query).

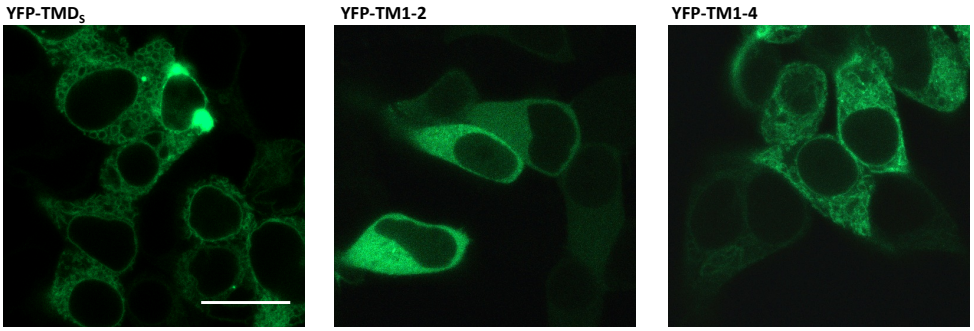

Figure S5.1: Confocal images for three different YFP-tagged truncated ABCG2 constructs expressed in single transfected HEK293T cells. Figure shows that all three constructs were retained intracellularly. Whilst YFP-TMD$_S$ and YFP-TM1-4 localisation pattern was consistent with retention in the endoplasmic reticulum, YFP-TM1-2 showed a diffuse cytoplasmic localisation. Scale bar = 20 µm.

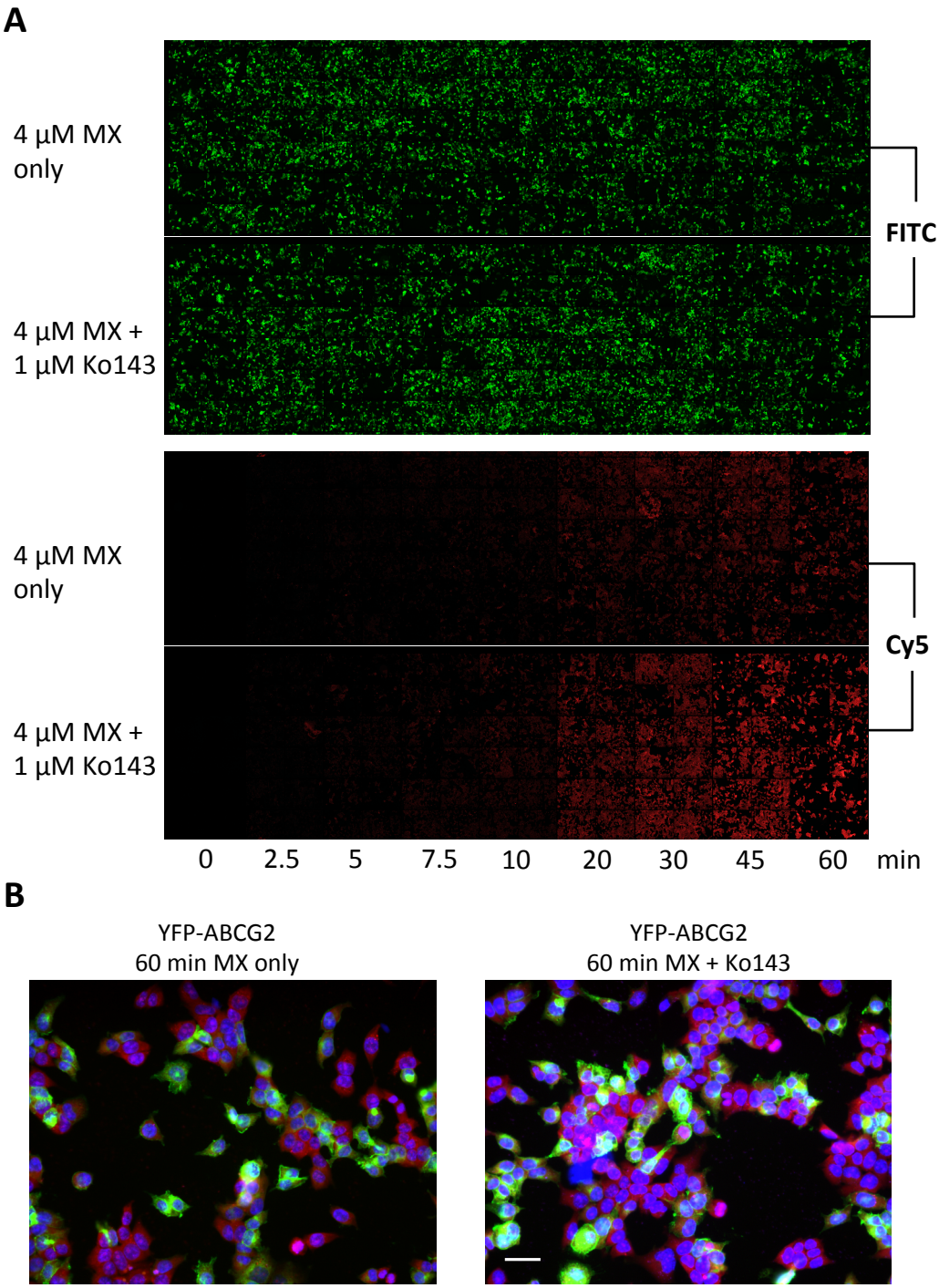

Figure S5.2: Fluorescence images acquired during the accumulation assay in HEK293T cells transiently expressing YFP-ABCG2. A – Fluorescence images of YFP-ABCG2 expressing cells (FITC channel, green, top) and the corresponding mitoxantrone (MX) accumulation (Cy5 channel, red, bottom) in a 96-well plate incubated with either 4 µM MX only or 4 µM MX + 1 µM Ko143, from 0 to 60 min at 37 °C. Images were acquired from 6 x 9 wells (4 sites each well). Nucleus staining was not indicated in this panel. **B –** Overlay images showing nucleus stain (DAPI channel, blue), YFP-ABCG2 (FITC channel, green), and MX (Cy5 channel, red) acquired at 60 min incubation with either MX only (right) or MX + Ko143 (left). Scale bar = 20 µm.

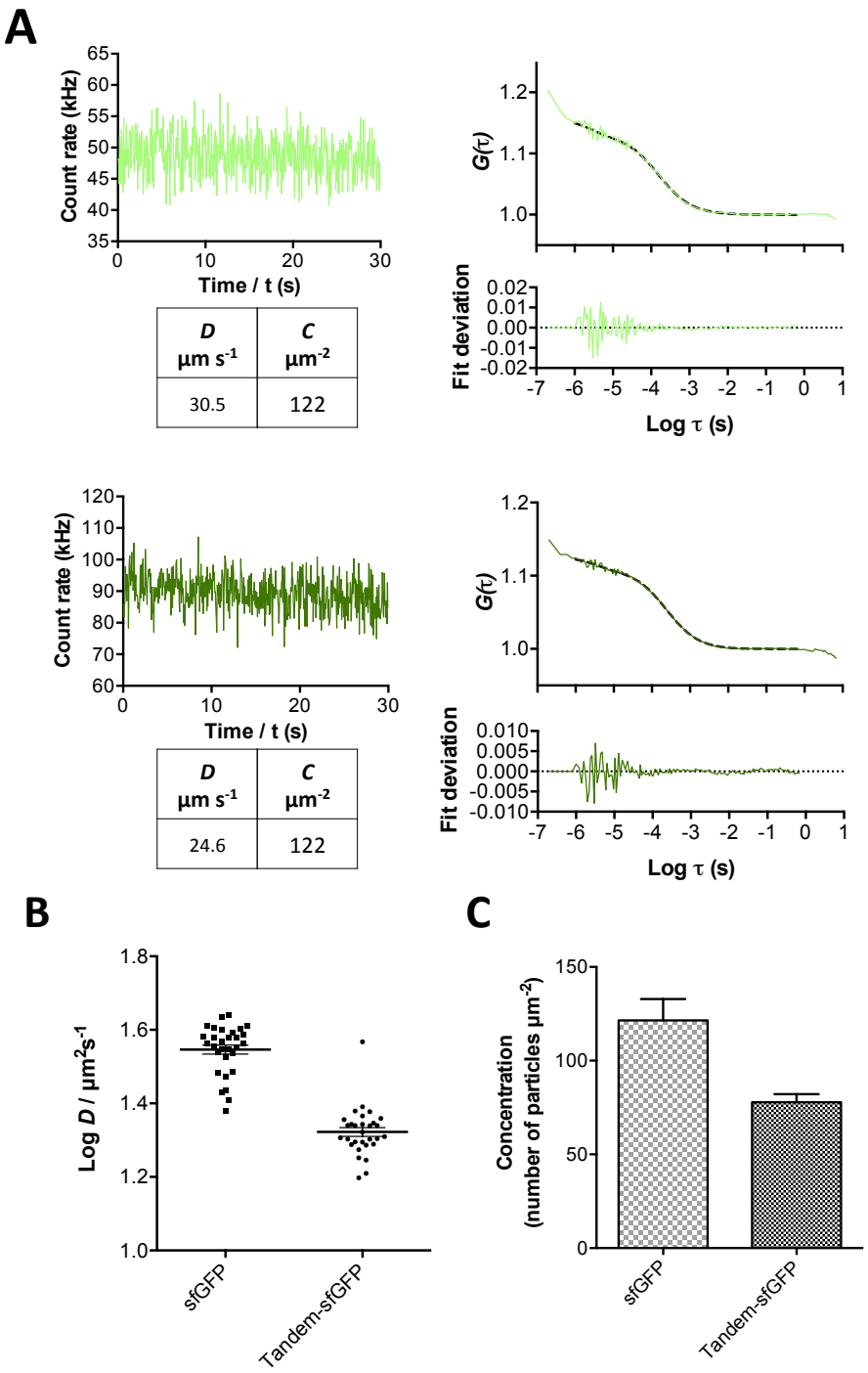

Figure S6.1: Diffusion coefficients (*D*) and membrane concentration (*C*) of sfGFP and tandem-sfGFP. A – Examples of FCS data for sfGFP (top panel, light green) and tandem-sfGFP (bottom panel, dark green). Fitting of autocorrelation curves with a single-component 3D diffusion model (black dotted line) are shown together with the deviations. The *D* and *C* values determined from the examples are also indicated in the tables. **B –** Diffusion coefficients of tandem-sfGFP and sfGFP were presented as Log *D* (mean ± SEM). **C –** Concentration (number of particles per µm^2, *C*, mean ± SEM) of the tandem-sfGFP and sfGFP. **B and C –** Results were obtained using the τ_{D1} and N_1 values from the single-component 3D diffusion autocorrelation analysis. Data were collected from at least 25 cells over 3 experiments.

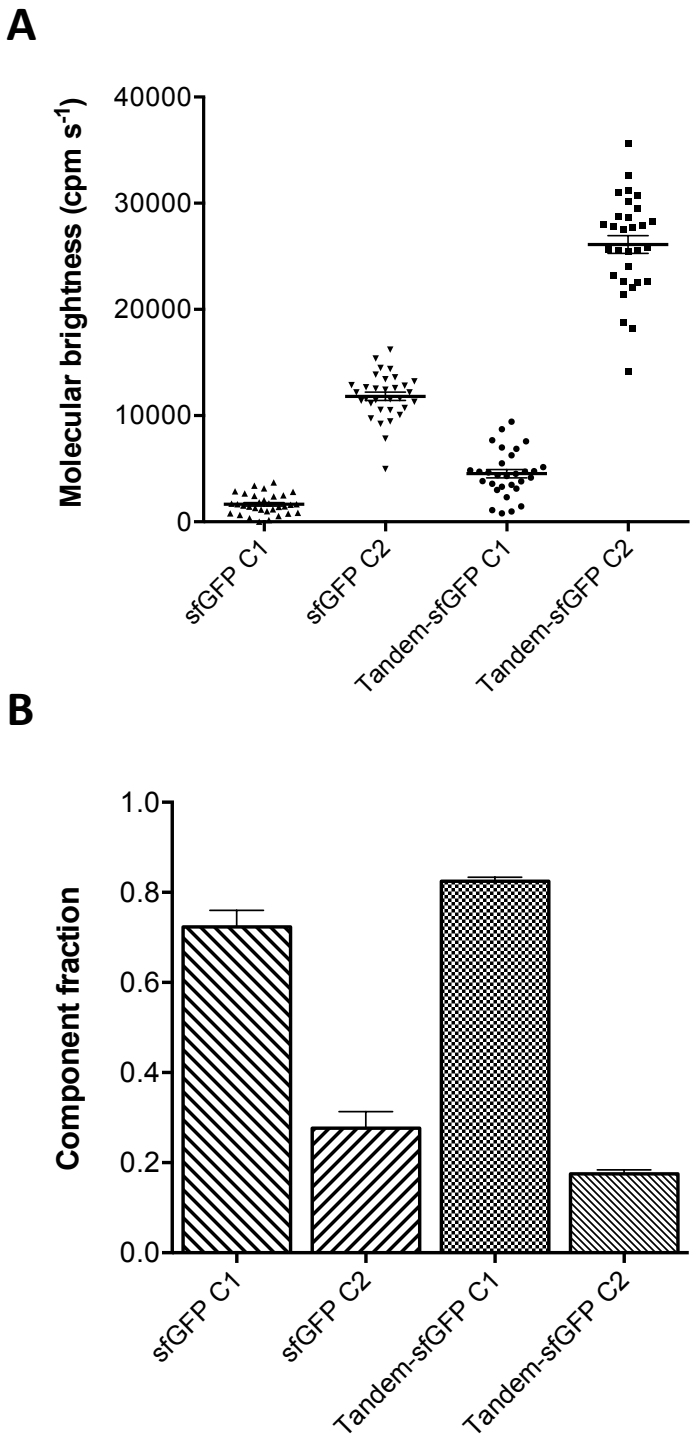

Figure S6.2: 2-component PCH analysis of sfGFP and tandem-sfGFP validates the PCH analysis methods. A – Molecular brightness (mean ± SEM) of component 1 (C1) and component 2 (C2) of sfGFP and tandem-sfGFP. **B –** Component fractions of C1 and C2 obtained for sfGFP and tandem-sfGFP. 2-component PCH analysis was performed in Zen 2010. Data were collected from at least 25 cells over 3 independent experiments.

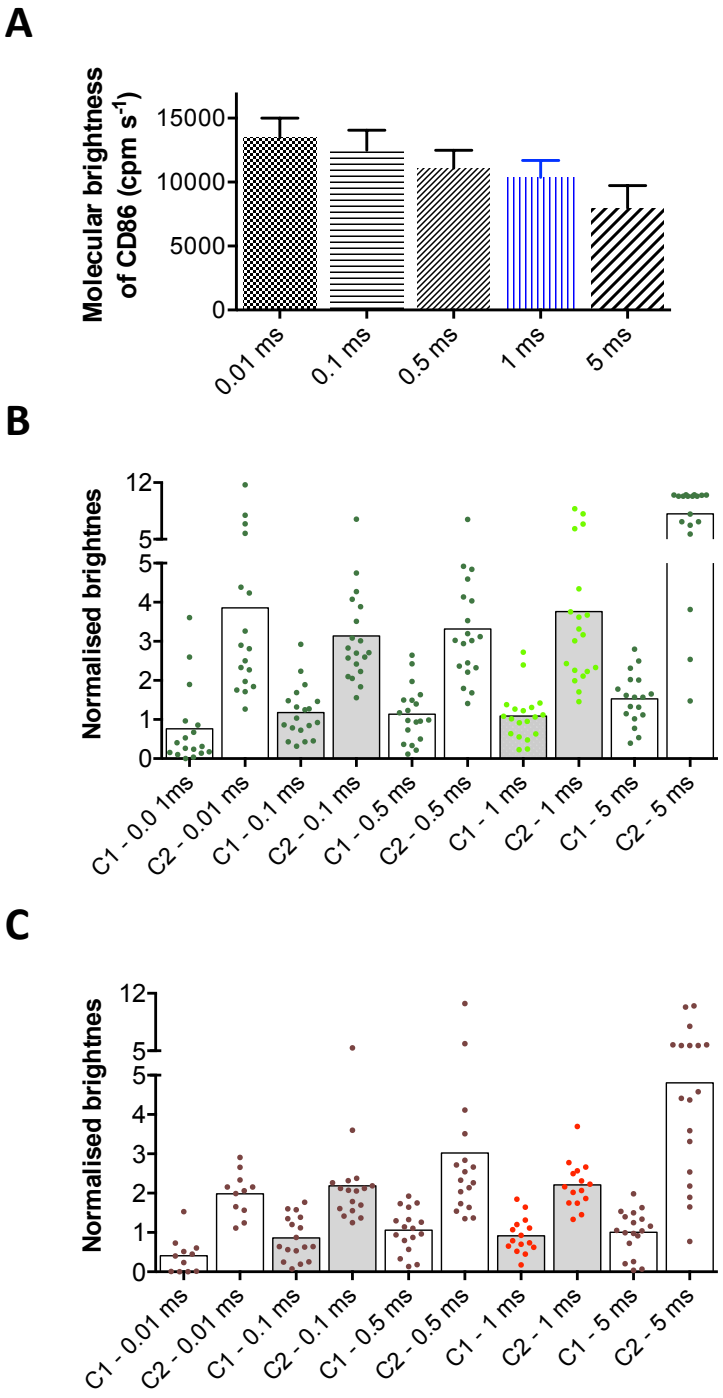

Figure S6.3: No apparent differences in molecular brightness of CD86-sfGFP and normalised brightness of CD28-sfGFP and sfGFP-ABCG2 using different binning times. A – Molecular brightness of CD86-sfGFP obtained using various binning times in 1-component PCH analysis. **B and C –** Normalised brightness of component 1 (C1) and component 2 (C2) of CD28-sfGFP and sfGFP-ABCG2 (relative to the average molecular brightness of CD86-sfGFP in A) obtained using various binning times in 2-component PCH analysis. **A, B and C –** Data were collected from at least 10 cells from two independent experiments. Apart from the increase in C2 normalised brightness using 5 ms binning time analysis, no other noticeable difference was observed using the different binning times.

A

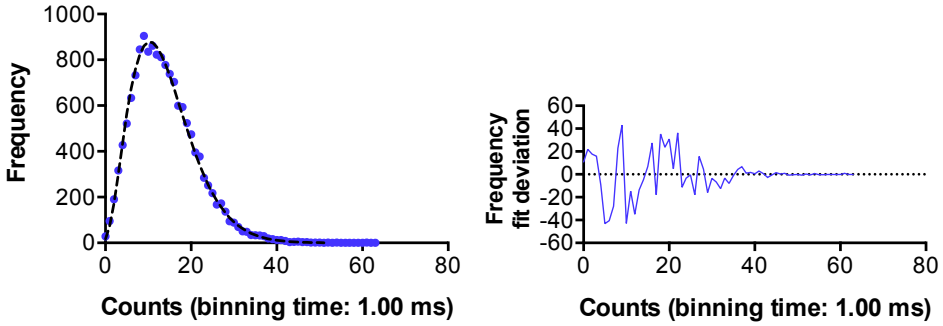

Counts per molecule (kHz)	C1 No. of molecules	C1 Brightness (cpm s^{-1})	First order correction	Reduced chi ²
3.73	4.9	9337	0.16	1.15

B

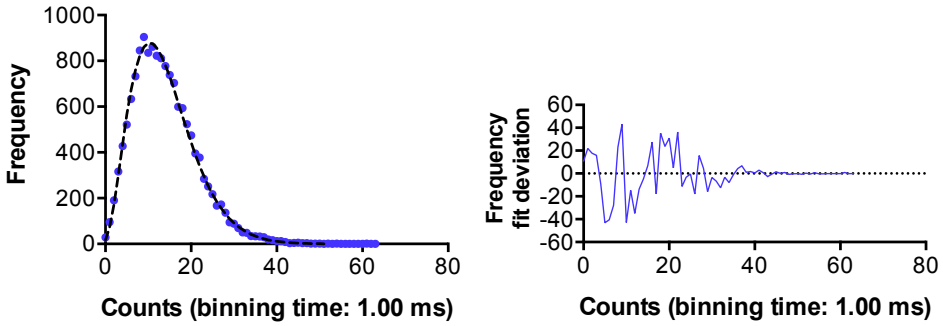

Counts per molecule (kHz)	C1 No. of molecules	C2 No. of molecules	C1 Brightness (cpm s^{-1})	C2 Brightness (cpm s^{-1})	First order correction	Reduced chi ²
3.73	2.6	2.2	9292	9392	0.16	1.20

Figure S6.4: Example PCH analysis from CD86-sfGFP data set. 1-component (**A**) and 2-component (**B**) 3D PCH models were used for the fitting of the PCH distributions obtained from one of the FCS traces of CD86-sfGFP, using 1 ms binning time. The fit deviations and reduced chi^2 values provide an indication of goodness of fit for the different PCH models. The average number of molecules and brightness values for component 1 (C1) and component 2 (C2, for 2-component analysis in B) are also shown in the tables. The applied first order correction was determined from calibration experiments to correct for single photon excitation employed (section 2.9.3). PCH analysis was performed in Zen 2010.

A

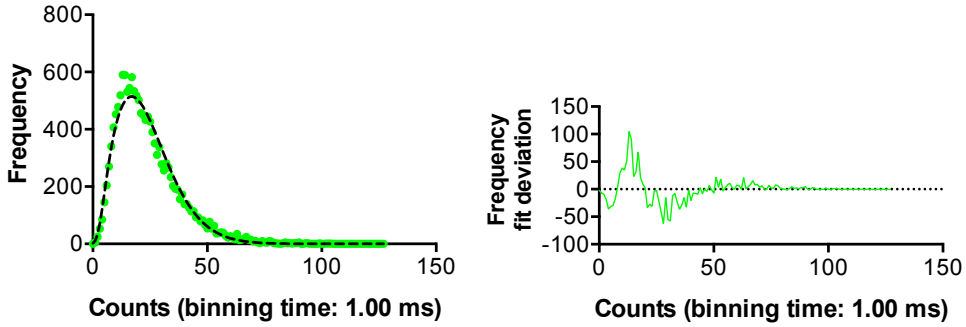

Counts per molecule (kHz)	C1 No. of molecules	C1 Brightness (cpm s^{-1})	First order correction	Reduced chi ²
8.73	4.1	18583	0.16	3.17

B

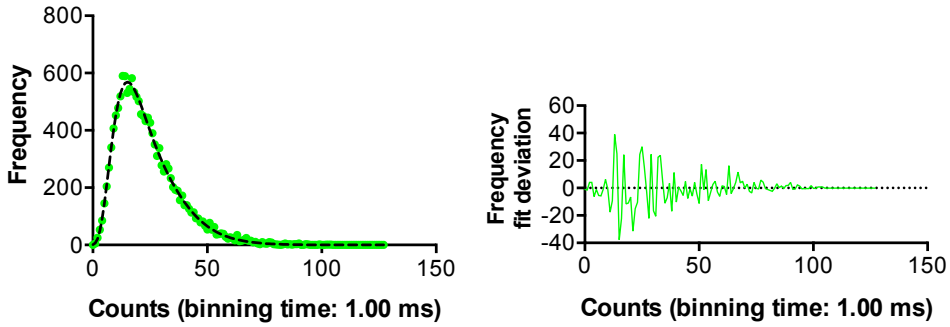

Counts per molecule (kHz)	C1 No. of molecules	C2 No. of molecules	C1 Brightness (cpm s^{-1})	C2 Brightness (cpm s^{-1})	First order correction	Reduced chi ²
4.47	4.5	1.5	6827	29969	0.16	1.13

Figure S6.5: Example PCH analysis from CD28-sfGFP data set. 1-component (**A**) and 2-component (**B**) 3D PCH models were used for the fitting of the PCH distributions obtained from one of the FCS traces of CD28-sfGFP, using 1 ms binning time. The fit deviations and reduced chi^2 values provide an indication of goodness of fit for the different PCH models. The average number of molecules and brightness values for component 1 (C1) and component 2 (C2, for 2-component analysis in B) are also shown in the tables. The applied first order correction was determined from calibration experiments to correct for single photon excitation employed (section 2.9.3). PCH analysis was performed in Zen 2010.

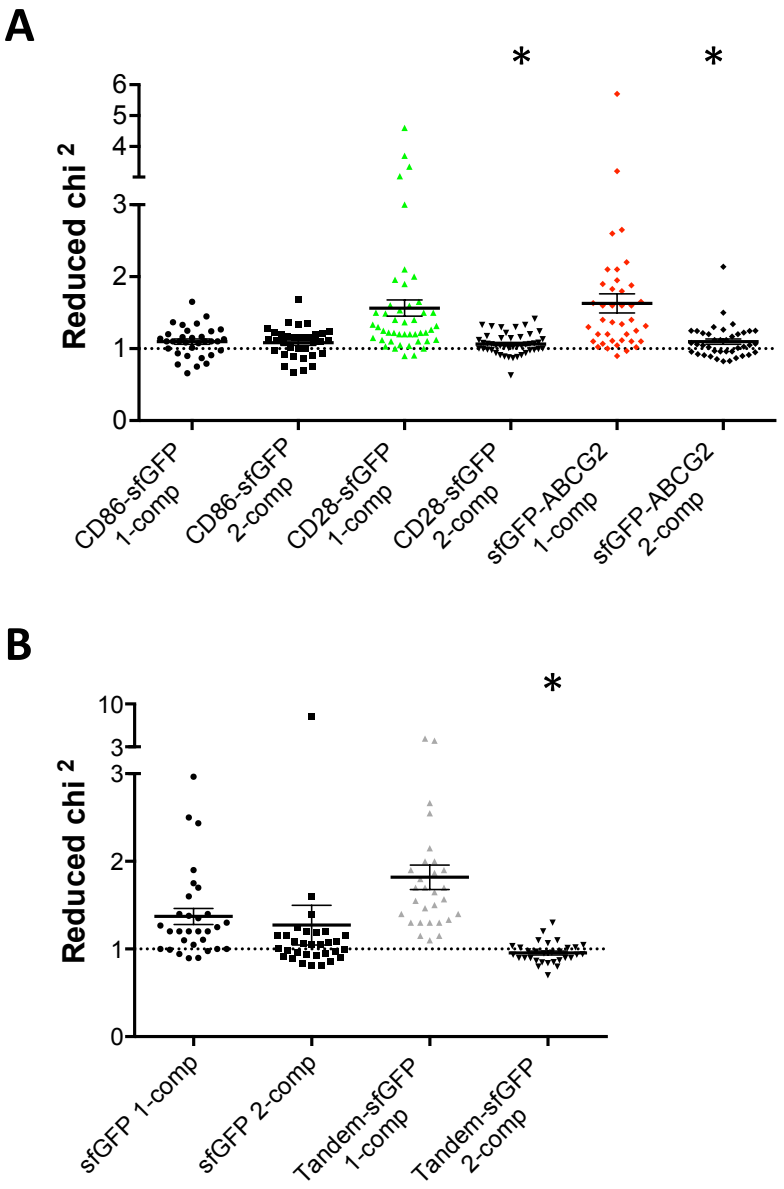

Figure S6.6: 2-component PCH model shows improved fitting for sfGFP-ABCG2 and CD28-sfGFP data sets. Reduced chi^2 values (mean ± SEM) obtained from 1-component (1-comp) or 2-component (2-comp) PCH analysis for the various data sets (CD86-sfGFP, CD28-sfGFP and sfGFP-ABCG2 in **A**; sfGFP and tandem-sfGFP in **B**). Reduced chi^2 values of 1 indicate optimal fits were obtained with respective models, whilst values of > 1 suggest less optimal fit and values of < 1 indicate "overfitting" and increased errors in the fit, for the respective models. 2-component PCH model significantly improved the fitting of CD28-sfGFP (green), sfGFP-ABCG2 (red), and tandem-sfGFP (grey) data sets, as the reduced chi^2 values were significant lower compared to those obtained from the respective 1-component PCH fits, $p < 0.05$ (*). Data were collected from at least 30 cells over 4 independent experiments (**A**) or 25 cells over 3 independent experiments (**B**). Statistical significance was assessed using non-parametric Kruskal-Wallis analysis followed by Dunnett's multiple comparisons test.

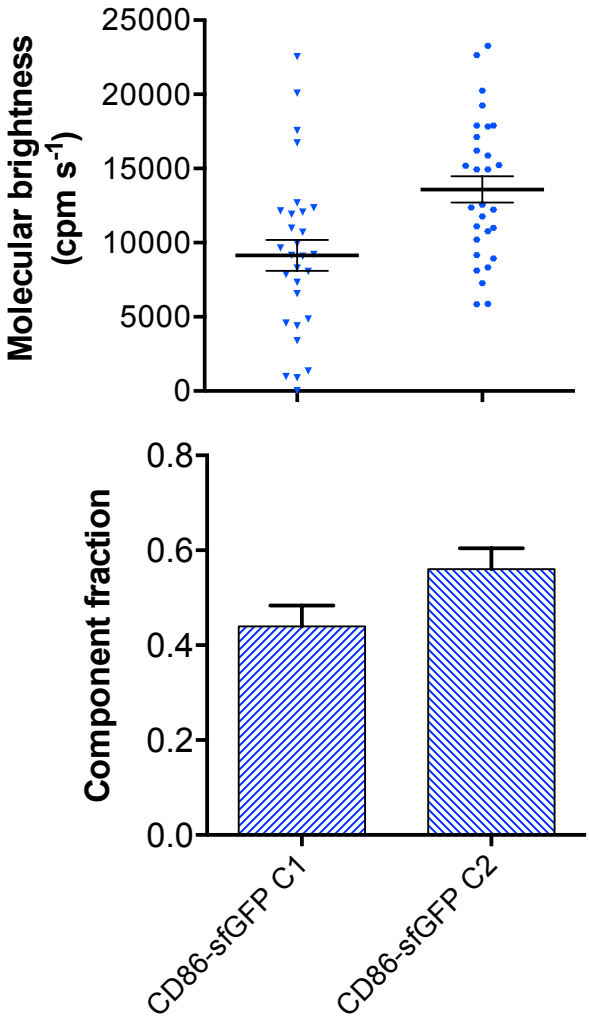

Figure S6.7: No difference in molecular brightness and component fractions between component 1 and component 2 of CD86-sfGFP. Top panel: Molecular brightness (mean ± SEM) of component 1 (C1) and component 2 (C2). Bottom panel: Component fractions of C1 and C2. 2-component analysis was performed in Zen 2010. Figure shows that 2-component PCH analysis did not identify a second component from the CD86-sfGFP data sets, as there were no differences between the molecular brightness and fractions obtained for C1 vs C2. Data were collected from at least 30 cells over 4 independent experiments.

Table S7.1: Goodness of fit assessment using R-values for the determination of the best oligomeric models. The goodness of fit of the various oligomeric models obtained with different probability of fluorescent sfGFP was assessed using the reduced chi^2 values (R-values) as shown in the table. R-values were calculated using the differences between the observed and expected values obtained from the respective models (section 2.10.3), R-values closer to 1 indicates better fit. Oligomeric models with p = 0.55 are shown to best describe the photobleaching step frequency histograms, from which the lowest combined R-value was obtained.

When p = 0.50	sfGFP-ABCG2	CD28-sfGFP	ABCC4-sFGFP
Dimer model	1162	254	185
Trimer model	83	4	3
Tetramer model	10	20	16
Pentamer model	10	57	43
When p = 0.55	**sfGFP-ABCG2**	**CD28-sfGFP**	**ABCC4-sfGFP**
Dimer model	850	180	135
Trimer model	52	5	3
Tetramer model	6	39	29
Pentamer model	27	101	74
When p = 0.60	**sfGFP-ABCG2**	**CD28-sfGFP**	**ABCC4-sfGFP**
Dimer model	638	128	122
Trimer model	34	13	8
Tetramer model	12	70	51
Pentamer model	56	169	98

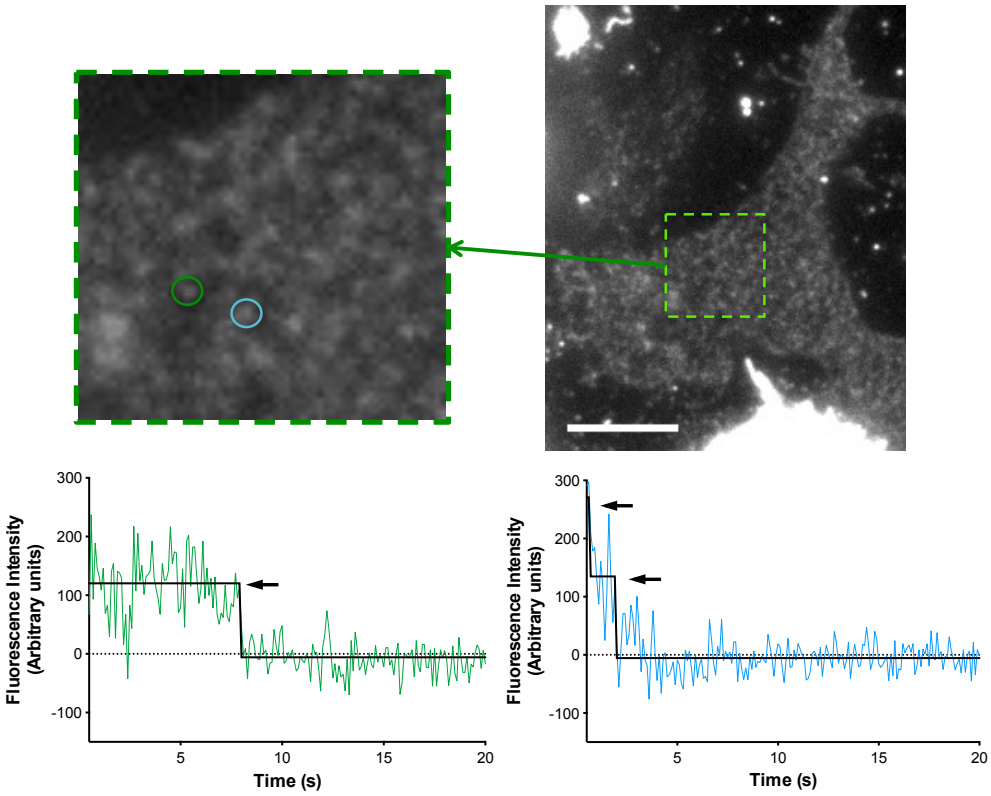

Figure S7.1: Examples of photobleaching step detection analysis in CD28-sfGFP expressing cell. Two selected fluorescent spots are highlighted in the magnified TIRF image of a HEK293T cell expressing CD28-sfGFP. Fluorescence intensity plots show the corresponding traces for the two fluorescent spots (according to colours). The arrows indicate the photobleaching steps determined in the final idealised step detection traces (black curves). Scale bar = 10 µm.

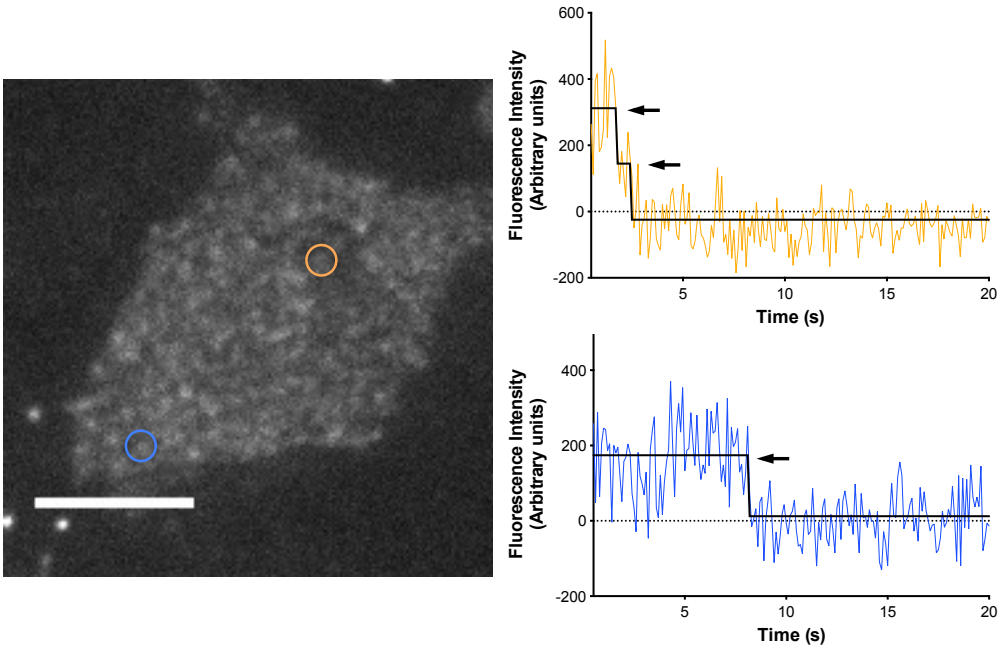

Figure S7.2: Examples of photobleaching step detection analysis in ABCC4-sfGFP expressing cell. Two selected fluorescent spots are highlighted in the magnified TIRF image of a HEK293T cell expressing ABCC4-sfGFP. Fluorescence intensity plots show the corresponding traces for the two fluorescent spots (according to colours). The arrows indicate the photobleaching steps determined by the final idealised step detection traces (black curves). Scale bar = 10 µm.

A

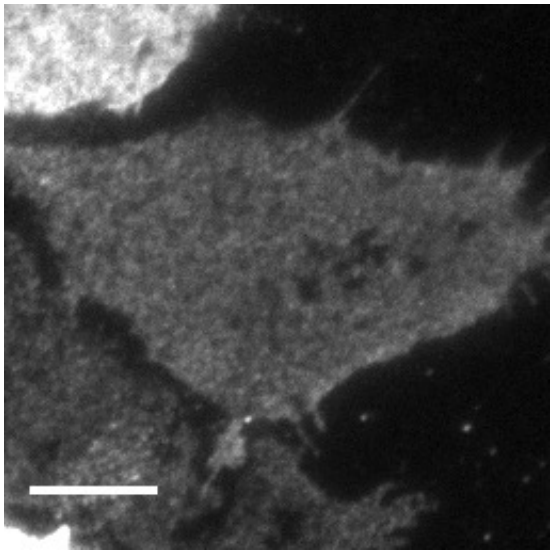

B

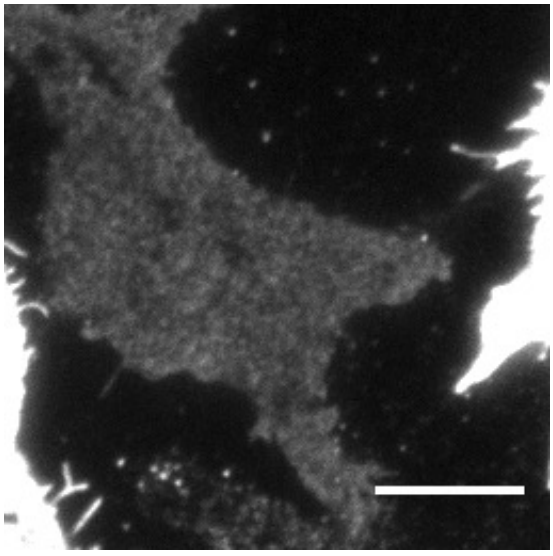

Figure S7.3: TIRF images of HEK293T cells expressing CD86-sfGFP. Two examples of TIRF images obtained for from low expressing CD86-sfGFP clones (**A and B**). These images (and most TIRF images obtained for CD86-sfGFP) were deemed inadequate for further analysis due to poor spot separation. Scale bar = 10µm.

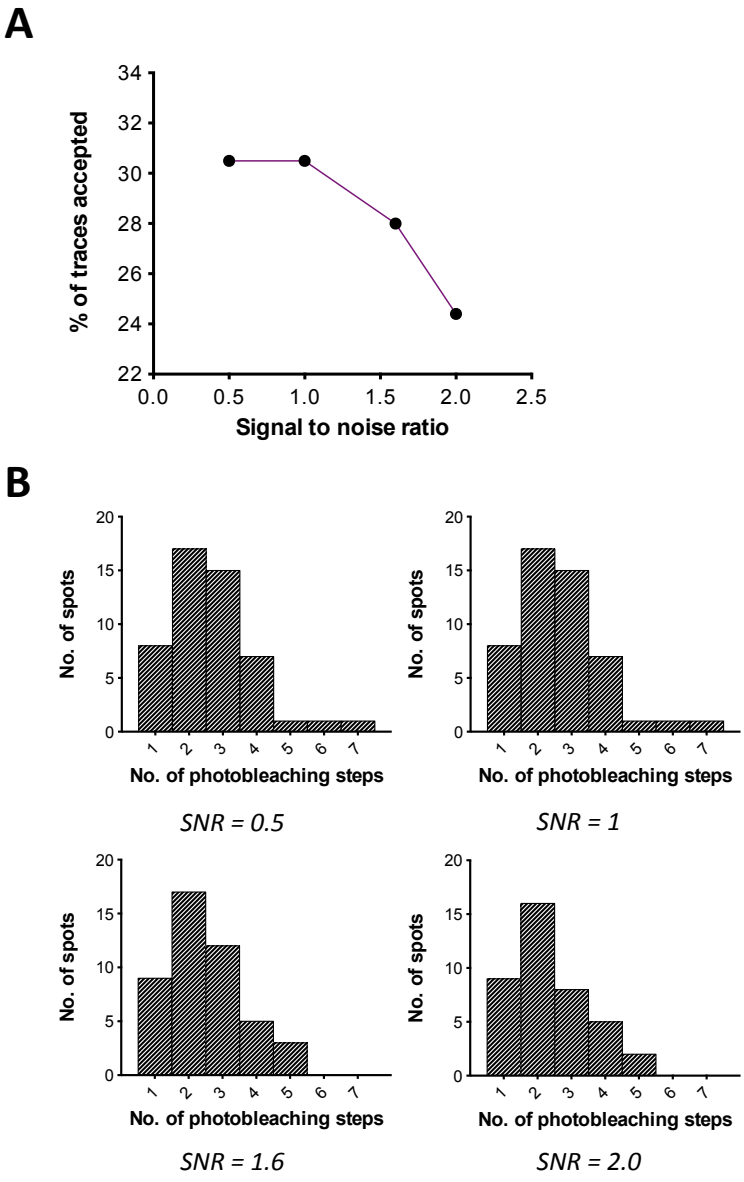

Figure S7.4: The effects of steps to noise ratios (SNR) on % of traces accepted and photobleaching step frequency histograms. A – As the minimum SNR employed for the analysis was increased, the % of traces accepted was reduced, i.e. more traces were rejected. **B –** The resultant photobleaching step frequency histograms using the corresponding SNRs are shown. **A and B –** Data were obtained from analysing the TIRF video shown in Figure 7.4 using different SNR whilst other parameters remained identical. The SNR chosen in this study was 1.6. It was lower compared to the SNR employed by (McGuire et al., 2012) (2.5) because the Chung-Kennedy (CK) filter incorporated within the software was not applied to the traces. The CK filter was shown to increase the fluorescence signal and SNR significantly (McGuire et al., 2012). However, in traces with higher SNR (> 2), a reduction of step detection accuracy was observed, and McGuire et al. recommended excluding traces with SNR of < 1.8 from the CK filter analysis. This feature in the software was not functioning and the authors acknowledged that a further update is required. Considering this technical limitation within the software, the CK filter was not applied to the fluorescence intensity traces in this study and the SNR was set to 1.6.